

LASER NOISE MITIGATION THROUGH TIME DELAY INTERFEROMETRY FOR
SPACE-BASED GRAVITATIONAL WAVE INTERFEROMETERS USING THE UF LASER
INTERFEROMETRY SIMULATOR

By

SHAWN J. MITRYK

A DISSERTATION PRESENTED TO THE GRADUATE SCHOOL
OF THE UNIVERSITY OF FLORIDA IN PARTIAL FULFILLMENT
OF THE REQUIREMENTS FOR THE DEGREE OF
DOCTOR OF PHILOSOPHY

UNIVERSITY OF FLORIDA

2012

© 2012 Shawn J. Mitryk

I dedicate this work to my parents, Jeff and Terry Mitryk, whom provided the opportunity and never questioned my desire to fulfill my dreams, whatever they may be.

ACKNOWLEDGMENTS

I'd like to give a special thanks to everyone who helped me with these projects. Guido Mueller, whom managed to be an research advisor, a career mentor, and a close colleague, all at the same time, provided insight and direction towards my education and scientific pursuits. Ira Thorpe was essential to my development as a effective and creative problem-solver and provided a base for my future experimental investigations. Thanks to Dylan Sweeney, Yinan Yu, Pep Sanjuan, and Syed Azer for allowing me to pick their brains and for assistance in deciphering complications with my experiments. Also, I'd like to specifically thank my high-school physics teacher, Mr. Steven Desanto, whom noted my talents in the sciences and particularly, in physics, and inspired me to cultivate them. And thanks to everyone else who worked in the UF-LISA project as well as those that came to visit for keeping my days in the lab interesting.

TABLE OF CONTENTS

	<u>page</u>
ACKNOWLEDGMENTS	4
LIST OF TABLES	9
LIST OF FIGURES	10
ABSTRACT	13
CHAPTER	
1 INTRODUCTION	15
1.1 Gravitation and General Relativity	15
1.2 The Gravitational Wave Spectrum	16
1.3 Space-Based Gravitational Wave Astronomy	17
1.4 Details of the Dissertation's Content	20
1.5 Note to the Reader	20
2 GENERAL RELATIVITY AND GRAVITATIONAL WAVES	21
2.1 Introduction to General Relativity	21
2.1.1 Newtonian Gravity	21
2.1.2 Einstein Field Equations	21
2.1.3 Proper Time Invariance	22
2.1.4 Metrics, Black Holes, and Curvature	23
2.1.5 Geodesics	27
2.1.6 Einstein Field Equations Revisited	28
2.2 Gravitational Wave Derivation	29
2.2.1 Polarized Plane Wave Solutions	29
2.2.2 Spacetime Strain	30
2.2.3 Weak-field GR Multipole Expansion	31
2.3 Gravitational Wave Sources and Detection Methods	35
2.3.1 Strain Estimation	35
2.3.2 Gravitational Wave Evidence	35
2.3.3 The Gravitational Wave Spectrum	36
2.3.4 LISA Gravitational Wave Sources	37
2.3.4.1 Compact Binaries	38
2.3.4.2 Binary Black Hole Mergers	38
2.3.4.3 Extreme Mass Ratio Inspirals	39
2.3.4.4 Other Suggested Sources	39
3 THE LASER INTERFEROMETER SPACE ANTENNA	40
3.1 LISA Overview	40
3.2 The Disturbance Reduction System	42

3.3	The Interferometry Measurement System	42
3.4	μ Cycle Accuracy Phase Measurement	47
3.4.1	Photodetector Noise	48
3.4.1.1	Shot-Noise	48
3.4.1.2	Dark Current Noise	49
3.4.1.3	Johnson-Nyquist Noise	49
3.4.1.4	Flicker Noise	50
3.4.1.5	Heterodyne Phase Measurements	51
3.4.2	μ Cycle Phasemeter	51
3.4.2.1	Clock Noise	52
3.4.2.2	ADC Quantization Noise	53
3.4.2.3	ADC Amplitude Noise	53
3.4.2.4	Clock-ADC Timing Jitter	54
3.4.2.5	Demodulation Noise Coupling	55
3.4.3	Heterodyne Time-Delay Interferometry	58
3.4.3.1	Fiber Noise	60
3.4.3.2	Spacecraft/Proof-Mass Motion	61
3.4.3.3	Inter-Spacecraft Motion	62
3.4.3.4	Basic TDI-Combinations and Considerations	65
4	TIME DELAY INTERFEROMETRY	69
4.1	Laser Noise Cancellation	69
4.1.1	Laser Noise	70
4.1.2	Clock Noise Transfers	70
4.1.3	Ranging Errors	71
4.1.4	Fractional Delay Filtering and Interpolation	72
4.2	Laser Pre-stabilization	73
4.2.1	Pound-Drever-Hall Locking	74
4.2.2	Arm Locking	75
4.3	TDI Theory	77
4.3.1	TDI Combinations	77
4.3.2	Sagnac Combinations	79
4.3.2.1	TDI Six-Pulse Combinations	79
4.3.2.2	TDI Symmetric-Sagnac Combination	80
4.3.3	Michelson X-combinations	80
4.3.3.1	TDI- $X_{0.0}$	81
4.3.3.2	TDI- $X_{1.0}$	82
4.3.3.3	TDI- $X_{2.0}$	84
4.3.4	LISA Orbital Dynamics and TDI Data Analysis	84
4.4	Ranging	85
4.4.1	Pseudo-random Noise (PRN) Code Ranging	86
4.4.2	Time-delay Interferometry Ranging (TDIR)	88
4.4.2.1	TDI Ranging Tone	89
4.4.2.2	TDI Ranging Parameter Search Algorithm	90

5	THE LISA PHASEMETER	94
5.1	Digital Signal Processing (DSP) System	94
5.2	μ Cycle Phase Measurements	94
5.2.1	Design	95
5.2.2	Phasemeter Readouts	100
5.2.2.1	Phase Quantization Noise	101
5.2.2.2	CIC Downsampling and Aliasing	102
5.2.3	Phasemeter Test-Measurements	103
5.2.4	Phasemeter Noise Model	105
5.2.5	Differential and Entangled Measurements	107
5.2.5.1	Digitally Split Differential Noise	107
5.2.5.2	Electronically Split Differential Noise	109
5.2.5.3	Entangled Phase Noise	113
5.2.6	Applications in LISA and LIGO	115
5.3	ADC Noise Estimation	116
5.4	Timing Jitter Extraction	122
5.4.1	Phase Dispersion Mitigation	126
5.4.2	Absolute Timing Jitter Extraction	127
5.5	Phasemeter Performance Review	128
6	THE UNIVERSITY OF FLORIDA LISA INTERFEROMETRY SIMULATOR	131
6.1	The LISA Laser Test-bench	131
6.2	The Electronic Phase Delay (EPD) Unit	134
6.2.1	Design	134
6.2.2	Verification	138
6.2.2.1	Time-changing Time Delay	142
6.2.2.2	Gravitational Wave Injection	142
6.3	UFLIS Simulations	144
6.3.1	Arm-Locking Stabilization	144
6.3.2	TDI Simulation Outline	148
7	TIME-DELAY INTERFEROMETRY SIMULATIONS	150
7.1	Transponder TDI Simulations	150
7.1.1	Static-Arm Transponder Simulation	152
7.1.2	Dynamic-Arm Transponder Simulation	154
7.2	LISA-like (Master-Slave Phase Locked Laser) TDI Simulations	157
7.2.1	Static-Arm LISA-like Simulation	158
7.2.2	Dynamic-Arm LISA-like Simulation	162
8	CONCLUSION	168
APPENDIX		
A	TIME VARYING FRACTIONAL DELAY INTERPOLATION FUNCTION	172

B	TDI 2.0 COMBINATION FUNCTION	174
	REFERENCES	177
	BIOGRAPHICAL SKETCH	185

LIST OF TABLES

<u>Table</u>	<u>page</u>
2-1 Primary LISA verification binary sources	36
2-2 Gravitational wave frequency range of emission	37
3-1 LISA characteristics and requirements	43
4-1 Orbital dynamics approximations for TDI generations	79
6-1 TDI experimental characteristics	148
7-1 Transponder TDI-ranging estimation	155
7-2 LISA-like TDI-ranging estimation	164

LIST OF FIGURES

<u>Figure</u>	<u>page</u>
1-1 NASA-ESA LISA solicitation	18
2-1 LISA/LIGO differential arm-length changes due to GW polarization	30
2-2 A theoretical model of a binary star system	33
2-3 An outline of GW detection methods and associated frequency ranges	37
3-1 Diagram of the LISA orbital dynamics	41
3-2 Diagram of the LISA constellation	45
3-3 Diagram of the interferometry measurement system	59
4-1 Model of the PDH locking scheme.	74
4-2 Diagrammatic models of the TDI-X and Sagnac combinations	79
4-3 Flow chart of the ranging-tone minimization process	93
5-1 A model of the LISA phasemeter	95
5-2 CIC filter transfer functions	97
5-3 Theoretical PM readout digitization limitations	102
5-4 Phasemeter noise caused by CIC filter aliasing	103
5-5 Software verification of PM performance	104
5-6 Hardware verification of PM performance	105
5-7 Verification of the PM feedback transfer function	106
5-8 Phasemeter noise model	108
5-9 Experimental models of ADC noise estimation measurements	109
5-10 PM/ADC Quantization and differential noise	110
5-11 ADC timing jitter noise limitations	112
5-12 ADC amplitude noise limitations	113
5-13 Entangled phase measurement results	114
5-14 N-stage CIC filter aliasing and entangled phase measurements	115
5-15 Model for estimating ADC phase and amplitude noise	117

5-16 Common source ADC phase and amplitude noise results	118
5-17 Zero-crossing timing jitter estimate	121
5-18 ADC timing jitter comparison	122
5-19 Timing jitter calibration model	124
5-20 Temperature dependent phase dispersion	125
5-21 RF transformer phase loss	126
5-22 Replacement RF transformer dispersion mitigation	127
5-23 Phasemeter noise model, estimation, and limits	129
5-24 Comparison of the PM noise characteristics	130
6-1 UFLIS laser benchtop	132
6-2 Measurements of commonly used sources	133
6-3 Model of the electronic phase delay (EPD) unit	135
6-4 EPD unit data-packing scheme	136
6-5 Noise limitations of the EPD unit	140
6-6 EPD Unit's phase-noise transmission accuracy	141
6-7 Time series of the interpolated delay difference	143
6-8 Interpolated delay differential measurements and corrections	144
6-9 Time series of an arbitrary gravitational wave	145
6-10 Spectral correction of an arbitrary gravitational wave	146
6-11 Long-arm hardware-based single-arm-locking experiment	147
7-1 Model of the TDI-Transponder experimental benchtop	151
7-2 Raw static transponder experimental results	153
7-3 Corrected static transponder experimental results	156
7-4 Ranging tone cancellation spectral results	157
7-5 Dynamic transponder experimental results	158
7-6 TDI laser phase noise suppression	159
7-7 Model of the LISA-like TDI experimental benchtop	160

7-8	Static LISA-like experimental results	161
7-9	Cross-correlated TDI combinations - Static Transponder and LISA-like	162
7-10	Dynamic LISA-like experimental results	165
7-11	Cross-correlated TDI combinations - Dynamic Transponder and LISA-like	166
7-12	Confusion noise time-series comparison	167
8-1	Compiled results and comparison with TDI for LISA	169

Abstract of Dissertation Presented to the Graduate School
of the University of Florida in Partial Fulfillment of the
Requirements for the Degree of Doctor of Philosophy

LASER NOISE MITIGATION THROUGH TIME DELAY INTERFEROMETRY FOR
SPACE-BASED GRAVITATIONAL WAVE INTERFEROMETERS USING THE UF LASER
INTERFEROMETRY SIMULATOR

By

Shawn J. Mitryk

May 2012

Chair: Guido Müller

Major: Physics

The existence of gravitational waves was theorized in 1916 by Albert Einstein in accordance with the linearized theory of general relativity. Most experiments and observations to date have supported general relativity, but now, nearly 100 years later, the scientific community has yet devise a method to directly measure gravitational radiation. With the first attempts towards a gravitational wave measurement in the 1960s, many methods have been proposed and tested since then, all failing thus far to provide a positive detection. The most promising gravitational radiation detection method is through the use of a space-based laser interferometer and with the advancement of modern technologies, these space-based gravitational wave measurements will eventually provide important scientific data to physics, astro-physics, and astronomy communities.

The Laser Interferometer Space Antenna (LISA) is one such space-based laser interferometer. LISA's proposed design objective is to measure gravitational radiation in the frequency range from $30 \mu\text{Hz}$ to 1 Hz using a modified Michelson interferometer. The interferometer arms are 5 Gm in length measured between each of the 3 spacecraft in the interferometer constellation. The differential arm-length will be measured to an accuracy of $18 \text{ pm}/\sqrt{\text{Hz}}$ resulting in a baseline strain sensitivity of $3.6 \times 10^{-21} / \sqrt{\text{Hz}}$. Unfortunately, the dynamics of the spacecraft orbits complicate the differential

arm-length measurements. The arms of the interferometer change in length resulting in time-dependent, unequal arm-lengths and laser Doppler shifts. Thus, to cancel the laser noise, laser beatnotes are formed between lasers on separate SC and, using these one-way laser phase measurements, one can reconstruct an equal-arm interferometer in post-processing. This is commonly referred to as time-delay interferometry (TDI) and can be exploited to cancel the laser phase noise and extract the gravitational wave (GW) induced arm-length strain.

The author has assisted in the development and enhancement of The University of Florida Laser Interferometry Simulator (UFLIS) to perform more accurate LISA-like simulations. UFLIS is a hardware-in-the-loop simulator of the LISA interferometry system replicating as many of the characteristics of the LISA mission as possible. This includes the development of laser pre-stabilization systems, the modeling of the delayed inter-SC laser phase transmission, and the μcycle phase measurements of MHz laser beatnotes.

The content of this dissertation discusses the general GW detection methods and possible GW sources as well as the specific characteristics of the LISA mission's design. A theoretical analysis of the phasemeter and TDI performance is presented along with experimental verification measurements. The development of UFLIS is described including a comparison of the UFLIS noise sources with the actual LISA mission. Finally, the enhanced UFLIS design is used to perform a second-order TDI simulation with artificial GW injection. The results are presented along with an analysis of relevant LISA characteristics and GW data-extraction methods.

CHAPTER 1 INTRODUCTION

1.1 Gravitation and General Relativity

Although a first-order theory of gravity was established in 1687 with the publication of 'Principia [1]' by Issac Newton and started the field of physics as we know it today, physicists are still trying to define the details of gravity's interactions. In 1916, over 200 years later, Albert Einstein published his theory of general relativity (GR) which defined the interaction of matter with the curvature of space and time [2, 3]. This provided physicists with new insights on gravity and re-defined our concepts on the structure of the universe. Even though Einstein's theories have yet to be dis-proven, modern discoveries are raising new questions and testing the limits of Einstein's equations.

For example, the standard-model of particle-physics does not include an explanation for gravity, although some physicists have proposed the existence of a 'graviton,' [4] the carrier of the gravitational force, despite the fact that it would extremely difficult to detect because of how weakly gravity interacts.¹ Proposals to explain an apparent 'missing matter' in galaxies and the accelerated expansion of the universe state that dark-matter and dark-energy [6–8] dominate over 'light' matter and largely determine the past and future evolution of the universe. If dark-matter particles² are discovered, the existence of dark-matter raises new questions about the composition of matter in the universe and, if not discovered, may indicate a need to modify Einstein's theories. Furthermore, the inability to quantize gravity and create a unified theory of forces which is consistent with relativity is arguably the greatest dilemma of modern-day physics.

That said, Einstein's theories on general relativity have, at this point, been supported by all experimental tests and observations from the bending of light by a

¹ Although, LISA could improve the upper bound on it's possible mass [5].

² Dark matter particles interact gravitationally but not electromagnetically.

massive body [9] to the prediction and observed evidence for black holes. Nonetheless, new questions are being raised. How do physicists explain both quantum mechanics and relativity simultaneously? Is there some way to find a 'grand unification' theory to explain both phenomenon? Is the theory of general relativity a complete explanation of gravity or does it have to be modified in some way? And finally, the question which will be the indirect focus of this dissertation, can we use space-based laser interferometry to measure a gravitational waves (GWs) [10], the space-time strain caused by the motion of massive bodies, accurately enough to learn more about the details of general relativity?

1.2 The Gravitational Wave Spectrum

Observationally, the question of whether or not GWs exist has been answered. In 1993, the Nobel Prize in Physics was awarded to Russell Hulse and Joseph Taylor for the indirect detection of GWs by demonstrating that the rotational energy loss of the binary pulsar system PSR B1913+16 equaled the rate predicted through the GW energy loss given by GR [11]. Unfortunately, scientists have yet to achieve a direct detection of GWs. The first efforts, using resonant Weber bars [12], were not nearly sensitive enough to make a positive detection and have a primary design disadvantage in that they can only measure at a single resonant frequency. More modern attempts to measure GWs include the use of ground based interferometers such as the Laser Interferometer Ground-Based Observatory (LIGO) [13, 14], pulsar timing analysis using radio telescopes such as the Square Kilometer Array (SKA) [15, 16], and cryogenic resonant Weber bars such as ALLEGRO [17, 18] and miniGRAIL [19]. Thus far, all attempts have failed to make a positive direct GW detection. On the other hand, LIGO and other GW collaborators have been able to set upper limits on the distribution and amplitude of many proposed GW sources [20–22].

The justification for the many assorted efforts to measure GWs goes beyond bragging rights for a first detection. As a compliment to the electromagnetic observations

of the universe from microwaves to x-rays, GWs provide a whole new spectrum through which to observe astro-physical events. The measurements of GWs will provide a map of black-hole space-times and verify relativistic black-hole models [23, 24], significantly improve the constraints on the Hubble constant [25], and provide early warning systems for electromagnetic observations and cross-correlated parameter estimation [26, 27]. Most importantly, the measurements of a GW signal could give scientists the necessary information to be able to narrow down the many, and growing, modern theories of gravity that are being used to explain the aforementioned complications to Einstein's GR.

Fortunately, physicists are working on a more promising detection method: space-based laser interferometers such as the Laser Interferometer Space Antenna (LISA) [28, 29], shown in Figure 1-1, and its conceptual successors like the Next Gravitational Wave Observatory (NGO) [30].

1.3 Space-Based Gravitational Wave Astronomy

Space-based GW detectors such as LISA, NGO, or the Deci-hertz Interferometer Gravitational Wave Observatory (DECIGO) [31] have many added benefits over ground-based observatories. The gravitationally 'quiet' environment of space allows space-based detectors to get away from the seismic and gravity gradient noise that limit the low-frequency detection capabilities of ground-based detectors. In addition, space-based satellites allows for Gigameter (G_m) baseline arm-lengths, in comparison to the few kilometer (km) arm-lengths of ground-based detectors, decreasing the requirements on the differential arm-length measurement resolution to obtain an equivalent strain precision.

The GW-frequency measurement band of space-based detectors, from about $30 \mu Hz$ to $1 Hz$ for LISA and from about $10 mHz$ to $100 Hz$ for DECIGO, has a number of scientifically interesting GW sources. This includes, but is not limited to, compact galactic binaries, extra-galactic binary black hole mergers, and extreme mass ratio inspirals (EMRIs) [33]. Measurements of GWs from compact binary systems could

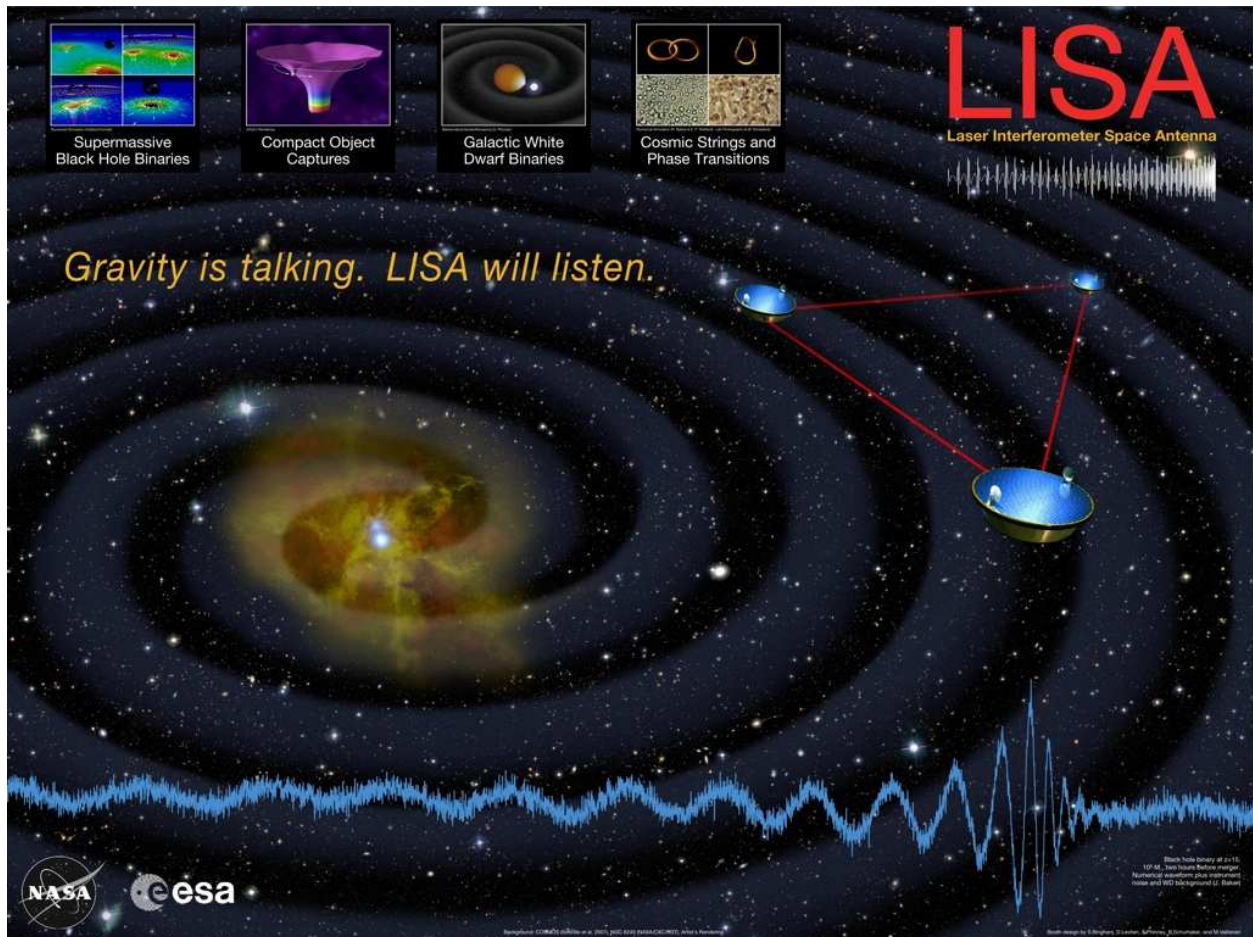


Figure 1-1. NASA-ESA LISA solicitation: This solicitation, released by NASA, shows a model of the LISA interferometry setup, including the 3 space-craft and the inter-space-craft laser links used to measure gravitational radiation. At the bottom of the solicitation is a simulation of a LISA-like GW signal including the expected instrumental noise; the objective of this thesis is to re-create a hardware-in-the-loop simulation much like the one shown. The figures at in the top, left corner show the expected LISA sources including black hole binaries mergers, extreme-mass ratio inspirals, compact star binaries, and finally, the gravitational background, and possibly, unknown, gravitational-quantum effects. [32]

be used to estimate the density of these binary systems within our galaxy. The GW measurement of a binary black hole merger along with an electromagnetic observation, could be used to put a more accurate constraint on the Hubble constant [25]. GWs from extreme mass ratio inspirals provide a perfect experimental test-bench to map out the space-time curvature around a black hole and verify Schwarzschild and Kerr black hole metric solutions [23, 24].

Space based gravitational wave detectors have their own complications though. The proof-masses, the objects with which the gravitationally induced motion is measured, must be kept in a gravitational free-fall and shielded from any other non-gravitational forces, such as those produced by electromagnetic radiation from the sun. Also, because the proof-masses must be in free-fall, their independent geodesic orbits cause the arm-lengths of the interferometer to change over time. As a result, the common-mode laser phase noise rejection inherent in most interferometers, is no longer maintained.

Space-based interferometers must make use of a sequence of laser phase noise stabilization techniques in combination with one-way laser phase measurements and the post-processing removal of laser phase noise to accurately extract GW signals from the photo-detector (PD) signals [29, 34]. Laser pre-stabilization techniques include various methods of locking the laser frequency to a stable reference; this could be an ultra low expansion (ULE) glass cavity or the interferometer arm-length itself. Once the lasers have been pre-stabilized, one-way laser phase measurements can be taken along the individual arms of the interferometer. By combining these one-way laser phase measurements in particular time-shifted and time-scaled linear combinations, one can cancel the common-mode laser phase noise and extract the phase modulated gravitational wave. This method of laser noise cancellation in an unequal-arm interferometer is known as time delay interferometry (TDI) [35].

1.4 Details of the Dissertation's Content

To begin, we will discuss the basics of general relativity, derive the GW propagation characteristics, outline GW detection methods, and provide an example of an interferometric GW measurement of a binary source. We will also give a brief introduction of the LISA design sensitivity and examine the expected LISA sources including their expected strain amplitude, frequency, and detection rates (chapter 2). We will then explain the details of the Laser Interferometer Space Antenna including the Disturbance Reduction System and the Interferometry Measurement System (chapter 3). Chapter 4 provides a more in-depth explanation of laser phase mitigation methods of the LISA Interferometry Measurement System (IMS) and a theoretical analysis of TDI. Chapter 5 analyzes the design, performance, and limiting noise sources of the UF-LISA phasemeter (PM) as well as presents a few experiments and results for ADC noise mitigation in LISA. The University of Florida Laser Interferometry Simulator (UFLIS) along with the electronic phase delay (EPD) unit and the pre-stabilized UF-LISA laser bench-top is then explored in detail. Some basic measurements are then presented to demonstrate the capabilities of UFLIS (chapter 6). Finally, the complete LISA constellation is simulated to test TDI 1.0 and 2.0 (chapter 7) linear combinations and verify laser noise cancellation, ranging estimation, and GW extraction.

1.5 Note to the Reader

The reader should note that, although this dissertation focuses on the design and science of the LISA mission as well as references LISA mission characteristics and publications, the specifications for the development of a future, space-based GW interferometer may differ from those referenced [36]. This may include changes in the arm-length, relaxed sensitivity requirements on the components, and a reduction in the number of laser links between SC. Nonetheless, the measurements and science presented in this dissertation still hold true and can be applied to any space-based interferometry mission.

CHAPTER 2 GENERAL RELATIVITY AND GRAVITATIONAL WAVES

The following introduction to GR as it pertains to gravitational wave emission and detection was derived from a combination of [37], [38], and [39] along with additional calculations and conceptual relationships provided by the author.

2.1 Introduction to General Relativity

2.1.1 Newtonian Gravity

Sir Issac Newton proposed that the gravitationally attractive force between two massive objects, m_a and m_b , is given by:

$$\vec{F}_{ab} = \frac{Gm_a m_b}{|\vec{r}_{ab}|^2} \hat{r}_{ab}, \quad (2-1)$$

where \vec{F}_{ab} is the force vector between the objects, \vec{r}_{ab} is the distance vector connecting the two objects, and G is the gravitational constant. One can also write the gravitational potential, $V(r)$, surrounding an object of mass M as:

$$V(|\vec{r}_{ij}|) = \frac{GM}{|\vec{r}_{ij}|}, \quad (2-2)$$

where \vec{r}_{ij} is the distance vector connecting the center of mass of the object, \vec{x}_i , to a point of interest, \vec{x}_j . These relationships became universally accepted based on confirmed observations and predictions throughout the 1700s and 1800s, giving rise to the Newtonian interpretation of gravity. However, some phenomena, such as the precession of the planet Mercury, were not entirely explained by Newton's Laws.

2.1.2 Einstein Field Equations

It was not until 200 years later when the Theory of General Relativity, as proposed by Albert Einstein in 1916 [3], revealed the true nature of gravity by defining the interaction of space and time with energy and mass. More specifically, GR asserted that the curvature of a tensor spacetime potential, $G_{\mu\nu}$, defines the gravitational force on an object while, at the same time, the mass/energy distribution of the object, $T_{\mu\nu}$, defines

how the spacetime around the object will distort. This is summed up by Einstein's tensor field equations:

$$G_{\mu\nu} = \frac{8\pi G}{c^4} T_{\mu\nu}, \quad (2-3)$$

where $G_{\mu\nu}$ is the symmetric, second-rank, covariant, Einstein tensor, $T_{\mu\nu}$ is the symmetric, second-rank, covariant, energy-momentum (or stress-energy) tensor, and c is the speed of light. Generally, $G_{\mu\nu}$, can be interpreted as the curvature and dynamics of spacetime while the Einstein stress-energy tensor, $T_{\mu\nu}$, defines the distribution and momentum of mass/energy being acted on, while simultaneously, changing the spacetime around it. This self-interactive nature of the 10 independent second-order, differential Einstein's equations makes them extremely hard to solve with only a few specific cases having a complete analytic solution.

2.1.3 Proper Time Invariance

To better understand the Einstein field equations and eventually be able to compute the strain and frequency of a GW source, we must first introduce 4-vectors, vector transformations, and explain the spacetime metric, $g_{\mu\nu}$. Consider a 4-vector for a parameterized curve, $x^\mu(\lambda) = [ct(\lambda), x(\lambda), y(\lambda), z(\lambda)]$, in a flat, non-moving coordinate basis, commonly referred to as Minkowski space:

$$\eta_{\mu\nu} = \begin{bmatrix} -1 & 0 & 0 & 0 \\ 0 & +1 & 0 & 0 \\ 0 & 0 & +1 & 0 \\ 0 & 0 & 0 & +1 \end{bmatrix} \quad (2-4)$$

such that we can write the 'spacetime distance' separating two infinitesimal points along the curve, $dx^\mu/d\lambda$, as:

$$ds^2 = \eta_{\mu\nu} dx^\mu dx^\nu = dx^2 + dy^2 + dz^2 - c^2 dt^2, \quad (2-5)$$

using Einstein summation notation. This 'spacetime distance' can be related to the proper time and is invariant under transformation to a new vector basis $x^{\acute{\mu}}$ such that:

$$ds^2 = -c^2 d\tau^2 = ds'^2 = \eta_{\acute{\mu}\acute{\nu}} dx^{\acute{\mu}} dx^{\acute{\nu}}. \quad (2-6)$$

Solving for $d\tau$, we can calculate the instantaneous change in the proper time in any reference frame using the equation:

$$d\tau = \frac{1}{c} \sqrt{-\eta_{\mu\nu} \frac{dx^\mu}{d\lambda} \frac{dx^\nu}{d\lambda}} d\lambda_\tau. \quad (2-7)$$

Using the fact that this quantity should not change as a function of the selected reference-frame, we can define a transformation from one vector space, x^μ , to another vector space, $x^{\acute{\mu}}$, using transformation matrices, $\Lambda^{\acute{\nu}}_\mu$. For example, it can be shown that the transformation to a reference frame moving in the x-direction at a velocity v with respect to a stationary reference frame takes the form of the Lorentz transformation:

$$\Lambda^{\acute{\nu}}_\mu = \begin{bmatrix} \cosh(\alpha) & -\sinh(\alpha) & 0 & 0 \\ -\sinh(\alpha) & \cosh(\alpha) & 0 & 0 \\ 0 & 0 & 1 & 0 \\ 0 & 0 & 0 & 1 \end{bmatrix}, \quad (2-8)$$

where $\alpha = \tanh^{-1}(v/c)$. This transformation is a member of the Poincaré transformation group which keeps the proper time interval invariant under reference frame transformations in a flat spacetime and is the basis for Special Relativity.

2.1.4 Metrics, Black Holes, and Curvature

Transformations in a 'curved' spacetime can be defined by replacing the Minkowski spacetime metric, $\eta_{\mu\nu}$, in (2-6), with a more generalized spacetime metric, $g_{\mu\nu}$, such that the invariance equation becomes:

$$ds^2 = g_{\mu\nu} dx^\mu dx^\nu. \quad (2-9)$$

The spacetime metric, $g_{\mu\nu}$, is a covariant, second-rank, tensor which contains all the information about the strain (current density) and dynamics (relative parameterized density) of spacetime.

Some examples of curved analytic metrics which help reveal the nature of the metric definition of spacetime include the theoretical models of stationary, non-rotating, black hole, known as the Schwarzschild metric:

$$g_{\mu\nu} = \begin{bmatrix} - \left[1 - \frac{2GM}{c^2 r} \right] & 0 & 0 & 0 \\ 0 & \left[1 - \frac{2GM}{c^2 r} \right]^{-1} & 0 & 0 \\ 0 & 0 & +1 & 0 \\ 0 & 0 & 0 & +1 \end{bmatrix} \quad (2-10)$$

and that of a rotating black hole, known as the Kerr metric:

$$g_{\mu\nu} = \begin{bmatrix} - \left[1 - \frac{2GM r}{c^2 \rho^2} \right] & 0 & 0 & - \frac{2GM \sin(\theta)}{c^2 \rho^2} \\ 0 & \frac{\rho^2}{\Delta} & 0 & 0 \\ 0 & 0 & \frac{\rho^2}{r^2} & 0 \\ - \frac{2GM \sin(\theta)}{c^2 \rho^2} & 0 & 0 & \frac{1}{\rho^2 r^2} [(r^2 + a^2)^2 - a^2 \Delta \sin^2(\theta)] \end{bmatrix}. \quad (2-11)$$

These relationships are written in spherical coordinates where M is the mass of the black hole, a is the ratio of the angular momentum to the mass (J/M) pointing in the \hat{z} -direction, and

$$\Delta(r) = r^2 - \frac{2GM r}{c^2} + a^2, \quad (2-12)$$

$$\rho(r, \theta) = r^2 + a^2 \cos^2(\theta). \quad (2-13)$$

Computing ds^2 as given by (2-9) using the Schwarzschild metric (2-10), we obtain:

$$ds^2 = - \left[1 - \frac{2GM}{c^2 r} \right] dt^2 + \left[1 - \frac{2GM}{c^2 r} \right]^{-1} dr^2 + r^2 d\theta^2 + r^2 \sin^2(\theta) d\phi^2, \quad (2-14)$$

which is a more common way to write out the metric equation.

To gain a better intuition on what the metric represents, we compare these black hole metrics to the flat spacetime Minkowski metric (2–4). It will be shown in chapter 2.1.5 that the first-order gravitational acceleration, written in terms of the spacetime metric, can be written as:

$$\frac{d^2x^i}{(dx^0)^2} = \frac{\partial_i * h_{00}}{2}, \quad (2-15)$$

where $h_{\mu\nu}$ is the deviation from the Minkowski metric,

$$h_{\mu\nu} = \eta_{\mu\nu} - g_{\mu\nu}. \quad (2-16)$$

Referencing the Schwarzschild metric for a stationary black hole, as in (2–10), we see that the dt^2 and dr^2 terms in the metric converge to -1 and +1, respectively, while the gravitational acceleration approaches zero in the limit that $r \rightarrow \infty$ or $M \rightarrow 0$, resulting in Minkowski-like flat spacetime. But as r is decreased, the spacetime curvature due to the black hole increases, thus increasing the gravitational acceleration. A useful way to analyze these black holes is to consider the radius at which spacetime goes from being 'time-like', $ds^2 > 0$, to 'space-like', $ds^2 < 0$, also known as the event horizon. Solving for the inversion point, or $ds^2 = 0$, we obtain the Schwarzschild radius:

$$R_S = \frac{2GM}{c^2}. \quad (2-17)$$

Now, changing our focus to the Kerr metric, given by (2–11), we see that the $g_{\theta\theta}$ and $g_{\phi\phi}$ terms are no longer equal to 1, indicating that the gravitational field is no longer spherically symmetric due to the black hole's angular momentum. Additionally, if we compute the gravitational acceleration near a rotating black hole, as given by (2–15), we will see that the curvature is greatest near the poles of the rotating black hole and that it does not approach infinity as r approaches zero. This is because the black hole's angular momentum causes the Schwarzschild-singularity to be stretched into a circular loop. Finally, one of the most interesting aspects of the Kerr black hole metric is the

non-zero $g_{\phi t}$ and $g_{t\phi}$ terms which represent the angular dynamics of space-time due to the rotation of the black hole, also referred to as frame dragging. This frame-dragging concept has recently been confirmed by Gravity Probe B [40] using the Earth as the source of rotational space-time frame dragging.

Another useful way to analyze the curvature of spacetime given a particular metric, $g_{\mu\nu}$, is through the use of the Riemann and Ricci Tensors. The Riemann Tensor defines how a vector changes as it is parallel transported around a closed curve defined by translation vectors, A^μ and B^ν , and can be given by the definition:

$$\delta x^\rho = R^\rho_{\sigma\mu\nu} x^\sigma A^\mu B^\nu. \quad (2-18)$$

We will refrain from going into the details of the derivation and simply provide a definition for the Riemann tensor in terms of partial derivatives of a spacetime metric, $g_{\mu\nu}$, which may be given by:

$$R^\rho_{\sigma\mu\nu} = \partial_\mu \Gamma^\rho_{\nu\sigma} - \partial_\nu \Gamma^\rho_{\mu\sigma} + \Gamma^\rho_{\mu\lambda} \Gamma^\lambda_{\nu\sigma} - \Gamma^\rho_{\nu\lambda} \Gamma^\lambda_{\mu\sigma}, \quad (2-19)$$

where $\Gamma^\sigma_{\mu\nu}$ are the Christoffel coefficients, also written in terms of partial derivatives of the metric, $g_{\mu\nu}$, as:

$$\Gamma^\sigma_{\mu\nu} = \frac{g^{\sigma\rho}}{2} (\partial_\mu g_{\nu\rho} + \partial_\nu g_{\rho\mu} - \partial_\rho g_{\mu\nu}), \quad (2-20)$$

and are defined by:

$$\nabla_\mu x^\nu = \partial_\mu x^\nu + \Gamma^\nu_{\mu\lambda} x^\lambda. \quad (2-21)$$

One can easily see that this curvature tensor is defined entirely as a function of the metric and it's partial derivatives. Although this is the generalized definition for the curvature on a given manifold, in General Relativity we will primarily be concerned with a

contracted version of the Riemann tensor, known as the Ricci Tensor:

$$R_{\mu\nu} = R^{\lambda}_{\mu\lambda\nu}. \quad (2-22)$$

By trace-reversing the Ricci Tensor, we finally arrive at the Einstein tensor:

$$G_{\mu\nu} = R_{\mu\nu} - \frac{1}{2}Rg_{\mu\nu} \quad (2-23)$$

where, R is the Ricci scalar, or:

$$R = g^{\mu\nu}R_{\mu\nu}. \quad (2-24)$$

The Einstein tensor is a symmetric, second-rank tensor which is equal to the null tensor when space-time is flat and has zero divergence such that, $\nabla^{\mu}G_{\mu\nu} = 0$.

2.1.5 Geodesics

Now that curvature and the metric have been sufficiently discussed, the next question becomes how does this spacetime curvature affect the motion of a particle? An object in free-fall within a given metric will follow a path known as a geodesic. The geodesic equation gives a parameterized space-time solution for what is considered a 'straight' line, or the shortest path between two points, within a given space-time metric, or comparatively, Newton's Laws for GR. The geodesic equation of motion is written as:

$$\frac{d^2x^{\sigma}}{d\lambda^2} + \Gamma^{\sigma}_{\mu\nu} \frac{dx^{\mu}}{d\lambda} \frac{dx^{\nu}}{d\lambda} = 0. \quad (2-25)$$

By considering a 'static' metric and non-relativistic motion, the interesting components of the Christoffel coefficients simplify to:

$$\Gamma^{\mu}_{00} = \frac{-g^{\mu\lambda}\partial_{\lambda}g_{00}}{2}. \quad (2-26)$$

Then, by evaluating (2-20) with $g_{\mu\nu} = \eta_{\mu\nu} - h_{\mu\nu}$, the geodesic equation reduces to the aforementioned gravitational acceleration within a given spacetime metric, (2-15).

2.1.6 Einstein Field Equations Revisited

At this point we have seen how a massive object distorts the local space-time metric as well as how this metric affects the motion of a nearby particle, but the basis of gravitational wave generation exists in the dynamics of Einstein's equations, when massive objects move through spacetime causing the metric to change. The basis for the derivation of Einstein's field equations lies in the attempt to dynamically equate the parameterized divergence from a flat Minkowski metric, $g_{\mu\nu} - \eta_{\mu\nu}$, or equivalently, the Einstein tensor, $G_{\mu\nu}$, to the matter energy distribution tensor, $T_{\mu\nu}$. Essentially, we want the Einsteinian equivalent of Poisson's equation for gravitation:

$$\nabla^2\Phi(r, \theta, \phi) = 4\pi G\rho(r, \theta, \phi), \quad (2-27)$$

where Φ is the 'gravitational potential' and ρ is the mass density. One can make a comparison between Poisson's equation and Einstein's field equations, again written as:

$$G_{\mu\nu} = \frac{8\pi G}{c^4}T_{\mu\nu}, \quad (2-28)$$

to better understand what the terms represent. A static, first-order comparison of these equations would equate the metric, $g_{\mu\nu}$ to the gravitational potential, Φ , the Einstein Tensor, $G_{\mu\nu}$ to the Laplacian of the gravitational potential, $\nabla^2\Phi$, and the stress-energy tensor, $T_{\mu\nu}$, to the mass density distribution, ρ . Although, when we take all the dynamics of the Einstein equations into consideration, we are required to solve 10 second-order inter-dependent differential equations, which have very few analytic solutions. Fortunately, if we consider a 'weak-field' expansion, the linearization of Einstein's equations will provide us with a first-order dynamic solution for the change in the metric due a change in the mass distribution. The solution of this weak field expansion is manifested as polarized plane GWs which propagate outward at the speed of light from the generation source.

2.2 Gravitational Wave Derivation

2.2.1 Polarized Plane Wave Solutions

We begin the weak-field solution for GR by defining a metric expansion as a Minkowski metric with a small perturbation added to it:

$$g_{\mu\nu} = \eta_{\mu\nu} + h_{\mu\nu} + O[h_{\mu\nu}^n], \quad (2-29)$$

while assuming $h_{\mu\nu} \ll 1$ so that the expansion converges. Evaluating this in Einstein's equation, (2-23), we obtain a relationship for the linearized field equations:

$$-\bar{h}_{\mu\nu,\alpha}{}^\alpha - \eta_{\mu\nu}\bar{h}_{\alpha\beta}{}^{\alpha\beta} + \bar{h}_{\mu\alpha,\nu}{}^\alpha + \bar{h}_{\nu\alpha,\mu}{}^\alpha = 16\pi T_{\mu\nu}, \quad (2-30)$$

where $\bar{h}_{\mu\nu}$ is the trace-reversed $h_{\mu\nu}$, given by

$$\bar{h}_{\mu\nu} = h_{\mu\nu} - \frac{\eta_{\mu\nu}h^\alpha{}_\alpha}{2}, \quad (2-31)$$

and $h_{\mu\nu,\alpha} = \partial_\alpha h_{\mu\nu}$. After applying the gauge conditions such that:

$$\bar{h}^{\mu\alpha}{}_{,\alpha} = 0, \quad (2-32)$$

we are left with a concise form for the linearized field equations:

$$\bar{h}_{\mu\nu,\alpha}{}^\alpha = 16\pi T_{\mu\nu}. \quad (2-33)$$

Although the weak-gravitational field equations have an extra degree of freedom, using Maxwell's electromagnetic field equations as our guide, we expect a gravitational analog to the polarized plane-wave solutions of electrodynamics. As well, we should be able to calculate the luminosity and frequency of a particular radiation source using a multi-pole expansion, as is commonly done in electrodynamics.

The GW solutions resulting from (2-32), after transforming $h_{\mu\nu}$ to the transverse-traceless gauge, $h_{\mu\nu}^{\text{TT}}$, where the temporal components are zero, can be broken down into two basis polarization states, h_+ and h_\times . Note that $h_{\mu\nu}^{\text{TT}}$ is its own trace-reverse,

such that $h_{\mu\nu}^{\text{TT}} = \bar{h}_{\mu\nu}^{\text{TT}}$, eliminating the trace-reversed basis needed to form the linearized field equations. Written explicitly in Cartesian coordinates, a GW propagating in the \hat{z} -direction will take the form:

$$h_{\mu\nu}^{\text{TT}} = \begin{bmatrix} 0 & 0 & 0 & 0 \\ 0 & h_{\text{xx}} & h_{\text{xy}} & 0 \\ 0 & h_{\text{yx}} & h_{\text{yy}} & 0 \\ 0 & 0 & 0 & 0 \end{bmatrix} = \begin{bmatrix} 0 & 0 & 0 & 0 \\ 0 & \Re[h_+ e^{-i\omega(ct-z)}] & \Re[h_\times e^{-i\omega(ct-z)}] & 0 \\ 0 & \Re[h_\times e^{-i\omega(ct-z)}] & -\Re[h_+ e^{-i\omega(ct-z)}] & 0 \\ 0 & 0 & 0 & 0 \end{bmatrix} \quad (2-34)$$

where $h_{+/\times}$ is the GW polarization amplitude and ω is the GW frequency. The complete analysis of the polarization states show that a ring of particles laid in the x/y plane will be modulated with the patterns shown in Figure 2-1, hence the assigned names.

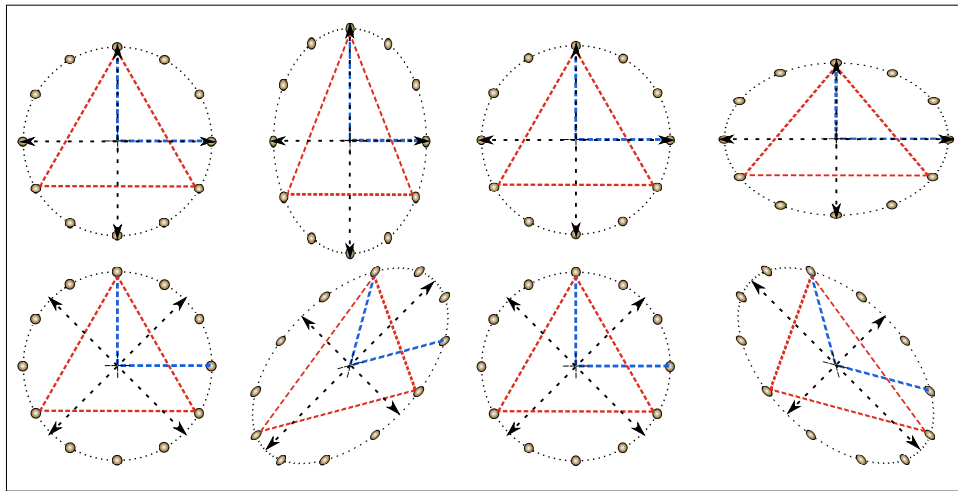


Figure 2-1. LISA/LIGO differential arm-length changes due to GW polarization: The affects of the $h_{+/\times}$ strain polarizations on a ring of particles is depicted. The LIGO (blue) and LISA (red) detectors are overlaid on the ring to show the polarization affects on the differential arm-length changes for each of the detectors types. The LIGO detectors are only sensitive to a single GW polarization, in this case, h_+ , while the LISA detector is sensitive to both polarizations but with a reduction factor of $2/\sqrt{3}$ due to the 60° angle between the differential arms. [29]

2.2.2 Spacetime Strain

Another interpretation of a GW's affect on matter is represented in terms of a space-time strain which is computed from $h_{\mu\nu}$. In this weak field transverse-traceless

gauge, the geodesic equation can be reduced to

$$\frac{\partial^2}{\partial t^2} x^\mu = \frac{x^\mu}{2} \frac{\partial^2}{\partial t^2} h^\mu{}_\sigma. \quad (2-35)$$

Considering two objects separated in the x-direction by a distance x_o , the geodesic equation is then calculated to be:

$$\frac{\partial^2}{\partial t^2} x(t) = \frac{x(t)}{2} \frac{\partial^2}{\partial t^2} h^x_x + \frac{x(t)}{2} \frac{\partial^2}{\partial t^2} h^x_y. \quad (2-36)$$

To simplify the analysis, we take $h_x = 0$ and $h_+ > 0$. The distance between these two objects in a 'flat' spacetime is given by:

$$x(t) = x_o \left\| 1 + \frac{h_+ e^{-i\omega(t)}}{2} \right\|. \quad (2-37)$$

Assuming $h_+ \ll 1$, we can define the relationship:

$$\frac{\delta x}{x_o} = h_+. \quad (2-38)$$

where δx is the amplitude of the separation distance ranging from $x_o - (\delta x/2)$ to $x_o + (\delta x/2)$. Thus, in this way, the metric can be interpreted as a space-time strain which changes the distance between two objects by it's magnitude. The measurement of this change in distance is the basis for interferometric detection of GWs.

2.2.3 Weak-field GR Multipole Expansion

The magnitude of a GW source can be calculated, as is commonly done in electrodynamics, in terms of Green's functions given by:

$$h_{\mu\nu}(x^\sigma) = -\frac{16\pi G}{c^4} \int G(x^\sigma - y^\sigma) T_{\mu\nu}(y^\sigma) d^4 y. \quad (2-39)$$

After applying boundary conditions in the far-field approximation, we can write the Fourier domain metric perturbation as:

$$\tilde{h}_{\mu\nu}(\omega, x^i) = \frac{4G e^{i\omega r}}{c^4 r} \int d^3 y \tilde{T}_{\mu\nu}(\omega, y^i), \quad (2-40)$$

or the time-domain perturbation as:

$$h_{\mu\nu}(\omega, x^i) = \frac{4G}{c^4 r} \int d^3y T_{\mu\nu}(ct - r, y^i). \quad (2-41)$$

Using a multi-pole expansion of the radiating system in the far-field approximation, we may write the observed strain from a quadrupole source as:

$$h_{ij} = \frac{2G}{c^4 r} \frac{d^2 I_{ij}}{dt^2}(t_r), \quad (2-42)$$

where I_{ij} is the quadrupole moment tensor:

$$I^{ij} = \int d^3x T^{00} x^i x^j, \quad (2-43)$$

and $t_r = ct - r$ is the retarded time. The monopole and dipole terms do not contribute to GW radiation while higher order terms fall off as $(1/r)^{(n-1)}$ and will be neglected in this far-field approximation.

One of the most common astrophysical GW sources are binary systems, where two masses are orbiting a common center of mass. Given a binary system with two masses, m_1 and m_2 , and a separation distance of $2a$, we can write the quadrupole moment of inertia of the system as:

$$I_{ij} = \mu a^2 \begin{bmatrix} \cos^2(\omega t) & \cos(\omega t)\sin(\omega t) & 0 \\ \cos(\omega t)\sin(\omega t) & \sin^2(\omega t) & 0 \\ 0 & 0 & 0 \end{bmatrix} \quad (2-44)$$

where $\mu = (m_1 m_2)/(m_1 + m_2)$ is the reduced mass and $\omega = \sqrt{(GM)/(a^3)}$ is the orbital frequency given by Kepler's Law, $M = m_1 + m_2 = \omega^2 a^3 / G$ [41]. Evaluating I_{ij} in (2-42),

the expected GW radiation strain can be written as:

$$h_{ij}(t, x^i) = \frac{4G\mu}{c^4 r} \omega^2 a^2 \begin{bmatrix} -\cos(2\omega t_r) & -\sin(2\omega t_r) & 0 \\ -\sin(2\omega t_r) & \cos(2\omega t_r) & 0 \\ 0 & 0 & 0 \end{bmatrix} \quad (2-45)$$

$$= \frac{4G^2 m_1 m_2}{c^4 r a} \begin{bmatrix} -\cos(2\omega t_r) & -\sin(2\omega t_r) & 0 \\ -\sin(2\omega t_r) & \cos(2\omega t_r) & 0 \\ 0 & 0 & 0 \end{bmatrix}. \quad (2-46)$$

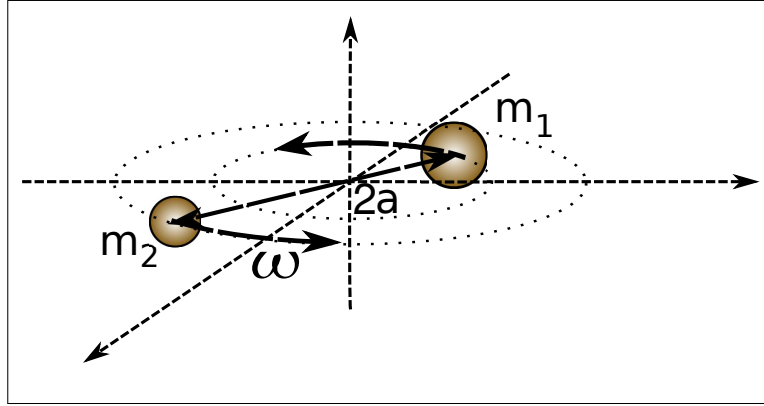


Figure 2-2. A theoretical model of a binary star system: Two masses, m_1 and m_2 rotate about a common center of mass with a separation distance of $2a$. As rotational energy is lost through GW radiation the separation distance will decrease (2-50) while the angular frequency increases (2-52).

The instantaneous power output through GW radiation, or rather the gravitational luminosity, can be calculated by the time-averaging over a single orbital period of the radiating source, given by:

$$L_{\text{GW}} = \frac{G}{5c^5} \left\langle \frac{dI_{ij}^3}{dt_r^3} \right\rangle^2 \quad (2-47)$$

For a binary system, this results in a luminosity given by:

$$L_{\text{Binary}} = \frac{32}{5} \frac{\mu^2 M^3}{a^5} \frac{G^4}{c^5} f(\epsilon), \quad (2-48)$$

where $f(\epsilon)$ is a correction function based on the eccentricity, ϵ , given by:

$$f(\epsilon) = \left[1 + \frac{73}{24}\epsilon^2 + \frac{37}{96}\epsilon^4\right][1 - \epsilon^2]^{(-7/2)}, \quad (2-49)$$

and may contribute an order of magnitude to the resulting luminosity [37].

As a result of the GW energy radiated by the binary source, the orbital kinetic energy will decay resulting in a reduced orbital distance, increased luminosity, and increased orbital frequency. These values can be derived in the first order Post-Newtonian approximation for a circular orbit ($\epsilon = 0$) as:

$$a = a_o \left(1 - \frac{t}{\tau_o}\right)^{1/4} \quad (2-50)$$

$$L = \frac{L_o}{\left(1 - \frac{t}{\tau_o}\right)^{5/4}} \quad (2-51)$$

$$\omega = \omega_o \sqrt{\frac{1}{\left(1 - \frac{t}{\tau_o}\right)^{3/4}}}, \quad (2-52)$$

respectively. In this equation, the time-scaling factor, τ_o , is the 'merger time' until the binary system inspirals into a single compact object:

$$\tau_o = \frac{5}{256} \frac{c^5 a_o^4}{G^3 \mu M^2}, \quad (2-53)$$

resulting from initial system values of a_o , L_o , and ω_o .

Post-Newtonian and Numerical Relativity Solutions.

Higher order Post-Newtonian and Numerical Relativity (NR) solutions provide more accurate descriptions to these binary in-spiral systems by taking into account orbital circularization and the relative angular momentum of the individual in-spiraling objects. Qualitatively, gravitational radiation from an in-spiraling system is minimized through a reduction in the eccentricity and circularization of the binary orbits. The relative angular momentum between the stars and the angular momentum of the binary may cause the actual merger time to either lead or lag the non-rotating merger time, τ_o . This can also

cause an asymmetric gravitational radiation which imparts a linear momentum to the binary system. These higher order solutions are necessary in order to accurately extract gravitational wave signals from the detector through wave-form matching.

2.3 Gravitational Wave Sources and Detection Methods

2.3.1 Strain Estimation

Now that we have a measure for the expected GW radiation from astrophysical quadrupole sources, we can estimate the GW strain from particular sources based on the parameters determined through electromagnetic observations. For example, the primary LISA 'verification' binary, RX J0806.3+1527, a known AM CVn binary system with an orbital period of 321 s [42], is expected to have binary stars with $m_1 = 0.13M_\odot$ and $m_2 = 0.5M_\odot$ with an observation distance of $r = 300$ pc, as seen in Table 2-1. Using Kepler's Law, we can calculate the separation distance between the binary stars as $a_{\text{RX-J}} = 37.97 \times 10^6$ m. Including the other known characteristics of the RX J0806.3+1527 system, we can calculate the strain magnitude observed on Earth from (2-45) as:

$$|h_{\mu\nu}| = \frac{4G^2\mu M}{c^4ra} = 1.608 \times 10^{-21} \frac{\text{m}}{\text{m}}. \quad (2-54)$$

A large number of known compact binaries have strain amplitudes on the order of $10^{-22} \rightarrow 10^{-21}$ m/m in the frequency range from $0.1 \rightarrow 10$ mHz and are primary LISA sources. Three other verification binaries and four other known, possible sources are outlined in Table 2-1 [42]. Further details of these sources are discussed in chapter 2.3.4.

2.3.2 Gravitational Wave Evidence

The current evidence for GW radiation from astronomical sources is based on the observation and orbital decay measurements of binary pulsar systems. The first orbital decay measurements were performed by Hulse and Taylor using the PSR B1913+16 binary pulsar. In 1993, Hulse and Taylor were awarded the Nobel Prize in Physics for

Table 2-1. Primary LISA verification binary sources: Here we list the top 8 most-probable verification binaries for the LISA-GW detector according to [42]. These binaries will also assist in constraining the Hubble constant [5]. The TDI experiments performed in chapter 7 will use the double white dwarf RXJ0806.3+1527 binary as the simulated GW source.

Name	f (mHz)	SNR [mean : max]	r (pc)	m ₁	m ₂
RXJ0806.3+1527	6.22027	[62 : 227]	300 – 1000	0.13	0.2 – 0.5
V407 Vul	3.51250	[30 : 79]	300 – 1000	0.068	0.7
ES Cet	3.22	[19 : 62]	350 – 1000	0.062	0.7
AM CVn	1.94414	[8 : 13]	606	0.14	0.85
HP Lib	1.813	[< 3 : 5]	197	0.032	0.57
4U 1820-30	2.92	[< 3 : 5]	8100	< 0.1	1.4
WZ Sge	0.04065	[< 3 : 5]	43	< 0.11	> 0.7
KPD 1930+2752	0.2434	[< 3 : 5]	100	0.5	0.97

showing the orbital decay of the PSR B1913+16 system equaled that predicted by GR, thus providing indirect evidence of energy loss through gravitational radiation [11]. To date, the orbital decay of the PSR B1913+16 system matches that predicted by GR to within 0.2% [43]. Other astronomical observations, such as the double binary pulsar PSR J0737-3039, are providing even tighter constraints and further supporting the validity of Einstein’s GR [44, 45]. Despite the certainty of GW existence, a direct observation along with electromagnetic counterparts would provide physicists vital information in support or opposition of modern post-Einsteinian theories.

2.3.3 The Gravitational Wave Spectrum

Astronomical GWs radiate from a wide variety of dynamic quadrupole sources including binary inspirals of compact star and black hole mergers, asymmetric spinning compact objects, super-nova star collapses, and black hole captures of compact objects. It is also expected that there is a gravitational wave background, much like the cosmic microwave background, resulting from quantum fluctuations shortly after the big-bang and the sub-sequential expansion of the universe. Each of these systems produces GWs within a characteristic frequency range from $10^{-18} \rightarrow 10^9$ Hz, each with an

Table 2-2. Gravitational wave frequency range of emission: This table outlines the gravitational wave emission spectrum, the GW emission sources, and the associated detection techniques. (BBHM: Binary Black Hole Mergers; EMRI: Extreme Mass Ratio Inspirals)

Freq. Range (Hz)	Name	Sources	Detection Method
$10^{-18} - 10^{-7}$	Very Low Freq.	Primordial GWs, Early Universe Dynamics	Pulsar Timing
$10^{-4} - 10^0$	Low Freq.	BBHM, EMRIs, Compact Binary Stars	Space-based Interferometers
$10^1 - 10^4$	High Freq.	Supernova, Compact Binary Inspirals	Ground-based Interferometers
$10^2 - 10^9$	Very High Freq.	Binary Inspirational Harmonics, Technological Applications	Resonant Detectors

associated possible method of detection. The frequency ranges and their proposed detection methods are outlined in Table 2-2 and depicted in Figure 2-3.

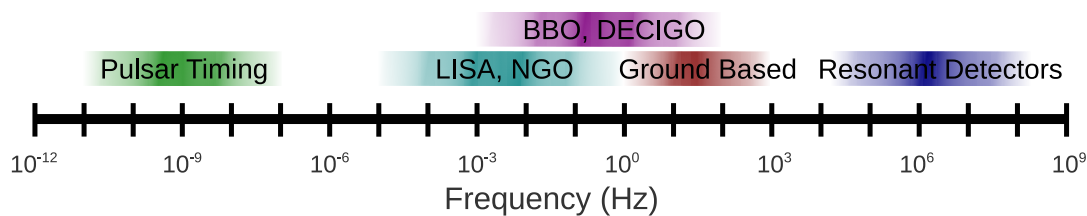


Figure 2-3. Outline of GW detection methods and associated frequency ranges: Very low-frequency (e.g. pulsar timing - Square Kilometer Array); Low frequency (e.g. space-based laser interferometers - Laser Interferometer Space Antenna, Next Gravitational Wave Observatory); High-frequency (e.g. ground-based laser interferometer - Laser Interferometer Gravitational Wave Observatory); Mid-freq. (e.g. space-based resonant cavities - Deci-Hertz Gravitational Wave Observatory (DECIGO)); Very high frequency (e.g. GW amplification and detection through the measured deformations in a resonant geometrical structures - Weber Bars/miniGRAIL:).

2.3.4 LISA Gravitational Wave Sources

The low-frequency/LISA measurement band, from 0.1 mHz to 1Hz contains a wide-array of interesting gravitational wave sources.

2.3.4.1 Compact Binaries

The strongest of these sources are monotonic GWs resulting from interacting and non-interacting binary star systems composed of binaries with one or both of the stars being a compact white dwarf (WD) or neutron star (NS) star. Although many non-interacting WD/WD, WD/NS, NS/NS systems have been observed, none are known to be in the LISA sensitivity range. At the same time, there are more than 10 known and electromagnetically observed interacting AM-CVn (WD accretor) and compact X-ray (NS accretor) binary systems which are expected to be excellent verification sources and are well within the LISA strain sensitivity. The strongest of these verification systems were introduced in Table 2-1.

The science motivating LISA's observations of these sources include estimations of the populations of these binary systems within our galaxy and an improved constraint on the Hubble constant (also referred to as redshift uncertainty). In fact, LISA is expected to be sensitive to so many company binary systems that their populations are expected to form a 'confusion noise background' due to the inability to differentiate between individual sources for frequencies below 2 mHz [46].

2.3.4.2 Binary Black Hole Mergers

One of LISA's most interesting astronomical observations will be that of extra-galactic near-equal-mass, $10^3 M_{\odot}$ - $10^7 M_{\odot}$, binary black hole mergers. These systems will appear, depending on the total mass of the system, near the low-frequency limits of the LISA measurement band, from 0.1 mHz to 1 mHz, and will increase in frequency and strain amplitude as the system evolves. The dynamics of these binary black hole mergers is not well defined, requiring numerical relativity simulations to produce theoretical merger wave-forms. Observations of these events will provide precision tests of these extreme self-interacting spacetimes as well as details about black hole formation and evolution. Although no systems are known, event rate estimates range from 1 to 100s per year depending on the population and LISA's achieved strain

sensitivity. As an example, a recent massive black hole binary system has been found, named NGC-3393 with binary system characteristics, $m_1 = 3 \times 10^7 M_\odot$, $m_2 = 1 \times 10^6 M_\odot$, $2a \simeq 5 \times 10^{18} \text{ m} = 162 \text{ pc}$, $r = 50 \text{ Mpc}$ [47]. If this system were closer to its merger time, the expected LISA sensitivity could provide a 10^5 to 10^6 signal-to-noise ratio on the GW emission waveform just before the black-hole merger. As a result of GW's non-interacting properties, cross-correlations between the GW signal and electromagnetic observations of these binary black hole mergers will allow LISA to estimate an absolute distance to the binary source, providing an improved constrain on the Hubble constant with an error of 1%¹ [25, 29].

2.3.4.3 Extreme Mass Ratio Inspirals

Binary black hole mergers with a large mass difference ratio, otherwise known as extreme mass ratio inspirals (EMRIs), will be visible near the 3 mHz corner frequency of the LISA sensitivity band (Figure 8-1) and are the primary driving motivation to improve the peak LISA sensitivity. EMRIs consist of a $\simeq 10^6 M_\odot$ massive black hole being closely orbited by and, eventually merging with, a smaller $10 - 100 M_\odot$ black hole. The smaller black hole will act as a test-particle to provide a spacetime map in the vicinity of the massive Kerr black hole beyond the singularity's event-horizon [23, 24].

2.3.4.4 Other Suggested Sources

Finally, LISA will provide some of the first direct tests of new physics including attempts to probe the microwave-background-like, gravitational wave stochastic background. This GW background is conjectured based on the inflation of first-order phase transitions of the early universe, shortly after the big bang and is expected to result in a white-noise GW background throughout the universe. For more information on this and the other LISA-like tests of new physics, refer to [48].

¹ Current methods of constraining the Hubble constant provide an error of 5%.

CHAPTER 3 THE LASER INTERFEROMETER SPACE ANTENNA

A majority of the characteristics for this description can be found in the LISA NASA/ESA Yellow-book [29].

3.1 LISA Overview

The LISA GW measurement scheme utilizes a modified-Michelson detection technique by taking one-way measurements between freely-falling proof-masses housed within three spacecraft (SC). These spacecraft follow independent, helio-centric orbits trailing 20° behind the Earth¹ while maintaining a nearly equilateral triangle configuration which is off-set by 60° to the orbital plane of the center-of-mass as shown in Figure 3-1. Housed within each of these space-craft are two proof-masses which are maintained in a gravitational free-fall by a disturbance reduction system (DRS). Meanwhile, the interferometric distance between the proof-masses on opposite SC are measured with an interferometry measurement system (IMS) as diagrammed in Figure 3-2. The data is then sent to Earth to form the post-processed combinations required to extract the GW signals. Using this design basis, the success of the LISA mission towards detecting GWs depends on a series of requirements (Table 3-1) which are defined to optimally measure the previously discussed GW sources while staying within the bounds of cost and feasibility. Generally, the primary sensitivity limiting noise sources in the LISA design are the DRS's acceleration noise for $f < 3 \text{ mHz}$ and the IMS's sensitivity noise for $f > 3 \text{ mHz}$.

The IMS's interferometry sensitivity, $\delta\tilde{x}_{\text{IMS}-\delta\phi}(f)$ adds to the DRS's acceleration noise, $\delta\tilde{a}_{\text{DRS}}(f)$, with the a scaling factor of $2/\omega^2$, in root-sum-square to produce the

¹ The SC orbit the L5 Lagrange point to maintain the stability and reduce the divergence of the orbits.

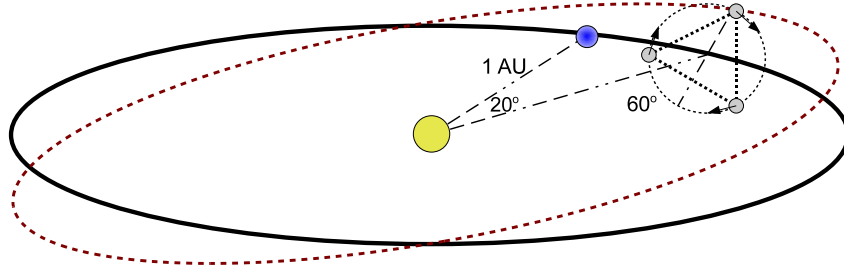


Figure 3-1. Diagram of the LISA orbital dynamics: Depicted is a diagram of the LISA constellation's orbital dynamics showing the triangular configuration of the SC, the geodesic path of an individual SC, and the relative angle between Earth's orbital plane and the LISA constellation.

effective differential length precision:

$$\delta\tilde{x}_{\text{LISA}}(f) = \sqrt{(\delta\tilde{x}_{\text{IMS}-\delta\phi}(f))^2 + \left(\frac{2\delta\tilde{a}_{\text{DRS}}(f)}{(2\pi f)^2}\right)^2} \quad (3-1)$$

When we take into consideration the sensitivity with respect to the GW sources, this length precision is scaled by a factor of $\sqrt{5}$ to account for a 1-year average over the $4\pi^2$ sky radians and a by factor of $2/\sqrt{3}$ to account for the non-orthogonal $\simeq 60^\circ$ angle between the interferometer arms. In addition, GW's which are smaller in wave-length than the LISA-arm have a reduced sensitivity due to a GW aliasing type effect resulting in multiple GW oscillations between the two proof-masses. The combined effects of these scaling factors results in a LISA GW-to-length sensitivity function given by:

$$T(f) \simeq \sqrt{5} \frac{2}{\sqrt{3}} \sqrt{1 + \left(\frac{f}{0.41f_0}\right)^2} \quad (3-2)$$

where $f_0 = c/(2L)$ [29].

Using this sensitivity function, the expected length precision as a result of the IMS and DRS noises, and the LISA arm-length, $L = 5 \text{ Gm}$, we can calculate the effective strain sensitivity:

$$\tilde{h}_{\text{LISA}}(f) = T(f) \frac{\delta\tilde{x}_{\text{LISA}}(f)}{L}. \quad (3-3)$$

This sensitivity function is plotted explicitly in $\text{cycles}/\sqrt{\text{Hz}}$ in Figure 8-1.

3.2 The Disturbance Reduction System

In order to accurately detect GWs, we must ensure that no other non-gravitational forces such as electromagnetic interactions or solar radiation dominate the dynamics of the proof-masses' motion. The proof-masses, 46 mm^3 cubes, will be composed of a gold-platinum alloy and will be shielded from these non-gravitational forces by the DRS. The SC and DRS themselves must largely follow the free-falling motion of these proof-masses, thus, micro-newton thrusters are used to move the SC and track the proof-masses' geodesic path. Capacitive sensors ensure that the proof-masses do not hit the walls of the housing and, at times, intentionally actuate the proof-masses to account for the independent motion of the two proof-masses on each SC. The goal of all these components working in collaboration is to keep the non-gravitational acceleration of the proof masses below:

$$\delta\tilde{a}_{\text{DRS}}(f) = \frac{3 \text{ fm/s}^2}{\sqrt{\text{Hz}}} \sqrt{1 + \left(\frac{f}{8 \text{ mHz}}\right)^4} \sqrt{1 + \left(\frac{0.1 \text{ mHz}}{f}\right)^2} \quad (3-4)$$

in the LISA measurement band. This defines the low-frequency sensitivity limit of the LISA detector. Testing the ability to achieve this acceleration noise goal, the LISA Pathfinder mission is being launched [49]. Collapsing a LISA-arm into a single spacecraft, the LISA Pathfinder mission will attempt to measure the distance between two free-falling test masses using heterodyned laser fields, providing an excellent platform to test many LISA-like complications and characteristics.

3.3 The Interferometry Measurement System

The LISA IMS's primary objective is to measure the differential distance between the free-falling proof masses to an accuracy of:

$$\delta\tilde{x}_{\text{IMS}-\delta\phi}(f) = \frac{18 \text{ pm}}{\sqrt{\text{Hz}}} \sqrt{1 + \left(\frac{2.8 \text{ mHz}}{f}\right)^4}. \quad (3-5)$$

Table 3-1. LISA characteristics and requirements: The requirements outlined in this table [29] define the resulting LISA GW-sensitivity curve (Figure 8-1) based on the pre-stabilized laser phase noise, the inter-SC ranging accuracy, the phasemeter measurement precision, the IMS's TDI noise extraction capability, and DRS isolated the acceleration noise of the proof-masses. Although a future space-based GW mission may use different characteristics [36], the requirements specified in this description focus on a LISA-like scenario.

$$(f_L = 0.1 \text{ mHz}, f_M = 2.8 \text{ mHz}, f_H = 8 \text{ mHz})$$

Characteristic	Specification
Laser Pre-stabilization	$\frac{280 \text{ Hz}}{\sqrt{\text{Hz}}} \sqrt{1 + \left(\frac{f_M}{f}\right)^4}$
Phasemeter Precision	$\frac{1 \mu\text{cycle}}{\sqrt{\text{Hz}}} \sqrt{1 + \left(\frac{f_M}{f}\right)^4}$
IMS Strain Sensitivity	$\frac{18 \text{ pm}}{\sqrt{\text{Hz}}} \sqrt{1 + \left(\frac{f_M}{f}\right)^4}$
DRS Acceleration Noise	$\frac{3 \text{ fm/s}^2}{\sqrt{\text{Hz}}} \sqrt{1 + \left(\frac{f}{f_H}\right)^4} \sqrt{1 + \left(\frac{f_L}{f}\right)^4}$
Ranging Accuracy	$\delta L = 1 \text{ meter}, \delta \tau = 3.3 \text{ ns}$
Arm-Length	$L = 5.0 \pm 0.1 \text{ Gm}$
Light-Travel Delay	$\tau = 16.66 \pm 0.33 \text{ s}$
Relative Velocity	$v = \pm 20 \text{ m/s}, \beta = \pm 66 \text{ ns/s}$

Each component in the IMS chain must be tested to ensure that this requirement is satisfactorily met [29]. This includes a laser pre-stabilization requirement to suppression the inherent free-running laser phase noise, a PD/phasemeter differential phase measurement precision requirement to perform heterodyne time-delay interferometry, and a ranging requirement to accurately shift and cancel the residual laser phase in the TDI combinations as shown in Table. 3-1. These values are defined such that the residual laser phase noise is cancelled beyond the shot-noise (3–8) and acceleration noise (3–4) limits.

First, the $\lambda = 1064 \text{ nm}$, $\nu = 282 \text{ THz}$, lasers must be pre-stabilized to an accuracy of:

$$\delta \tilde{\nu}_{\text{Pre-Stab}}(f) = \frac{280 \text{ Hz}}{\sqrt{\text{Hz}}} \sqrt{1 + \left(\frac{2.8 \text{ mHz}}{f}\right)^4} \quad (3-6)$$

by locking to a frequency reference. A well-known method of frequency-referencing a laser is by Pound-Dever-Hall (PDH) locking to a ULE cavity [50–52]. Another method, which is also being used on the LISA-Pathfinder mission, is Mach-Zehnder locking.

This has an advantage over PDH locking in that it uses the two laser fields which are already part of the LISA design. Either of these frequency reference methods could be assisted or, possibly, completely replaced by using the LISA arm itself as the frequency reference in a tracking technique known as arm-locking [53, 54]. Some of the work in this dissertation (chapter. 6.3.1) will focus on the first long-arm hardware-in-the-loop tests of this arm-locking technique.

The pre-stabilized laser fields are fiber-coupled through electro-optical modulators (EOM) to add the clock-noise transfers (chapter 4.3) and SC-to-SC laser communication signals. Each of these modulated fields are then fiber-coupled onto an ULE optical bench which distributes them to the back-link fiber, telescope, and the local optical bench's proof mass. The back-link fiber transmits the laser field to the adjacent optical bench on the same SC while the telescope transmits the field to the the adjacent SC as shown in Figure 3-2. The three laser fields on each optical bench (the local laser, the adjacent optical-bench's laser, and the adjacent SC's laser) are heterodyned to form the three main beatnote observables as depicted with more detail in Figure 3-3. These observables can be interpreted to represent the differential laser phase between lasers on the same SC, χ_{sr} , the local-SC to local-proof-mass distance, b_{sr} ,² and the local-SC to the far-SC distance, s_{sr} . The subscripts allow us to differentiate between the measurements on different spacecraft where the 's' subscript refers to the sending SC_s while 'r' refers to the receiving SC_r . The time-changing arm-lengths and resulting inter-SC light-travel time-delays, $\tau_q = \tau_q(0) + \beta_q t$, are indexed such that SC_q is opposite 'Arm-q' with q referring to clock-wise light propagation and q'

² Other TDI descriptions [55] use τ_{sr} or z_{sr} for these variables but we will use b_{sr} to avoid confusion with the light-travel time delay, $\tau_q(t)$.

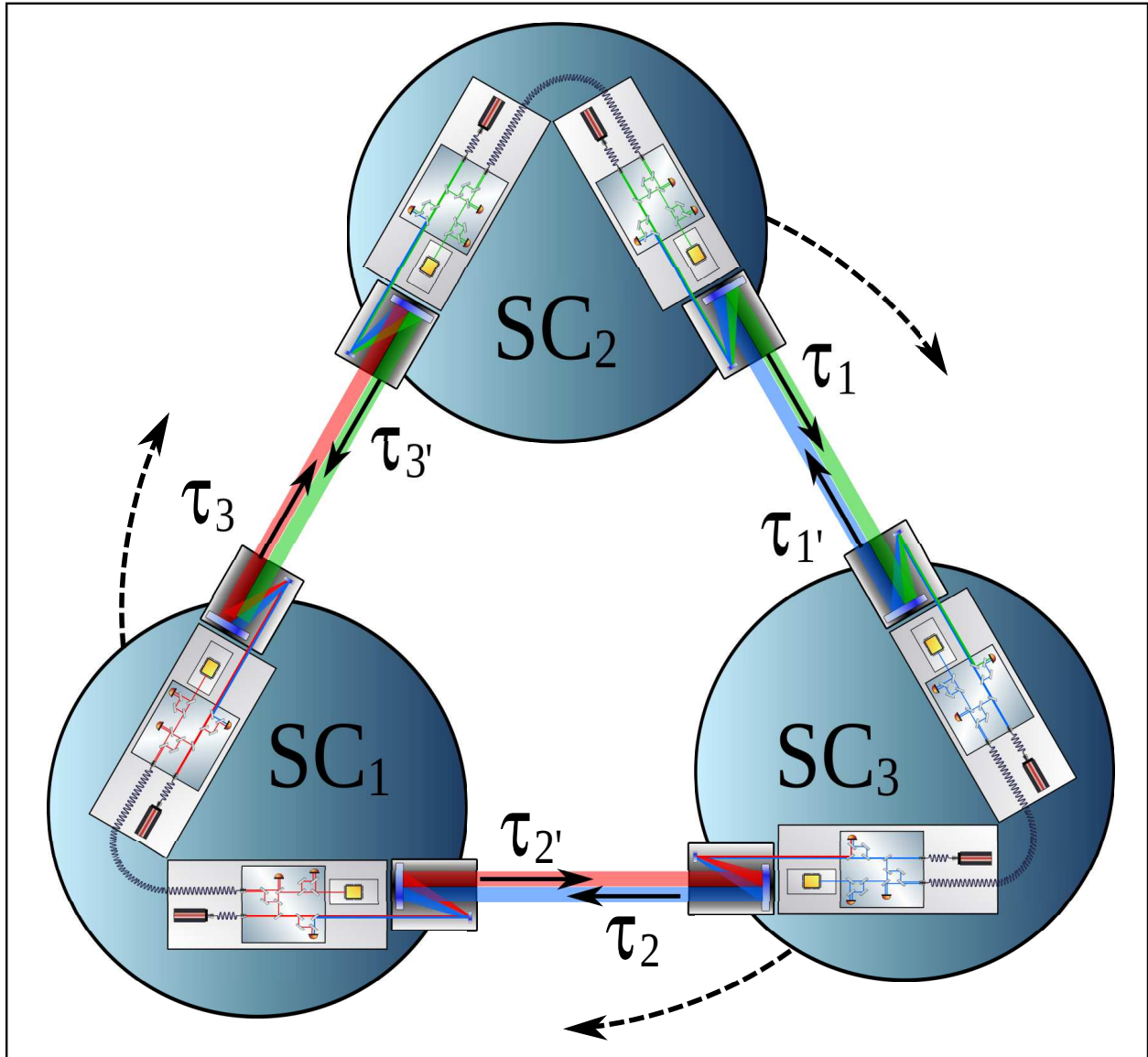


Figure 3-2. Diagram of the LISA constellation: A model of the complete LISA constellation depicting the three space-craft, the six individual laser benchtops, the inter-SC laser links, and the names of each of the arm-length light travel times, $\tau_{q/q'}$, opposite SC_q.

referring to counter-clock-wise propagation³ as shown in Figure 3-3. From each of these measurements we are able to re-construct the differential distance between the proof-masses on opposite SC in post-processing (chapter 3.4.3) and, thus, determine the GW strain.

The complications to this measurement scheme are many-fold. None of the components in the laser transfer chain can exceed a specified requirement so that added noise terms are not introduced into the interferometry measurement. This includes the EOMs used to apply the clock transfers and SC-to-SC laser communications, the fibers used to transfer the laser field between optical benches, and the telescopes used to transfer the laser fields between the SC. The fiber-backlink may introduce 'non-reciprocal' (different in counter-propagating directions) noise. The telescope length may change over time, causing an apparent arm-length change. In addition, the angle between the optical benches and telescope pointing direction must be actuated to account for the breathing of the constellation.

Another complication to the IMS measurement is the received power from adjacent SC. Of the 2 W of laser power emitted from the local SC, the divergence of the laser field over the 5 Gm arm-length results in only 100 pW being received on the adjacent SC's photodetector. This results in a shot-noise limited heterodyned field which must be measured to an accuracy of 1 μ cycle.

Generally, the basis and details of the IMS system described here for the LISA mission are analyzed and outlined in [29] and [34]. Although new proposals for a more cost effective design are being considered [30, 56, 57], they must still use the same set of principles to perform gravitational wave measurements. These changes may include

³ Note that the following description is done without a loss of generality by differentiating between independent $\tau_q(t)$ and $\tau_{q'}(t)$, and accounting for different counter-propagating time-delays along the same arm due to the constellation's orbital rotation.

shorter arm-lengths, the reduction to a two-arm measurement with only four inter-SC laser links, a geocentric orbit, or the use of a single spherical proof-mass.

3.4 μ Cycle Accuracy Phase Measurement

The IMS differential path-length measurement precision, $\delta\tilde{x}_{\text{IMS}-\delta\phi}(f)$ (3–5), is primarily based on the cumulative error from the photo-detectors and phasemeters used to measure the heterodyned MHz beatnotes. Independent of shot noises, the photodetector error must be less than 3 pm while the phasemeter error must be less than:

$$\delta\tilde{x}_{\text{PM}}(f) = \frac{1 \text{ pm}}{\sqrt{\text{Hz}}} \sqrt{1 + \left(\frac{2.8 \text{ mHz}}{f}\right)^4} \simeq \frac{1 \mu\text{cycle}}{\sqrt{\text{Hz}}} \sqrt{1 + \left(\frac{2.8 \text{ mHz}}{f}\right)^4}. \quad (3-7)$$

Applying the expected shot-noise limitation:

$$\delta\tilde{x}_{\text{Shot-Noise}}(f) = \frac{7.7 \text{ pm}}{\sqrt{\text{Hz}}}, \quad (3-8)$$

and the $7 \text{ pm}/\sqrt{\text{Hz}}$ path-length noise requirement, the overall root sum squared differential phase of each pair of laser fields is measured to an accuracy of:

$$\delta\tilde{x}_{\delta\phi-\text{Total}}(f) = \frac{11.7 \text{ pm}}{\sqrt{\text{Hz}}} \sqrt{1 + \left(\frac{2.8 \text{ mHz}}{f}\right)^4}. \quad (3-9)$$

Finally, the individual measurements are added in the linear time-shifted TDI combinations to achieve the $\delta\tilde{x}_{\text{IMS}-\delta\phi}(f)$ IMS requirement (3–5).

These low-frequency LISA band requirements are usually hindered by long-term errors such as sampling biases, temperature dependent phase dispersion, and interferometric length changes which couple into the phase measurements. For example, if the voltage bias which is used in sampling and converting the beat signal drifts over the course of the measurement, this will result in an un-accounted phase coupling. Also, if the temperature of the filters or RF transformers used to prepare and distribute the beat signal changes in time, this may result in a time-changing transfer

function phase response. The details of these noise sources are outlined in the following sections.

3.4.1 Photodetector Noise

The phase noise of a photo-detector with respect to the MHz heterodyned beatnote can be determined by a linear combination of three independent noise sources: (1) shot noise, (2) Johnson-Nyquist noise, and (3) flicker noise. The shot noise limitation is defined by the limited number of photons per second which are received on the photodetector. Johnson-Nyquist noise results from temperature dependence of resistive devices in the photo-detector electronics which may be influenced by both internal heating and fluctuations in the laser power. Flicker noise scales with a pink, $1/f$, or more generally $1/f^n$, power spectrum which result from a combination of long-term processes. This includes any non-shot-noise based relaxation processes or fluctuations in the semi-conductor characteristics which range from white noise ($1/f^0$) to Brownian-quantum noise ($1/f^2$) [58].

3.4.1.1 Shot-Noise

The theoretical basis for shot noise results from the inability to distinguish between individual photons when incident on a photo-current producing semi-conductor. This well-understood measurement limitation presents itself with a Poissonian distribution and an uncertainty that scales with the square root of the number of photons in Δt measurement time, $\sigma_N = \sqrt{N\Delta t}$, where

$$N\Delta t = \frac{P_{\text{Laser}}}{E_{\text{photon}}} \Delta t, \quad (3-10)$$

for a total laser power on the photo-detector, P_{Laser} , with an average photon energy $E_{\text{photon}} = h\nu$. Exploiting Heisenberg's Uncertainty Principle, we can write the RMS phase limitation as:

$$\delta\phi_{\text{RMS-SN}} = \frac{1}{\sigma_N} = \frac{1}{\sqrt{N\Delta t}} = \sqrt{\frac{h\nu}{P_{\text{Laser}}\Delta t}}. \quad (3-11)$$

The phase error, $\delta\tilde{\phi}_{\text{Shot-Noise}}(f)$, presents as a white noise spectrum defined by $\delta\phi_{\text{RMS-SN}}$. Evaluating this with LISA-like values, $P = 200 \text{ pW}$, $\nu = c/\lambda = 282 \text{ THz}$, and $\Delta t = 1 \text{ s}$ we obtain a phase noise of $5 \mu\text{cycles}/\sqrt{\text{Hz}}$. This is far from a complete derivation which should also consider the photon-electron conversion efficiencies, η , but it gives us an idea of the expected phase noise.

For comparison to the dark-current, we can extend this result and write the shot-noise current error as:

$$\delta i_{\text{RMS-SN}} = \sqrt{\sigma_{i_{\text{SN}}}} = \sqrt{\int_{-f_{\text{BW}}}^{f_{\text{BW}}} (e^2 \eta(f) N) df} = \sqrt{2e^2 f_{\text{BW}} \eta N} \quad (3-12)$$

where we have integrated the limited efficiency electro-current over the band-width of the photo-detector, f_{BW} . [59]

3.4.1.2 Dark Current Noise

The semi-conductors used to convert the photons incident on a photo-diode to an electro-current have a characteristic dark-current which results from randomly created and destroyed current producing electrons in the semi-conductor. This random process also results in a shot-noise like Poissonian error which can cause RMS white noise current errors from 1 to 500 nA. [59, 60] These processes result in a current error given by:

$$\delta i_{\text{RMS-Dark}} = \sqrt{\sigma_{i_{\text{Dark}}}} = \sqrt{\int_{-f_{\text{BW}}}^{f_{\text{BW}}} e i_{\text{dark}}(f) df} = \sqrt{2e i_{\text{dark}} f_{\text{BW}}}, \quad (3-13)$$

which can be linearly combined with the photo-detector's shot noise to find the total quantum noise:

$$\delta i_{\text{RMS-Total}} = \sqrt{\delta i_{\text{SN}}^2 + \delta i_{\text{Dark}}^2} = \sqrt{2e f_{\text{BW}} (i_{\text{dark}} + [e\eta N])}. \quad (3-14)$$

3.4.1.3 Johnson-Nyquist Noise

Thermal heating of the photo-diode, whether from internal or external sources, causes the shunt resistance's Johnson-Nyquist noise to add errors to the output current.

This noise couples as a function of the temperature with a magnitude given by:

$$\delta i_{\text{RMS-JN}}(T) = \frac{\sqrt{\int_0^{f_{\text{BW}}} 4Rk_{\text{B}}T}}{R} = \sqrt{\frac{4k_{\text{B}}Tf_{\text{BW}}}{R}} \quad (3-15)$$

where R is the photo-diode's shunt resistance, T is the temperature in Kelvin, and k_{B} is Boltzmann's constant. [61]

Explicitly stated, these shot noise, dark current noise, and Johnson-Nyquist noises are all white noise sources such that the noise contribution increases linearly with the integration time. LISA refers all measurements to a 1 second integration time and plots these white phase noise spectra in cycles/ $\sqrt{\text{Hz}}$.

3.4.1.4 Flicker Noise

Flicker noise may result from a number of sources which are all characterized by having a $1/f^n$ power noise spectrum where $0 < n < 2$. These are largely influenced by long-term non-quantum fluctuations. Long term temperature variations may modify the photo-amplifier's transfer function causing a time-changing phase response, and thus, a long term temperature correlated phase error. Fluctuations in the individual laser powers will also couple into the phase (chapter 3.4.1.5).

Long-term fluctuations in the laser field intensity might be attributed to long term characteristic changes in the coherent field producing Nd:YAG laser crystals including a temperature dependent cavity finesse and the availability of excited states to produce stimulated emission. High-frequency components of the laser intensity will also couple into the measurement and are generally based on the laser's resonant relaxation oscillation [62, 63]. This amplitude-phase coupling can also be introduced by other sources including a photo-detector polarization dependency, electronic noise in the photo-detectors and ADCs resulting from LISA's digitized demodulation measurement scheme. The ill-defined nature of these long-term processes justifies further investigation with lab-based differential PD measurements.

3.4.1.5 Heterodyne Phase Measurements

Consider two laser fields given by:

$$\epsilon_1(t) = E_1(t)e^{i\omega_1(t)t} \quad \epsilon_2(t) = E_2(t)e^{i\omega_2(t)t}. \quad (3-16)$$

Superimposing and combining these laser fields on a photo-detector, we obtain a current given by:

$$\begin{aligned} i_{\text{beat}}(t) &\propto (\epsilon_1(t) + \epsilon_2(t)) (\epsilon_1(t) + \epsilon_2(t))^* \\ &\propto |E_1(t)|^2 + |E_2(t)|^2 + E_1(t)E_2(t) \cos([\omega_1(t) - \omega_2(t)]t) \end{aligned} \quad (3-17)$$

In heterodyne interferometry, the DC portions of $|E_1(t)|^2$ and $|E_2(t)|^2$ are generally AC coupled with RF transformers, although these may still introduce high-frequency components. Combining the independent field terms, $E_{\text{Tot}}(t) = E_1(t)E_2(t) = E_o(1 + \delta E(t))$, and introducing the mean MHz beat frequency, $\omega_{\Delta} = \langle \omega_1(t) - \omega_2(t) \rangle$, we can pick out the, $E_1(t)E_2(t) \cos([\omega_1 - \omega_2]t)$ terms by demodulating this PD output with $\sin(\omega_{\Delta}t)$. Integrating the demodulated DC output, we can get a measure of the differential laser phase:

$$\phi_{\Delta}(t) = \int_0^t [\omega_1(\tau) - \omega_2(\tau) - \omega_{\Delta}] d\tau. \quad (3-18)$$

Variations in the differential field intensity fluctuation, $\delta E(t)$, at frequencies of ω_{Δ} could be coupled into the measurement such that complete description should be written as:

$$\phi_{\Delta}(t) = \int_0^t [\omega_1(\tau) - \omega_2(\tau) - \omega_{\Delta}] + \left[E_o \delta E(\tau) \frac{e^{i\omega_{\Delta}\tau} + e^{-i\omega_{\Delta}\tau}}{2} \right] d\tau \quad (3-19)$$

3.4.2 μ Cycle Phasemeter

The photo-currents produced by the photo-diodes will be sampled with Ω -bit analog-to-digital converters (ADCs). The clocked sampling process which digitizes the PD signals to perform the phasemeter measurements introduces it's own independent noise sources. The 2 – 20 MHz PD-beatnote is sampled with a 50 MHz clock reference

comparing $\phi_{\Delta}(t)$ to the clock phase, $\phi_{\text{CLK}}(t)$, which is not a perfect timing reference, thus, introducing it's own phase noise. The digitization process provides a limited resolution with which to measure the beatnote phase, meanwhile, voltage-bias noise from the ADC voltage reference can also couple into the phase measurement. Timing jitter, the error caused by the time-dependent delay between voltage conversion time and the clock's rising-edge, couples into the measurement as a $1/\sqrt{f}$ phase noise and scales with the input beatnote frequency. These are all discussed in more detail below.

3.4.2.1 Clock Noise

Digitizing the 2 – 20 MHz PD signals with a 50 MHz clock, we sample the PD current driven voltage bias across a load resistor at the 'rising-edge' of the clock oscillation. The PD voltage is compared to a voltage biased resistor bank within the ADCs resulting in a Ω -bit read-out of the load resistance voltage. Given an input oscillation with an ideal amplitude written as:

$$x_{\text{in}}(t) = A_{\text{in}} \sin(2\pi f_{\text{in}} t + \phi_{\text{in}}(t)) \quad (3-20)$$

we sample the input signal with a clock source given by:

$$x_{\text{CLK}}(t) = A_{\text{CLK}} \sin(2\pi f_{\text{CLK}} t + \phi_{\text{CLK}}(t)). \quad (3-21)$$

where $\phi_{\text{in}}(t)$ is the input phase noise with respect to the input frequency, f_{in} , and $\phi_{\text{CLK}}(t)$ is the clock phase noise with respect to f_{CLK} [64].

Using an ideal clock the phase error in the digitization conversion would be limited by the bit-resolution, discussed in the following section. In practice, the phase noise in the clock source with respect to the theoretical clock frequency is interpreted as input phase noise scaled by the ratio of their frequencies such that:

$$\phi_{\text{Measured}}(t) = \int_0^t \frac{\omega_{\text{in}}(\tau)}{\omega_{\text{CLK}}(\tau)} d\tau = \phi_{\text{in}}(t) - \frac{f_{\text{in}}}{f_{\text{CLK}}} \phi_{\text{CLK}}(t). \quad (3-22)$$

In LISA, these clock noise terms must be accounted for by performing inter-SC clock noise transfers and measuring the differential clock noise terms against the local SC's clock. Afterwards, the differential phase and differential clock measurements are interpolated to compare them against one global master clock.

3.4.2.2 ADC Quantization Noise

When sampling a voltage signal, $V_{in}(t)$, with a clock, f_{Clk} , the ADC compares the input voltage against the ADC internal voltage bias reference. This comparison process produces a series of samples given by:

$$x_{in}[n] = \frac{V_{in}(n/f_{Clk})}{V_{Bias}} \quad (3-23)$$

where we have taken the bias voltage to be a constant, stable reference. This -1 to 1 ratio is converted to a series of Ω -bit values with a $2^{1-\Omega}$ resolution [65]. Thus, given this bit-accuracy we obtain a standard-deviation in the measured amplitude given by:

$$\delta\tilde{\phi}_{ADC \text{ Amp.-Quant.}}(\omega) = \frac{|V_{Bias}|}{|V_{in}|} \frac{2^{1-\Omega}}{\sqrt{6}f_s}. \quad (3-24)$$

The extra factor of $1/\sqrt{6}$ comes from the white-noise properties of the quantization probability density function [65, 66]. The factor of V_{Bias}/V_{in} accounts for the fact that the signal amplitude may not span the full Ω -bits of the ADC's conversion-amplitude. Additional quantization errors can and will be applied to this hard-ware based quantization limit as these digitized signals are measured with bit-limited fixed point processors and rate-limited read-outs introducing their own quantization errors.

3.4.2.3 ADC Amplitude Noise

Extending this description, we consider fluctuations in the voltage bias against which the photo-current is measured. More generally one can write the bias voltage as:

$$V_{Bias}(t) = V_{Bias_0}G(t) + V_{Gnd}(t) \quad (3-25)$$

where $G(t)$ is the gain factor on the voltage bias with $\langle G(t) \rangle \simeq 1$ and V_{Gnd} is the voltage of the ground reference in comparison to the input's 'ideal' ground. Ignoring the ground term for the moment, this fluctuation in the bias voltage scales the amplitude error as:

$$\delta\tilde{X}_{\text{ADC Amp-Quant.}}(\omega) = \delta\tilde{G}(\omega) \frac{|V_{\text{Bias}_0}|}{|V_{\text{in}}|} \frac{2^{1-\Omega}}{\sqrt{6f_s}} \quad (3-26)$$

which shows how these gain factors can couple directly into the measured amplitude. Since LISA measurements are focused on phase noise, the coupling of these amplitude quantization and bias noise error sources into the phase measurements are analyzed in chapter [3.4.2.5](#)

It is often difficult to distinguish between the ADC amplitude noise, the laser intensity noise, and the PD electronic current amplitude noise since they all couple into the phase measurement with the same characteristics. On the other hand, we can get some measure of the ADC amplitude bias noise by verifying the inverse dependence on the input voltage. Often-times, these low frequency amplitude variations are dominated by temperature variations; thus, thermal correlation coefficients can be measured by observing the phase variation with a change in temperature. Given these correlation coefficient measurements we can define an electronic temperature environment stability requirement.

3.4.2.4 Clock-ADC Timing Jitter

ADC timing jitter is defined as the time-changing delay between the well-defined rising edge of the clock and the actual sample triggering of the ADC input signal. This timing jitter value can have a frequency dependence, $\delta\tilde{t}(\omega)$, which scales proportionately with the beat-frequency, $f_{\text{in}} = \langle d\phi/dt \rangle$, to phase noise [\[67\]](#):

$$\delta\tilde{\phi}(\omega) = f_{\text{in}} \delta\tilde{t}_{\text{Jit}}(\omega). \quad (3-27)$$

This frequency coupling can and will be exploited to estimate the ADC timing jitter.

3.4.2.5 Demodulation Noise Coupling

Now that we have seen how each of these individual noise sources scale with their input characteristics, we evaluate how these measurements will couple into the demodulated phasemeter readout. First, as an example of how this readout is performed, we consider an input signal with some phase and amplitude variation where $\delta A(t), \delta\phi(t) \ll 1$, while ω_{in} and 'A' are constant, given by:

$$x(t) = A[1 + \delta A(t)] \sin(\omega_{in}t + \delta\phi(t)). \quad (3-28)$$

If we demodulate this with the in-phase and quadrature components of the input at the same frequency, such that $\omega_{off} = \omega_{in}$, we obtain following terms:

$$\begin{aligned} y_{In-phase}(t) &= x(t) \times \sin(\omega_{off}t) & (3-29) \\ &= \frac{A[1 + \delta A(t)]}{2} [\cos(\delta\phi(t)) - \cos((\omega_{in} + \omega_{off})t + \delta\phi(t))], \end{aligned}$$

$$\begin{aligned} y_{Quad}(t) &= x(t) \times \cos(\omega_{off}t) & (3-30) \\ &= \frac{A[1 + \delta A(t)]}{2} [\sin(\delta\phi(t)) + \sin((\omega_{in} + \omega_{off})t + \delta\phi(t))]. \end{aligned}$$

After low-pass filtering to remove the sum, $(\omega_{in} + \omega_{off})$ term, we can write the result as a function of the amplitude and phase error as:

$$y_{In-phase}(t) = \frac{A[1 + \delta A(t)]}{2} [\cos(\delta\phi(t))], \quad (3-31)$$

$$y_{Quad}(t) = \frac{A[1 + \delta A(t)]}{2} [\sin(\delta\phi(t))] \quad (3-32)$$

Based on the definitions of the in-phase and quadrature components, one can exactly reconstruct the amplitude

$$A_{Read-Out}(t) = 2\sqrt{y_{In-phase}(t)^2 + y_{Quad}(t)^2} = A[1 + \delta A(t)] \quad (3-33)$$

and phase,

$$\phi_{\text{Read-Out}}(t) = \tan^{-1} \left[\frac{y_{\text{Quad}}(t)}{y_{\text{In-phase}}(t)} \right] = \delta\phi(t). \quad (3-34)$$

On the other hand, using the small value assumption, $\delta\phi(t) \ll 1$, we can make the approximations, $\cos(\delta\phi(t)) = 1$ and $\sin(\delta\phi(t)) = \delta\phi(t)$, such that the amplitude and phase read-outs simplify. Using the in-phase component only we could write the amplitude as:

$$A_{\text{Read-Out}}(t) \simeq 2y_{\text{In-phase}}(t) = A[1 + \delta A(t)] \cos(\delta\phi(t)). \quad (3-35)$$

Using the same argument we can write two approximations for the phase, given by:

$$\delta\phi(t) \simeq \frac{y_{\text{Quad}}(t)}{y_{\text{In-phase}}(t)} = \tan(\delta\phi(t)), \quad (3-36)$$

or

$$\delta\phi(t) \simeq \frac{2}{A} y_{\text{Quad}}(t) = (1 + \delta A(t)) \sin(\delta\phi(t)). \quad (3-37)$$

These approximations are useful in reducing the load on the digital processing devices but, as we can see from these calculations, they also tend to couple the amplitude and phase noise sources together which must be considered for LISA-like high-precision phase measurements.

The details of the phasemeter phase tracking and read-out become more complicated when we allow for $A(t)$ and $\phi(t)$ to change arbitrarily, but this model will give us an idea of how un-desired noise terms will couple into the demodulated phase measurement. At this point we can see that, depending on the type of readout approximation used, these error terms will couple in differently. Our focus will be on (3-37) since, as we will see in chapter 5.2.1, this is the phasemeter read-out scheme we use to measure the input phase. Already we can see how the amplitude noise couples into the phase ($G(t)$ in (3-25) for example). Unfortunately, this fails to give a complete understanding of the noise coupling since this first order approximation fails to

consider how high-frequency terms couple into the measurement through the clocking and feed-back tracking demodulation processes.

The clock-sampling demodulation will alias high-frequency terms into the digital ADC output such that the input phase terms at $n f_{\text{clk}} \pm f_{\text{in}}$ will superimpose with a gain of 1 directly into the f_{in} frequency bin. Following standard electronics procedures, RF transformers are used to AC couple the input and low-pass anti-aliasing filters are used to suppress any information at frequencies greater than f_{in} .

Even though the input signal is AC coupled, we will include an offset error in the extended measurement-demodulation treatment such that we now write the input as:

$$x(t) = \delta A_{\text{Off}}(t) + A[1 + \delta A(t)] \sin(\omega_{\text{in}} t + \delta \phi(t)). \quad (3-38)$$

Again, demodulating with the quadrature component we obtain:

$$y_{\text{Quad}}(t) = \frac{A[1 + \delta A(t)]}{2} [\sin(\delta \phi(t)) + \sin(2\omega_o t + \delta \phi(t))] + \delta A_{\text{Off}}(t) \cos(\omega_o t). \quad (3-39)$$

where we have set $\omega_o = \omega_{\text{in}} = \omega_{\text{off}}$.

Taking a deviation from the previous treatment we expand out these results to explicitly show the DC, ω_o , and $2\omega_o$ terms:

$$y_{\text{Quad}}(t) = \frac{A[1 + \delta A(t)]}{2} [\sin(\delta \phi(t)) + \sin(2\omega_o t) \cos(\delta \phi(t)) + \cos(2\omega_o t) \sin(\delta \phi(t))] + \delta A_{\text{Off}}(t) [\cos(\omega_o t)]. \quad (3-40)$$

Finally applying the $\delta \phi, \delta A, \delta A_{\text{off}} \ll 1$ approximation, low-pass filtering the terms which have no noise coupling, applying (3-37), and expanding explicitly, we obtain:

$$\delta \phi_{\text{Est}}(t) = \frac{2}{A} y_{\text{Quad}}(t) \quad (3-41)$$

$$\begin{aligned} &= \delta \phi(t) \left(1 + \frac{\delta A(t)}{A} \right) + \delta \phi(t) \left(1 + \frac{\delta A(t)}{A} \right) \cos(2\omega_o t) \\ &\quad + \delta \phi(t) \cos(2\omega_o t) + \frac{\delta A(t)}{A} \sin(2\omega_o t) + \frac{\delta A_{\text{Off}}(t)}{A} \cos(\omega_o t). \end{aligned} \quad (3-42)$$

From this we can read off the noise-coupling of each term. The term we are interested in, $\delta\phi(t)$, is scaled by $1 + \delta A(t)/A$. Generally, since $\delta A(t)/A \ll 1$, this effect is small, but may be a limiting noise source when attempting to form differential phase cancellation combinations. Although, since this term scales inversely with the amplitude, it can be reduced, depending on the source, by increasing the signal power. If the amplitude noise comes from fluctuations in the laser power, for example, increasing the signal power tends to also increase the noise such that $\delta A(t)/A$ remains constant. Next we notice both the $\delta\tilde{\phi}(2\omega_o)$ and $\delta\tilde{A}(2\omega_o)$ terms of the input wave-form couple into the phase measurement. Finally, we notice that the offset error, $\delta\tilde{A}_{\text{Off}}(\omega_o)$, term couples directly into the measurement. This term would be of an error like $V_{\text{Gnd}}(t)$ in (3–25).

We can mitigate the $2\omega_o$ terms by anti-alias low-pass filtering the input signal at frequencies greater than ω_o . Unfortunately, if these terms are generated by the ADC after the anti-aliasing filter they will, again, couple into the phase data. Taking this into account, extensive low-frequency testing of the ADCs must be performed to ensure these errors do not limit the phase measurement sensitivity. We will see how the UF-phasemeter's ADCs are tested and characterized in chapter 5.3.

3.4.3 Heterodyne Time-Delay Interferometry

Until now, we have not specifically stated how the one-way interferometry observables, χ_{sr} , b_{sr} , and s_{sr} , are measured and mitigated. Here we derive the terms on SC_1 but the procedure used can be employed to derive the observables on the other SC. For the χ_{sr} and b_{sr} observables, we consider the two local SC_1 lasers, Laser_{21} and Laser_{31} , which transmit their fields to SC_2 and SC_3 , respectively, having a laser frequencies, ω_{21} and $\omega_{31} = \omega_{21} + \omega_{\Delta}$, and laser phases, $\phi_{21}(t)$ and $\phi_{31}(t)$, such that we can could write the laser fields as:

$$\epsilon_{21}(t) = E_{21}(t)e^{i(\omega_{21}t + \phi_{21}(t))} \quad \epsilon_{31}(t) = E_{31}(t)e^{i((\omega_{21} + \omega_{\Delta})t + \phi_{31}(t))}. \quad (3-43)$$

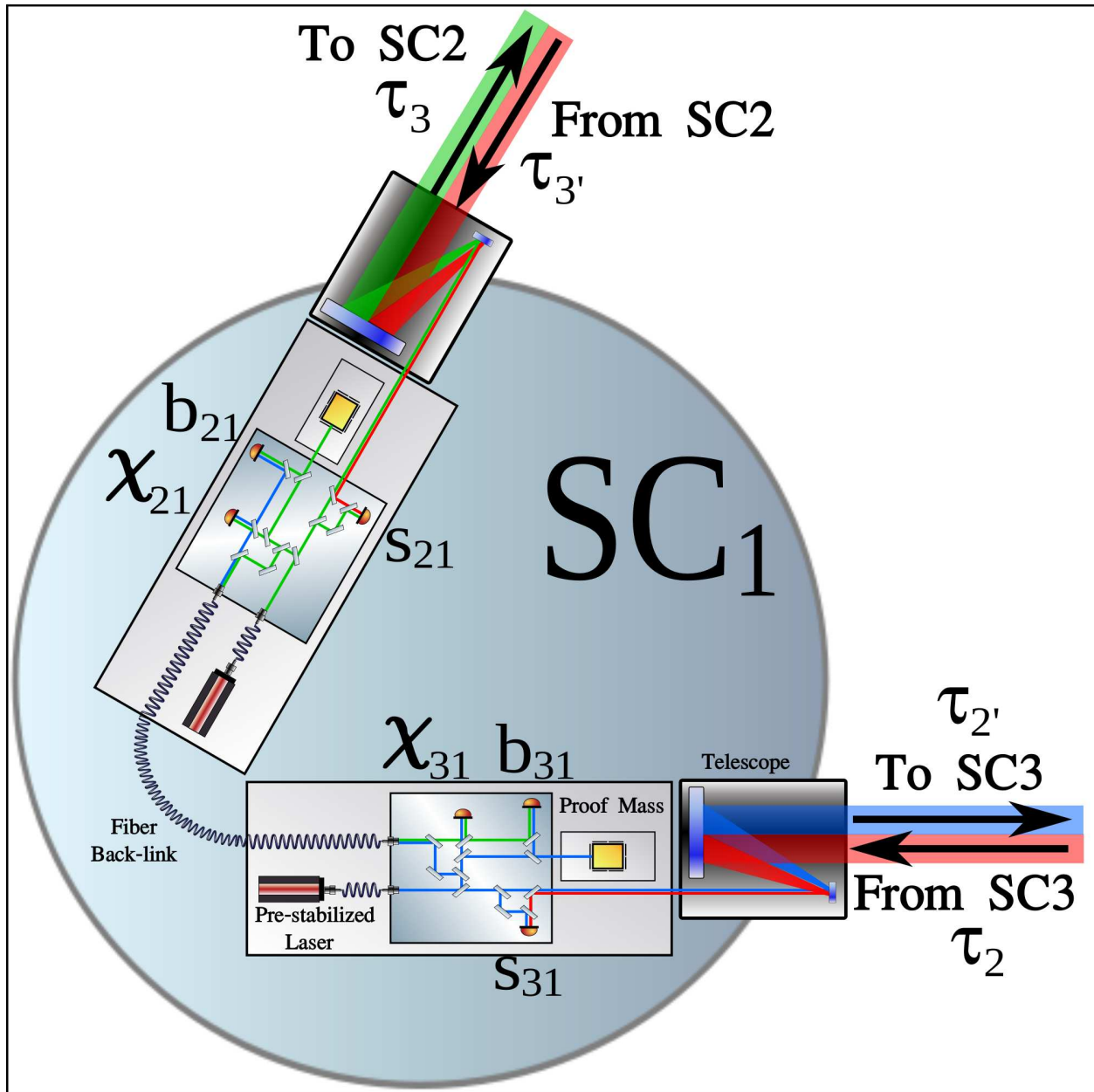


Figure 3-3. Diagram of the interferometry measurement system: This model shows a more detailed depiction of the individual satellites shown in Figure 3-2. Here we see the beam path and heterodyned laser fields resulting from the two local lasers and the two laser fields being transmitted from the far SC. The LISA observables, χ_{sr} , b_{sr} , and s_{sr} and how they are generated with the heterodyned laser fields is shown explicitly.

These laser noise sources are used to track the major phase noise coupling terms through the interferometer although, from here on, we will ignore the amplitude terms and take $E_{21}(t) = E_{31}(t) = E$.

3.4.3.1 Fiber Noise

The independent laser fields are passed through a fiber bank-link adding both common-mode and non-reciprocal phase noise such that the fields after passing through the back-link fibers can be written as:

$$\epsilon_{21,\text{fb}}(t) = E e^{i(\omega_{21}t + \phi_{21}(t) + \phi_{\text{fb},C}(t) + \phi_{\text{fb},21}(t))} \quad (3-44)$$

$$\epsilon_{31,\text{fb}}(t) = E e^{i(\omega_{31}t + \phi_{31}(t) + \phi_{\text{fb},C}(t) + \phi_{\text{fb},31}(t))} \quad (3-45)$$

where $\phi_{i1,\text{fb}}$ are the independent, counter-propagating fiber noise terms and $\phi_{\text{fb},C}$ are the common fiber noise terms.

Superimposing these laser fields from either side of the fiber onto a photo-detector and AC coupling the PD output, we obtain photo-currents given by:

$$\begin{aligned} \text{PD}_{\chi_{21}}(t) &= \sqrt{(\epsilon_{21}(t) + \epsilon_{31,\text{fb}}(t))(\epsilon_{21}(t) + \epsilon_{31,\text{fb}}(t))^*} \\ &\propto \cos(\omega_{\Delta}t + \phi_{31}(t) - \phi_{21}(t) + \phi_{\text{fb},C}(t) + \phi_{\text{fb},31}(t)) \end{aligned} \quad (3-46)$$

$$\begin{aligned} \text{PD}_{\chi_{31}}(t) &= \sqrt{(\epsilon_{31}(t) + \epsilon_{21,\text{fb}}(t))(\epsilon_{31}(t) + \epsilon_{21,\text{fb}}(t))^*} \\ &\propto \cos(\omega_{\Delta}t + \phi_{31}(t) - \phi_{21}(t) - \phi_{\text{fb},C}(t) - \phi_{\text{fb},21}(t)) \end{aligned} \quad (3-47)$$

Demodulating these signals with $\sin(\omega_{\Delta}t)$ and measuring the phase terms we obtain two phase read-outs given by:

$$\chi_{21}(t) = \phi_{31}(t) - \phi_{21}(t) + \phi_{\text{fb},C}(t) + \phi_{\text{fb},31}(t) + \frac{f_{\Delta}}{f_{\text{CLK}}} \delta\phi_{\text{CLK}}(t) \quad (3-48)$$

$$\chi_{31}(t) = \phi_{31}(t) - \phi_{21}(t) - \phi_{\text{fb},C}(t) - \phi_{\text{fb},21}(t) + \frac{f_{\Delta}}{f_{\text{CLK}}} \delta\phi_{\text{CLK}}(t) \quad (3-49)$$

with the expected differential laser phase, $\phi_{31}(t) - \phi_{21}(t)$, counter-propagating fiber noise terms, and clock noise terms. The common fiber noise terms couple into each PD

with the opposite phase such that the sum of these observables gives a measure of the differential counter-propagating phase noise terms:

$$\phi_{\chi\text{-Sum}} = \chi_{21} + \chi_{31} = 2 \left(\phi_{31}(t) - \phi_{21}(t) + \frac{f_{\Delta}}{f_{\text{CLK}}} \delta\phi_{\text{CLK}}(t) \right) + \phi_{\text{fib},31} - \phi_{\text{fib},21} \quad (3-50)$$

while the difference of these terms gives a measure of the common mode fiber terms:

$$\phi_{\chi\text{-Dif}} = \chi_{21} - \chi_{31} = 2\phi_{\text{fib},C}(t) + \phi_{\text{fib},31} + \phi_{\text{fib},21}. \quad (3-51)$$

The individual counter-propagating phase noise terms must be smaller than 1 μcycle since there is no way to differentiate between this and the independent laser noise terms. In the next section we will see how these differential laser phase and common mode fiber terms cancel when evaluating the proof-mass to spacecraft distance.

3.4.3.2 Spacecraft/Proof-Mass Motion

Now that we have a measure of the fiber noise, we use the same laser fields to get a measure of the individual SC to proof-mass distance. If we define the distance between the SC beam-splitter and the proof-mass as $\delta d(t)$ we can convert this to laser phase noise after reflecting off the proof mass by re-writing the fiber terms, $\epsilon_{21,\text{fib}}(t)$ and $\epsilon_{21,\text{fib}}(t)$, as:

$$\epsilon_{21,\text{mass}}(t) = \text{E}e^{i(\omega_{21}t + \phi_{21}(t) + \phi_{\text{fib},C}(t) + \phi_{\text{fib},21}(t) + \frac{\delta d_{31}}{\lambda})} \quad (3-52)$$

$$\epsilon_{31,\text{mass}}(t) = \text{E}e^{i(\omega_{31}t + \phi_{31}(t) + \phi_{\text{fib},C}(t) + \phi_{\text{fib},31}(t) + \frac{\delta d_{21}}{\lambda})}. \quad (3-53)$$

Demodulating these with the local bench's laser field, we obtain the b_{sr} signals:

$$\begin{aligned} \text{PD}_{b_{21}}(t) &= \sqrt{(\epsilon_{21}(t) + \epsilon_{31,\text{mass}}(t))(\epsilon_{21}(t) + \epsilon_{31,\text{mass}}(t))^*} \\ &\propto \cos(\omega_{\Delta}t + \phi_{31}(t) - \phi_{21}(t) + \phi_{\text{fib},C}(t) + \phi_{\text{fib},31}(t) + \frac{\delta d_2}{\lambda}) \end{aligned} \quad (3-54)$$

$$\begin{aligned} \text{PD}_{b_{31}}(t) &= \sqrt{(\epsilon_{31}(t) + \epsilon_{21,\text{mass}}(t))(\epsilon_{31}(t) + \epsilon_{21,\text{mass}}(t))^*} \\ &\propto \cos(\omega_{\Delta}t + \phi_{31}(t) - \phi_{21}(t) - \phi_{\text{fib},C}(t) - \phi_{\text{fib},21}(t) - \frac{\delta d_3}{\lambda}). \end{aligned} \quad (3-55)$$

Measuring the beatnote phase with phasemeters, we can write the b_{sr} observables as:

$$b_{21}(t) = \phi_{31}(t) - \phi_{21}(t) + \phi_{\text{fib},C}(t) + \phi_{\text{fib},31}(t) + \frac{\delta d_2}{\lambda} + \frac{f_{\Delta}}{f_{\text{CLK}}} \delta \phi_{\text{CLK}}(t) \quad (3-56)$$

$$b_{31}(t) = \phi_{31}(t) - \phi_{21}(t) - \phi_{\text{fib},C}(t) - \phi_{\text{fib},21}(t) - \frac{\delta d_3}{\lambda} + \frac{f_{\Delta}}{f_{\text{CLK}}} \delta \phi_{\text{CLK}}(t) \quad (3-57)$$

Linear combinations of these four signals, $\chi_{21}(t)$, $\chi_{31}(t)$, $b_{21}(t)$, and $b_{31}(t)$ provide us with a local measure of the SC to proof mass distance and the differential laser phase terms:

$$\delta d_2 = \lambda [b_{21} - \chi_{21}], \quad (3-58)$$

$$\delta d_3 = \lambda [\chi_{31} - b_{31}], \quad (3-59)$$

$$\phi_{31} - \phi_{21} = \frac{\chi_{21} + \chi_{31}}{2} + \frac{\phi_{\text{fib},21} - \phi_{\text{fib},31}}{2} - \frac{f_{\Delta}}{f_{\text{CLK}}} \delta \phi_{\text{CLK}}(t) \quad (3-60)$$

We notice in these equations that the SC-to-proof-mass distances, δd_2 and δd_3 , are independent of any fiber noise terms. Meanwhile, the differential laser phase terms are limited by the individual counter-propagating fiber terms $\phi_{\text{fib},31}$ and $\phi_{\text{fib},21}$. The δd terms are independent of clock noise since they are measured on the same spacecraft at the same heterodyne offset frequency, ω_{Δ} , and the common clock noise cancels in these differential measurements.

3.4.3.3 Inter-Spacecraft Motion

Now that we have a method of evaluating the local-SC to local-proof-mass distance we must measure the inter-SC arm-length terms to be able to construct the complete differential inter-proof-mass interferometer. In this description we will focus on a single one-way inter SC link between SC_1 and SC_2 where Laser_{12} , having a laser frequency $\omega_{12}(t)$, is transmitted along Arm-3' acquiring a time-delay, $\tau_{3'}(t)$, and then is heterodyned with Laser_{21} , having a laser frequency $\omega_{21}(t)$. Inter-SC length changes at velocities of

0 – 20 m/s for LISA⁴ , cause relativistic Doppler shifts and time-domain phase scaling of the laser fields.

To calculate the field transformation, we first define the measured phase as the integration of the laser beat frequency with respect to a retarded time, $t_r = t - x/c$, such that both position and time changes affect the measured phase:

$$\phi(t) = \int_0^t \omega(t_r) dt_r \quad (3-61)$$

Taking SC₂ as the stationary frame of reference we define the inter-SC light travel time from SC₂ to SC₁ as $\tau_{3'}(t) = \tau_{3'}(0) + \beta_{3'}t$ where $\beta_{3'} = v_{3'}/c = d\tau(t)/dt$. A positive velocity refers to an increasing inter-SC distance such that SC₁ is moving away from the SC₂. In the stationary SC₂ frame we can write the laser field generated by Laser₂₁ as:

$$\epsilon_{12;\emptyset}(x, t) = Ee^{-i(t-\frac{x}{c})} \omega_{12}(t-\frac{x}{c}) \quad (3-62)$$

and the measured phase evaluated at x=0:

$$\phi_{12}(t) = \int_0^t \omega_{12} \left(\tau - \frac{0}{c} \right) d\tau \quad (3-63)$$

We can transform this to the moving SC₁ reference frame through a relativistic Lorentz transformation as:

$$\epsilon_{12;3'}(x', t') = Ee^{i\gamma(1-\beta)(t'-\frac{x'}{c})} \omega_{12}(\gamma(1-\beta)(t'-\frac{x'}{c})) \quad (3-64)$$

where, for this arm, $\beta = \beta_{3'}$ and $\gamma = \gamma_{3'} = 1/\sqrt{1-\beta^2}$ and $t_r = \gamma(1-\beta)(t' - x'/c)$.

From this equation, we see the relativistic Doppler shift transforming $\omega_{12} \rightarrow \gamma(1-\beta)\omega_{12}$.

Integrating the beatnote frequency in this moving frame:

$$\phi(t') = \gamma(1-\beta) \int_0^{t'} \omega_{12} \left(\gamma(1-\beta) \left(\tau - \frac{L_q(0)}{c} \right) \right) d\tau \quad (3-65)$$

⁴ Other missions may have differential velocities which are significantly larger[56]

such that we can write the measured phase relationship:

$$\phi'(t')_{;q} = \phi(\gamma_q(1 - \beta_q)(t' - \tau_q(0))) \quad (3-66)$$

where $\tau_q(0) = L_q(0)/c$. In most LISA-like cases, we ignore the small factors of $\beta^2 < 10^{-12}$ and so, will drop the γ factors in the analysis from this point forward. Notice the ';' notation used to transform the laser field between moving frames in (3-64) and (3-66). In general $\phi_{sr;q}(t) = \phi_{sr}((1 - \beta_q)(t - \tau_q(0)))$ where we have taken $t \rightarrow (1 - \beta_q)(t - \tau_q(0))$. We will use this same notation through the rest of the TDI analysis.

The field from the far SC is reflected through a transmitting telescope, transmitted to the local SC acquiring a multi-second time-delay⁵, and captured by the local receiving telescope.

Heterodyning these laser fields we obtain a photo-current given by:

$$PD_{s_{21}}(t) = \sqrt{(\epsilon_{21}(t) + \epsilon_{12;3'}(t))(\epsilon_{21}(t) + \epsilon_{12;3'}(t))^*} \quad (3-67)$$

$$\propto \cos((\omega_{21} - (1 + \beta_{3'})\omega_{12})t \pm (\phi_{21}(t) - \phi_{12}((1 - \beta_{3'})(t - \tau_{3'}(0)))) \quad (3-68)$$

where we notice that the sign of the phase information depends on the relative magnitude of the local laser frequency in comparison with the inter-SC Doppler shifted laser's frequency. Although this may be easily corrected in post-processing, the relative laser frequencies and inter-SC Doppler shifts will change the sign on both the observable and clock noise corrections terms in the TDI combinations and must be kept in mind when forming the post-processed TDI combinations.

Generalizing to include the clock noise and GW terms we can write the s_{21} inter-SC term as:

$$s_{21} = \phi_{21}(t) - \phi_{12}((1 - \beta_{3'})(t - \tau_{3'}(0))) + h_{21}(t) + \frac{f_{21}}{f_{\text{Clk}}} \phi_{\text{Clk};1}(t), \quad (3-69)$$

⁵ $\tau = 5\text{Gm}/c = 16.7 \text{ s}$ for LISA

where we have introduced the GW strain modulation of $h(t) = \delta L(t)/L_o$, and a local SC_i clock noise term, $\phi_{\text{Clk};i}(t)$, scaled by the PD beatnote frequency, f_{21} . We have also made assumptions about the sign of the differential measured phase based on the relative laser and Doppler frequencies for evaluating the TDI combinations.

3.4.3.4 Basic TDI-Combinations and Considerations

At this point, we have formed and evaluated all the observables required to completely re-construct the differential proof-mass interferometer. These signals, χ_{sr} , b_{sr} , and s_{sr} , can be evaluated for each of the 3 SC and 6 inter-SC laser links resulting in 18 different observables. When any of these observables are measured with a phasemeter, clock noise terms given by $(f_{\text{in}}/f_{\text{Clk}})\phi_{\text{Clk};i}(t)$ where is the phase noise of clock located on SC_i , are added to the digital signals and must be accounted for with the inter-SC side-band clock noise transfers [68–70]. These observables can also be used to phase-lock the adjacent optical bench lasers or the adjacent inter-SC lasers into order to transfer the laser stability and obtain common-mode laser noise cancellation to within the accuracy of the phase lock loops (PLLs) [71].

The focus of this dissertation is to form the TDI combinations based on the inter-SC laser links, s_{sr} . To simplify the analysis, from this point on we will make some assumptions about the measured observables. First, assuming the local-SC to local-proof-mass motion can be measured through heterodyne interferometry and that the acceleration noise of the proof-mass can be effectively reduced with the DRS, it is reasonable to imagine the proof-masses as being mounted directly to the SC, thus setting $\delta d_{\text{sr}} = 0$. Next, assuming the non-reciprocal fiber-backlink noise can be reduced beyond the $1 \mu\text{cycle}$ requirement, we will have a reasonable measure of the adjacent bench-top differential laser noise and can ignore the χ_{sr} signals, referencing all measurements to a single Laser_i on SC_i with a laser phase $\phi_i(t)$.

In this specific case we can write a complete basis⁶ for all 6 inter-SC interferometry measurements including clock noise terms as:

$$\begin{aligned}
s_{21}(t) &= \phi_1(t) - \phi_2((1 - \beta_{3'}) (t - \tau_{3'}(0))) + h_{21}(t) + \frac{f_{21}}{f_{\text{Clk}}} \phi_{\text{Clk}:1}(t), \\
s_{31}(t) &= \phi_1(t) - \phi_3((1 - \beta_2) (t - \tau_2(0))) + h_{31}(t) + \frac{f_{31}}{f_{\text{Clk}}} \phi_{\text{Clk}:1}(t), \\
s_{12}(t) &= \phi_2(\Lambda_{12}t) - \phi_1((1 - \beta_3) (\Lambda_{12}t - \tau_3(0))) + h_{12}(\Lambda_{12}t) + \frac{f_{12}}{f_{\text{Clk}}} \phi_{\text{Clk}:2}(\Lambda_{12}t), \\
s_{32}(t) &= \phi_2(\Lambda_{12}t) - \phi_3((1 - \beta_{1'}) (\Lambda_{12}t - \tau_{1'}(0))) + h_{32}(\Lambda_{12}t) + \frac{f_{32}}{f_{\text{Clk}}} \phi_{\text{Clk}:2}(\Lambda_{12}t), \\
s_{13}(t) &= \phi_3(\Lambda_{13}t) - \phi_1((1 - \beta_{2'}) (\Lambda_{13}t - \tau_{2'}(0))) + h_{13}(\Lambda_{13}t) + \frac{f_{13}}{f_{\text{Clk}}} \phi_{\text{Clk}:3}(\Lambda_{13}t), \\
s_{23}(t) &= \phi_3(\Lambda_{13}t) - \phi_2((1 - \beta_1) (\Lambda_{13}t - \tau_1(0))) + h_{23}(\Lambda_{13}t) + \frac{f_{23}}{f_{\text{Clk}}} \phi_{\text{Clk}:3}(\Lambda_{13}t).
\end{aligned} \tag{3-70}$$

where we have differentiated between the different clock phase noise terms, $\phi_{\text{Clk}:i}$, and absolute clock frequency offsets⁷:

$$\Lambda_{ij} = \frac{f_{\text{Clk}:j}}{f_{\text{Clk}:i}}. \tag{3-71}$$

The clock phase noise terms are removed with the inter-SC clock noise transfers when forming the TDI combinations while the clock frequency offsets are accounted for by time-scaled interpolation [72, 73] of the 'far' SC signals by the inverse clock ratio, Λ_{ij} , before forming the TDI combinations with respect to the local reference clock, in the above example case, $f_{\text{Clk}:1}$.

Two useful combinations for further analysis will be the single-arm round-trip sensor signals Δ_{sr} and the counter-propagating Sagnac signals ζ_{sr} , as diagrammed in

⁶ Assuming SC-1 is our stationary frame of reference and Clock-1 is our absolute clock frequency reference.

⁷ The clock frequency offsets from clocks on different SC cause an error in the reference to an absolute time which is defined by the frequency of the clock on SC₁.

Figure 4-2 which provide us with a measure of the constellation interferometry dynamics referred to a single laser source.

The local sensor signals can be derived from the s_{sr} data streams by time-scaling the far SC measurements by the respective inverse clock ratio (Λ_{ij}^{-1}), then time-shifting and time-scaling the result by the return trip's delay transformation, $s_{sr;q}$.

$$\Delta_{21}(t) = s_{21}(t) + s_{12;3'}(\Lambda_{12}^{-1}t) \quad (3-72)$$

$$\begin{aligned} &= \phi_1 - \phi_{2;3'} + h_{21} + \frac{f_{21}}{f_{\text{Clk}}}\phi_{\text{Clk}:1} + (\phi_2 - \phi_{1;3} + h_{12} + \frac{f_{12}}{f_{\text{Clk}}}\phi_{\text{Clk}:2})_{;3'} \\ &= \phi_1 - \phi_1((1 - \beta_3)((1 - \beta_{3'})(t - \tau_{3'}(0)) - \tau_3(0))) \\ &\quad + h_{21}(t) + h_{12}((1 - \beta_{3'})(t - \tau_{3'}(0))) \\ &\quad + \frac{f_{21}}{f_{\text{Clk}}}\phi_{\text{Clk}:1}(t) + \frac{f_{12}}{f_{\text{Clk}}}\phi_{\text{Clk}:2}((1 - \beta_{3'})(t - \tau_{3'}(0))) \end{aligned} \quad (3-73)$$

and, for Arm-3,

$$\Delta_{31}(t) = s_{31}(t) + s_{13;2}(\Lambda_{13}^{-1}t) \quad (3-74)$$

$$\begin{aligned} &= \phi_1 - \phi_{3;2} + h_{31} + \frac{f_{31}}{f_{\text{Clk}}}\phi_{\text{Clk}:1} + (\phi_3 - \phi_{1;2'} + h_{13} + \frac{f_{13}}{f_{\text{Clk}}}\phi_{\text{Clk}:3})_{;2} \\ &= \phi_1 - \phi_1((1 - \beta_{2'})(((1 - \beta_2)(t - \tau_2(0)) - \tau_{2'}(0))) \\ &\quad + h_{31}(t) + h_{13}((1 - \beta_2)(t - \tau_2(0))) \\ &\quad + \frac{f_{31}}{f_{\text{Clk}}}\phi_{\text{Clk}:1}(t) + \frac{f_{13}}{f_{\text{Clk}}}\phi_{\text{Clk}:3}((1 - \beta_2)(t - \tau_2(0))) \end{aligned} \quad (3-75)$$

which cancel the far SC's laser phase noise and reference all phase modulations to a single laser source, $\phi_1(t)$. Here we can explicitly see the clock-noise coupling which enters into the sensor signals' data-streams with the form:

$$\Delta - \text{Clk}_{s1}(t) = \frac{f_{s1}}{f_{\text{Clk}:1}}\phi_{\text{Clk}:1}(t) + \frac{f_{1s}}{f_{\text{Clk}}}\phi_{\text{Clk}:s}((1 - \beta_q)(t - \tau_q(0))). \quad (3-76)$$

As we will see in Ch. 4.1.2 and Ch. 4.3, these terms can be accounted for by the clock-noise transfers in (4-3).

Another set of useful combinations are (Ch. 4.3.2.1) the counter-propagating round-trip Sagnac signals:

$$\theta_{21}(t) = s_{21} + s_{32}(\Lambda_{12}^{-1}t)_{;3'} + s_{13}(\Lambda_{13}^{-1}t)_{;1'3'} \quad (3-77)$$

$$= \phi_1 - \phi_{1;2'1'3'} + [h_{21} + h_{32;3'} + h_{13;1'3'}] \quad (3-78)$$

and

$$\theta_{31}(t) = s_{31} + s_{23}(\Lambda_{13}^{-1}t)_{;2} + s_{12}(\Lambda_{12}^{-1}t)_{;12} \quad (3-79)$$

$$= \phi_1 - \phi_{1;312} + [h_{31} + h_{23;2} + h_{12;12}]. \quad (3-80)$$

Finally, the last combination of interest is the fully symmetric Sagnac combination:

$$\zeta = s_{31;1} + s_{12;2} + s_{23;3} - (s_{21;1'} + s_{32;2'} + s_{13;3'}) \quad (3-81)$$

$$= [(\phi_1 - \phi_{3;2})_{;1} + (\phi_2 - \phi_{1;3})_{;2} + (\phi_3 - \phi_{2;1})_{;3}] \quad (3-82)$$

$$- [(\phi_1 - \phi_{2;3'})_{;1'} + (\phi_2 - \phi_{3;1'})_{;2'} + (\phi_3 - \phi_{1;2'})_{;3'}]$$

which is independent of laser noise for a non-rotating⁸ constellation.

We have ignored the clock noise terms for the sake of simplicity since these Sagnac combinations are not the focus of this dissertation.

⁸ ($\tau_q(t) = \tau_{q'}(t)$)

CHAPTER 4 TIME DELAY INTERFEROMETRY

Now that we have developed a method of characterizing the signals with which to measure the inter-proof-mass noise terms the question enters: How do we combine these signals to cancel the laser phase terms and extract the GW modulations?

4.1 Laser Noise Cancellation

The ability to cancel the laser noise the IMS is largely based on the accuracy with which we can measure the time-dependent distance¹ between the space-craft and interpolate the phase signals to account for this distance. To get an idea of why this is the case, let's consider two laser phase signals, $\phi(t)$ and $\phi((1 - \beta)(t - \tau)) + g(t)$. These signals are independently measured on different SC producing two digitally sampled signals:

$$x_1[n] = \phi(f_s n) + \frac{f_{in1}}{f_s} \phi_{Clk1}(f_s n), \quad (4-1)$$

$$x_2[n] = \phi((1 - \beta)(n(f_s + \Delta f_s) - \tau)) + h(n(f_s + \Delta f_s)) + \frac{f_{in2}}{f_s + f_{\Delta s}} \phi_{Clk2}(n(f_s + \Delta f_s)). \quad (4-2)$$

The $(1 - \beta)$ factor is introduced to account for the laser phase time-scaling as a result of SC motion while the Δf_s factor accounts for the small difference in the absolute clock frequencies. Although this Δf_s factors will be small,² they can cause accumulated errors in the phase corrections if they are not accounted for.³ These can be related to the Λ_{ij} factors defined in (3-71) with $f_{Clki} = f_s$ and $f_{Clkj} = f_s + \Delta f_s$. The ability to extract $g(t)$ from these signals depends on four things: (1) the initial laser-phase

¹ Or equivalently, the laser light travel time-delay: $\tau(t) = L(t)/c$

² $f_s \simeq 50$ MHz, $\Delta f_s \simeq 1 - 10$ Hz depending on clock tolerances.

³ Relativistic time-dilation causes the same effect but it is small, $\beta^2 < 10^{-12}$, and can simply incorporated into the clock frequency error term.

spectral density, $\tilde{\phi}(\omega)$, (2) the ability to measure the differential clock noise terms, (3) the accuracy of our knowledge of the time delay, τ , and (4) the ability to perform fractional delay filtering and interpolation to time-shift and time-scale these signals to account for the τ , $f_{\Delta s}$, and $(1 - \beta)$ factors.

4.1.1 Laser Noise

Obviously, the initial laser noise level, $\tilde{\phi}(\omega)$, plays a large roll in our ability to extract the $g(t)$ terms⁴ from the above signals. The frequency references proposed to stabilize the lasers in LISA include optical cavities, Mach-Zander interferometers, molecular resonators, and arm locking. Optical cavity references and the associated locking methods are well tested and robust but the EOMs and cavities used as a frequency reference add to weight of the SC. Mach-Zander interferometers fit well with the LISA interferometry base design but, in comparison to cavities, lack low-frequency stability [34]. Molecular hyper-fine resonance is beneficial in providing an absolute laser frequency reference but is generally complicated in implementation. Arm-locking has the greatest advantage for LISA since it requires no additional hardware and can be implemented completely through digital signal readouts and controls which are already in the LISA design. At the same time, arm-locking is at a great dis-advantage since it has only been tested through electronic simulations and a possible risk of failure when implemented in LISA. (chapter. 6.3.1)

4.1.2 Clock Noise Transfers

The laser fields on each SC are modulated with up-converted⁵ clock noise side-bands [74] such that the side-band beat-notes between laser fields from adjacent SC, s_{sr} , also produce differential clock noise terms. Given that the clock signals are up-converted by a factor, G_{up} , and that the side-band beatnote produced when the clock

⁴ Generally, $h(\omega) < 100\mu\text{Cycles}/\sqrt{\text{Hz}}$

⁵ From 50 MHz to 2 GHz, $G_{up} \simeq 40$

from SC_2 is transmitted to SC_1 is measured with a phasemeter at a frequency of $f_{\Delta-Clk}$, we obtain:

$$\phi_{Clk-Sidebands}(t) = G_{up} (\phi_{Clk1} + \phi_{Clk2;3}) + \frac{f_{\Delta-Clk}}{f_{Clk1}} \phi_{Clk1}, \quad (4-3)$$

$$= G_{up} \left(\left(1 + \frac{f_{\Delta-Clk}}{G_{up} f_{Clk1}} \right) \phi_{Clk1} + \phi_{Clk2;3} \right) \quad (4-4)$$

$$\simeq G_{up} (\phi_{Clk1} + \phi_{Clk2;3}). \quad (4-5)$$

As we'll see in chapter. 4.3, these are the same terms which show up in the TDI combinations and are used to correct for this clock noise coupling.⁶

4.1.3 Ranging Errors

Before we outline the methods of inter-SC ranging in chapter. 4.4, we derive a general relationship between the ranging error and the input laser noise. Given that we have a measurement of some $\phi(t)$ as well as some time-delayed measurement $\phi_{delayed}(t) = \phi(t - \tau) + g(t)$, we time-shift and subtract these signals to extract $g(t)$. Assuming we have some time-shifting error, $\tau + \delta\tau$, when we fractional-delay interpolate the time-delayed signal, $\phi_{delayed}(t)$, and subtract it from the input signal we estimate the noise cancellation. Using the Taylor approximation we can write,

$$X_{Err} \simeq \phi(t) - \phi(t - \tau + \tau + \delta\tau),$$

$$\tilde{X}_{Err} \simeq [e^{-i\omega t} - e^{-i\omega(t+\delta\tau)}] \tilde{\phi},$$

$$|\tilde{X}_{Err}| \simeq \omega \delta\tau |\tilde{\phi}|.$$

where ω is the angular Fourier-transformation frequency. Now we can estimate a simplified but reasonable measure of the relationship between laser noise cancellation

⁶ For more information on the clock noise transfers and corrections, see [68–70, 75].

and the ranging precision as a function of frequency for $\omega\delta\tau \ll 1$ with the relationship:

$$X_{\text{Err}}(\omega) = \omega \delta\tau \phi(\omega)\alpha_{\phi}(\omega). \quad (4-6)$$

Thus, given a certain ranging capability we can derive the required laser prestabilization, or visa-versa, given a laser pre-stabilization level we can derive the required ranging accuracy to meet the interferometry sensitivity specifications. The complete TDI derivation includes complex phase factors, $\alpha_{\phi}(\omega)$, which may range in magnitude from 0 to 4 depending on the location of the arm-length dependent Δ_{sr} zeros (chapter. 4.4.2.1).

4.1.4 Fractional Delay Filtering and Interpolation

Depending on the finalized design, LISA will produce satellite to Earth data-streams of the TDI observables at a $f_{\text{data}} = 3 - 10$ Hz data rate. Integer sample shifts of these data-sets will result in a shifting error of $0.33 - 0.1$ s/s, respectively. But, given the expected laser pre-stabilization level, LISA will have to time-shift and time-scale these data-streams to a 3.3 ns accuracy⁷. Thus, assuming a 10 Hz data-rate, LISA requires a fractional shifting accuracy of $\delta\tau/T_{\text{data}} = 3.3 \text{ ns}/0.1 \text{ s} = 3.3 \times 10^{-8}$.

Fractional delay interpolation [72] is used to interpolate the data-sets and apply the fractional shift [73]. In LISA applications, the Lagrange filter is ideally suited for data-interpolation due to the constant low-frequency phase loss⁸. Generally we can write the interpolated data-set, $s(n - D)$ where D is the fractional shift $D = \Delta\tau/T_{\text{data}}$, as a function of the input data-set, the Lagrangian filter window, and the sinc(x) function as:

$$s(n - D) = \sum_{k=-\frac{(N-1)}{2}}^{\frac{(N-1)}{2}} s(n + k) w(k) \text{sinc}(D - k) \quad (4-7)$$

⁷ $\delta L = 1$ meter, $\delta\tau = 3.3$ ns

⁸ constant group delay

where $t_D = D + (N - 1)/2$,

$$w(n) = \frac{\pi N}{\sin(\pi t_d)} B(t_d, N) B\left(N - 1, n + \frac{N - 1}{2}\right), \quad (4-8)$$

and [76]

$$B(n, k) = \frac{\Gamma(n)\Gamma(k)}{\Gamma(n + k)}. \quad (4-9)$$

In the following description, we default to a filter length of $N = 51$ which provides us with a shifting accuracy of greater than 10^{-12} [73]. Generalizing this to incorporate time-scaling as well as time-shifting, we can write the time-changing time delay as a function of the integer, n_D , and fractional shift, $D(t)$ as:

$$\tau(t) = \tau(0) + \beta t = n_D * T_{\text{data}} + D(t) * T_{\text{data}}. \quad (4-10)$$

In this manner we advance the fractional delay, D , as a function of the data-sample, n , for each iteration of the loop: $D(n) = D(0) + n\beta$. The MATLAB code required and used to perform the data filtering and interpolation is outlined in Appendix A.

4.2 Laser Pre-stabilization

Based on the expected ranging accuracy, the current LISA design requires a laser frequency stability of:

$$\delta\omega_{\text{Pre-Stabilization}}(f) = \frac{280 \text{ Hz}}{\sqrt{\text{Hz}}} \sqrt{1 + \left(\frac{2.8 \text{ mHz}}{f}\right)^4}. \quad (4-11)$$

This could be achieved through a single stabilization method or by some combination of these methods. The costs and benefits of each of these methods are outlined

well in the LISA frequency control white paper [34]. The following discussion will focus on two methods: (1) Pound-Drever-Hall cavity stabilization⁹ and (2) arm-locking¹⁰.

4.2.1 Pound-Drever-Hall Locking

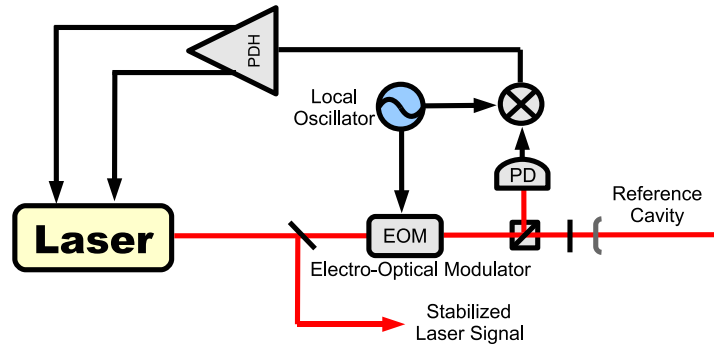


Figure 4-1. Model of the PDH locking scheme: A model of the Pound, Drever, Hall laser frequency locking technique is depicted. The laser field is modulated with side-bands and aligned through a polarizing beam splitter incident on the cavity. The back reflected field is used to control the laser frequency after demodulating the side-bands.

The application of Pound-Drever-Hall (PDH) laser stabilization [50] involves stabilizing the frequency of a laser to the length of an ultra-low expansion (ULE) cavity such that an integer multiple of the laser’s wavelength, $\lambda = 1064 \text{ nm}$, equals the length of the cavity:

$$N\lambda = L. \quad (4-12)$$

⁹ This is used as the pre-stabilized input for the TDI simulations as well as a stable reference against which to compare other laser stability measurements

¹⁰ These experiments mutually provided a proof-of-concept for the UFLIS electronics along with the verification of the arm-locking stabilization methods themselves.

This gives us a relationship between the laser frequency, $f + \delta f(t)$, and the cavity length, $L + \delta L(t)$ given by [52]:

$$\frac{\delta f(\omega)}{f} = \frac{\delta L(\omega)}{L}, \quad (4-13)$$

transferring the length stability of the cavity to the frequency stability of the laser.

The PDH frequency stabilization is accomplished by modulating the laser phase using an electro-optical modulator with MHz side-bands [51] as shown in Figure 4-1. The phase relationship of these off-resonance side-bands reflected from the cavity are scaled by a complex reflection coefficient which is a function of the cavities mirrors' reflection and transmission coefficients. Demodulating the PD signal against the modulation generating oscillator using an electronic mixer cancels the common frequency noise of the local oscillator¹¹ and results in an error signal which is proportional to the phase offset of laser carrier phase to the cavities resonant length. This error signal can then be used with the appropriate proportional-integrating-differentiating (PID) or finite-impulse-response (FIR) control electronics to feedback to the piezo-electric transducer (PZT) and temperature controls of the laser output frequency. For more information on this locking technique and it's applications in LISA, refer to [34, 51, 52].

4.2.2 Arm Locking

Arm locking is a laser stabilization technique proposed by Sheard, et. al. [53] which exploits the long-term stability of the LISA arm-lengths¹² as a reference against which to stabilize the long-term laser frequency. Utilizing the sensor signals from (3-72) and (3-74), we have a first-order measure of the change in the laser frequency over the

¹¹ This could be a voltage controlled oscillator, a function generator, or any relatively stable MHz oscillator

¹² 5 ± 0.1 Gm over one year.

individual round-trip arm-length delays with a transfer function given by:

$$T_{AL:s}(s) = \left(\frac{\mathcal{L}(\Delta_{s1}(t))}{\mathcal{L}(\phi_1(t))} \right) \quad (4-14)$$

$$= \phi_1(s) (1 - e^{-s\tau}). \quad (4-15)$$

where the functional variable, 's,' is the complex Laplace frequency $s = \sigma + i\omega$ while Δ_{s1} refers to the round-trip delay to SC_s . A filtered output of a single arm sensor signal¹³ [53, 77, 78] or some filtered linear combination of the two individual arm signals¹⁴ [79–81] can be used to control the local, $\phi_1(t)$, laser phase with the complete open-loop transfer function given by:

$$T_{AL:Comp}(s) = T_{Sum}(s)A_{sum}(s) + T_{Dif}(s)A_{dif}(s). \quad (4-16)$$

where

$$A_{sum}(t) = \Delta_{21}(t) + \Delta_{31}(t), \quad (4-17)$$

$$A_{dif}(t) = \Delta_{21}(t) - \Delta_{31}(t) \quad (4-18)$$

resulting in a laser noise suppression given by the closed loop transfer function:

$$T_{Closed} = \frac{1}{1 + T_{AL:Comp}(s)}. \quad (4-19)$$

The implementation of arm-locking requires real-time construction of the sensor signals as well as some method of actuating the laser frequency either through a PZT-mounted cavity [82], offset phase-locked lasers [78], or side-band locking [83]. Special care must be taken to estimate the Doppler shifts since integration of Doppler errors cause

¹³ Single arm-locking

¹⁴ Dual-modified arm locking

a frequency-pulling effect which limits the noise suppression and causes the laser frequencies to drift as a function of the integrated Doppler error [84].

The electronic components described in chapter. 6 in combination with The University of Florida Laser Interferometry Simulator (UFLIS) benchtop were used by the author and others to perform the first hardware implemented proof-of-concept single arm-locking experiment (chapter. 6.3.1) revealing the yet-to-be-discovered frequency pulling effects [41, 77, 84]. Expansions to the simulator have also proven dual and modified arm-locking configurations along with frequency pulling effects. [54, 81].

4.3 TDI Theory

Prior to now, we have simply mentioned that we must form particular time-shifted and time-compressed linear combinations to account for the time-changing unequal arm-lengths and cancel the dominant laser phase noise but we have not defined these specific combinations. These linear combinations fall into two major categories: (1) TDI-Sagnac combinations and (2) TDI-X combinations. The three TDI-Sagnac combinations are constructed by completing the laser transfer chain around counter propagating directions of the LISA constellation. These combinations are significantly less sensitive to gravitational waves, thus providing an estimation of non-laser noise sources such as PD noise or scattered light effects. The TDI-X combinations are constructed by completing the laser transfer chain along individual arms of the interferometer canceling the laser phase noise and extracting the GW signals. As previously stated, the ability to form these combinations depends directly on the accuracy of the measured arm-lengths (chapter. 4.1.3), but at the same time, these combinations can be exploited to estimate the arm-lengths (chapter. 4.4.2.1).

4.3.1 TDI Combinations

We begin our analysis by constructing the two major TDI combinations which are shown diagrammatically in Figure 4-2. The TDI-X combination is representative of a Michelson-type interferometer while the TDI- ζ combination is representative of

a Sagnac-type interferometer. The TDI formulations have not been consistent within the literature [55] such that in this description, we will use the same notation as those defined in chapter. 3.4.3.

The TDI-analysis and combinations used depend on the dynamics of the orbits. The different TDI generations are derived based on the orbital dynamics approximation used. The TDI – $X_{0.0}$ combination assumes the arm-lengths are constant, $d\tau_q(t)/dt = 0$, non-rotating $\tau_q(0) = \tau_{q'}(0)$, and equal, $\tau_q(0) = \tau_{\bar{q}}(0)$ ¹⁵. The TDI – $X_{1.0}$ combination assumes the arm-lengths are constant, $d\tau_q(t)/dt = 0$ and non-rotating $\tau_q(0) = \tau_{q'}(0)$, but unequal, $\tau_q(0) \neq \tau_{\bar{q}}(0)$. The TDI – $X_{1.5}$ combination assumes the arm-lengths are constant, $d\tau_q(t)/dt = 0$, but rotating, $\tau_q(0) \neq \tau_{q'}(0)$, and unequal, $\tau_q(0) \neq \tau_{\bar{q}}(0)$. Finally, the TDI – $X_{2.0}$ combination assumes the arm-lengths are non-constant, $d\tau_q(t)/dt \neq 0$, rotating, $\tau_q(0) \neq \tau_{q'}(0)$, and unequal, $\tau_q(0) \neq \tau_{\bar{q}}(0)$. These are outlined in Table 4-1. Thus, the TDI – $X_{2.0}$ combination should completely account for the laser noise coupling given the linear arm-length rate of change we have considered in the previous sections. Assuming we have a continuous data-stream of the observables for SC acceleration terms to have an effect on the data combinations, this could be accounted for with further expansion of the TDI combinations. This is usually un-necessary given the likely-hood of a 'unbroken' data-set, but none-the-less, we will see in chapter. 4.4 that this can be accounted for, given the LISA-orbital dynamics, with segmented data-analysis.

¹⁵ The $\tau_{\bar{q}}$ refers to the 'opposite' arm of the τ_q -arm vs. $\tau_{q'}$ -arm Michelson-type interferometer.

Table 4-1. Orbital dynamics approximations for TDI generations

Generation	Michelson Arm-Length	Counter-Propagating Delay	Delay Dynamics
TDI 0.0	$\tau_q(t) = \tau_{\bar{q}}(t)$	$\tau_q(0) = \tau_{q'}(0)$	$d\tau_q(t)/dt = 0$
TDI 1.0	$\tau_q(t) \neq \tau_{\bar{q}}(t)$	$\tau_q(0) = \tau_{q'}(0)$	$d\tau_q(t)/dt = 0$
TDI 1.5	$\tau_q(t) \neq \tau_{\bar{q}}(t)$	$\tau_q(0) \neq \tau_{q'}(0)$	$d\tau_q(t)/dt = 0$
TDI 2.0	$\tau_q(t) \neq \tau_{\bar{q}}(t)$	$\tau_q(0) \neq \tau_{q'}(0)$	$d\tau_q(t)/dt = \beta_q$
TDI 3.0+	$\tau_q(t) \neq \tau_{\bar{q}}(t)$	$\tau_q(0) \neq \tau_{q'}(0)$	$d\tau_q(t)/dt = \beta_q(t)$

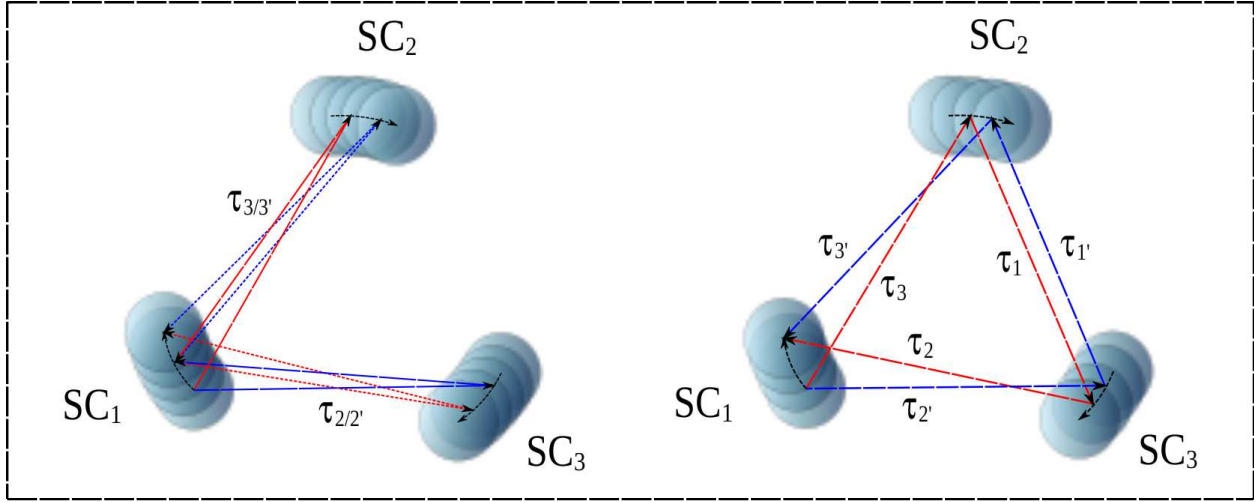


Figure 4-2. Diagrammatic models of the TDI-X and Sagnac combinations: Here we present the geometric representation of the LISA constellations in parallel to those developed in [85]. The laser transfer chain in these diagrammatic representations show how to time-shift the observables to form the TDI combinations and ensure that the laser noise sources will cancel when the laser transfer chain is a closed loop.

4.3.2 Sagnac Combinations

4.3.2.1 TDI Six-Pulse Combinations

The first order six-pulse combination, named α are constructed from the θ_{sr} combinations (3-77 and 3-79) from each of the respective SC and take the form:

$$\alpha_{1.0} = \theta_{21} - \theta_{31} \quad (4-20)$$

$$\begin{aligned} &= \phi_1 - \phi_{1;2'1'3'} - [\phi_1 - \phi_{1;312}] \\ &\quad + [h_{21} + h_{32;3'} + h_{13;1'3'}] - [h_{31} + h_{23;2} + h_{12;12}] \\ &= \phi_{1;312} - \phi_{1;2'1'3'} + [h_{21} + h_{32;3'} + h_{13;1'3'}] - [h_{31} + h_{23;2} + h_{12;12}]. \end{aligned} \quad (4-21)$$

Generally¹⁶, these combinations cancel the laser phase terms and leave six h_{sr} GW terms in the TDI $-\alpha_{1.0}$ approximation. They are named based on the fact that a delta-function gravitational wave input is replicated six times in the resulting combination. If we extend this to the TDI $-\alpha_{2.0}$ approximation by accounting for time-changing delays and un-equal counter-propagating light travel time-delays, we would have to trace the laser chain back to the starting point resulting in a 12 s_{sr} -term expression and a twelve-pulse GW response.

4.3.2.2 TDI Symmetric-Sagnac Combination

The first order Sagnac combination written as:

$$\zeta_{1.0} = s_{31;1} + s_{12;2} + s_{23;3} - (s_{21;1'} + s_{32;2'} + s_{13;3'}) \quad (4-22)$$

is free of laser phase noise in a non-rotating constellation and is orders of magnitude less sensitive to GW signals. This could be used to discriminate between instrument noises and GW stochastic background signals [86, 87]. This combination is shown geometrically in Figure 4-2; one notes that the rotation of the constellation in the geometric representation causes an open laser transfer chain for a rotating constellation which destroys the common mode laser phase cancellation the Sagnac-1.5 combinations [85, 88]. Again, this is accounted for by the modified Sagnac combination which re-traces the time-delay path resulting in a 12-term TDI $-\zeta_{2.0}$ function.

4.3.3 Michelson X-combinations

The Michelson X combinations¹⁷ form three interferometers combinations which collectively form a basis in the 2-dimensional plane of the constellation for the h_+ and

¹⁶ Ignoring clock-noise terms

¹⁷ Using other SC as our frame of reference, we can obtain the 'Y' and 'Z' combinations

h_x strain. In the following sections, we construct the Michelson X combinations from the round-trip single-arm sensor signals, Δ_{sr} , defined in (3-72) and (3-74).

4.3.3.1 TDI- $X_{0,0}$

In the special case where the total round trip delay-times are equal ($[\tau_q(0) + \tau_{q'}(0)] = [\tau_{\bar{q}}(0) + \tau_{\bar{q}'}(0)]$) and the differential SC velocities are zero ($d\tau_q(t)/dt = \beta_q = 0$), the difference of the sensor signals, (3-72) and (3-74),

$$X_{0,0} = \Delta_{21} - \Delta_{31}, \quad (4-23)$$

generates the standard equal-arm Michelson interferometer output, independent of laser phase noise. Expanding explicitly,

$$\begin{aligned} X_{0,0} = & \phi_1 - \phi_1(t - \tau_{3'}(0) - \tau_3(0)) + h_{21}(t) + h_{12}(t - \tau_{3'}(0)) \\ & + \frac{f_{21}}{f_{\text{Clk}}}\phi_{\text{Clk}-1}(t) + \frac{f_{12}}{f_{\text{Clk}}}\phi_{\text{Clk}-2}(t - \tau_{3'}(0)) \\ & - [\phi_1 - \phi_1(t - \tau_2(0) - \tau_{2'}(0)) + h_{31}(t) + h_{13}(t - \tau_2(0))] \\ & + \frac{f_{31}}{f_{\text{Clk}}}\phi_{\text{Clk}-1}(t) + \frac{f_{13}}{f_{\text{Clk}}}\phi_{\text{Clk}-3}(t - \tau_2(0)) \end{aligned} \quad (4-24)$$

which reduces in this special case to:

$$\begin{aligned} X_{0,0} = & h_{21}(t) + h_{12}(t - \tau_{3'}(0)) - h_{31}(t) - h_{13}(t - \tau_2(0)) \\ & + \frac{f_{21}}{f_{\text{Clk}}}\phi_{\text{Clk}-1}(t) + \frac{f_{12}}{f_{\text{Clk}}}\phi_{\text{Clk}-2}(t - \tau_{3'}(0)) \\ & - \frac{f_{31}}{f_{\text{Clk}}}\phi_{\text{Clk}-1}(t) - \frac{f_{13}}{f_{\text{Clk}}}\phi_{\text{Clk}-3}(t - \tau_2(0)) \end{aligned} \quad (4-25)$$

where we see the four-pulse GW response and clock noise coupling. Maintaining the $\beta = 0$ assumption, the laser fields are not Doppler shifted and the beatnote frequencies on opposite SC will be equal such that we can further simplify this combination and write

it as:

$$\begin{aligned}
X_{0,0} = & h_{21}(t) + h_{12}(t - \tau_{3'}(0)) - h_{31}(t) - h_{13}(t - \tau_2(0)) \\
& + \frac{f_{21}}{f_{\text{Clk}}}[\phi_{\text{Clk-1}}(t) + \phi_{\text{Clk-2}}(t - \tau_{3'}(0))] \\
& - \frac{f_{31}}{f_{\text{Clk}}}[\phi_{\text{Clk-1}}(t) + \phi_{\text{Clk-3}}(t - \tau_2(0))].
\end{aligned} \tag{4-26}$$

We notice that these clock noise terms are the same clock-noise transfer terms described in (4-3). Rescaling the clock-noise transfer sideband measurements and subtracting them from the TDI $- X_{0,0}$ combination, we obtain a Michelson GW output free of any other noise sources:

$$X_{0,0} = h_{21}(t) + h_{12}(t - \tau_{3'}(0)) - h_{31}(t) - h_{13}(t - \tau_2(0)) \tag{4-27}$$

Now that we have shown how the clock-noise terms are accounted for, we will ignore them in the rest of the TDI description. Light field Doppler shifts from inter-SC motion change the beatnote to clock frequency ratio, $(f_{\text{sr}} \pm f_{\text{Dop}})/f_{\text{Clk}}$, but can be subtracted from the sensor signals Δ_{sr} before any of the following combinations are formed. That said, we will revisit how these terms couple into the UFLIS-TDI simulations described in Ch. 7.

Unfortunately, despite all this work, the TDI- $X_{0,0}$ combination is rarely a reasonable laser phase cancellation technique since the LISA arm-lengths are almost always un-equal. None-the-less, this serves as a first order example of how heterodyne GW interferometry is performed. The considerations beyond this show the techniques to account for orbital dynamics and changes in the light-travel time-delays between the SC.

4.3.3.2 TDI- $X_{1,0}$

The TDI- $X_{1,0}$ combination [89], written as

$$X_{1,0} = \Delta_{21} - \Delta_{31} - \Delta_{21;2'2} + \Delta_{31;33'}, \tag{4-28}$$

replicates the equal-arm phase delays and cancels the common laser phase noise in the case where $([\tau_2 + \tau_{2'}] \neq [\tau_3 + \tau_{3'}])$ and $\beta_2 - \beta_3 \simeq 0$ as shown geometrically in Figure 4-2.

Expanding explicitly, but still allowing for non-zero β -values, we can write:

$$X_{1,0} = [\phi_1 - \phi_{1;33'}] - [\phi_1 - \phi_{1;2'2}] - [\phi_1 - \phi_{1;33'}]_{;2'2} + [\phi_1 - \phi_{1;2'2}]_{;33'} \quad (4-29)$$

$$+ [h_{21} + h_{12;3'}] - [h_{31} + h_{13;2}] - [h_{21} + h_{12;3'}]_{;2'2} + [h_{31} + h_{13;2}]_{;33'}$$

$$= [\phi_{1;33'2'2} - \phi_{1;2'233'}] \quad (4-30)$$

$$+ [[h_{21} - h_{21;2'2}] + [h_{12;3'} - h_{12;3'2'2}]] - [[h_{31} - h_{31;33'}] + [h_{13;2} - h_{13;233'}]].$$

From the expansion we notice the TDI – $X_{1,0}$ eight-pulse GW response. Failing to account for the SC-motion and time-changing delays, the TDI- $X_{1,0}$ combination is limited by the $[\phi_{1;33'2'2} - \phi_{1;2'233'}]$ terms which do not cancel completely since the time-delay transformations are performed in a different order. Calculating the delay error as a result of the transformation order using the leading $(1 - \beta)$ terms¹⁸ we can write:

$$\delta\tau = \tau(4[1 - \beta_2] - 4[1 - \beta_3]) = 4\tau[\beta_3 - \beta_2] \quad (4-31)$$

where τ is the mean one-way delay time¹⁹. Evaluating this the result in (4-6), we obtain[90]:

$$\tilde{X}_{1,0} > 4\tau|\beta_2 - \beta_3|\dot{\phi}_1 \quad (4-32)$$

where $\dot{\phi}_1$ is the time-differentiated laser phase spectrum. Given orbital characteristics where this limit is large enough to restrain the IMS sensitivity, we must further expand to the general TDI – $X_{2,0}$ combination to account for this residual noise.

¹⁸ We maintain the assumption that $\beta \ll 1$, $(1 - \beta) \simeq 1$, and approximate $(1 - \beta)^n = 1$.

¹⁹ $\tau \simeq 16.7$ s

4.3.3.3 TDI- $X_{2,0}$

The TDI- X_2 combination, written as [91, 92],

$$\begin{aligned} X_{2,0} = & \Delta_{21} - \Delta_{31} - \Delta_{21;2'2} + \Delta_{31;33'} \\ & - \Delta_{21;33'2'2} + \Delta_{31;2'233'} + \Delta_{21;2'22'233'} - \Delta_{31;33'33'2'2} \end{aligned} \quad (4-33)$$

is used to cancel the, $[\phi_{1;33'2'2} - \phi_{1;2'233'}]$, laser phase noise terms left in the TDI - $X_{1,0}$ combination. This produces a 16-pulse response to gravitational waves, written explicitly as:

$$\begin{aligned} X_{2,0} = & [[h_{21} + h_{12;3'}] - [h_{31} + h_{13;2}] - [h_{21} + h_{12;3'}]_{;2'2} + [h_{31} + h_{13;2}]_{;33'}] \\ & - [[h_{21} + h_{12;3'}]_{;33'2'2} - [h_{31} + h_{13;2}]_{;2'233'} \\ & - [h_{21} + h_{12;3'}]_{;2'22'233'} + [h_{31} + h_{13;2}]_{;33'33'2'2}] \end{aligned} \quad (4-34)$$

but, given the correct time-delays, cancels all the laser phase noise and accounts for the independent linear-time-delays, $\tau_q(t)$, assuming $d^2\tau(t)/dt^2 = 0$. Annual changes in β , or SC acceleration terms ($d^2\tau(t)/dt^2 \neq 0$), may be accounted for with the further expansion of these TDI combinations although, this is unnecessary as argued in following section (chapter. 4.3.4). The MATLAB code required to form these data-combinations using the s_{sr} data-sets is provided in Appendix B.

4.3.4 LISA Orbital Dynamics and TDI Data Analysis

In the following experiments, β is assumed to be constant and we will focus on the TDI- $X_{2,0}$ velocity corrections. Thus, in order to utilize the TDI-ranging methods outlined in chapter. 4.4.2.1 for LISA-TDI data-analysis, the β value will have to be adjusted to avoid the acceleration-dependent accumulated error. Although a continuous measure and correction to the β values are possible, this can simply be accomplished by segmenting the data-analysis, in the worst case LISA-like scenario, every $\sqrt{\delta\tau T_{\text{year}}/(\beta \pi)} = \sqrt{3.3 \text{ ns} * 3.15 \times 10^7 \text{ s}/(66 \text{ ns/s} * \pi)} = 708 \text{ s}$ [55]. Given the time-frame for the acceleration effects to couple into the data-analysis, even in this

worst-case scenario, it is easier to adjust the β -value in the data-analysis than it is to form a TDI – $X_{3,0}$, 32-pulse GW response, combination.

4.4 Ranging

As we have stated in chapter. 4.1.3 and as we can see explicitly from the Δ_{sr} and TDI – $X_{1.0/2.0}$ combinations, the laser noise cancellation directly depends on our ability to estimate the one-way inter-SC arm-lengths and form these linear combinations. From (4–6) we can calculate the ranging accuracy needed to cancel the $280 \text{ Hz}/\sqrt{\text{Hz}}$ laser pre-stabilization input noise.

Generally, the cancellation of the local $\phi_1(t)$ laser phase noise from the far s_{1s} signals depends on the accuracy of the out-going delay times, $\tau_3(t)$ and $\tau_{2'}(t)$, while the cancellation of the far laser phase noise from the local s_{s1} signals depends on the accuracy of the in-coming delay times, $\tau_{3'}(t)$ and $\tau_2(t)$. Assuming the lasers on separate SC are independently stabilized such that $\phi_1 \neq \phi_2 \neq \phi_3$, then each of the one-way inter-SC time-delay functions, $\tau_q(t) = \tau_q(0) + \beta_q t$, must be evaluated to a 1 meter (3.3 ns) accuracy.

Exploiting the phase-locking techniques described in [71], we can phase-lock the far lasers, ϕ_2 and ϕ_3 , to the delayed ϕ_1 field from the master SC and transfer the stability of the master laser to these far lasers. This results in expressions for the far SC's laser phase noise given by:

$$\phi_2(t) = \phi_{1;3}, \quad \phi_3(t) = \phi_{1;2'}, \quad (4-35)$$

to within the tracking accuracy of the PLL. In this special case, the one-way delays are accounted for by controlling the far sensor signals with a PLL such that, $s_{1s} = \phi_{\text{PLL-Error}} \simeq 0$. Taking the expressions for ϕ_2 and ϕ_3 described in (4–35), and evaluating them in Δ_{s1} (3–72 and 3–74), we see that these expressions simplify to:

$$\Delta_{21}(t) = s_{21}(t), \quad \Delta_{31}(t) = s_{31}(t). \quad (4-36)$$

Thus, since the s_{1s} terms do not effect the noise cancellation in this phase-locked configuration, we can reduce the delay constraints to two, round-trip delays given by:

$$\begin{aligned}\tau_{2'2}(t) &= [(1 - \beta_2)((1 - \beta_{2'})(t - \tau_{2'}(0)) - \tau_2(0))] \\ \tau_{33'}(t) &= [(1 - \beta_{3'})((1 - \beta_3)(t - \tau_3(0)) - \tau_{2'}(0))].\end{aligned}\tag{4-37}$$

Meanwhile, the constraints on the individual one-way delays are greatly reduced resulting from the relatively-stable²⁰ PLL noise. These reduced ranging constraints result from the fact that the 'input' PLL noise used in (4-6), allows for large values of $\delta\tau$ while still meeting the X-combination's IMS sensitivity.

Two methods, Pseudo-random Noise (PRN) ranging [75, 93, 94] and TDI-Ranging [95] have been proposed to measure the inter-SC arm-lengths (light-travel times). The PRN ranging method, described in the next chapter involves the use of additional optical components to modulate the laser carriers with PRN-codes; the cross-correlation of the six inter-SC ranging codes with the local copies of each of these PRN codes provides an independent, real-time measure of the one-way inter-SC distances. TDI-Ranging, on the other hand, requires no additional components and determines the inter-SC ranging values in post-processing by exploiting the laser cancellation characteristics of the TDI-combinations. Provided with the ease of implementation of the TDI-Ranging technique, the TDI experiments described in chapter. 7 will attempt to experimentally develop and improve upon the TDI-Ranging methods proposed in [95].

4.4.1 Pseudo-random Noise (PRN) Code Ranging

Pseudo-random noise (PRN) code cross-correlation techniques are well understood inter-device distance tracking methods which have been developed and verified for use in global positioning satellites (GPS). The application of these methods in LISA involves

²⁰ $1\mu\text{Hz}/\sqrt{\text{Hz}} - 1\text{mHz}/\sqrt{\text{Hz}}$

modulating one of six local codes (one for each laser source) onto the carrier laser field. After the inter-SC/intra-SC laser field transmission and detection, the PRN codes from the adjacent laser field is cross-correlated with the local PRN codes. The six PRN codes have the designed property such that they do not correlate with each-other, but do periodically correlate with themselves depending on the length of the PRN code. A positive cross-correlation of the PRN code is used in conjunction with a delay-lock-loop to actively track the 'incoming' code from the adjacent benchtop and produce an inter-SC delay read-out. Assuming the measured delays correctly account for electronic and special relativistic delay terms, these delay read-outs can be directly used to form Δ_{sr} and TDI $- X_{1.0/2.0}$ combinations in real time.

This ranging method has both benefits and complications. The real-time PRN delay measurements allow us to form the Δ_{sr} and TDI $- X_{1.0/2.0}$ combinations in real-time on the SC. The Δ_{sr} terms can be used for arm-locking as described in chapter. 6.3.1. The TDI $- X_{1.0/2.0}$ combinations can be formed on-board from the s_{sr} observables and sent in their pre-constructed TDI-form to Earth rather than having to transmit the 18 individual χ_{sr} , b_{sr} , and s_{sr} observable signals.

On the other hand, as we'll see comparatively in the next section, this ranging method adds unnecessary complications to the LISA design. Electro-optical modulators (EOMs), which might introduce additional noise terms, must be used to modulate the laser-field with the PRN codes before the inter-SC transmission, adding weight and complexity to the LISA design. Also, there is no guarantee that the delays measured by the PRN ranging methods are equal to those needed to form the TDI combinations since the laser noise cancellation in the TDI-combinations depends on the time-delay from the laser field's generation to observables' detection.²¹ TDI-ranging, on the other

²¹ Including PD, ADC, and phasemeter phase delay responses.

hand, does not require an additional EOM and determines the one-way delays, including electronic phase delays, in post-processing.

4.4.2 Time-delay Interferometry Ranging (TDIR)

Time-delay interferometry ranging [95] is a method of determining the LISA signal travel times in post-processing by minimizing the total root mean squared (RMS) power in the LISA measurement frequency band. Taking the measured, s_{SR} , combinations, we form the theoretical TDI-2.0 combinations using initial estimates of the six variable,²² light travel time delays. The time-delay parameters are scanned over the possible values²³ until the total RMS power in the TDI – $X_{2.0}$ is minimized. The initial delay offset parameters, $\tau_q(0)$, can vary by 0.66 seconds and must be measured to an accuracy of less than 3.3 nanoseconds (4–6). Thus, assuming no previous knowledge of the time-delay values, we have a large parameter-space over which to scan with each of the four time-delay offset parameters taking one of 2×10^8 possible values.²⁴ Unless some tracking method is developed, this parameter search could be computationally intensive.

Although [95] proves the capabilities and limitations of the RMS minimization ranging method, it does not provide a method of actively determining the time-dependent delay parameters. In addition, the RMS minimization method's delay parameter calculation introduces errors in the time-delay values caused by low-frequency gravitational wave signals. In this experiment, we will present and employ a new method of TDI-ranging by modulating the laser field with a ranging tone at a frequency outside of the LISA measurement band, in this case, 1 – 1.5 Hz. Although this method has been used for spacecraft ranging on active projects [96] and has been considered for use on LISA [97], the author is not aware of a formal analysis in the literature. In the following

²² We assume that $\beta_q = \beta_{q'}$ and $\tau_q(0) \neq \tau_{q'}(0)$.

²³ ($16.33 \text{ s} < \tau_q(0) < 17 \text{ s}$), ($-66 \text{ ns/s} < \beta < 66 \text{ ns/s}$)

²⁴ $0.66 \text{ s} / 3.3 \text{ ns} = 2 \times 10^8$

sections, we attempt to present this formal analysis of the TDI ranging-tone application and realization, including a time-delay search algorithm developed by the author.

4.4.2.1 TDI Ranging Tone

The TDI-ranging tones can be placed on each of the six LISA laser fields by adding a $f_{\text{Tone}} - \text{Hz}$ sinusoidal modulation to the piezo-electric transducer which controls the laser frequency. This is significantly more straight-forward than the EOMs required to implement the PRN-ranging method. On the other hand, the real-time measure of the arm-lengths provided by the PRN ranging method has the advantage of producing the sensor and TDI variables in real-time which is beneficial towards the implementation of arm-locking and reducing the satellite-to-Earth data transmission demands.

Extending the RMS minimization concept, the application of a ranging tone effectively increases the laser noise by introducing more signal power at the specified ranging tone frequencies. As shown by (4-6), this results in a better estimation of the ranging error, $\delta\tau$, than the inherent laser noise cancellation would provide. In addition, because we are only interested in the power minimization near the ranging tone frequency, this ranging method should not be affected by low frequency gravitational waves.

The ranging tone is optimally modulated onto the laser field at a frequency mid-way between the frequency-domain zeros of the inter-SC sensor signals, Δ_{sr} , to avoid inherent tone cancellation along a single arm²⁵ :

$$\frac{N}{\tau_q(0) + \tau_{q'}(0)} < f_{\text{Tone}} < \frac{N + 1}{\tau_q(0) + \tau_{q'}(0)}. \quad (4-38)$$

Also, to avoid confusion between the individual laser modulations, each of the Laser_{sr} fields should be modulated at a different frequency, $f_{\text{Tone-sr}}$. Using the reverse argument of the ranging requirement derivation, the cancellation of the local $\phi_1(t)$ tone from the far

²⁵ This can be seen graphically in Figure 7-4.

s_{1s} signals constrains the out-going delay times, $\tau_3(t)$ and $\tau_{2'}(t)$, while the cancellation of the far laser tones from the local s_{s1} signals constrains the in-coming delay times, $\tau_{3'}(t)$ and $\tau_2(t)$, resulting in all four one-way time-delay functions.

Revisiting the LISA-model where the far lasers are phase-locked to the delayed master laser field, (4–35), the delayed local laser modulation is transmitted back to local SC. This results in two round-trip time-delay function constraints, (4–37), using the cancellation of the local tones in the TDI combinations. In spite of this, the phase-locked lasers could still be modulated with their own ranging tones restoring all four, one-way constraints.

4.4.2.2 TDI Ranging Parameter Search Algorithm

The method used to determine the six-parameters which define the four one-way delay-functions is outlined in Figure 4-3. The first step involves providing an estimate of the time-delay functions. The estimate does not need to be accurate; any estimation error will be corrected by the convergent properties of the search algorithm. The β estimates are then used to time-scale the s_{sr} signals by the appropriate factors as defined by the TDI – $X_{2,0}$ combination²⁶. The time-scaled data set is then broken into 'N' sections which are individually used to determine the four time-delay offsets, $\tau_q(0)$, for each section.

As we've previously stated, the span of possible values of the time-delay offsets in comparison with the required time-delay ranging accuracy results in a large parameter space over which these values can vary. Brute force scanning and computing the TDI combination for all 10^{32} values is effectively impossible. Instead, we begin by evaluating the TDI combination for each-time delay in the range of possible values from 16.2 s to 17.2 s with a precision of 0.1 s. In this specific case, the delay-segmentation results

²⁶ The TDI- X_2 combination is used in favor of the the TDI- X_1 combination because of the possible inherent constraints of the TDI- X_1 : (4–32)

in 10 possible delays values for each of the four dimensions of the one-way delay times, resulting in 10^4 possible delay permutations. The RMS power of the TDI- $X_{2.0}$ combination in the $f_{\text{Tone}} \text{ Hz} \pm 1 \text{ mHz}$ frequency band is calculated for each of the 10^4 possible values. The set of delays which contains the minimum RMS power is used as a new reference point. The time-delay parameter space around this minimum ($\pm 0.1 \text{ s}$) is, broken into more precise delay values (0.01 s). The RMS power minimization scan in this new parameter space is performed to, again, determine the delay parameters to a better precision. The process is repeated improving the precision by a factor of 10 each time until the four delay-time offsets are constrained to a 1 ps precision and the ranging tone is dominated by instrument noise sources.²⁷ The delay segmentation precision, in this case a factor of 10 for each iteration, is chosen to avoid the possibility of converging on a local minima and obtaining the wrong delay-time estimate. A more effective method might include the evaluation of a surface gradient which converges on the RMS-minimized delay times which has been fitted to the time-delay grid through Monte-Carlo analysis; this method could accelerate the data-analysis, assist in confirming the result is not a local minima, and ensure that the actual optimized delay-times have been determined.

Once the four time-delay offsets are calculated for each of the N data-segments, a linear regression of the offsets is performed to obtain a functional definition of all four of the one-way time delays:

$$\begin{aligned} \tau_2(t) &= (1 - \beta_2)(t - \tau_2(0)), & \tau_{3'}(t) &= (1 - \beta_3)(t - \tau_{3'}(0)), & (4-39) \\ \tau_{2'}(t) &= (1 - \beta_2)(t - \tau_{2'}(0)), & \tau_3(t) &= (1 - \beta_3)(t - \tau_3(0)). \end{aligned}$$

²⁷ Although we scan the delay parameters to a 1 ps precision, the actual delay error is determined based on the ranging tone cancellation which is limited by instrument noise sources.

The calculated slope provides a more accurate evaluation of β -values for this section of data than the original estimation. Assuming the ranging-tone cancellation and time-delay offset calculation was limited by (4–32), the improvement in the β estimation increases the precision of the time-delay offsets in the second iteration of the ranging-tone cancellation algorithm. Generally, after three iterations the one-way delay functions are optimally evaluated. The first iteration determines the β values. The second iteration determines the delay-offsets. The third iteration optimizes the values over the entire data-set. Once the four one-way delay functions are derived, they are used to calculate the TDI- X_2 combination for the entire data-set. In addition, the variance on the linear-regression provides us with a means of determining the ranging precision in comparison with the precision defined by the ranging tone cancellation using (4–6). The process is simplified to a four-parameter $(\beta_2, \beta_3, \tau_{2'2}(0), \tau_{33'}(0))$ estimation when the far laser are slave phase locked to the master local laser.

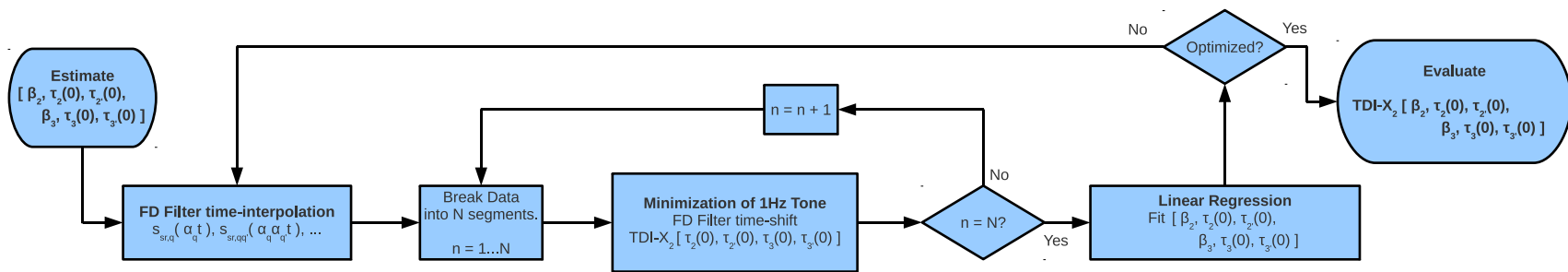


Figure 4-3. Flow chart of the ranging-tone minimization process: The process depicted by this flow chart minimizes the ranging tone and maximally constrains the six variable light travel time delays. The results of this process for the different experimental configurations are presented in Table 7-1 and Table 7-2

CHAPTER 5 THE LISA PHASEMETER

5.1 Digital Signal Processing (DSP) System

The phasemeter read-outs, digital control systems, and electronic inter-SC delay simulation components were developed using programmable DSP equipment acquired from Pentek, Inc. The Pentek system is constructed from three basic components. The 6256¹ is a four-channel, 14-bit, analog to digital signal converter (ADC) sampling card containing a field programmable gate array (FPGA) capable of high-speed real-time fixed-point data-processing. Meanwhile, the 6228² is a four-channel, 16-bit, digital to analog converter (DAC) read-out card with the same FPGA capabilities. These two daughter cards are connected through the master processing and control card, the 4205.³ The 4205 handles the data transfers between the daughter cards and can be controlled through a serial based user interface. The 4205's processor can perform floating point calculations on the measured data and store the results in 1 GByte of synchronous dynamic random-access memory (SDRAM) or send the data through an Ethernet transfer to an external data-storage computer. Both the input ADCs and output DACs can be externally clocked either by the same source or by two independent clock sources.

5.2 μ Cycle Phase Measurements

The phasemeter, programmed to the 6256's FPGA, is designed to measure the phase of a 2 – 20 MHz PD beatnote signal with an accuracy of $1 \mu\text{cycle}/\sqrt{\text{Hz}}$ (Table 3-1). This device is used, not only to measure LISA-like science observables, but also to generate the phase data for the electronic simulation of inter-SC field transmission delay

¹ Model 6256 Dual/Quad 105 MHz A/D w/Virtex-II Pro FPGA - VIM-2

² Model 6228 4-Ch. D/A, Digital Up-converter & FPGA VIM-2 Module

³ Model 4205 VIM/PMC Carrier and MPC7457 PowerPC VME Board

and phase modulation effects. It can also be used to generate high-speed frequency read-outs for real-time digital control systems such as arm-locking. In the following sections we outline the design, characteristics, noise sources, and performance of the University of Florida phasemeter.

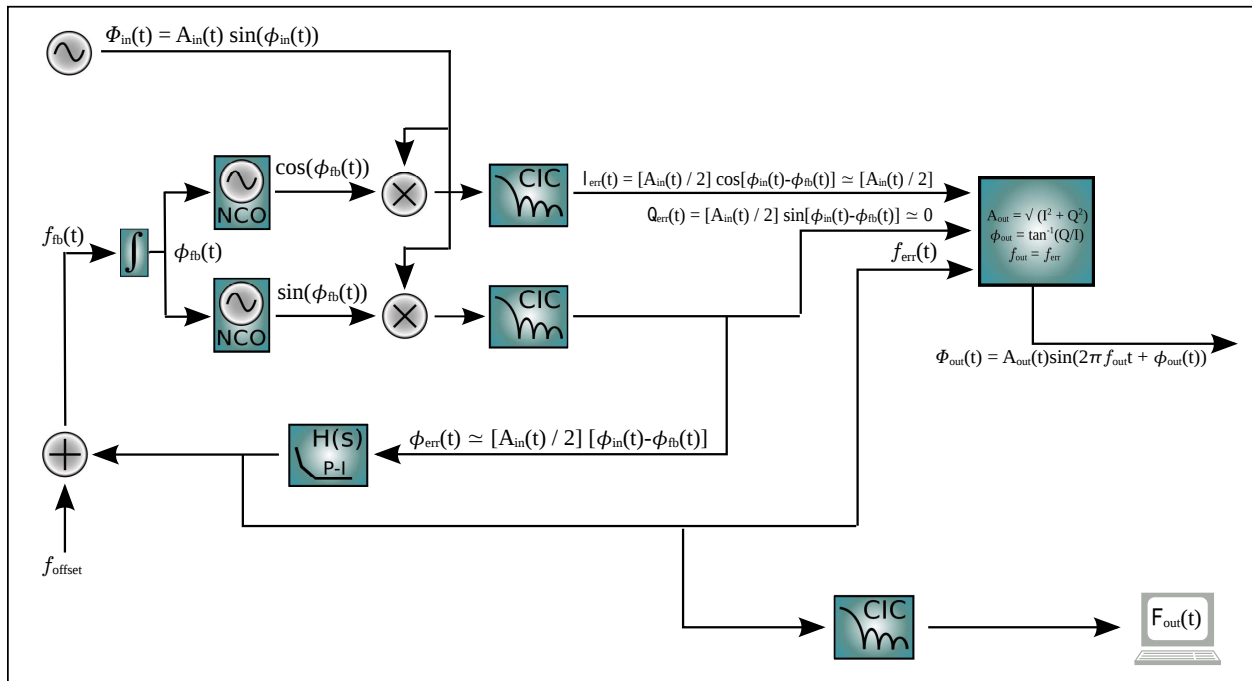


Figure 5-1. A model of the LISA phasemeter: Here we show how a digital offset phase lock loop is locked to the sampled input signal. Meanwhile, the feedback frequency signal, $f_{fb}(t)$, and the multiplier demodulated outputs, $Q(t)$ and $I(t)$, are recorded to reconstruct the phase and amplitude of the input signal. The details and theoretical analysis of the phasemeter operation can be found in the text (chapter 5.2.1)

5.2.1 Design

The phasemeter design is modeled off of a standard offset phase lock loop (PLL) tracking controller. The name 'phasemeter' is misleading since the PM core actually records a 64-bit frequency-proportional feedback signal in a digital PLL which is then integrated in post-processing to generate the phase. As shown in Figure 5-1, an input signal, $\Phi_{in}(t) = A_{in}(t) \sin(\phi_{in}(t))$, is sampled with a 14-bit accuracy at a sampling

frequency, f_s .⁴ The digitized beatnote is then mixed with sine and cosine components of a digital feedback signal with a constant amplitude, A_{fb} , and a time varying feedback phase, $\phi_{fb}(t) = \int dt(f_{fb}(t) + f_{offset})$, given a user-defined offset frequency, f_{offset} . The feedback sinusoids, $A_{fb}\sin(\phi_{fb}(t))$ and $A_{fb}\cos(\phi_{fb}(t))$, are generated with numerically controlled oscillators (NCOs) using a $\Omega_{LUT} = 28$ -bit look-up table (LUT). Once the feedback and input signals are multiplied,⁵ the signal is filtered with a N stage cascaded-integrating-comb (CIC) filter [98]. The data is down-sampled by a factor of R and low-pass filtered by the CIC-transfer function such as those shown in Figure 5-2.

The transfer function of the CIC filter in the Laplace domain takes the form:

$$G(s) = R^{1-N} \left| \frac{(1 + z^{-R})^N}{(1 - z^{-1})^N} \right| \quad \text{where } z = e^{-\frac{s}{f_s}}. \quad (5-1)$$

An example of the CIC transfer functions for $f_s = 50.0$ MHz, $R_{fb} = 16$, and $N = 2, 4, 8$ stage filters are plotted in Figure 5-2. f_s is chosen at a frequency with a lower bound defined by the Nyquist sampling frequency, $f_s > 2f_{Ny}$, where f_{Ny} is the signals largest frequency component of interest, and with an upper bound defined by the timing constraints of the FPGA and ADCs. A larger down-sampling factor, R, reduces the tracking loop's update rate, reducing the timing requirements of the FPGA, but also results in an increase of the PLL's in-loop phase delay, reducing the tracking bandwidth. The number of stages, N, defines by what factor the high-frequency data is suppressed before down-sampling and aliasing the high-frequency information into the measurement. With regards to the LISA mission, a nice benefit of using the CIC filter for this down-sampling process is that the 'zeros' of the transfer function are aliased to DC, significantly suppressing any out-of-band information before it is aliased into the LISA science data frequency band (DC - 1 Hz). This is discussed further in chapter 5.2.2.2.

⁴ $f_s = 40 - 100$ MHz

⁵ The 14-bit ADC out and the 28-bit LUT sinusoid result in a $\Omega_Q = 42$ -bit I/Q precision

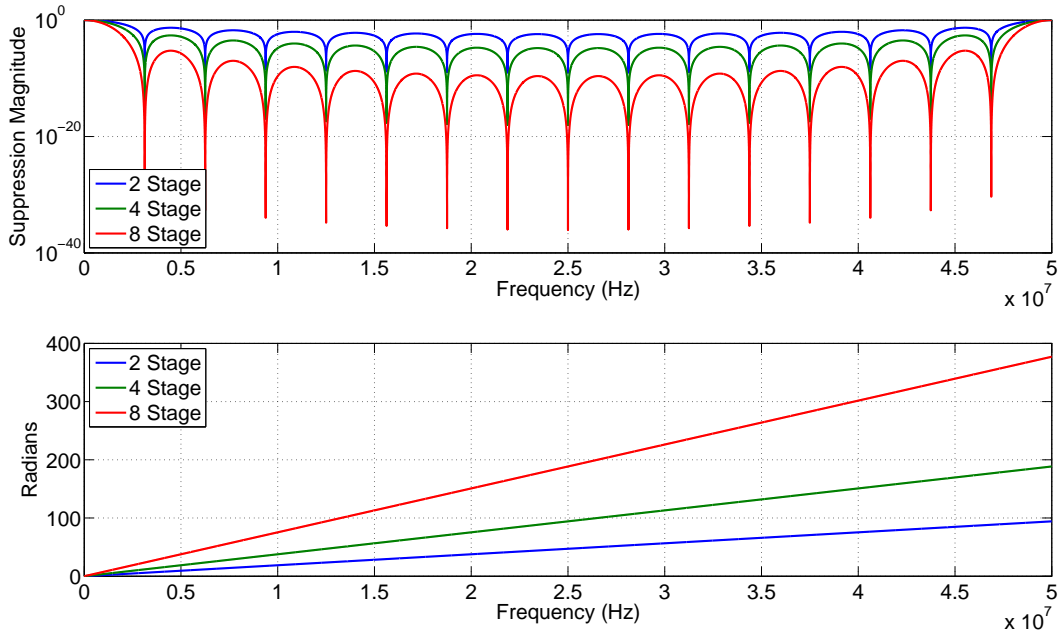


Figure 5-2. CIC filter transfer functions: The magnitude and phase response of the $N = 2, 4, 8$ stage CIC filters using a data-rate, $f_s = 50$ MHz, and a down-sampling factor, $R = 16$, is plotted. A larger number of stages, although increasing the suppression of higher-order aliased frequency bands, also causes an increase in the filter's phase delay.

Switching our focus to the PM's PLL tracking loop, if we assume that $f_{in} = d\phi_{in}(t)/dt \simeq f_{offset}$, and suppress the sum term of the demodulated signal with a CIC low-pass filter, it results in the sine and cosine of the difference phase, $\phi_{err}(t) = \phi_{in}(t) - \phi_{fb}(t)$. The CIC filter also reduces the tracking loop's data rate to $f_{Core} = f_s/R_{fb}$. As a result of the sine/cosine multiplication and filtering we obtain two signals which are proportional to the in-phase and quadrature components of the feed-back error signal,

$$Q(t) \propto G(s)[A_{in}(t)\sin(\phi_{in}(t))A_{fb}\cos(\phi_{fb}(t))] = \frac{A_{fb}A_{in}(t)}{2}\sin(\phi_{err}(t)) \quad (5-2)$$

$$I(t) \propto G(s)[A_{in}(t)\sin(\phi_{in}(t))A_{fb}\sin(\phi_{fb}(t))] = \frac{A_{fb}A_{in}(t)}{2}\cos(\phi_{err}(t)). \quad (5-3)$$

Using $Q(t)$ as the error signal for the PLL, it is filtered using fixed-point bit-shifters and cascaded accumulators which are constructed to produce the feed-back controller, $H(s)$,

given by:

$$H(s) = \left[2^{-N_1} + 2^{-N_2} \frac{f_s}{s} + 2^{-N_3} \frac{f_s^2}{s^2} \right]. \quad (5-4)$$

The $N_{1,2,3}$ values are the bit-shifting factors in the P-I-I² feed-back filter, where $N_1 < N_2 < N_3$,⁶ defines the gain and frequency-zeros of the P-I-I² filter. This filter generates the phase-proportional feed-back frequency signal, $f_{fb}(t)$, with a 60-bit precision⁷. The user-defined offset frequency, f_{offset} , is added to this feed-back signal, integrated with a fixed-point accumulator⁸ to generate the feed-back phase, $\phi_{fb}(t)$, and used to drive the NCO/LUT mentioned above. Assuming the system is 'locked' the feedback signal should track the input signal such that, within the bandwidth of the controller:

$$Q(t) \simeq 0 \quad \phi_{fb}(t) \simeq \phi_{in}(t). \quad (5-5)$$

Since we are interested in the phase fluctuations, the frequency feedback signal, $f_{fb}(t)$, will be integrated to generate the in-band phase output, $\phi_{in-band}(t)$. Using the feed-forward, $G(s)$, and feed-back, $H(s)$, transfer functions in combination with basic control theory [99], we can calculate the expected closed-loop in-band and out-of-band transfer functions based on the feed-forward and feed-back transfer functions as defined above:

$$\frac{\delta\phi_{fb}(s)}{\delta\phi_{in}(s)} = A_{fb} \left[\frac{A_{in}H(s)G(s)}{\frac{s}{f_s} + A_{in}H(s)G(s)} \right] \simeq 1 \quad (5-6)$$

$$\frac{\delta Q(s)}{\delta\phi_{in}(s)} = A_{fb} \left[\frac{A_{in}G(s)}{\frac{s}{f_s} + A_{in}H(s)G(s)} \right] \simeq 0. \quad (5-7)$$

⁶ For most designs, $N_1 \simeq 11$, $N_2 \simeq 18$, $N_3 \simeq 28$

⁷ $\Omega_{fb} = \Omega_Q + N_3 = 42 + 28 = 70$ bits, which are then truncated to 60 bits.

⁸ $T_{Accum}(s) = f_s/s$

The time-changing input amplitude coupling, analyzed in chapter 3.4.2.5, is assumed as being constant for this feed-back analysis such that amplitude fluctuations of the input will have little affect on the transfer function. From the definitions in (5-6) and (5-7), we can interpret these as the in-band and out-of-band frequency information based on these closed-loop transfer functions:

$$\phi_{\text{in-band}}(t) = \phi_{\text{fb}}(t) \quad \phi_{\text{out-of-band}}(t) = \text{atan} \left(\frac{Q(t)}{I(t)} \right) = \phi_{\text{err}}(t). \quad (5-8)$$

Thus, we can reconstruct the entire input signal's phase information by simply adding these signals:

$$\phi_{\text{Out}}(t) = \phi_{\text{in-band}}(t) + \phi_{\text{out-of-band}}(t) \simeq \phi_{\text{in}}(t) \quad (5-9)$$

We can also calculate the input amplitude:

$$A_{\text{Out}}(t) = \sqrt{I(t)^2 + Q(t)^2} \simeq A_{\text{in}}(t) \quad (5-10)$$

The expected bandwidth, depending on the amplitude of the input signal and the timing delays of the FPGA, should be at least a few kHz such that in the LISA frequency band, the phase information of the input signal is completely contained in the in-band information and, thus, we can ignore the out-of-band information:

$$f_{\text{out-of-band}}(t) \simeq 0 \quad (5-11)$$

$$\phi_{\text{Out}}(t) = \phi_{\text{fb}}(t) \simeq \phi_{\text{in}}(t) \quad (5-12)$$

This eliminates the need for the sine component of the mixer multiplication and reduces the constraints on the FPGA design if amplitude measurements are not needed.

To generate the phasemeter data, the $\Omega_{\text{fb}} = 60$ -bit feedback signals, $f_{\text{fb}}(t)$, for each of the four ADC inputs and PM outputs are packed into a series of 32-bit values, transfered through the DSP system to the 4205, and communicated to a

data-storage computer through an Ethernet connection. This provides us with a frequency quantization precision of $\delta f = f_s/2^{\Omega_{fb}}$ (Figure 5-3).

In the following chapters the sampling rate and down-sampling factor vary based on the experiment being performed and the computational demands on the FPGA. The primary clock rates used are 40 MHz, 62.5 MHz, and 100 MHz⁹. To get an idea of the frequency precision, taking $f_s = 50.0$ MHz, we produce frequency data with a quantization precision of $50.0 \text{ MHz}/2^{60} = 54 \text{ pHz}$. This is unnecessarily precise, but since the FPGA and processor perform computations based on 32-bit 'words,' and the 32-bit precision, $62.5 \text{ MHz}/2^{60} = 14.5 \text{ mHz}$, is not sensitive enough to meet the LISA requirements, we are required to use two 'words' per data-point which allows for up-to 64-bit fixed point frequency outputs.¹⁰ This is explored more in chapter 5.2.2.1.

5.2.2 Phasemeter Readouts

Now that we have presented the design and capabilities of the PM core, the 60-bit, $f_{\text{Core}} = f_s/R_{fb}$ frequency output data can be used for three purposes: (1) to record LISA-like science data of PD observables, (2) to generate the phase/frequency data for simulating the inter-SC phase/frequency delays, (3) for high-speed digital feedback control systems such as arm-locking and phase-locking. Maintaining the LISA precision throughout the system, we keep the 60-bit frequency precision for all possible LISA-like usages of the PM core. The read-out rate, on the other hand, varies depending on the application. LISA science measurements call for 3-10 Hz PD phase readouts [29]. Simulations of the inter-SC delays require a relatively high data-rate to maintain the phase data-rate for accurate data-interpolation (chapter 6.2.2.1) and to prevent aliasing into the measurement band when electronically replicating the LISA-like laser field

⁹ LISA is expected to use a 50 MHz ultra stable oscillator (USO) clock [29].

¹⁰ 4 bits are used to label the frequency value with an indexing number based on the associated ADC channel.

delays. PM readouts for digital control systems such as arm-locking use the maximum allowed data-rate to minimize the phase delays applied by the digital controller which reduce the tracking band-width.

To achieve the desired data-rate for LISA-science measurements and electronic phase delay (EPD) simulations, the PM frequency readout data is down-sampled again by CIC filters. The CIC filters down-sample the data to a fast, $f_{PLL} \simeq 400$ kHz, medium, $f_{EPD} \simeq 50$ kHz, or slow, $f_{LISA} \simeq 10$ Hz, readout rate, which vary slightly depending on the down-sampling factor, R , and the clock rate, f_s . The important point here is to consider the aliasing effects of the CIC filter and the quantization noise of the frequency read-out.

5.2.2.1 Phase Quantization Noise

We can calculate the phasemeters' quantization phase noise based on the bit-resolution and readout rate of the frequency information from the same arguments used to derive, (3–24), and is written explicitly as:

$$\delta\phi_{\text{Dig}}(\omega) = \frac{1}{\omega} \frac{f_s 2^{-\Omega_{\text{fb}}}}{\sqrt{6} f_{\text{data}}} \frac{\text{Cycles}}{\sqrt{\text{Hz}}} \quad (5-13)$$

where Ω_{fb} is the bit precision of the frequency feedback data and f_{data} is the CIC down-sampled output data rate. To see how this compares to the LISA phasemeter precision requirements, the low-frequency phase quantization limit, scaled to a clock rate of $f_s = 50$ MHz, is plotted for two different read-out rates, 3 Hz and 10 Hz, and three different bit precisions, 47, 48, and 49 bits, in Figure 5-3. Assuming we have a 3 Hz data-rate, we require 49-bits scaled to the 50 MHz clock. Using a 10 Hz data-rate we can reduce this to a 48-bit precision. We also plot the quantization precision for the 10 Hz, 60-bit UF-LISA science phasemeter. Despite that the 60-bit PM precision is far beyond the LISA requirements, we maintain this high bit-precision simply as a result of the DSP system's capabilities.

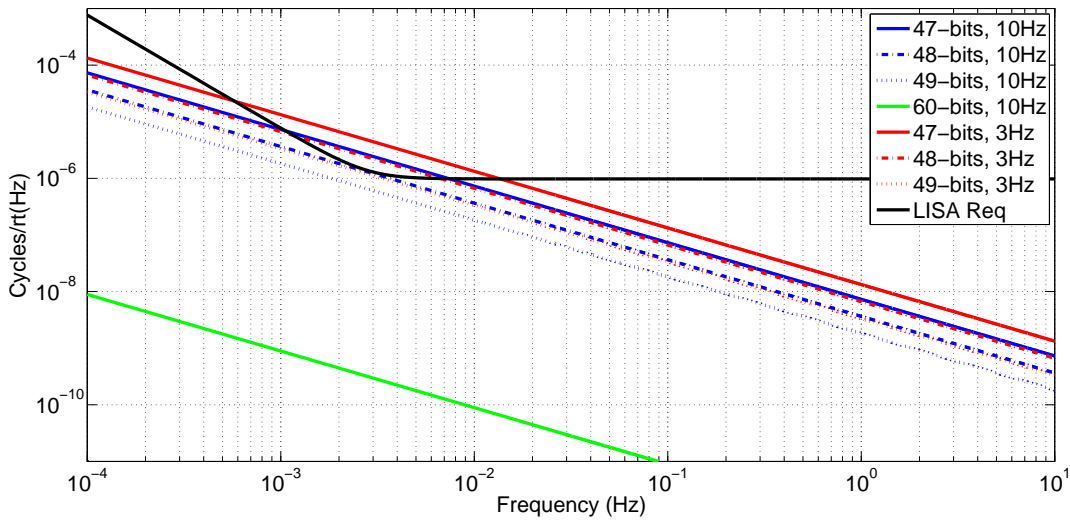


Figure 5-3. Theoretical PM readout digitization limitations: The frequency bit-precision and data read-out rate couple to limit the digitization-limited PM measurement sensitivity through quantization noise (5–13). Although this specifies how many bits are needed in the PM tracking loop, the data precision could be reduced for satellite-to-Earth transmission once it has been read out of the PM tracking loop by removing the frequency offset and retaining only the dynamic bits.

5.2.2.2 CIC Downsampling and Aliasing

The CIC filter is used to down-sample the data because of the relative ease of programming on an FPGA since it consists of cascaded differentiators and integrators which may be constructed using fixed-point accumulators and subtractors. In addition, as shown in Figure 5-4, aliased terms have an infinite suppression at all frequencies which are aliased to DC. Despite this feature, we must ensure that the CIC aliased phase-noise is suppressed beyond the LISA requirement in the LISA measurement band, up to 1 Hz. As an example, we take the pre-stabilized laser input noise of $280 \text{ Hz}/\sqrt{\text{Hz}}$ and plot the magnitude of the pass-band and first aliased frequency band for a 10 Hz data rate down-sampled with $N = 2$ and $N = 6$ stage CIC filters in Figure 5-4. We can see that, given this data-rate and a 6-stage CIC down-sampling filter, we obtain a first-aliased band suppression which meet the LISA requirements. This is verified by an experimental measurement as shown in Figure 5-14. A finite impulse response

(FIR) filter with a flat pass-band and significant suppression in the stop-band to prevent aliasing could be used to improve the performance near the sampling rate and reduce the data rate to 3 Hz but this is computationally demanding for a fixed-point FPGA.

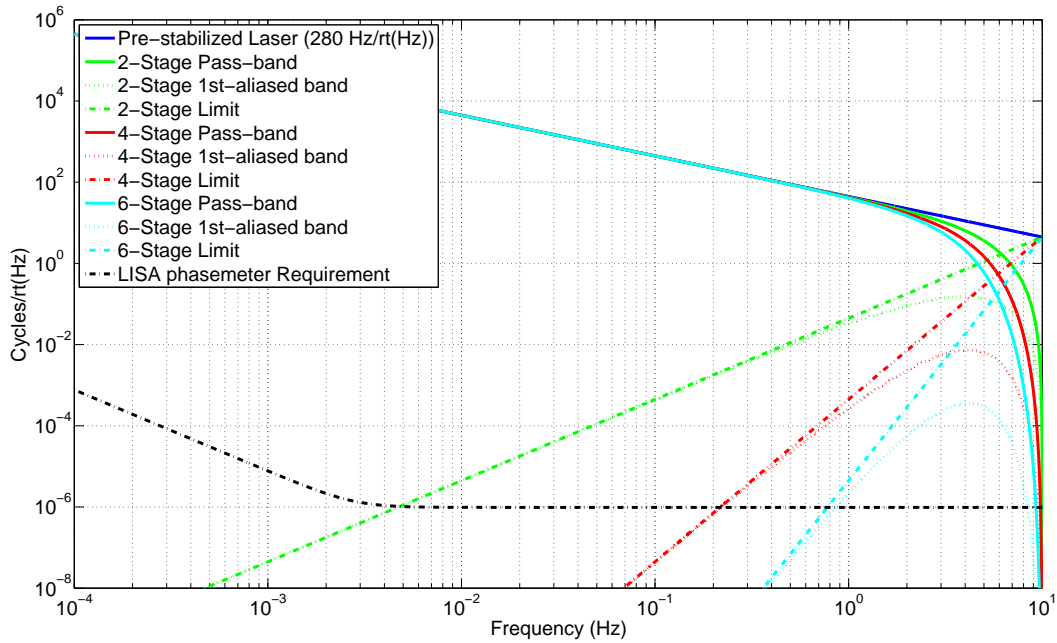


Figure 5-4. Phasemeter noise caused by CIC filter aliasing: The down-sampling filters used to read out the phasemeter data must ensure that the noise in the aliased frequency bands are sufficiently suppressed before being folded into the measurement band. The first aliased band of the $N = 2, 4, 6$ stage CIC filters used to down-sample the PM core data in the UF-phasemeter are plotted as a function of the expected input laser noise. Using a 10 Hz data-rate, the CIC-filter down-sampling filters require at least $N=6$ -stages to meet the LISA requirements.

5.2.3 Phasemeter Test-Measurements

We begin the verification and noise analysis process by performing software simulations in MATLAB-Simulink using the fixed-point Xilinx-DSP toolkit and hardware simulations with a voltage controlled oscillator (VCO) test input.¹¹ In both the software

¹¹ Our VCOs have similar noise characteristics as the pre-stabilized laser beatnotes and is used as a test input for many verification measurements as shown in Figure 6-2.

and hardware simulations, we record the 60-bit feedback, $f_{fb}(t)$, and the 30-bit quadrature error, $Q(t)$, and in-phase, $I(t)$, signals.

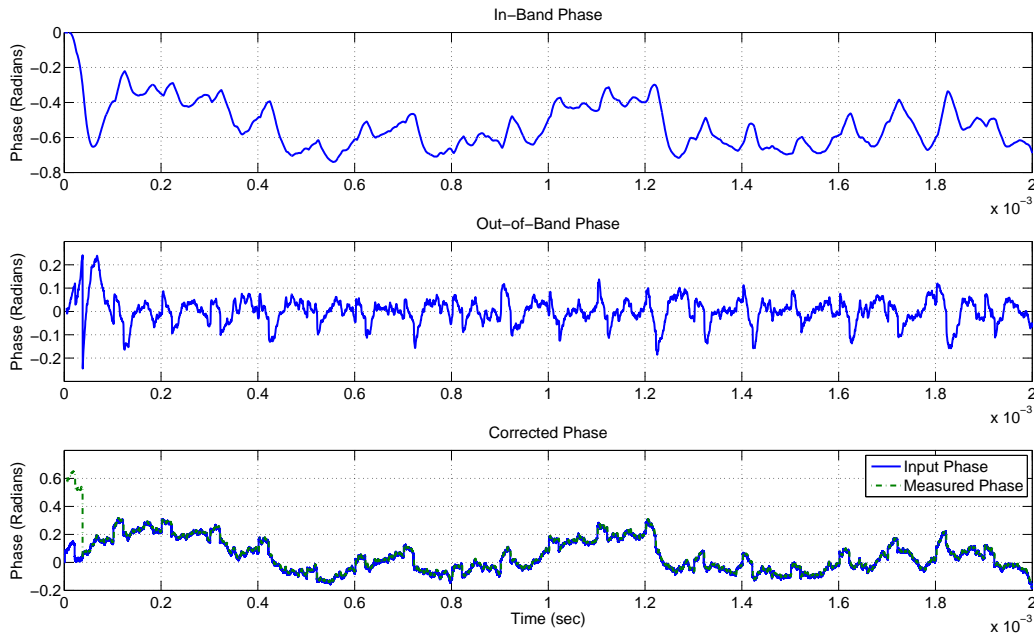


Figure 5-5. Software verification of PM performance: The in-band (top) and out-of-band (middle) phase information is plotted for a simulated laser-like noise input for 2 ms. The bottom curve shows the input phase compared against the summed in-band and out-of-band phase information. The initial tracking transients are seen at the beginning of the simulation and the curves match as expected once the phasemeter has locked onto the input signal.

The time-series output of a software simulation is shown in Figure 5-5 while the spectral results of a hardware experiment using a VCO input source is shown in Figure 5-6. From the hardware experiment we can see that the out-of-band phase error is well below the LISA requirement, justifying (5-11). The 'difference' terms refer to the subtraction of two different ADCs, but which sample the same input source being electronically split, effectively showing the combined un-common ADC and phasemeter phase noise limitation. This will be discussed extensively in the following chapters. At this point, it simply verifies that both ADC's and phasemeters are measuring the same signals to a $0.1 \mu\text{cycle}/\sqrt{\text{Hz}}$ accuracy, at least in the high frequency range.

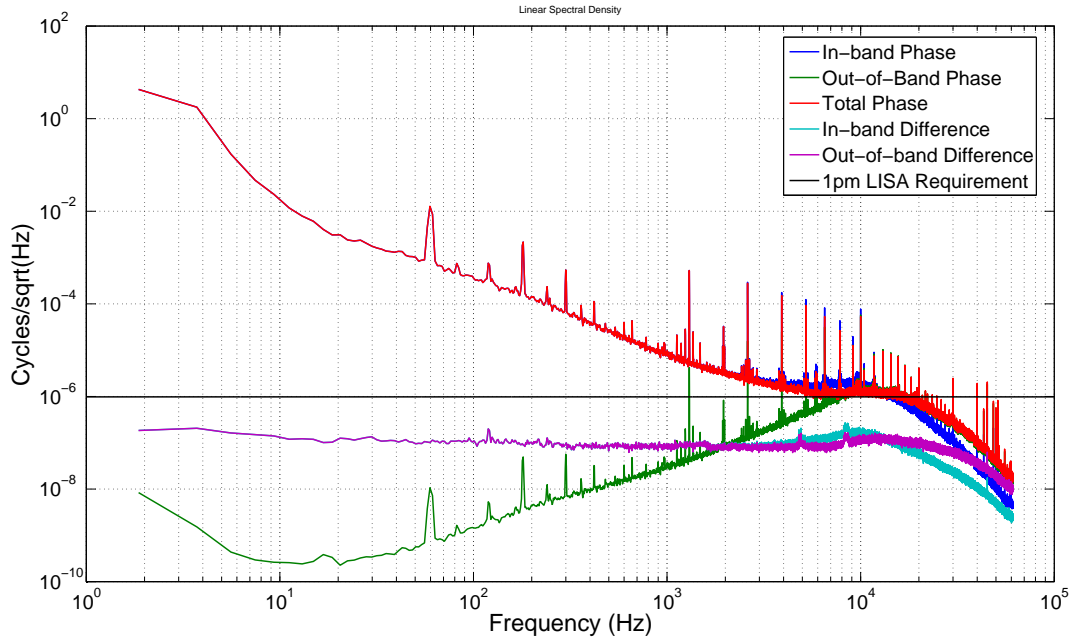


Figure 5-6. Hardware verification of PM performance: The high-frequency noise spectrum of the hardware tested phasemeter using a VCO input source is plotted. The in-band phase (blue curve) matches the VCO input noise to a level of $0.1 \mu\text{cycles}/\sqrt{\text{Hz}}$ (cyan curve) when performing a differential ADC measurement (Figure. 5-9). The out-of-band error (green curve) immediately drops below the LISA requirement and continues to track the input noise to a better precision at lower frequencies due to the P-I-I² feedback transfer function (Figure. 5-7). Thus, including the out-of-band error in the measured phase does little to improve the phase precision (purple curve).

Dividing the spectra of the frequency feedback signal, $\tilde{f}_{fb}(\omega)$, by the quadrature error spectra, $\tilde{Q}(\omega)$, as shown in Figure 5-7, we obtain the expected feedback transfer function based on the programmed FPGA controller design. More on the design and verification aspects of the phasemeter can be found by referencing the groundwork experiments performed by Ira Thorpe [41].

5.2.4 Phasemeter Noise Model

Taking into consideration phasemeter, ADC, and clock noise sources, we can write the sampled phasemeter signal as:

$$\phi_{PM,i} = \phi_{in} + \delta\phi_{PM} + \delta\phi_{ADC} + \frac{f_{in}}{f_s} \delta\phi_{Clk} \quad (5-14)$$

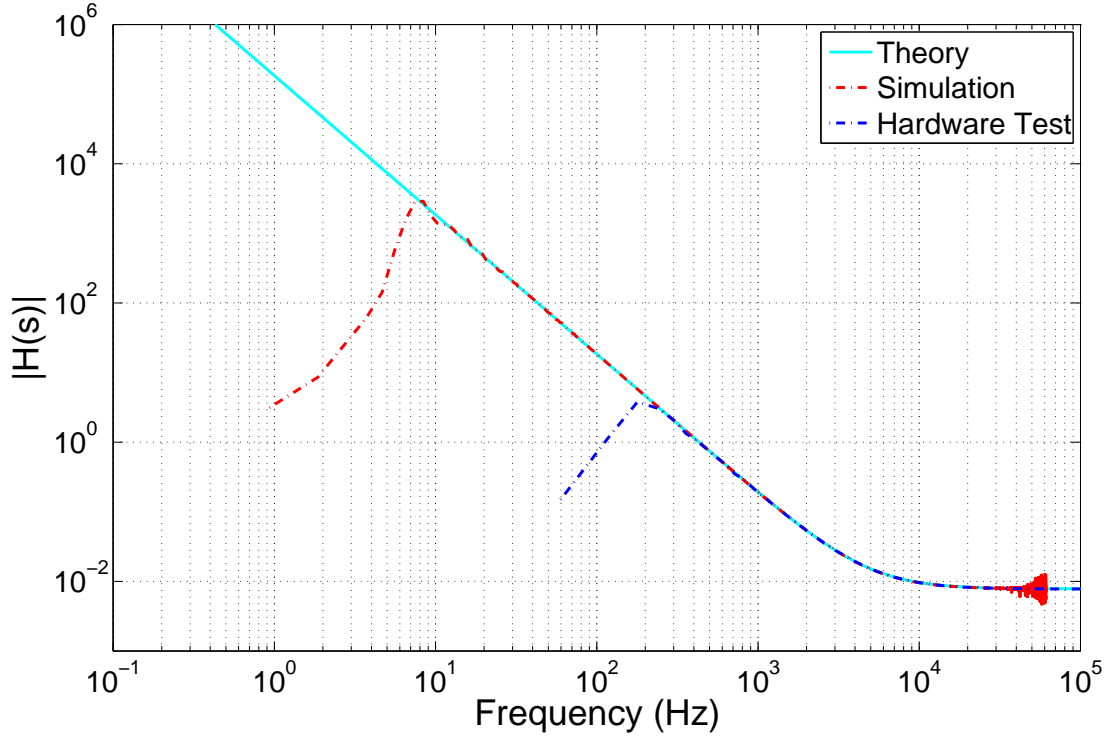


Figure 5-7. Verification of the PM feedback transfer function: Dividing the spectra of the feedback frequency signal by the out-of-band error signal, we obtain the expected feedback transfer function (5-6) for both the software and hardware verification tests.

where

$$\delta\phi_{\text{PM}} = \delta\phi_{\text{CIC,o}} + \delta\phi_{\text{Quant,i}} \quad (5-15)$$

$$\delta\phi_{\text{Clk}} = \delta\phi_{\text{CLK,o}} + \delta\phi_{\text{CLK,i}} \quad (5-16)$$

$$\delta\phi_{\text{ADC}} = \delta\phi_{\text{ADC,o}} + \delta\phi_{\text{ADC,i}} \quad (5-17)$$

so that we may differentiate between noise terms which are common between all the channels, $\delta\phi_{x,o}$, and terms which are independently applied to the 'i-th' channel, $\delta\phi_{x,i}$. The CIC noise is labeled with an 'o' since it correlates with the input noise. The quantization noise, on the other hand, is applied to each channel independently. In chapter 5.3, we will further investigate the ADC noise terms. To distinguish between the clock noise and ADC noise terms, we will define the clock noise sources as any signal

which scales proportionately with the input frequency, such as timing jitter, while ADC noise sources are defined as absolute, frequency-independent additive noise signal.

In an attempt to model these different noise sources, a diagram of where they are introduced in the measurement process is shown in Figure 5-8.

5.2.5 Differential and Entangled Measurements

To distinguish between these terms, we take three types of measurements, as shown in Figure 5-9, with each attempting to probe a different noise source as outlined in the following sections.

5.2.5.1 Digitally Split Differential Noise

The first measurement uses a 1 MHz VCO test input which is sampled at a rate of $f_s=62.5$ MHz with a single ADC. The ADC sampled data is passed to two different phasemeter cores with two different PLL offset frequencies. This results in two data-streams which are only limited by the phasemeter core's measurement and digitization precision, $\delta\phi_{\text{Quant},i}$, in (5-14). The measurements are taken at four different rates then plotted together to span the 100 μHz to 10 kHz frequency range as shown in Figure 5-10. The 'quantization noise' limit is at the 100 pcycle/ $\sqrt{\text{Hz}}$ level for frequencies above 10 mHz and equals the PM phase quantization limit at frequencies below 10 mHz. Using the amplitude-phase quantization noise level as given by (3-24) and considering the $f_{\text{in-loop}} = 62.5/128$ MHz in-loop data rate, we can solve for the ADC-noise-free effective in-loop phase quantization, Ω_{fb} :

$$\delta x_{\text{ADC Amp.}-\text{Quant.}}(\omega) = \frac{2^{1-\Omega_{\text{fb}}}}{\sqrt{6f_{\text{in-loop}}}} \simeq 100 \frac{\text{pcycles}}{\sqrt{\text{Hz}}}, \quad (5-18)$$

resulting in an effective phasemeter amplitude quantization precision of $\Omega_{\text{fb}} = 23.5$ -bits.

Again, these noise sources, being well below the LISA measurement requirements, are not of concern to us. Although, the digitization precision calculations can be useful in determining the amount of data that must be transmitted to Earth for data-processing of the science PM read-outs.

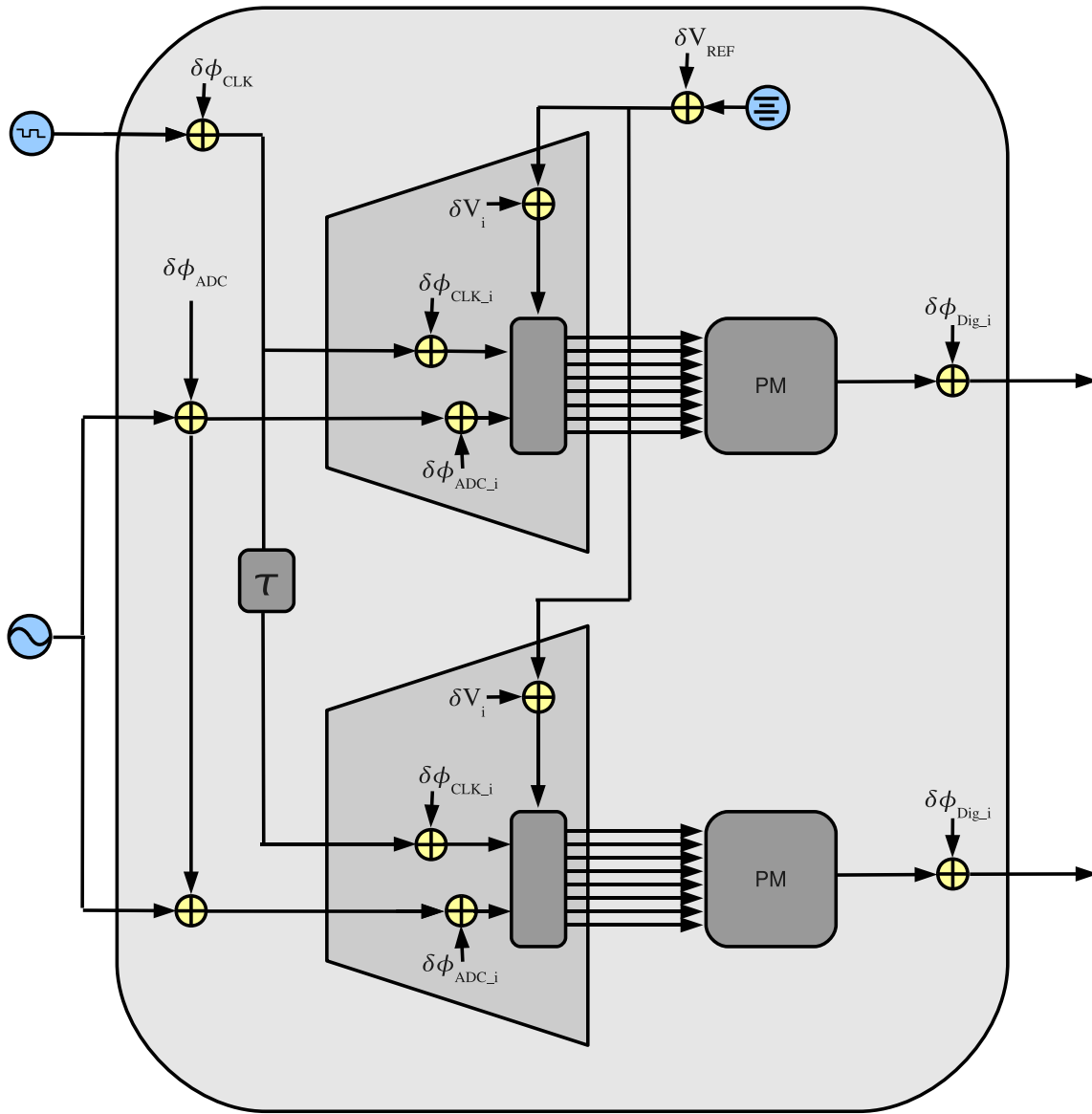


Figure 5-8. Phasemeter noise model: A model of the ADC inputs and clock distribution is depicted. Common and independent noise terms are added to the ADC input and clock input signals in to represent the $\delta\phi_{CLK}$ and $\delta\phi_{ADC}$ terms in 5–14. The ADC itself has a ground reference which produces an additive phase noise and independent voltage references for the ADC-comparators which represent the $V_{Gnd}(t)$ and $G(t)$ (3–25) terms respectively and discussed in chapter 3.4.2.3. These terms are also representative of the $A_{Off}(t)$ and $\delta A(t)$ (3–38) terms in chapter 3.4.2.5.

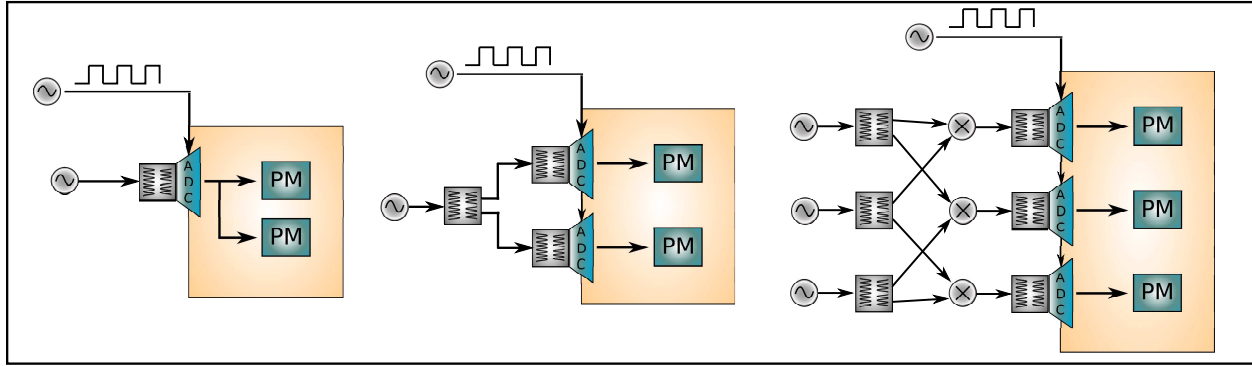


Figure 5-9. Experimental models of ADC noise estimation measurements: The quantization noise experiment (left) maintains the common ADC noise terms but distinguishes between independent PM core quantization noise terms. The differential noise experiment (middle) distinguishes between independent ADC noise terms but cancels common ADC noise terms as explained in chapter 5.2.5.2. The entangled phase measurement (right) provides a measure of the common-mode ADC noise terms (chapter 5.2.5.3).

5.2.5.2 Electronically Split Differential Noise

The next measurements are taken to probe the un-common clock, ADC, and phasemeter noise sources. Splitting a demodulated 1 MHz VCO output using an electronic radio-frequency (RF) transformer splitter, we measure the signal phase using two different ADCs, sampled with the same clock source. In this case, the common noise sources, $\delta\phi_{CIC,o}$, $\delta\phi_{ADC,o}$, and $\delta\phi_{Clk,o}$ cancel from the measurement while the un-common sources, $\delta\phi_{ADC,i}$ and $\delta\phi_{Clk,i}$, do not. We expect the $\delta\phi_{Clk,i}$ to be dominated by timing-jitter terms while $\delta\phi_{ADC,i}$ might introduce phase and amplitude noise terms outlined in chapter 3.4.2.5. A complete spectrum of the 1 MHz input and the two-channel differential output is plotted in Figure 5-10. The measurement precision is limited at low frequencies, below 10 Hz, by a combination of timing-jitter and ADC/transformer dispersion. The precision is limited at high frequencies, above 10 Hz, by the coupling of the amplitude-sampling noise terms described in chapter 3.4.2.3. This is verified by varying the signal frequency and amplitude, then comparing the PM measurement sensitivity with the changes in the measurement characteristics.

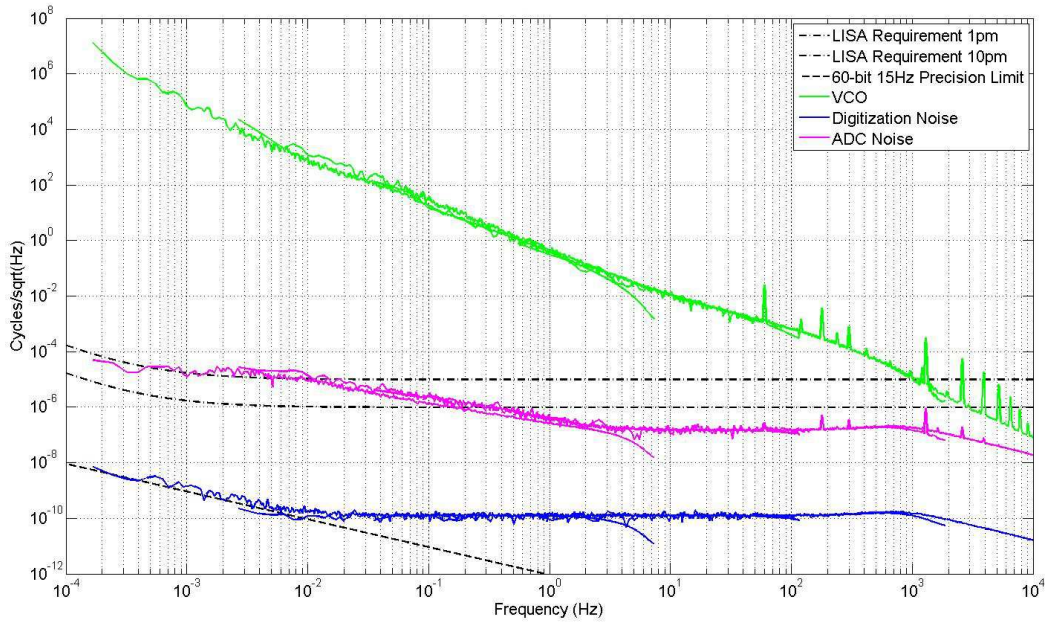


Figure 5-10. PM/ADC Quantization and differential noise: Here we plot the results of the quantization and differential noise measurements modeled in Figure 5-9 from $100 \mu\text{Hz}$ to 10 kHz . The quantization noise shows an in-loop white $\Omega_{fb} = 23.5$ -bit quantization phase noise for frequencies above 10 mHz the expected 60-bit frequency quantization PM read-out limitation for frequencies above 10 mHz . The differential measurement is limited by the $\Omega_{\delta V} = 13.78$ -bit effective amplitude quantization noise level for frequencies above 10 Hz and a timing jitter limited noise given by (5-19) for frequencies below 10 Hz .

In order to probe the timing jitter terms, we take long-term, low-frequency measurements of input beatnote frequencies ranging from 1.0 MHz to 79.5 MHz . The measurement at 79.5 MHz is aliased into the measurement-band by the $f_s=60 \text{ MHz}$ clock, producing a measurable oscillation at 19.5 MHz . The results, Figure 5-11, show that the measured phase noise decreases as the measurement frequency is decreased from 79.5 MHz , to 12.0 MHz , to 8.0 MHz . Based on the noise level and scaling of these signals, we estimate a timing jitter noise of,

$$\delta t_{\text{Jit}}(\omega) = \frac{40 \text{ fs}}{\sqrt{f} \sqrt{\text{Hz}}}. \quad (5-19)$$

Confirming this estimate numerically we obtain a phase noise of:

$$\begin{aligned}
 \delta\phi_{\text{Jit}}(\omega) &= f_{\text{in}}\delta t(0.1 \text{ Hz}) && (5-20) \\
 &= (79.5 \times 10^6) \cdot \delta t(0.1 \text{ Hz}) = \frac{31.8 \mu\text{Cycles}}{\sqrt{f} \sqrt{\text{Hz}}} \\
 &= (12.0 \times 10^6) \cdot \delta t(0.1 \text{ Hz}) = \frac{4.8 \mu\text{Cycles}}{\sqrt{f} \sqrt{\text{Hz}}} \\
 &= (8.00 \times 10^6) \cdot \delta t(0.1 \text{ Hz}) = \frac{3.2 \mu\text{Cycles}}{\sqrt{f} \sqrt{\text{Hz}}} \\
 &= (4.00 \times 10^6) \cdot \delta t(0.1 \text{ Hz}) = \frac{1.6 \mu\text{Cycles}}{\sqrt{f} \sqrt{\text{Hz}}}
 \end{aligned}$$

all of which match with the measured phase noise for frequencies larger than 8 MHz. Unexpectedly, lower frequencies (4.0, 2.0, and 1.0 MHz) result in a higher phase noise precision and a reduced measurement sensitivity. The increased noise at these lower frequencies is caused by temperature correlated phase dispersion introduced by the RF transformers used to AC couple the ADC signal input; see chapter 5.4.1 for a description of the experiments and methods used to correct for this noise.

In an attempt to evaluate (3-25), we vary the input amplitude of a demodulated 10 MHz VCO input. Using two peak-to-peak input amplitudes, 200 mV and 600 mV, we observe a factor of 3 improvement in the measurement sensitivity at high frequencies when the signal is not limited by timing jitter. The tracking bandwidth for this PM design also increases from $\simeq 3$ kHz to $\simeq 10$ kHz. The amplitude noise coupling allows us to evaluate the $G(\omega)V_{\text{Bias}}$ factor in (3-25). Based on the maximum peak-to-peak input amplitude of 2000 mV, we can estimate this amplitude-to-phase noise coupling as:

$$\delta\phi_{\text{Amp}}(\omega) = \frac{2000 \text{ mV}}{V_{\text{Pk-Pk.in}} (\text{mV})} \cdot 7.5 \frac{\text{nCycles}}{\sqrt{\text{Hz}}} \quad (5-21)$$

Note that the amplitude noise is not a result of aliased amplitude noise from 2ω (chapter 3.4.2.5) since these would not scale with the signal power. We have also accounted for the out-of-band phase terms ($\tan^{-1}(Q/I)$) in these measurements, which indicates that this is not a result of variations in the signal's amplitude as described by

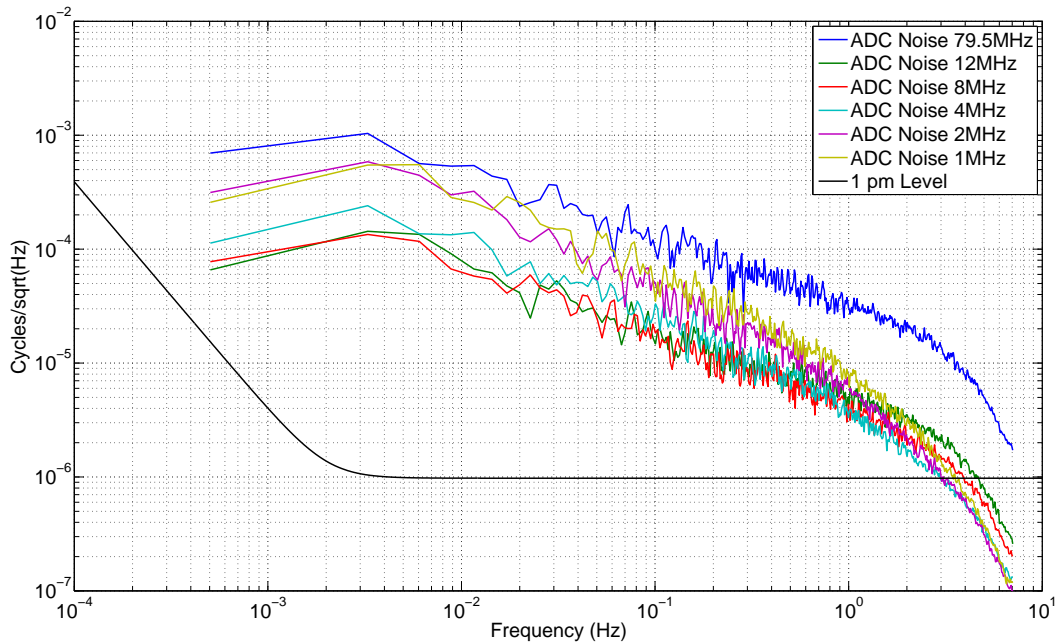


Figure 5-11. ADC timing jitter noise limitations: The phase noise due to the timing jitter scales inversely with the f_{in} MHz input frequency (3–27) and matches the theoretically calculated jitter values for $f_{in} > 8$, MHz for $\delta t_{Jit}(\omega)$ (5–19). The phase measurement for input frequencies with $f_{in} < 8$ MHz are limited by temperature dependent dispersion due to the RF transformers (chapter 5.4.1).

chapter 3.4.2.5. Using the inverse argument used to derive (3–26), we can calculate the effective quantization precision of $\Omega_{\delta V} = 13.78$ which is nearly equal to the full 14-bit ADC precision.

We will have an independent measure of this noise source using a different experimental setup in chapter 5.3.

At this point, we claim the measurement is limited by a combination of timing jitter and RF transformer phase dispersion in the low-frequency range and limited by amplitude noise in the high-frequency range. Since the ADC's, although independent integrated circuits, are on the same printed circuit board they may have some common temperature dependent phase delay or common amplitude-voltage reference noise. In order to differentiate between these common terms, we take an entangled phase

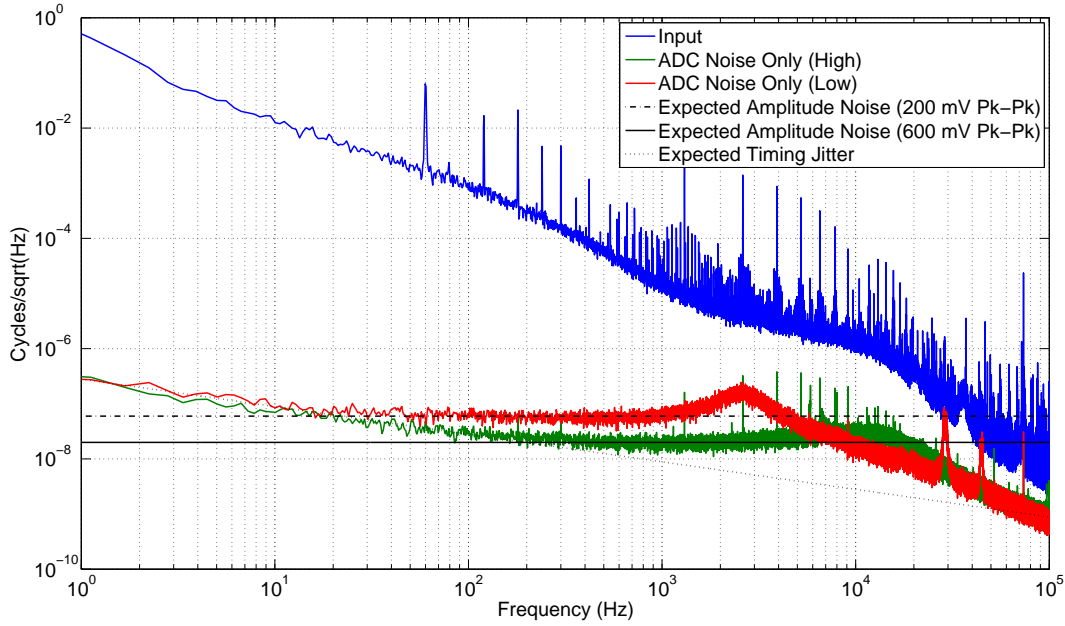


Figure 5-12. ADC amplitude noise limitations: The amplitude noise scales inversely with the input amplitude and indicates that the noise floor is due to the ADC quantization bit-limitation. Using this assumption, we find an effective number of bits $\Omega_{\delta V} = 13.78$ which is nearly equal to the specified 14-bit ADC precision.

measurement involving 3 different signals which combine to cancel the input and clock noise sources but leave the common ADC and phasemeter noise sources.

5.2.5.3 Entangled Phase Noise

Finally, we perform what is commonly known as an entangled phase measurement. This measurement involves mixing three independent VCO signals ($\phi_{VCO1}(t)$, $\phi_{VCO2}(t)$, $\phi_{VCO3}(t)$) with frequencies (f_{VCO1} , f_{VCO2} , f_{VCO3}) and measuring the differential noise between each of the VCOs with three ADCs and PMs to obtain three signals ($\phi_A(t)$, $\phi_B(t)$, $\phi_C(t)$) given by:

$$\phi_A(t) = \phi_{VCO1}(t) - \phi_{VCO2}(t) + \frac{f_{VCO1} - f_{VCO2}}{f_{Clk}} \phi_{Clk}(t) + \phi_{ADC,A}(t) + \phi_{PM,A}(t) \quad (5-22)$$

$$\phi_B(t) = \phi_{VCO2}(t) - \phi_{VCO3}(t) + \frac{f_{VCO2} - f_{VCO3}}{f_{Clk}} \phi_{Clk}(t) + \phi_{ADC,B}(t) + \phi_{PM,B}(t) \quad (5-23)$$

$$\phi_C(t) = \phi_{VCO1}(t) - \phi_{VCO3}(t) + \frac{f_{VCO1} - f_{VCO3}}{f_{Clk}} \phi_{Clk}(t) + \phi_{ADC,C}(t) + \phi_{PM,C}(t) \quad (5-24)$$

Taking a linear combination of the differential noise measurements, namely:

$$\phi_{\text{Ent}}(t) = \phi_A(t) + \phi_B(t) - \phi_C(t) \quad (5-25)$$

we cancel the VCO and clock noise terms in the final combination but are left with noise due to the individual phasemeter and ADCs.

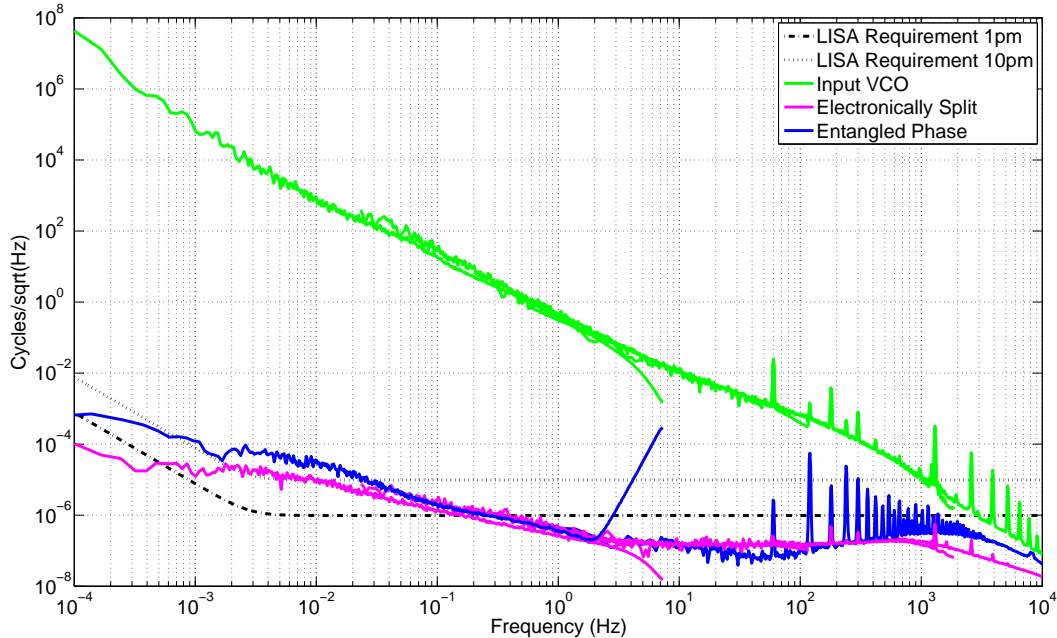


Figure 5-13. Entangled phase measurement results: The entangled phase measurements show an increased noise at low frequencies by up to a factor of 10 due to the independent RF transformer phase dispersion terms (chapter 5.4.1). The measurement couples in aliased noise near the sampling rate due to the CIC down-sampling filters (chapter 5.2.2.2).

The results plotted in Figure 5-13, show up to a factor of 10 increased noise at low frequencies due to a common ADC noise which cancels in the 2-channel differential measurement. The additional low-frequency error in comparison to the differential measurement results from common-mode temperature dependent phase dispersion of the RF transformers (chapter 5.4.1). We also notice an increased noise level near the sampling rate because of the aliasing limitations of the CIC down-sampling filter described in chapter 5.2.2.2. Verifying the CIC filter aliasing error, we perform the same

measurement with a 2-stage, 4-stage, and 6-stage, CIC down-sampling filters. As we can see in Figure 5-14, the 2-stage CIC down-sampling filter will not meet the LISA requirements at frequencies above 10 mHz.

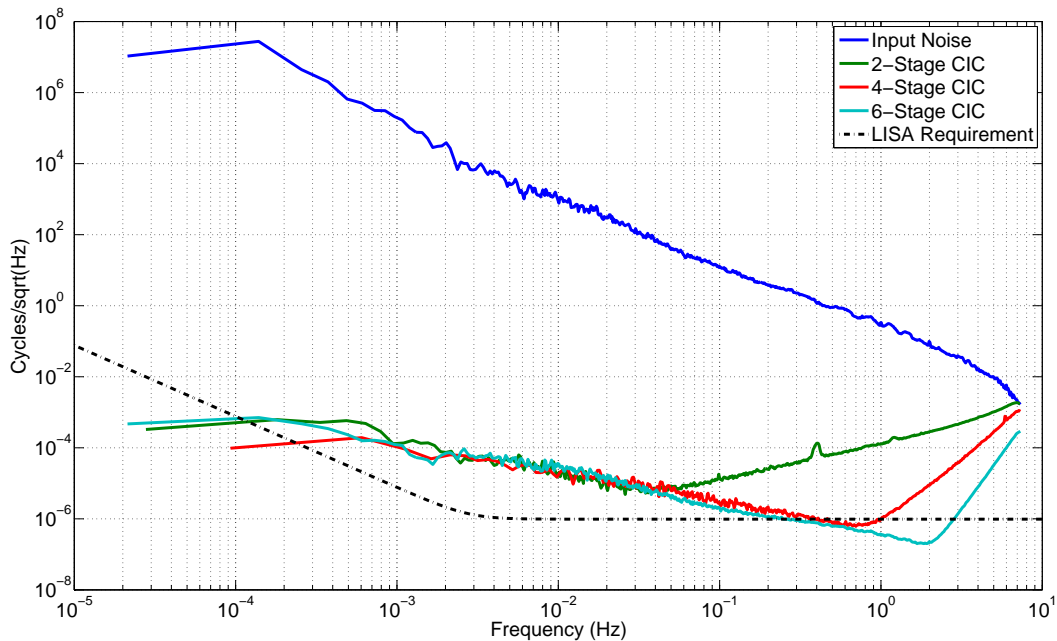


Figure 5-14. N-stage CIC filter aliasing and entangled phase measurements: The entangled phase measurements are performed using a PM-core which down-samples the measured PM data with a $N = 2, 4, 6$ stage CIC filter. As described in chapter 5.2.2.2 and shown in Figure 5-4, the CIC filter down-sampling filter aliases noise into the measurement band, limiting the phase precision of the measured input.

5.2.6 Applications in LISA and LIGO

Although the LISA phasemeter design was motivated by the need to measure the phase of LISA's heterodyne beatnotes to a $1 \mu\text{Cycle}$ accuracy, the phasemeter has applications in many heterodyne and homodyne interferometry schemes. LISA will use the PM to measure not only the LISA observables, but also the clock-noise sidebands and inter-SC data communication signals. The PM frequency readouts are required to perform arm-locking controls and is also applicable in Mach-Zehnder

laser pre-stabilization and digital heterodyne phase-locking. The high-frequency PM sensitivity can also evaluate thermal coating noise for LIGO [100].

5.3 ADC Noise Estimation

We employ a novel ADC phase-noise measurement technique to obtain a better understanding of the noise coupling added by the ADCs. Using the clock as the input source as shown in Figure 5-15, we adjust the length of the cable feeding the input signal, ΔL , to change the phase relationship between the input signal and the clock source.

When there is an offset phase of 0 between the input and the clock trigger, we sample the clock itself at it's zero crossing. In this case, we are sensitive to the linear combination of the ground-reference, $V_{\text{Gnd}}(t)$ in (3-25), timing jitter noise, $\delta\tilde{t}_{\text{Jit}}(\omega)$ in (3-27), and other un-accounted-for white-noise terms, $\phi_{\text{Thermal}}(t)$. Assuming the signal has a slope of $\psi = 2\pi f_{\text{Clk}} V_{\text{Clk}}$, measured in [V/s] with V_{Clk} being the clock amplitude, we can write the sampled output of this measurement as:

$$V_{\Delta\phi=0}(t) = V_{\text{Gnd}}(t) + \psi(f_{\text{Clk}})\delta t_{\text{Jit}}(t) + \phi_{\text{Thermal}}(t). \quad (5-26)$$

When there is an offset phase of $\pi/2$ between the input and clock trigger, we sample the signal's peak. In this case, we are sensitive to the ADC amplitude fluctuations, the $G(t)V_{\text{Bias}_o}$ term in (3-25), the clock amplitude fluctuations, $V_{\text{Clk}}(t)$, and the ground offset term, $V_{\text{Gnd}}(t)$, as in the zero-crossing measurement. Assuming the clock oscillator source has an amplitude of $V_{\text{Clk}}(t)$, we can now write the sampled output as:

$$V_{\Delta\phi=\pi/2}(t) = \frac{V_{\text{Gnd}}(t) + V_{\text{Clk}}(t)}{G(t)V_{\text{Bias}_o}} \quad (5-27)$$

Splitting the clock input signal and performing the same prescription for a second ADC, we can compare the two ADC measurements to cancel common noise terms such as the clock's amplitude fluctuations, $V_{\text{Clk}}(t)$, or common $V_{\text{Gnd}}(t)$ terms.

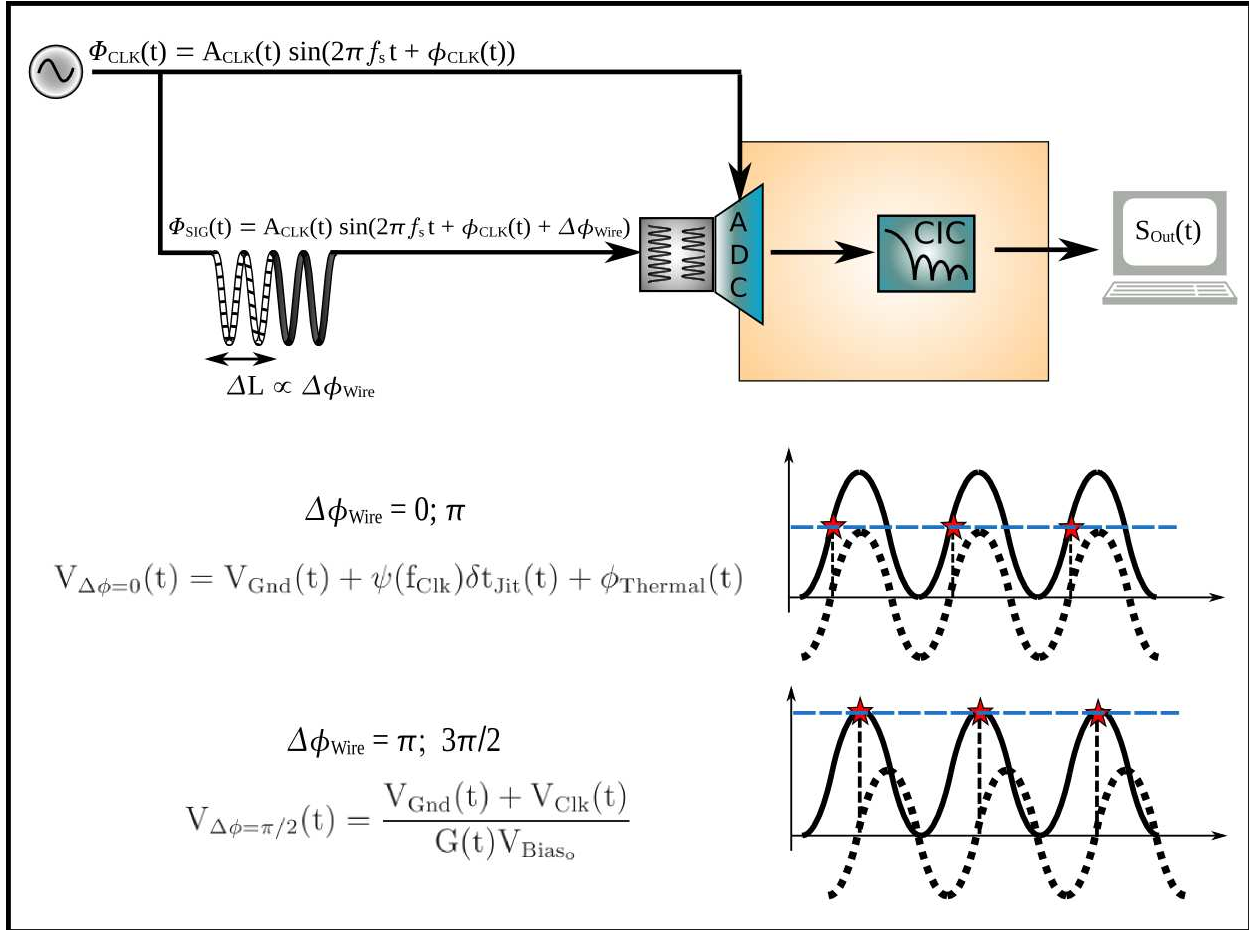


Figure 5-15. Model for estimating ADC phase and amplitude noise: Splitting a clock source and adjusting the phase relationship between the clock and the ADC input, we effectively sample the clock with itself canceling the common clock noise. When the phase relationship between the clock and the input, $\Delta\phi = 0$, we sample at the zero-crossing which couples in timing jitter terms with a proportionality factor given by the 'slope', ψ . When the phase relationship between the clock and the input, $\Delta\phi = \pi/2$, we sample the peak of the clock oscillation; differential measurements will cancel the common clock amplitude noise and be limited by the ADC amplitude noise factor, $G(t)$ (3–25).

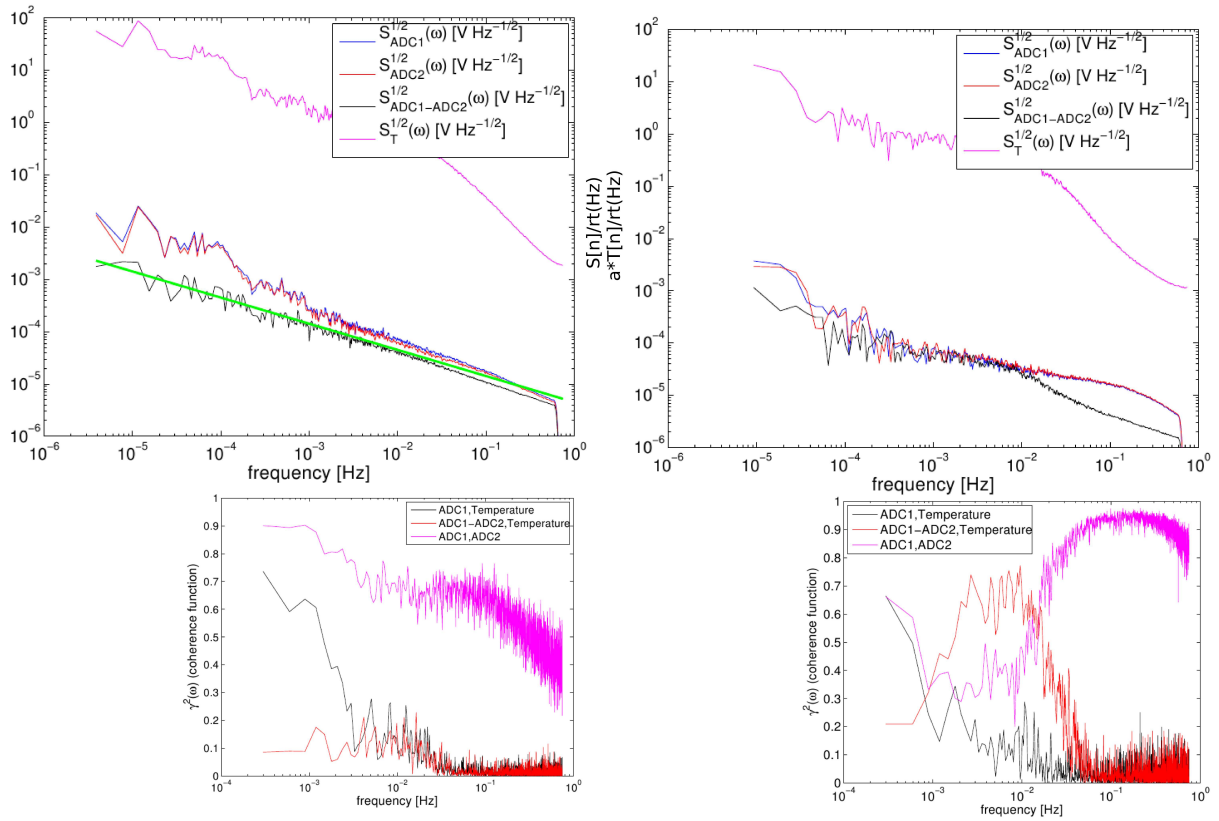


Figure 5-16. Common source ADC phase and amplitude noise results: The zero-crossing measurements (left column) show a strong ADC noise correlation which, when differential measurements are performed, cancel to reveal the thermal and timing jitter noise sources (top-left) as explicitly shown in Figure 5-17. The individual ADC noise sources correlate strongly with the temperature at frequencies below 2 mHz indicating the coupling of temperature dependent RF dispersion. The individual peak-sampling measurements (right column) also show a strong low-frequency correlation with the temperature. The loss of correlation between the individual ADC samples below 2 mHz (bottom-left), indicates that the sampling precision is dominated by voltage bias reference noise, $V_{Bias_0} G(t)$ in (3–25).

The following zero-crossing and peak-sampling measurements use a 62.5 MHz clock input which has a amplitude of $V_{\text{Clk}} = 0.45 \text{ V}$. The phasemeter core is replaced with CIC down-sampling filters to produce the sampled voltage ADC output at a 14.9 Hz down-sampled rate. At the same time, we measure the temperature of the ADC's to see if there is any thermal noise correlations in the measurements.

The results of the zero-crossing measurement, as shown in the left column of Figure 5-16, show a strong correlation between the two individual ADC measurements (red and blue curve in top-left, pink in bottom-left) which cancels in the difference between the signals (black curve in top-left). This individual ADC noise is strongly temperature correlated at frequencies at and below 1 mHz and indicates common mode phase dispersion. Subtracting the signals we obtain a voltage noise estimated by (green curve in top-left of Figure fig:ADCPhaseAmpNoise):

$$\Delta \tilde{V}_{\Delta\phi=0}(\omega) = 5 \times 10^{-6} \sqrt{\frac{1 \text{ Hz Volts}}{f \sqrt{\text{Hz}}}} \quad (5-28)$$

Scaling this by ψ , we obtain a timing jitter of:

$$\begin{aligned} \delta \tilde{t}(\omega) &= \frac{\Delta \tilde{V}_{\Delta\phi=0}(\omega)}{\psi} & (5-29) \\ &= 5 \times 10^{-6} \sqrt{\frac{1 \text{ Hz Volts}}{f \sqrt{\text{Hz}}}} \cdot \frac{1}{2\pi f_{\text{Clk}} V_{\text{Clk}}} \frac{\text{s}}{\text{Volt}} \\ &= 5 \times 10^{-6} \sqrt{\frac{1 \text{ Hz Volts}}{f \sqrt{\text{Hz}}}} \cdot \frac{1}{2\pi \cdot 62.5 \text{ MHz} \cdot 0.45 \text{ Volts}} \\ &\simeq 28 \sqrt{\frac{1 \text{ Hz}}{f} \frac{\text{fs}}{\sqrt{\text{Hz}}}}. & (5-30) \end{aligned}$$

This is smaller, yet, comparable to the timing jitter measured in chapter 5.2.5.2. If this is actually the timing jitter term it should scale with respect to the clock frequency through the ψ dependence. To probe this dependence, we take the same measurement at 50 MHz, 75 MHz, and 100 MHz. The results (Figure 5-17), show the same noise level for the 50 MHz and 75 MHz signals as we observe here. This indicates that the noise source we are measuring is not timing jitter, but rather, a phase error which is likely due

to the internal electronic thermal noise background, $\phi_{\text{Thermal}}(t)$. The 100 MHz signal shows a slight increase in the phase noise error indicating that we have now made ψ large enough to dominate over the thermal background terms in (5-26). Given this assumption, we re-evaluate the jitter level:

$$\delta\tilde{t}(\omega) = \frac{\Delta\tilde{V}_{\Delta\phi=0}(\omega)}{\psi} \quad (5-31)$$

$$\begin{aligned} &= 9 \times 10^{-6} \sqrt{\frac{1 \text{ Hz Volts}}{f \sqrt{\text{Hz}}}} \cdot \frac{1 \text{ s}}{2\pi f_{\text{Clk}} V_{\text{Clk}} \text{ Volt}} \\ &= 9 \times 10^{-6} \sqrt{\frac{1 \text{ Hz Volts}}{f \sqrt{\text{Hz}}}} \cdot \frac{1}{2\pi 100.0 \text{ MHz} 0.45 \text{ Volts}} \\ &\simeq 32 \sqrt{\frac{1 \text{ Hz}}{f}} \frac{\text{fs}}{\sqrt{\text{Hz}}} \end{aligned} \quad (5-32)$$

which is closer to the estimate given by (5-19). Scaling this 100 MHz zero-crossing, voltage noise measurement to a 10 MHz input signal and comparing it against a 10 MHz measurement, the results match the measured jitter as shown in Figure 5-18.

Moving on to the peak-sampling measurements as shown in the right column of Figure 5-16, we observe some common amplitude noise at frequencies below 1 mHz and at frequencies above 10 mHz. The amplitude noise at these frequencies is likely due to common mode fluctuations in the input signal or in the voltage bias reference, $G(t)V_{\text{bias}}$, although, without an independent measure of the input amplitude, there is no way to differentiate between these terms. The differential ADC noise shows some temperature correlation at frequencies between 2 and 20 mHz. This is most probably due to temperature dependent noise in the voltage bias, $G(t)V_{\text{bias}}$, since it is not likely that the amplitude of the clock source correlates with the temperature of the ADCs. That said, these noise sources on this absolute voltage scale are smaller than the timing jitter sources and are scaled by the inverse amplitude before coupling into the measured phase as explained in chapter 3.4.2.5. Although, because of the 'white' nature of the voltage noise in this 1-20 mHz region of $\simeq 5 \times 10^{-5} \text{ Volts}/\sqrt{\text{Hz}}$, it indicates that we should be about to calculate the effective number of bits in this low-frequency range. Assuming

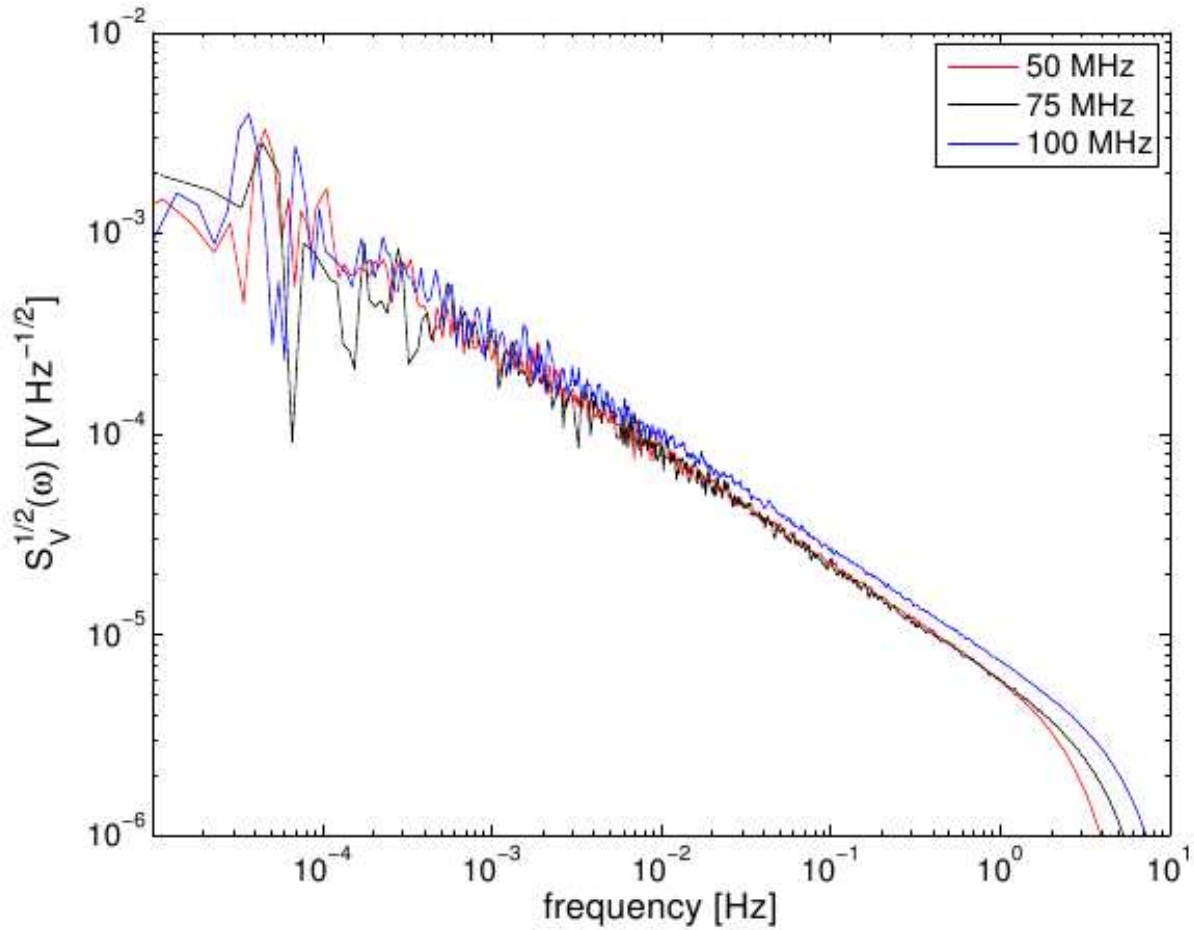


Figure 5-17. Zero-crossing timing jitter estimate: The differential zero-crossing timing jitter measurements provide us with the ability to directly probe the ADC timing jitter and its frequency dependence. The input frequency dependence of Ψ allows us to differentiate between $\phi_{\text{Thermal}}(t)$ and $\psi(f_{\text{CLK}})\delta t_{\text{Jit}}(t)$ in (5-26). The 50 and 75 MHz measurements show the same noise level and are dominated by $\phi_{\text{Thermal}}(t)$. The 100 MHz measurement increases $\psi(f_{\text{CLK}})$ to allow us to probe $\delta t_{\text{Jit}}(t)$ (5-32).

(3-24) still holds, we calculate the effective number of bits from,

$$\frac{|V_{\text{Bias}}| 2^{1-\Omega}}{|V_{\text{In}}| \sqrt{6f_s}} = \frac{5 \times 10^{-5} \text{ Volts}}{V_{\text{Full-Scale}} \sqrt{\text{Hz}}} \quad (5-33)$$

$$\frac{0.5 \text{ Volts}}{0.225 \text{ Volts}} \frac{2^{1-\Omega}}{\sqrt{6 \cdot 14.9 \text{ Hz}}} = \frac{5 \times 10^{-5} \text{ Volts}}{1.0 \text{ Volts} \sqrt{\text{Hz}}} \quad (5-34)$$

The solution gives a bit-resolution of $\Omega = 13.2$ and, thus, it seems that thermal fluctuations have decreased the effective number of bits in this frequency range. These

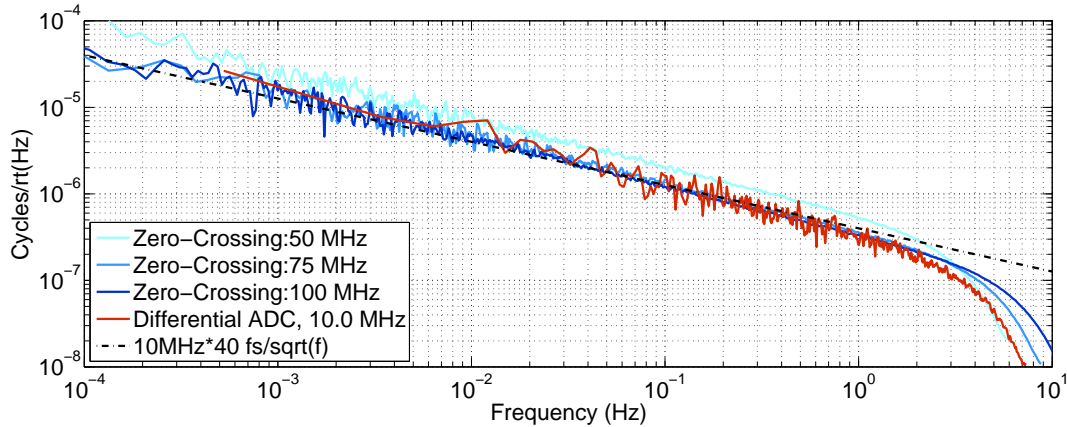


Figure 5-18. The timing jitter estimate obtained from Figure 5-17 is scaled and compared directly to an experimental PM measurement of a 10 MHz input signal. The results indicate that we have obtained an accurate estimate of the ADC timing jitter given by $\approx 30 - 40/\sqrt{f}$ fs/ $\sqrt{\text{Hz}}$ which will limit the LISA measurement precision such that the PMs and ADCs do not meet the $1 \mu\text{cycle}/\sqrt{\text{Hz}}$ measurement requirement by up to an order of magnitude near the 3 mHz corner frequency.

low-frequency amplitude-phase fluctuation terms will become apparent once the timing jitter terms have been extracted in the next chapter.

Now that we know that timing jitter is the limiting noise source of these measurements, we attempt to estimate and correct for these terms. Also, we must further investigate and correct non-jitter limitations of the phasemeter in the 1-8 MHz frequency range, of which, these zero-crossing and peak measurements do not probe. That said, the correlation between the ADC input phase and the temperature at low frequencies in Figure 5-16 (bottom left) indicate a temperature dependent phase response of the ADCs. If the slope of this phase-response is large enough, it might over-come and dominate the timing jitter terms.

5.4 Timing Jitter Extraction

Timing jitter correction is based off the concept that, although the timing jitter terms are ADC independent, a second modulation, added to the ADC input signal, can be used as a reference to measure and correct for the timing jitter. As shown in Figure 5-19, a second oscillator is added using an RF transformer-splitter. The summed

output is split again into two different ADCs. The phase of the input and the ranging tone on each ADC is measured with its own phasemeter. Measuring the input signals, we obtain PM outputs which take the form:

$$\phi_{\text{In:ADC1}}(t) = \phi_{\text{In}}(t) + \frac{f_{\text{In}}}{f_{\text{Clk}}}(-\phi_{\text{Clk}}(t) + f_{\text{Clk}}\delta t_{\text{ADC-1}}) \quad (5-35)$$

$$\phi_{\text{In:ADC2}}(t) = \phi_{\text{In}}(t) + \frac{f_{\text{In}}}{f_{\text{Clk}}}(-\phi_{\text{Clk}}(t) + f_{\text{Clk}}\delta t_{\text{ADC-2}}) \quad (5-36)$$

Repeating this for the added reference-tone signals, we obtain:

$$\phi_{\text{Tone:ADC1}}(t) = \phi_{\text{Tone}}(t) + \frac{f_{\text{Tone}}}{f_{\text{Clk}}}(-\phi_{\text{Clk}}(t) + f_{\text{Clk}}\delta t_{\text{ADC-1}}) \quad (5-37)$$

$$\phi_{\text{Tone:ADC2}}(t) = \phi_{\text{Tone}}(t) + \frac{f_{\text{Tone}}}{f_{\text{Clk}}}(-\phi_{\text{Clk}}(t) + f_{\text{Clk}}\delta t_{\text{ADC-2}}) \quad (5-38)$$

Using these, we are able to probe the differential timing jitter terms to correct for the input signal's timing jitter. Note that a higher frequency reference tone is desirable since the timing jitter scales with this frequency. In fact, the jitter tone can be placed at a frequency above the sampling rate; measuring the aliased oscillation results in stronger jitter couplings as shown in Figure 5-11.

Subtracting the two input signals and the two reference signals, we are able to evaluate the differential timing jitter at each frequency, f_{in} and f_{Tone} :

$$\Delta_{\phi}(t) = f_{\text{In}}[\delta t_{\text{ADC-1}} - \delta t_{\text{ADC-2}}] \quad (5-39)$$

$$\Delta_{\text{Tone}}(t) = f_{\text{Tone}}[\delta t_{\text{ADC-1}} - \delta t_{\text{ADC-2}}] \quad (5-40)$$

Rescaling and subtracting these signals we cancel the differential ADC timing jitter and obtain a calibrated result which cancels all the noise sources we have considered:

$$\Delta\phi_{\text{Calib.}} = \Delta_{\phi}(t) + \frac{f_{\text{In}}}{f_{\text{Tone}}}\Delta_{\text{Tone}}(t) \quad (5-41)$$

Note that this differential timing jitter correction method will not give a measure of the absolute, individual timing jitter terms from which we can obtain a true measurement

of $\phi_{In}(t)$. A few possible methods of performing this absolute jitter correction are discussed in chapter 5.4.2.

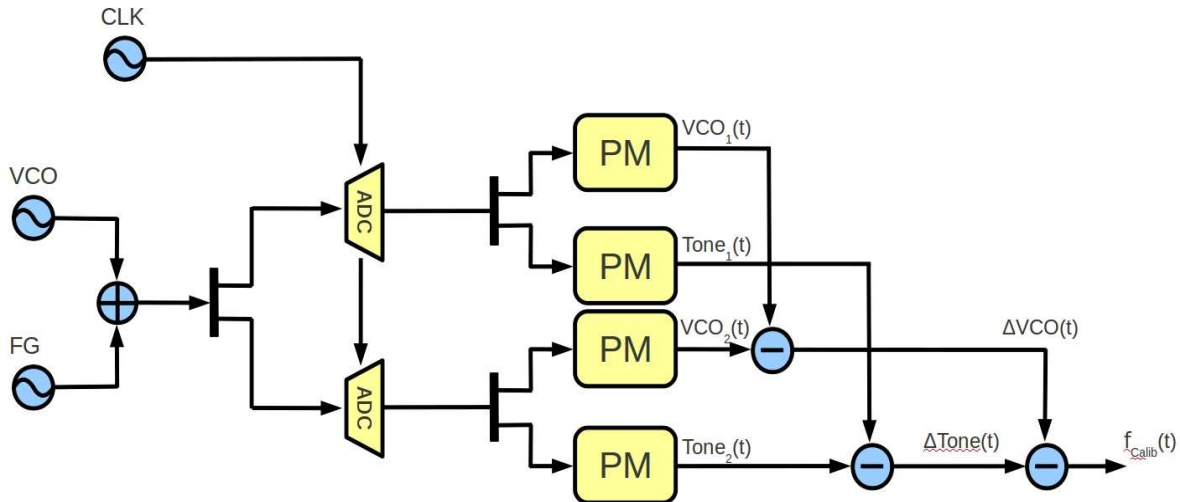


Figure 5-19. Timing jitter calibration model: Here we show a model of how the input signal, in this case, a VCO, is added to a calibration signal [oscillator/function generator(FG)] with an inversely driven splitter. The two summed oscillations are split and sampled with two independent ADCs but with the same clock source. The PM cores measure the phase of the VCO-input and calibration signals which are each contain the timing jitter of their respective ADCs scaled by the magnitude of the measured input frequency as described in chapter 5.4.

A series of initial tests performed well when the ranging tone and input signal were relatively equal in frequency as shown in the right column of Figure 5-20, nearly obtaining the $1 \mu\text{cycle}/\sqrt{\text{Hz}}$ requirement. The temperature measurements and correlations for the ADC noise estimation of chapter 5.3 are also used here to see if the measured phase correlates with the ADC temperature. The top-right plot of Figure 5-20 showed no correlation with either input signal or the differential timing jitter indicating that temperature effects play little role in the noise coupling at these high frequencies. When the timing jitter correction is attempted using a low-frequency (4 MHz) input signal and a high-frequency (15 MHz) tone, we obtain no noticeable improvement in the phase measurement precision.

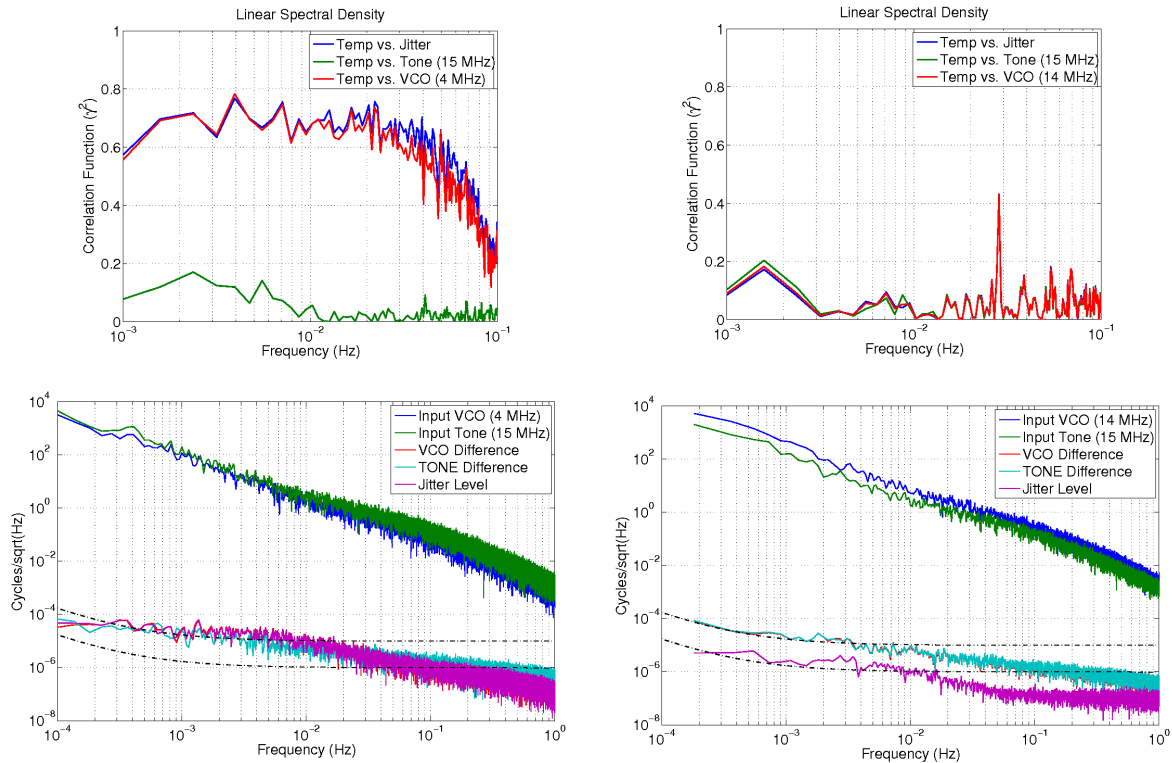


Figure 5-20. Temperature dependent phase dispersion: Placing the input oscillation at 4 MHz and the jitter calibration input at 15 MHz, the timing jitter extraction is limited by jitter-uncorrelated noise in the input oscillation. The differential phase noise of this 4 MHz input signal correlates strongly with temperature of the RF transformers which introduce dispersion terms that are not accounted for in the timing jitter extraction. Placing the input oscillation and jitter calibration tone close to each-other, 14 and 15 MHz respectively, we reduce the temperature dependent dispersion and the timing jitter extraction works as explained in chapter 5.4

Correlating each of these with the measured temperature, we see a strong correlation between the low-frequency input and the measured temperature as shown in the top-left plot of Figure 5-20. This indicates that there is some phase loss which changes as a function of temperature at these low frequencies. This low-input-frequency limit had already been indicated to some extent by the results plotted in Figure 5-11. To see how strong the temperature coupling effect is, we perform the timing jitter extraction for three different frequencies across the 2-20 MHz LISA input-frequency range (2 MHz,

8 MHz, and 16 MHz) and attempt to calibrate them against a (19 MHz) oscillator tone. The results are shown in the top plot of Figure 5-22.

5.4.1 Phase Dispersion Mitigation

A detailed look into the Pentek design indicates that the RF transformers used to AC couple the input signal, the ADT4-5WT, have a strong input return loss and, thus, a steep phase dependence at these low frequencies as shown in the left column of Figure 5-21. Temperature variations change the transfer function response and phase loss for these RF transformers which couple into the low-frequency measured phase (Figure 5-11). Mini-circuits, the integrated-circuit production company which makes the ADT4-5WT also produces another model, the ADT1-6T, which has a significantly more constant input return loss, and thus, a smaller phase change in the LISA-frequency range. After the risks and costs were weighed, we decided to replace the RF transformers on the Pentek boards to better suit the 2 – 20 MHz LISA input frequency range of interest.

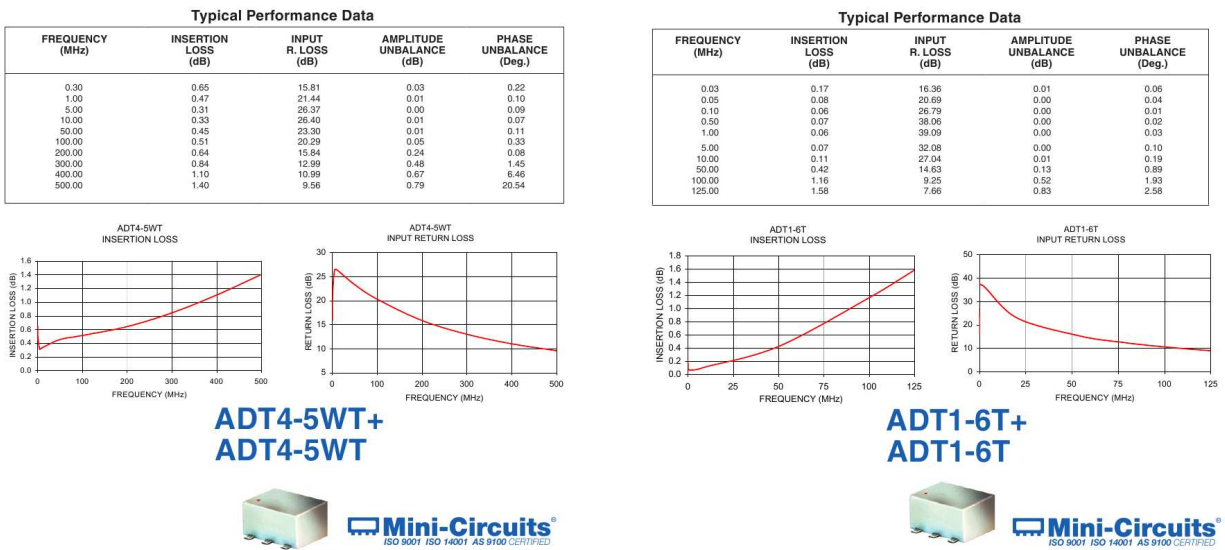


Figure 5-21. The stock ADT4-5WT has a bandwidth between 300 kHz and 500 MHz. The replacement ADT1-6T's bandwidth is from 30 kHz to 125 MHz, providing a better suited AC coupler to make PM measurements at LISA-like frequencies. [101, 102]

Thankfully, changing in RF transformers did not damage the Pentek’s electronics and improved the low-frequency performance as shown by the improved timing jitter result in Figure 5-22. At this point, we can see that provided with the reference tone’s measure of the timing jitter, we should be able to correct for the timing jitter of the measured input phase across the entire 2 – 20 MHz LISA input-frequency range.

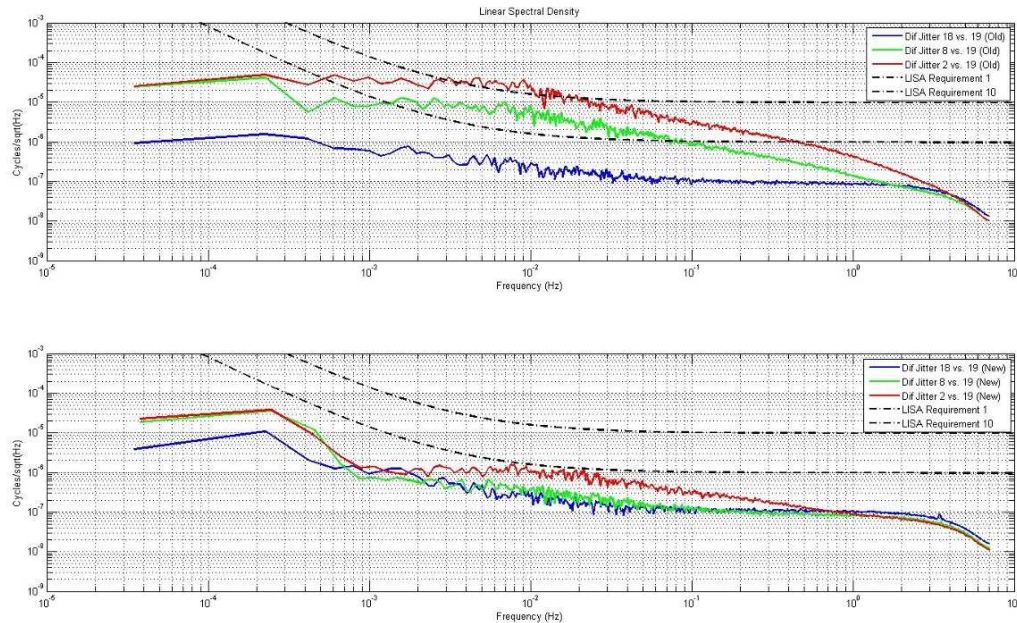


Figure 5-22. Replacement RF transformer dispersion mitigation: Repeating the timing jitter extraction tests with the old (ADT4-5WT) and new (ADT1-6T) RF transformers, we find the RF transformer phase dispersion has been corrected and the timing jitter extraction has been significantly improved. The jitter extraction results using the new ADT1-6T RF transformers meet the LISA measurement requirement of $1 \mu\text{cycle}/\sqrt{\text{Hz}}$ for all frequencies in the 2-20 MHz range. Once the timing jitter has been removed, the phase precision is limited by the signal-amplitude dependent quantization noise floor; chapter 5-12 for $f > 20 \text{ mHz}$, (5-33) for $f < 20 \text{ mHz}$, over the frequencies for which the RF transformer dispersion no longer limits the results.

5.4.2 Absolute Timing Jitter Extraction

Performing absolute timing jitter extraction is somewhat more difficult since we need the same reference phase noise, $\phi_{\text{Tone}}(t)$, at two different frequencies, f_{Tone1} and f_{Tone2} ,

such that we can form the combination:

$$\begin{aligned}
\phi_{\text{In-Calib}}(t) &= \phi_{\text{In:ADC1}}(t) - \frac{f_{\text{In}}}{f_{\text{Tone1}} - f_{\text{Tone2}}} [\phi_{\text{Tone1:ADC1}}(t) - \phi_{\text{Tone2:ADC1}}(t)] \quad (5-42) \\
&= \phi_{\text{In}}(t) + \frac{f_{\text{In}}}{f_{\text{Clk}}} (-\phi_{\text{Clk}}(t) + f_{\text{Clk}} \delta t_{\text{ADC-1}}) \\
&\quad - \frac{f_{\text{In}}}{f_{\text{Tone1}} - f_{\text{Tone2}}} \left[\frac{f_{\text{Tone1}} - f_{\text{Tone2}}}{f_{\text{Clk}}} (-\phi_{\text{Clk}}(t) + f_{\text{Clk}} \delta t_{\text{ADC-1}}) \right] \\
&\simeq \phi_{\text{In}}(t)
\end{aligned}$$

This would be accomplished by up-converting or down-converting a common signal with a $1 \mu\text{cycle}/\sqrt{\text{Hz}}$ accuracy, or rather, an accuracy better than the timing jitter noise limitation, which may or may not be feasible based on the noise characteristics of the electronics and methods used to perform the frequency-conversion.

5.5 Phasemeter Performance Review

Compiling the results of all of these measurements, we have a well-defined model of the limiting noise sources in the PM measurement process. The regions of which over these terms couple is shown in Figure 5-23. The frequency range from 10 Hz to 10 kHz is dominated by white amplitude noise which couples into the phase from a combination of variations in the input beatnote's amplitude (chapter 5.2.5.2) and quantization noise (chapter 3.4.2.5). Increasing the signal voltage decreases the quantization noise and reduces the measured phase noise proportionately.

The LISA measurement band, 0.1 mHz to 1 Hz, is dominated by timing jitter and temperature dependent phase dispersion. The timing jitter scales proportionately with a decrease in the signal frequency and can be corrected for by the methods mentioned in chapter 5.4 and chapter 5.4.2. Once the timing jitter has been removed, the limiting noise sources is suppressed to the amplitude noise limit with a $1/\sqrt{f}$ flicker-type noise sources coupling in at frequencies below 10 mHz.

The phase dispersion from the RF transformers plays a large roll in limiting the phasemeter phase sensitivity. Internal or external heating of any filtered element,

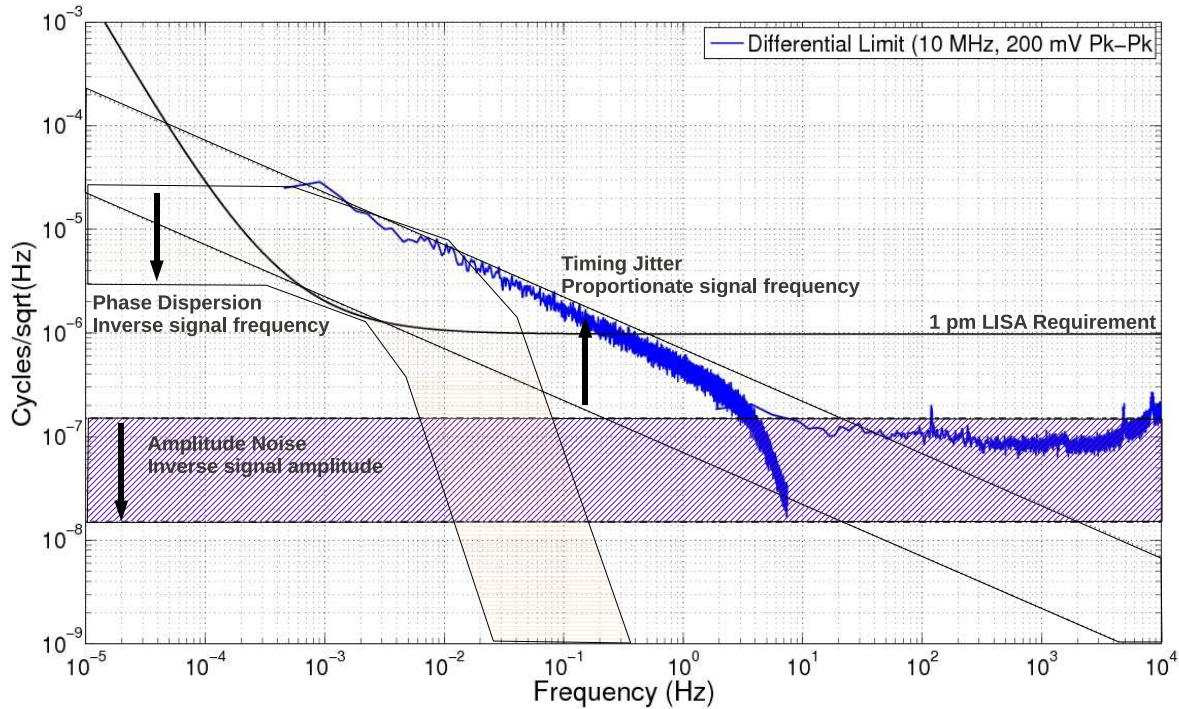


Figure 5-23. Phasemeter noise model, estimation, and limits: The primary phase precision limiting effects have been identified and plotted in comparison with the $1 \mu\text{cycle}/\sqrt{\text{Hz}}$ phasemeter requirement. The frequency range above 10 Hz is dominated by amplitude-quantization noise and scales inversely with the input amplitude from 2 Volts peak-to-peak to 200 mVolts peak-to-peak. The $40/\sqrt{f}$ fs/ $\sqrt{\text{Hz}}$ timing jitter dominates the frequencies below 1 Hz and scales proportionately with the 2-20 MHz input frequency. This assumes that any temperature-correlated low-frequency phase dispersion, which scales based on the slope of the transfer functions' phase response, has been mitigated; that said, a constant phase response in the 2-20 MHz range is desirable.

including photo-detectors, transformer-splitters or AC couplers, and mixers, will have a transfer function with some defined phase response. If the phase response is not flat over the 2 to 20 MHz LISA heterodyne beatnote frequency band, the temperature dependent electronics will produce a time-changing phase loss which couples into measured phase. The dominate heating source in the 1 to 100 mHz frequency range in these experiments resulted from internal heating of the ADCs upon power up more so than environmental temperature changes. Thus, despite the quiet temperature

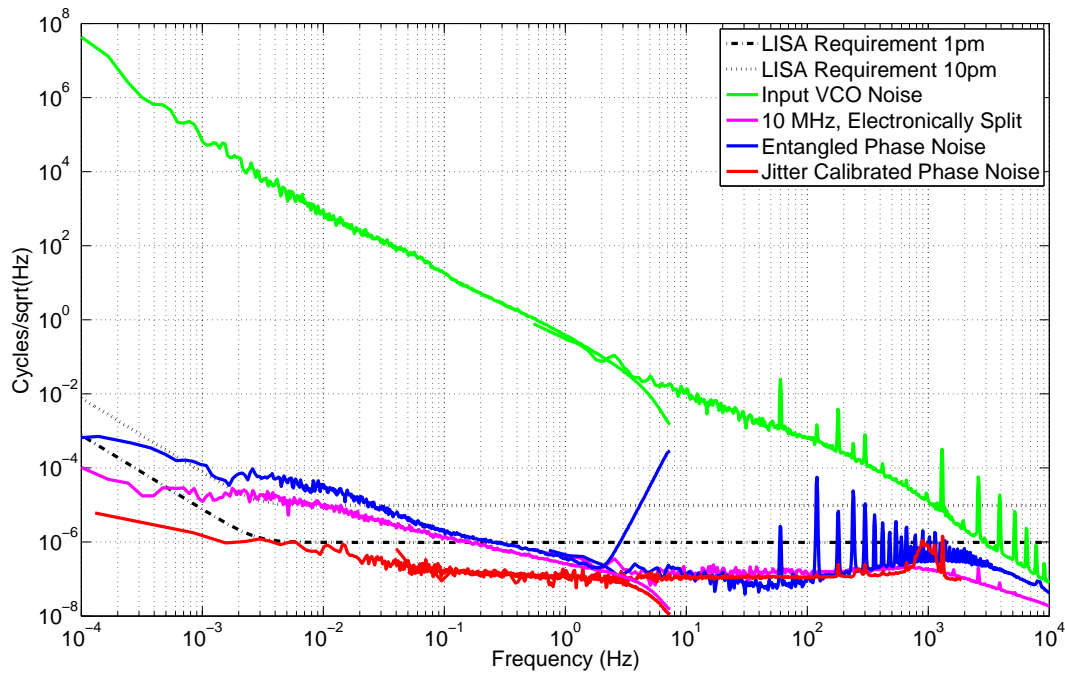


Figure 5-24. Comparison of the PM noise characteristics: The 10 MHz differential phase (chapter 5.2.5.2), entangled phase (chapter 5.2.5.3), and timing jitter extraction (chapter 5.4) results are plotted together for a direct comparison of PM experimental results and noise performance.

environment of the LISA mission, these noise sources will still be present from electronic heating and cooling.

CHAPTER 6
THE UNIVERSITY OF FLORIDA LISA INTERFEROMETRY SIMULATOR

6.1 The LISA Laser Test-bench

The UFLIS experimental benchtop as pictured in Figure 6-1 consists of four controllable Nd:YAG, 1064 nm lasers, $\text{Laser}_{\text{Ref}}$, Laser_1 , Laser_2 , and Laser_3 , which generate laser fields with phase signals given by $\phi_{\text{Ref}}(t)$, $\phi_1(t)$, $\phi_2(t)$, and $\phi_3(t)$. We interpret each individual Laser_i as the laser on SC_i producing the laser field $\phi(t)$ as described in chapter 3.4.3.4. Heterodyned PD signals between $\text{Laser}_{\text{Ref}}$ and the other three laser fields produce differential measurements of the laser phases:

$$\phi_{1R} = \phi_1 - \phi_{\text{Ref}} \quad \phi_{2R} = \phi_2 - \phi_{\text{Ref}} \quad \phi_{3R} = \phi_3 - \phi_{\text{Ref}} \quad (6-1)$$

such that combinations of these signals will cancel the common $\text{Laser}_{\text{Ref}}$ noise. Thus, the reference laser is used as a global reference with which the other three laser fields can be measured. Reproducing the expected LISA pre-stabilized laser noise, we PDH lock $\text{Laser}_{\text{Ref}}$ and Laser_1 to a ULE cavity. The following section reports on the phasemeter measurements of this pre-stabilized laser noise. The next section describes the methods used to simulate the inter-SC electronic delay including the multi-second time-changing laser phase delay, MHz laser field Doppler shifts, and μCycle GW modulations. The last section describes how these three components are combined to perform advanced arm-locking and TDI simulations.

Reference Cavity Stabilization.

The University of Florida laser benchtop PDH locks two lasers, $\text{Laser}_{\text{Ref}}$ (or RL) and Laser_1 (or L1), to two different cavities, 26.0 cm and 22.5 cm in length respectively, resulting in a laser beat-notes between the two lasers with a frequency stability given by the relationship:

$$\delta f_{\text{RL/L1}}(\omega) = \sqrt{\delta f_{\text{RL}}(\omega)^2 + \delta f_{\text{L1}}(\omega)^2}. \quad (6-2)$$

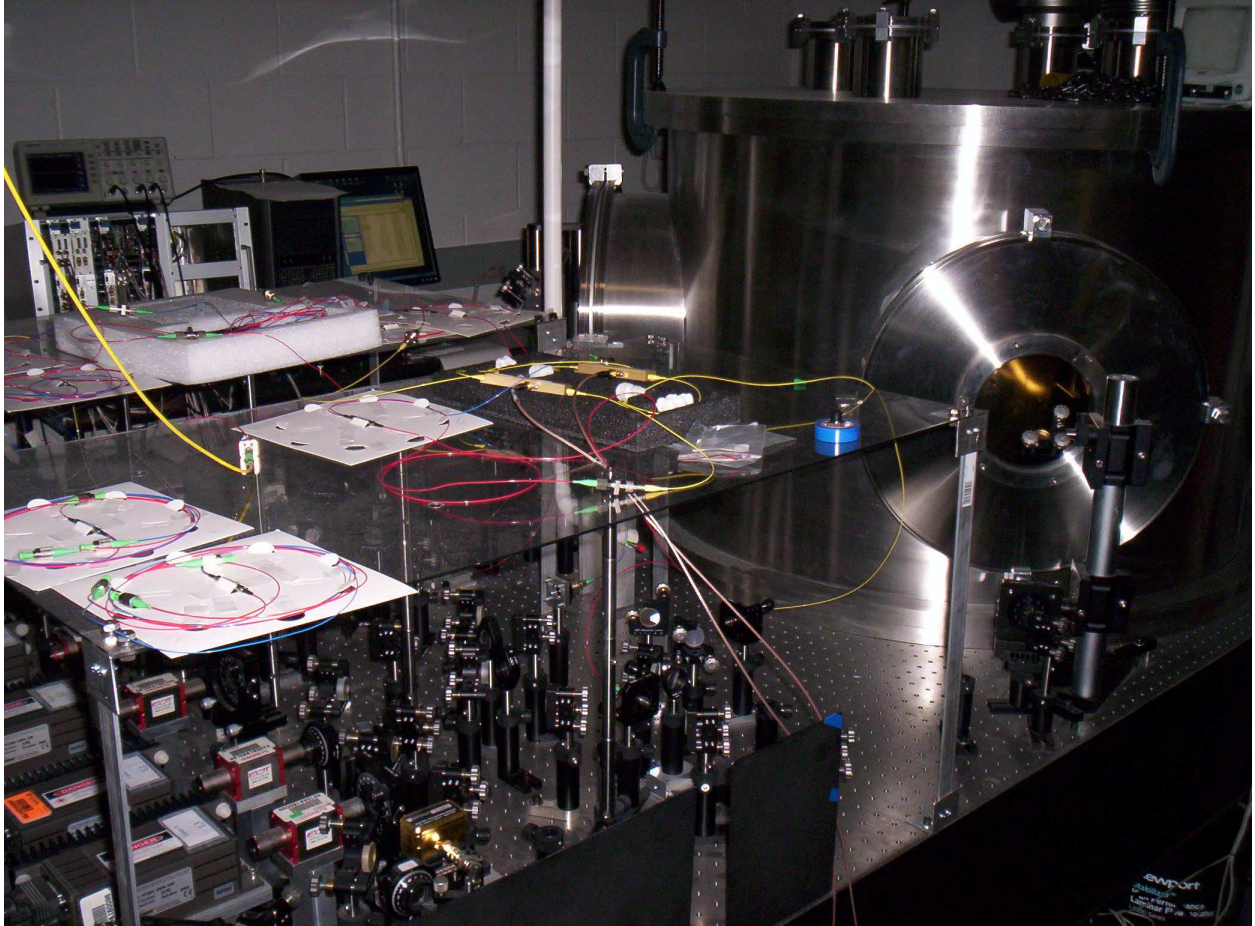


Figure 6-1. UFLIS laser benchtop: The laser benchtop, pictured here, PDH pre-stabilizes the lasers and forms all the necessary PD signals to perform the LISA interferometry simulations. The four lasers, three representing the individual SC and one acting as an optical clock, can be seen in the bottom left corner. The vacuum tank on the right contains the ULE cavities and provides the necessary temperature and pressure shielding required to transfer the cavity stability to the laser frequency. The phasemeter data acquisition and EPD data processing DSP electronics can be seen in the background near the top-left of the image.

The stability of these lasers depends highly on the feedback electronics whose gain can be adjusted to achieve a $\simeq 30 - 300\text{Hz}/\sqrt{\text{Hz}}$ stability and are limited by the temperature stability of the cavity length [52]. Phasemeter measurements of the free-running laser stability in comparison with the cavity stabilized laser stability are plotted in Figure 6-2 from which we observe an improvement in the laser phase noise by 4 orders of magnitude at 10 mHz. Also, as a comparison, we plot the VCO noise level used for many of the previous phasemeter verification measurements. In LISA, the lasers can be individually locked to their own reference cavity or one master cavity stabilized laser can be transferred to the other lasers by phase-locking the differential heterodyned laser fields. Thus, from this point on, we assume that Laser₁ is the master stabilized field on SC₁ and that the other laser fields are phase-locked as described in [71].

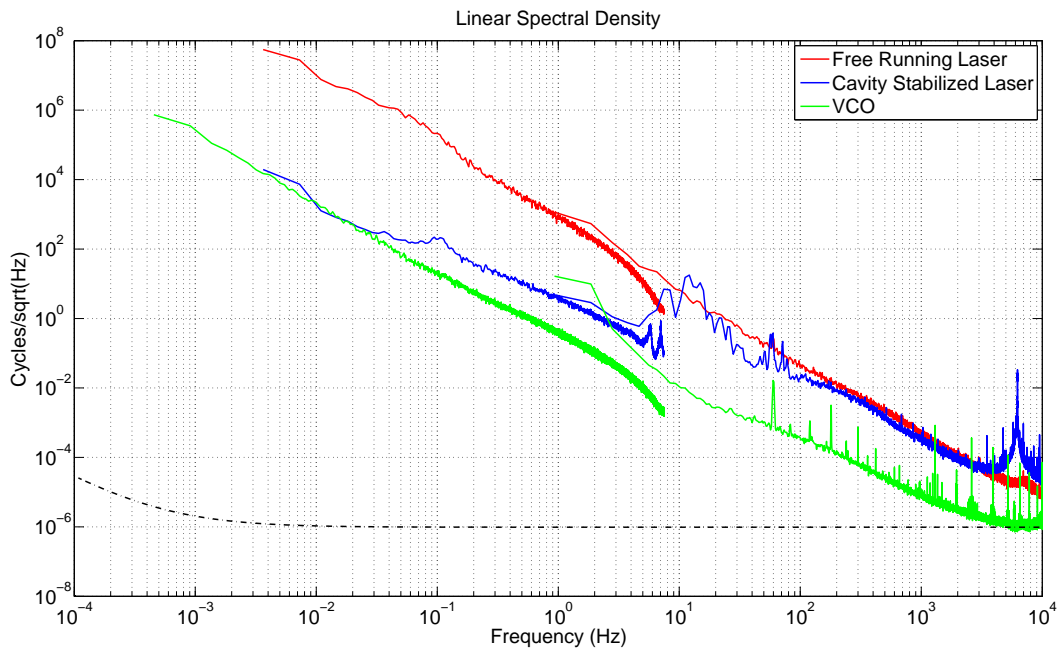


Figure 6-2. Measurements of commonly used sources: Here we have plotted the phasemeter measurements of the spectral noise of the free-running, cavity stabilized, and VCO noise sources used in the UFLIS simulations. Cavity pre-stabilization provides us with 4 order of magnitude free-running noise suppression at 10 mHz. The VCO provides similar noise characteristics to the cavity stabilized lasers below 10 Hz and is used as a test input for many simulations.

6.2 The Electronic Phase Delay (EPD) Unit

The electronic phase delay (EPD) unit is constructed out of all three Pentek components described in chapter 5.1. Generally described, the Pentek-6256 phase-meter front-end produces frequency information at a 10-100 kHz data rate which is then passed to the Pentek-4205. The frequency information is stored on the Pentek-4205 in a buffer whose length is based on the data-rate and the desired hold time.¹ Once the delay is applied the frequency information is interpolated to introduce the time-changing delay. The interpolated data is added to a large MHz Doppler modulation and small mHz GW modulation. The processed frequency information is then sent to the Pentek-6228 where it is integrated to generate the phase and used to drive a numerically controlled oscillator (NCO). The NCO signal is reconstructed using the Pentek-6228's DACs. The details of the design and noise are described in the following sections.

6.2.1 Design

A diagrammatic model of a single channel of the EPD unit is shown in Figure 6-3. The Pentek-6256 has 4 ADC's and two FPGA's which are connected to four independent phasemeters producing 60-bit frequency data at a CIC down-sampled rate of $f_{\text{EPD}} = 10 - 400 \text{ kHz}$ depending on the application and clock rate. Assuming the EPD measures a signal, $A\sin(2\pi f_{\text{in}}(t)t)$, with a clock given by $A\sin(2\pi f_{\text{clk}}(t)t)$, the phasemeter output takes the form:

$$f_{\text{EPD}}[n] = f_{\text{in}}[n] + \frac{f_{\text{in}}}{f_{\text{clk}}} f_{\text{clk}}[n] \quad (6-3)$$

with $n = t/f_{\text{EPD}}$ due to the down-sampled EPD data-rate.

This data is packed into 16, 32-bit packets which take the form shown in Figure 6-4. The last two bits of each packet are used as a tag with which to ensure proper data-communication. Data-space for 60 bits of Doppler and 60 bits of GW information

¹ delay time (τ)

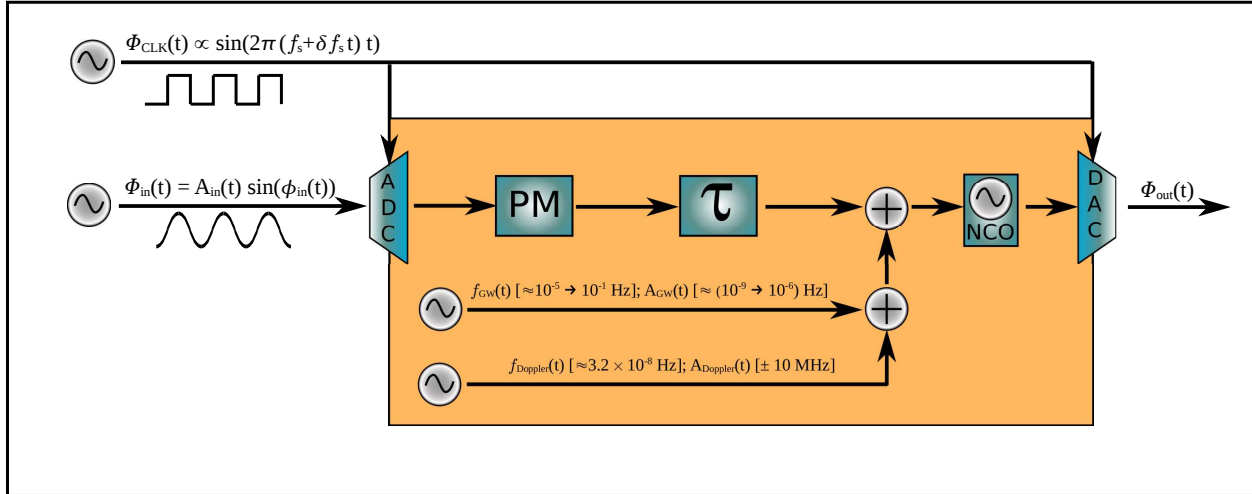


Figure 6-3. Model of the electronic phase delay (EPD) unit: Here we have depicted a model of EPD unit, which is constructed using the DSP systems described in chapter 5.1. The input signal is measured with a PM core and the frequency data is stored in memory for a pre-defined storage time representing the inter-SC light travel time delay. The delayed frequency data is linearly interpolated to simulate a time-changing delay (not pictured) and added to a Doppler offset/modulation and the simulated GW signal. A numerically controlled oscillator (NCO) reconstructs the delayed frequency information and an DAC regenerates the signal with the same clock used to sample the input.

is left open in the packing scheme which is be populated with data on the Pentek-4205 once the frequency data has been read from the 6256. Depending on the desired delay, τ , the storage space for the τ/f_{EPD} data-points must be reserved for each channel.

After the frequency data is stored for the proper amount of time, it is linearly interpolated to apply a time-changing delay. It is important that the interpolation take the right form; LISA will have a linear change in the phase rather than a linear change in the frequency. As a result, assuming we are trying to interpolate the data such that $t \rightarrow t(1 - \beta)$, a factor of $(1 - \beta)$ must be introduced to account for the time-integration nature of the frequency to phase conversion. That is, where one might normally use:

$$f[n(1 + \beta)] = (1 - \beta n)f[n] + f[n + 1] \quad (6-4)$$

F_1 (in) Bits(60..30)	01
F_1 (in) Bits(29..0)	00
Dop_1 Bits(60..30)	00
Dop_1 Bits(29..0)	00
GW_1 Bits(60..30)	00
GW_1 Bits(29..0)	00
NAN_1 Bits(29..0) = 0	00
NAN_1 Bits(29..0) = 0	00
F_2 (in) Bits(60..30)	02
F_2 (in) Bits(29..0)	00
Dop_2 Bits(60..30)	00
Dop_2 Bits(29..0)	00
GW_2 Bits(60..30)	00
GW_2 Bits(29..0)	00
NAN_2 Bits(29..0) = 0	00
NAN_2 Bits(29..0) = 0	00

Figure 6-4. EPD unit data-packing scheme: The 60-bit frequency, Doppler, and GW modulation data of the two independent EPD channels is multiplexed into a 16 point data-stream of 32-bit values. Numerical flags are added to the most-significant-bits of the frequency data to ensure that the data is correctly interpreted and data-points are not missed.

to apply a linear interpolation between $f[n]$ and $f[n + 1]$, we will use:

$$f[n(1 + \beta)] = (1 - \beta)(1 - \beta n)f[n] + f[n + 1] \quad (6-5)$$

to account for the frequency to phase conversion.

Once the linear interpolation is applied the frequency data is packed with a $1 \mu\text{Hz}$ to 1 mHz GW modulation signal and a $\pm 20 \text{ MHz}$ Doppler signal. It is possible to modulate the Doppler signal to account for the breathing of the LISA constellation but in the following experiments, we will always use a constant Doppler shift. The GW signal can be arbitrarily generated using the on-board processor or the GW data can be uploaded to the EPD unit from the data-processing computer before the delay process is begun. Once the GW, $f_{\text{GW}}(t)$, and Doppler, f_{Dop} , information is packed along with the time-interpolated frequency data, again, as shown in Figure 6-4, the information is added together, integrated to generate the phase information, and generated using the NCO/DAC output described above.

Zero-Delay EPD Unit (Frequency Control Filtering).

Bypassing the Pentek 4205 data-storage and, instead, filtering and transmitting the PM generated data directly to the NCO, we can design high-speed frequency control filters for heterodyne locking, phase locking, and arm-locking experiments. The 60-bit phasemeter frequency data, $f_{\text{PM}}[n]$, is passed through a digital fixed point finite impulse response (FIR) filter; the filtered data can be reconstructed by an NCO with less than a 1 ms delay^2 and used to control the laser frequency. For more detail on these filtering and locking methods, refer to [54] and chapter 6.3.1.

² Optimal performance results in a $\sim 0.06 \text{ ms}$ filter delay. A first order approximation results in a 17 kHz feed-back bandwidth.

6.2.2 Verification

The EPD unit's noise can be written in terms of the input-frequency data, $f_{in}(t)$, the delay, τ , and the sampling ($\phi_{\text{Clk,ADC}}(t)$) and regeneration ($\phi_{\text{Clk,DAC}}(t)$) clocks³ as:

$$\begin{aligned} \phi_{\text{EPD}}(t) &= \phi_{in}(t - \tau(t)) + h_{\text{GW}}(t) \\ &+ \frac{f_{in} \pm f_{\text{Dop}}}{f_{\text{Clk}}} \phi_{\text{DAC,Clk}}(t) - \frac{f_{in}}{f_{\text{Clk}}} \phi_{\text{ADC,Clk}}(t - \tau(t)) \end{aligned} \quad (6-6)$$

from which we can see the clock noise terms coupling into the measurement. Interestingly, these clock noise terms take the same form as those described in (3-70) and (4-3). In this way, the EPD unit produces the differential clock noise terms which cancel in (3-70) and would normally need to be accounted for by clock noise transfers.

Testing the EPD performance, we use a VCO signal as a phase noise source and measure the original VCO and EPD-delayed VCO signals with phasemeters. This produces two signals of the form:

$$\phi_{\text{VCO,PM}}(t) = \phi_{\text{VCO}}(t) - \frac{f_{\text{VCO}}}{f_{\text{Clk}}} \phi_{\text{PM,Clk}}(t), \quad (6-7)$$

$$\begin{aligned} \phi_{\text{VCO,EPD,PM}}(t) &= \phi_{\text{VCO}}(t - \tau(t)) + h_{\text{GW}}(t) + \frac{f_{\text{VCO}} \pm f_{\text{Dop}}}{f_{\text{Clk}}} \phi_{\text{DAC,Clk}}(t) \\ &- \frac{f_{\text{VCO}}}{f_{\text{Clk}}} \phi_{\text{ADC,Clk}}(t - \tau(t)) - \frac{f_{\text{VCO}} \pm f_{\text{Dop}}}{f_{\text{Clk}}} \phi_{\text{PM,Clk}}(t). \end{aligned} \quad (6-8)$$

Time shifting the phasemeter measurement and subtracting it from the EPD measurement we obtain a differential result given by:

$$\Delta\phi_{\text{EPD}}(t) = \phi_{\text{VCO,EPD,PM}}(t) - \phi_{\text{VCO,PM}}(t - \tau) \quad (6-9)$$

$$\begin{aligned} &= h_{\text{GW}}(t) + \frac{f_{\text{VCO}} \pm f_{\text{Dop}}}{f_{\text{Clk}}} (\phi_{\text{DAC,Clk}}(t) - \phi_{\text{PM,Clk}}(t)) \\ &- \frac{f_{\text{VCO}}}{f_{\text{Clk}}} (\phi_{\text{ADC,Clk}}(t - \tau(t)) - \phi_{\text{PM,Clk}}(t - \tau(t))). \end{aligned} \quad (6-10)$$

³ Although these are generally the same source, they may have non-common terms which do not cancel.

If we assume that the clock used to drive the EPD input ADC and output DAC are based on the same source, $\phi_{\text{EPD,Clk}}(t)$, we can write the expected noise level as:

$$\Delta\tilde{\phi}_{\text{EPD}}(t) = \tilde{h}_{\text{GW}}(t) + \frac{f_{\text{VCO}} |1 - e^{-2\pi i\tau}| \pm f_{\text{Dop}}}{f_{\text{Clk}}} [\tilde{\phi}_{\text{EPD,Clk}}(\omega) - \tilde{\phi}_{\text{PM,Clk}}(\omega)]. \quad (6-11)$$

Thus, we couple in the differential clock noise scaled by the arm transfer function, $|1 - e^{-2\pi i\tau}|$. Taking measurements of this form with independent clock sources, phase-locked clock sources, and split clock sources, and comparing the noise levels to the differentially subtracted EPD measurements as shown in Figure 6-5 we see that the phase noise of the measurement (solid lines) equals the clock noise (dotted lines) scaled by the arm transfer function, $|1 - e^{-2\pi i\tau}|$, with $\tau = 16.6$ s, as expected by (6-11). Obviously we will use the split clock source to drive both the EPD units and PM measurements to reduce this clock noise coupling.

Using a 4 MHz VCO input source and a split clock source we take a long-term EPD measurement to see the over-all noise level of the EPD unit. The results, with and without a 7.2 mHz GW modulation are plotted in Figure 6-6 and compared against the phasemeter noise level. Thus, it is reasonable to say that the EPD unit reproduces the inter-SC light travel time delay to within a $10 \mu\text{Cycle}/\sqrt{\text{Hz}}$ accuracy⁴.

Although the EPD unit meets the requirement, we must check to see how the clock noise sources couple into a heterodyned differential arm measurement. To reproduce the sensor signals described in (3-72) or (3-74) we take the EPD delayed signal, (6-6), and electronically mix it with the same VCO used as the input to the EPD unit. The

⁴ The minimized time-delay is found using the methods described in Chapters. 4.4.2.1 and 4.4.2.2

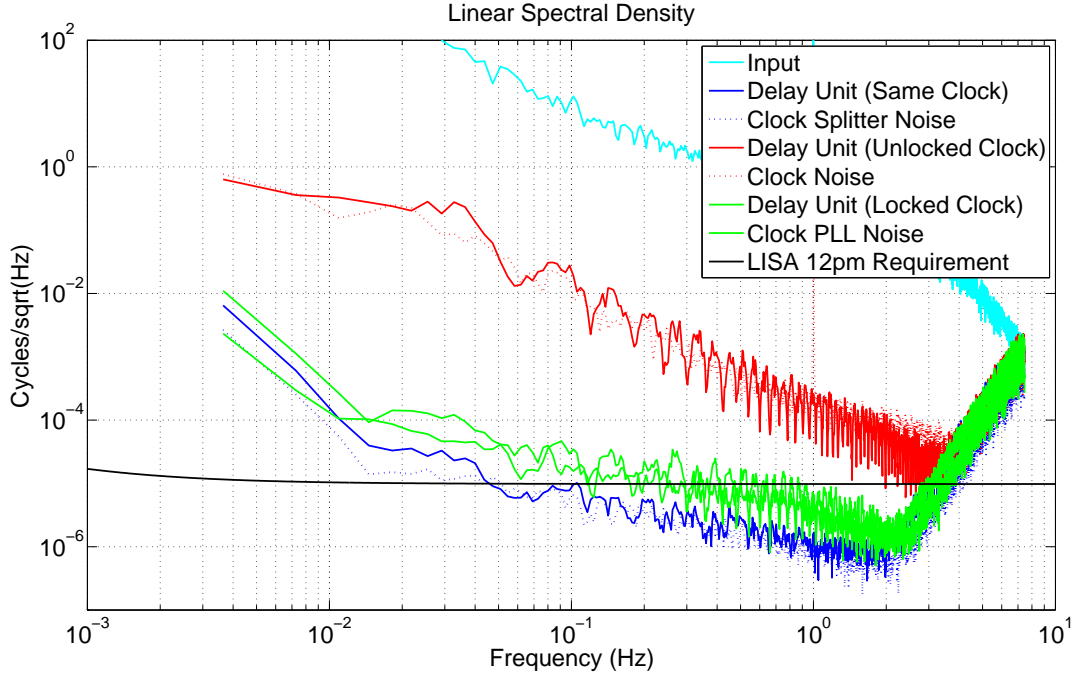


Figure 6-5. Noise limitations of the EPD unit: The differential clock noise between the EPD unit and the phasemeter used to verify the EPD noise limits the measured performance derived in (6–11) for $f_{Dop} = 0$. The clock noise (dotted lines) for the three different cases, (1) free-running, unlocked clocks (2) phase locked clocks, and (3) electronically split clocks are estimated by taking a differential measurement of the same 1 MHz VCO source using different clock sources. The EPD noise scales with this differential clock noise multiplied by the delayed-comparison (or sensor) transfer function, $|1 - e^{-2\pi i \tau}|$, as expected.

mixed output of the prompt and delayed signals takes the form⁵ :

$$\begin{aligned}
 \Delta\phi_{Arm}(t) &= \phi_{VCO}(t) - \phi_{EPD}(t) & (6-12) \\
 &= \phi_{VCO}(t) - \phi_{VCO}(t - \tau(t)) - h_{GW}(t) \\
 &\quad - \frac{f_{VCO} - f_{Dop}}{f_{Clk}} \phi_{DAC,Clk}(t) + \frac{f_{VCO}}{f_{Clk}} \phi_{ADC,Clk}(t - \tau(t))
 \end{aligned}$$

⁵ We assume the Doppler shift is negative in this case.

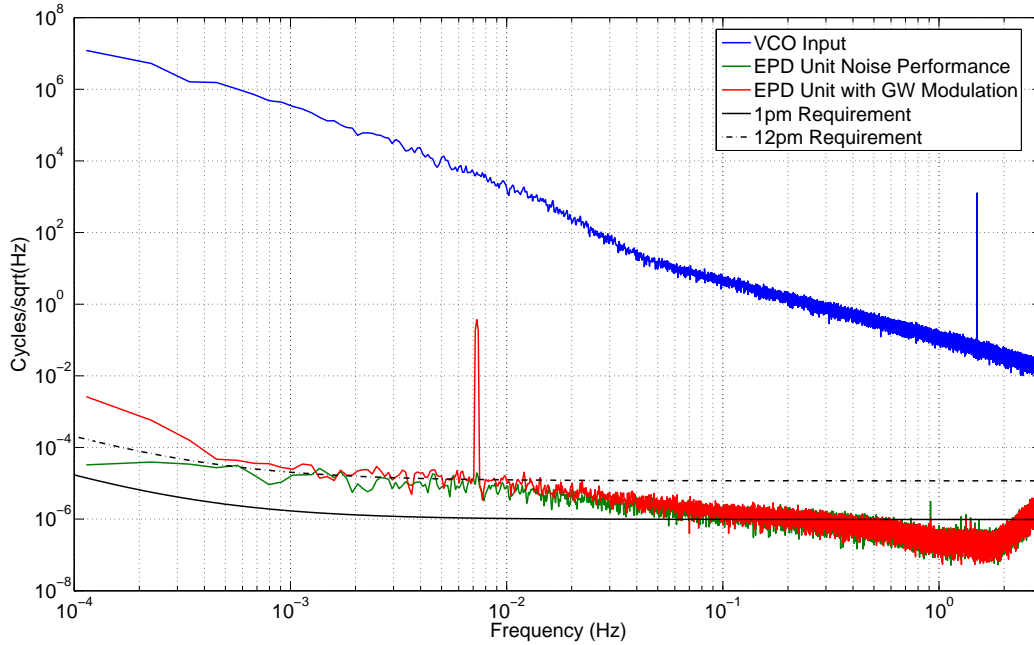


Figure 6-6. EPD Unit's phase-noise transmission accuracy: When using the same clock source for the EPD sampling, EPD regeneration and PM measurement systems, the common clock noise terms cancel to within the accuracy of the clock distribution and the EPD unit results in the plotted transmission replication accuracy. A 7.2 mHz GW modulation is added to one of the measurements to verify that the $h_{GW}(t)$ terms in (6-11) do not cancel.

Measuring this with a phasemeter:

$$\begin{aligned} \Delta\phi_{\text{Arm,PM}}(t) = & \phi_{\text{VCO}}(t) - \phi_{\text{VCO}}(t - \tau(t)) - h_{\text{GW}}(t) \\ & - \frac{f_{\text{VCO}} - f_{\text{Dop}}}{f_{\text{Clk}}} \phi_{\text{DAC,Clk}}(t) + \frac{f_{\text{VCO}}}{f_{\text{Clk}}} \phi_{\text{ADC,Clk}}(t - \tau(t)) \\ & - \frac{f_{\text{Dop}}}{f_{\text{Clk}}} \phi_{\text{PM,Clk}}(t). \end{aligned} \quad (6-13)$$

which, reduces in the case where $\phi_{\text{PM,Clk}}(t) = \phi_{\text{DAC,Clk}}(t) = \phi_{\text{ADC,Clk}}(t)$ to:

$$\begin{aligned} \Delta\phi_{\text{Arm,PM}}(t) = & \phi_{\text{VCO}}(t) - \phi_{\text{VCO}}(t - \tau(t)) - h_{\text{GW}}(t) \\ & - \frac{f_{\text{VCO}}}{f_{\text{Clk}}} (\phi_{\text{DAC,Clk}}(t) + \phi_{\text{ADC,Clk}}(t - \tau(t))). \end{aligned} \quad (6-14)$$

where we have left $\phi_{\text{DAC,Clk}}(t)$ and $\phi_{\text{ADC,Clk}}(t)$ shown explicitly with which we can compare these directly to (3-72) and (3-74). Again, this measured EPD unit signal

acquires the same input and clock noise scaling as the clock noise corrected inter-SC observables, (3–70).

6.2.2.1 Time-changing Time Delay

To verify the capabilities of the electronic replication of the time-changing delay, we take the prompt measurement of a VCO signal and compare it with the an EPD-processed signal as described in the previous section. The experimental delay is set to $\tau(t) = 16.6 \text{ s} + 100t \text{ ns/s}$. If we simply minimize the noise without considering the time-changing delay, we will obtain the average delay for the measurement as the calculated offset delay time. The difference between the signals as plotted in Figure 6-7 shows that the of the difference is in-phase with the prompt signal at the beginning of the measurement and out-of-phase with the prompt signal near the end of the measurement. This obviously limits the noise cancellation capabilities as shown explicitly in Figure 6-8

Accounting for the time-changing delay, we perform a the fractional delay interpolation of the input signal using the methods defined in chapter 4.1.4 and 4.4.2.2. Once the prompt data has been correctly interpolated we subtract it from the EPD processed signal. Comparing the results with the base-line EPD noise performance as shown in Figure 6-8, we see that once the time-changing delay has been accounted for, the noise performance matches the EPD noise level.

6.2.2.2 Gravitational Wave Injection

To test the GW injection accuracy we inject a frequency modulation with a power-function increasing frequency enveloped by a Gaussian amplitude modulation given by:

$$f_{\text{GW}}(t) = \sin \left(\frac{2\pi(10^{-3} \text{ Hz})t}{\left(1 - \frac{t}{3.7*10^4 \text{ s}}\right)^{3/8}} \right) e^{-\frac{(t-t_0)^2}{2*10^7 \text{ s}^2}} \quad (6-15)$$

Granted, this is not a realistic GW modulation source but, none the less, it provides a test of the ability to reconstruct the signals injected by the EPD unit. Using a VCO

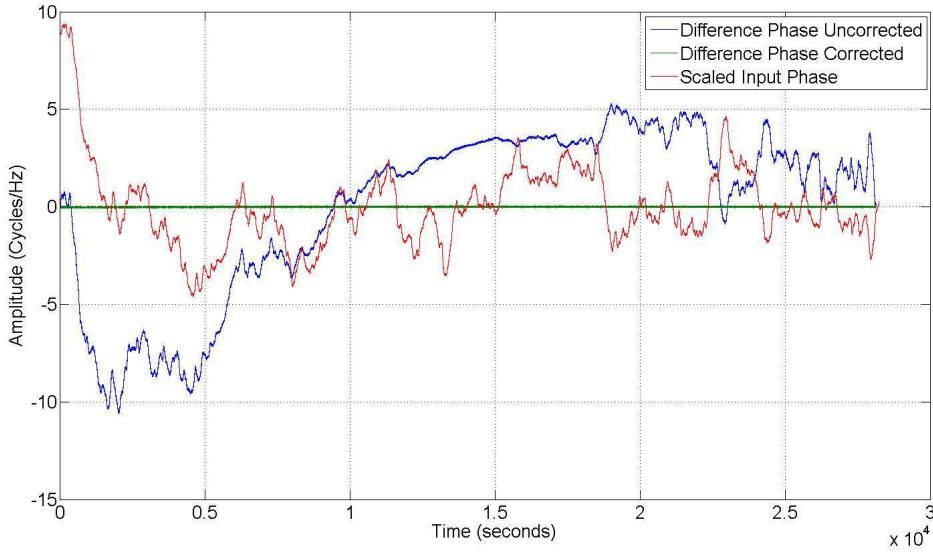


Figure 6-7. Time series of the interpolated delay difference: The time-series of the input signal subtracted from the time-delay interpolated signal shows that, at first, the differential phase leads the input phase due to a small positive timing error but towards the end of the measurement the differential phase lags the input phase due to a small negative timing error causing an apparent phase inversion. Once the time-changing delay has been accounted for the differential phase cancels to the EPD precision floor.

source we time-shift the EPD delayed signal and subtract it from the post-processed time-shifted measurement of the prompt signal. The time-series of the injected input modulation, the measured GW modulation, and their difference is plotted in Figure 6-9. From the spectrum of these measurements, we see that the noise level of the GW injected EPD unit matches the base-line EPD noise level once the expected GW signal has been removed from the EPD processed measurement.

Another GW source of concern is the low-frequency binary confusion noise background. Estimates of this background noise vary [46, 103] such that we will generally estimate the binary confusion noise level as:

$$\tilde{h}_{\text{GW-Background}}(\omega) \simeq \frac{.01}{\frac{s}{2\pi} + .001} \frac{\text{mHz}}{\sqrt{\text{Hz}}}. \quad (6-16)$$

This is plotted explicitly in Figure 8-1.

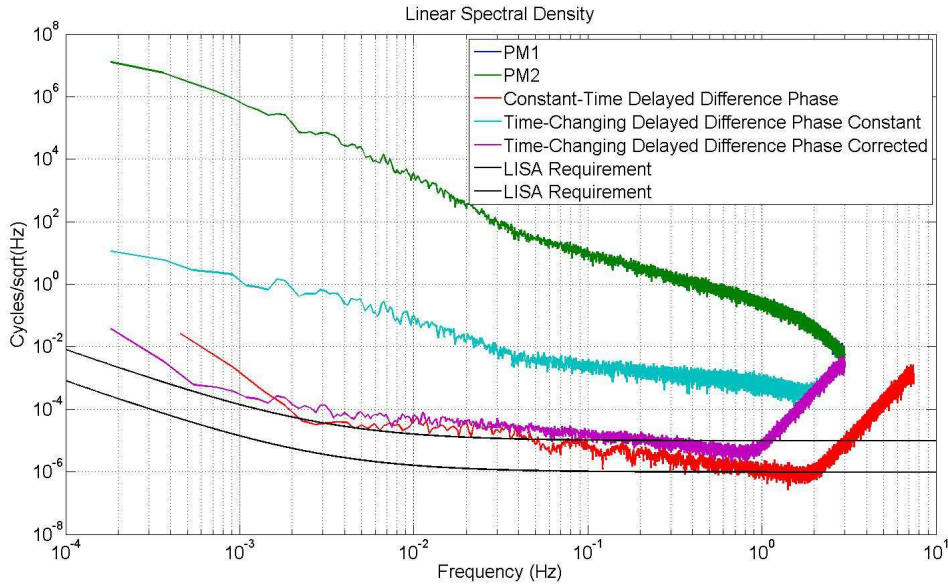


Figure 6-8. Interpolated delay differential measurements and corrections: The time-changing delay causes a spectral noise floor which scales with the delay error $\delta\tau = \beta T/2$ where T is the measurement time as defined by (4–6). If we time-scale the measured input signal using fractional delay interpolation and subtract it from the EPD processed time-changing delay signal, we account for the additional delay error and cancel the noise to within the EPD unit’s noise floor precision.

6.3 UFLIS Simulations

Using the laser bench-top, EPD unit, control filters, and phasemeter measurements, we are able to perform many LISA-like tests of the interferometry system including advanced arm-locking and TDI simulations. Although a more refined and in-depth analysis of the arm-locking tests and results can be found in [54], we present a first test of the UFLIS electronics by performing a single-arm arm-locking experiment as outlined in chapter 4.2.2. Next we outline the time-delay interferometry simulations and set up the TDI characteristics which are to be explored in the next chapter.

6.3.1 Arm-Locking Stabilization

The UFLIS electronic components were first used to test the single arm-locking methods being presented in [53, 77]. Since a much more in-depth analysis has been presented since these simulations were performed we will briefly discuss the

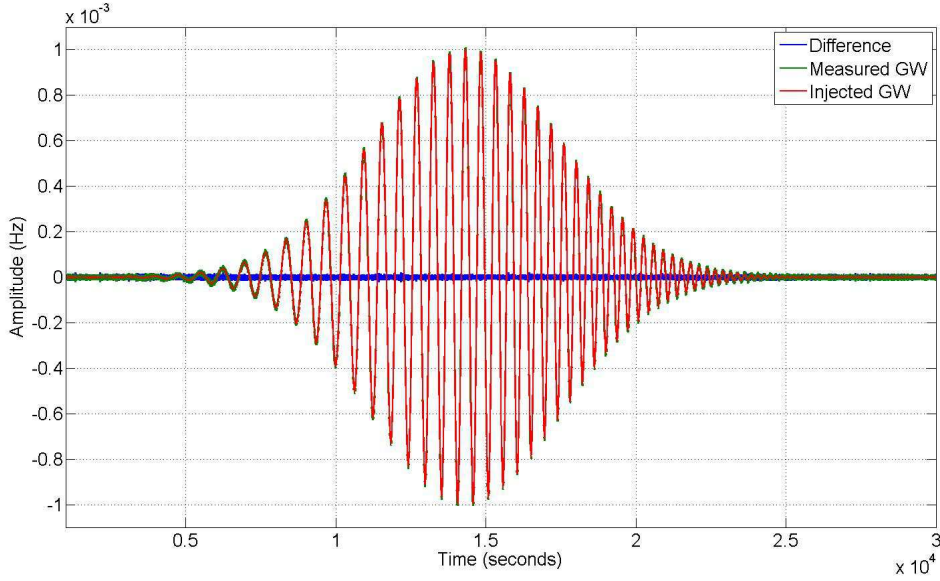


Figure 6-9. Time series of an arbitrary gravitational wave: The gravitational wave modulation defined by (6–15) is injected into the EPD unit and extracted with a differential input measurement using the appropriate time-shift to cancel the noise. The extracted signal and the theoretically injected signal agree well; subtracting the measured GW signal from the theoretical signal, we completely cancel the injected GW signal to within the EPD unit precision.

experimental setup, the results obtained, and the un-anticipated limitations. The single arm-locking experiment is presented at the top of Figure 6-11. The PDH pre-stabilized Laser_{L1} is heterodyned with Laser_{PL} which is offset phase-locked to Laser_{RL}. The frequency off-set in the phase-lock is driven by an oscillator modulated with the arm-locking control signal. The arm-locking control signal is generated by taking the Laser_{L1}/Laser_{PL} beat-note and forming the sensor signals as defined in (3–72) using an EPD unit with a Doppler offset, f_{Dop} , and time delay of $\tau = 1$ s. This sensor signal is filtered with the frequency feed-back controller described in chapter 6.2.1. The feed-back filter is defined in terms of the frequency as:

$$T_{AL}(f) = \left[\frac{a_4}{f^4} + \frac{a_3}{f^3} + \frac{a_2}{f^2} + \frac{a_1}{f} \right] + \frac{a_0}{\sqrt{f}}. \quad (6-17)$$

The $f^{1/2}$ provides the an additional phase advance in the region of the locking frequency. This is because the sensor signal's phase swings between $-\pi$ and π with respect to the

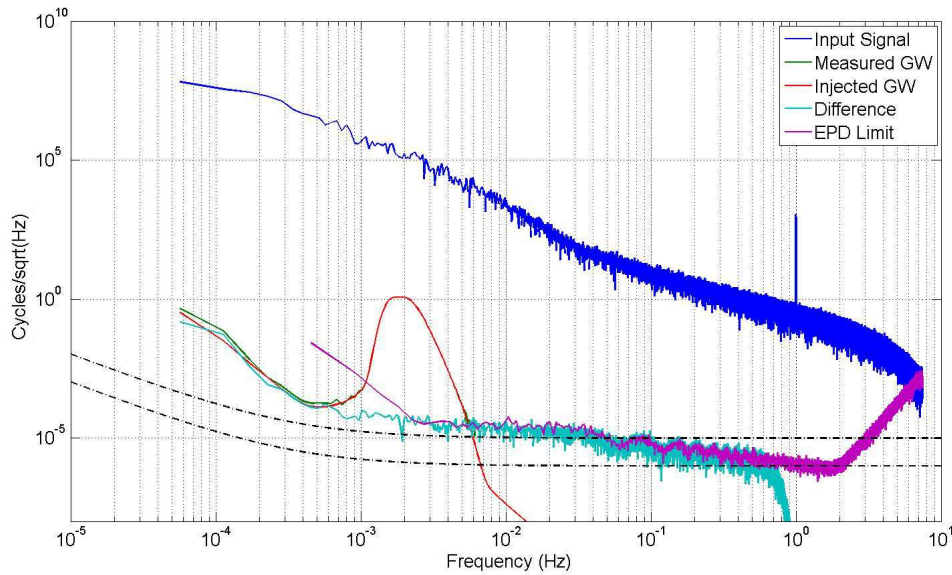


Figure 6-10. Spectral correction of an arbitrary gravitational wave: The EPD unit with a VCO input is injected with the GW modulation defined by (6–15); the EPD output and input are measured with phasemeter and then fractional delay filtered to cancel the common VCO noise. The measured GW signal (green) matches the spectral density of the injected wave-form (red) exactly. Subtracting out the GW modulation (cyan) we are left with a noise level which equals the EPD precision (purple). The GW modulated curve (cyan) is low-pass filtered so that the GW modulation is apparent in the time-series (Figure. 6-9)

input laser phase at frequencies above the first zero, $1/\tau$. Meanwhile, the low-frequency integrators kick in at frequencies below the first zero, $1/\tau$, and scale with the coefficients such that $a_4 < a_3 < a_2 < a_1$ to maintain locking stability. The results, shown in Figure 6-11, show an additional five orders of magnitude noise suppression of the laser frequency noise at 10 mHz and significantly reduced frequency fluctuations in the time-series. The low-frequency stabilization limit is defined by the accuracy of the control electronics [54].

Advanced Arm-Locking Controllers.

The primary complication with achieving the locking condition described in the previous chapter was the user-defined Doppler and phasemeter frequencies. Unless these values were exactly equal the experiment encountered an integration of the

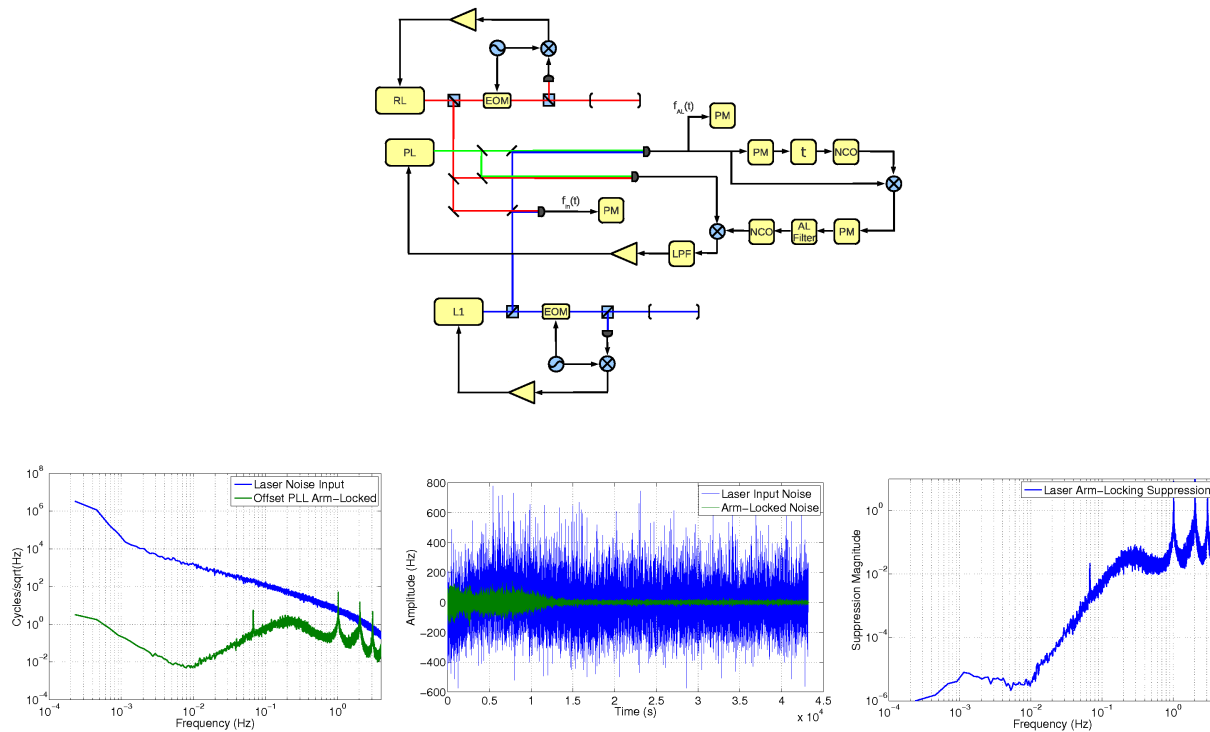


Figure 6-11. Long-arm hardware-based single-arm-locking experiment: The model at the top depicts the experimental setup of the first hardware based heterodyne single-arm-locking experiment. The RL/L1 beatnote provides a measure of the 'input' noise while the PL (phase-locked)/RL beatnote is stabilized according to the proposed arm-locking techniques [53]. The low-frequency noise is suppressed by 5 orders of magnitude at frequencies below 10 mHz. The measurement is limited by quantization noise in the EPD unit. Refer to [54] for more information on the details and advancements to this simulation in performing LISA-like tests of the arm-locking capabilities. These simulations provided a first test of the UFLIS/DSP system's capabilities to perform LISA-like simulations.

frequency error which caused system instability. This indicated a frequency pulling effect which has since been described in [79] and [84].

Since the single arm-locking experiment was performed, more in-depth experiments have been conducted by the author and colleagues. A detailed presentation of the single arm-locking experiment and results can be found in [78]. The same arm-locking methods were used in combination with a PDH side-band locking scheme to prove the capabilities of laser frequency control in LISA [83]. These components were also used to

Table 6-1. TDI experimental characteristics: Five 40000 s experiments are performed with increasingly more complicated, yet more LISA-like, characteristics. The transponder experiment provides us with a baseline measure of the experimental setup's noise performance. The 'dynamic' experiments demonstrate the ability to determine and account for the time-changing delay-times. The 'LISA-like' experiment proves the ability to remove independent SC noise sources and constrain one-way delay times. Finally, the confusion noise experiment verifies that the TDI-ranging capability will not be limited by low-frequency LISA noise sources.

Simulation Name	s_{1r}	Inter-SC Velocity β (ns/s)	Injected GW Signal
Static Transponder (2-Way)	$s_{1r} \simeq 0$	$\beta_2 = 0$ $\beta_3 = 0$	6.227 mHz Binary
Dynamic Transponder (2-Way)	$s_{1r} \simeq 0$	$\beta_2 = -100$ $\beta_3 = +150$	6.227 mHz Binary
Static LISA-like (4-Way)	$s_{1r} = \phi_{PLLr}$ $\simeq (1.0/f)\text{mCycle}/\sqrt{\text{Hz}}$	$\beta_2 = 0$ $\beta_3 = 0$	6.227 mHz Binary
Dynamic LISA-like (4-Way)	$s_{1r} = \phi_{PLLr}$ $\simeq (1.0/f)\text{mCycle}/\sqrt{\text{Hz}}$	$\beta_2 = -100$ $\beta_3 = +150$	6.227 mHz Binary
Confusion-Noise (4-Way)	$s_{1r} = \phi_{PLLr}$ $\simeq (1.0/f)\text{mCycle}/\sqrt{\text{Hz}}$	$\beta_2 = -100$ $\beta_3 = +150$	6.227 mHz Binary + CN

verify the dual and dual-modified arm-locking schemes presented in [79] and validated in [84] and [81].

6.3.2 TDI Simulation Outline

The TDI measurements the following sections are generated using the 2-4 sensor observables, s_{1r} and/or s_{s1} , defined in (3-70) over a 10-12 hour simulations. The five TDI experiments we will perform are outlined in Table. 6-1. Each stage will introduce a new noise source into the measurement such that we can decipher the noise couplings based on the results of each simulation.

We begin with a 'static transponder' measurement in which we will use constant, but unequal, $\tau_{2/2} \neq \tau_{33}$ ⁶, arm-lengths to test the TDI- $X_{1,0}$ combinations. The transponder

⁶ $[\tau_{2'} \simeq \tau_{2'} \simeq 16.55 \text{ s}] \neq [\tau_{3'} \simeq \tau_3 \simeq 16.75 \text{ s}]$

measurements, as shown in Figure 7-1, will simulate LISA in a noise-less far-SC configuration, as though the 'outgoing' master laser fields are reflected perfectly off the far SC and where $s_{1r} = 0$. The ranging methods described in chapter 4.4.2.2 are used to calculate the round-trip delay time⁷ and cancel the laser phase noise. Next, we introduce time-changing arm-lengths with the β_2 and β_3 values outlined in Table. 6-1^{8 9} to validate the capabilities of the TDI- $X_{2,0}$ combinations through 'dynamic' simulations.

Next, we introduce the noise coupling from the far SC signals, s_{1r} , by phase locking the lasers on the far SC to the delayed 'out-going' laser fields and measuring the resulting PD sensor signals as shown in the experimental model (Figure 7-7)¹⁰ Again, we repeat the 'static' and 'dynamic' simulations, including the additional laser phase noise signals, s_{1r} , in the combinations; meanwhile, we are able to test the ranging-accuracies of the one-way delay times using the methods described in chapter 4.4.2.2. Finally, we introduce a low-frequency confusion-noise background signal to investigate the limitations, if any, of this additional low-frequency noise on the ranging accuracies.

⁷ The one-way delay times are un-defined in these simulations.

⁸ $\beta_2 = -100.0\text{ns/s ns/s}(v_2 = -30.0\text{ m/s})$; $\beta_3 = +150.0\text{ns/s ns/s}(v_2 = 45.0\text{ m/s})$

⁹ $|\beta_2 - \beta_3| = 250.0\text{ ns/s}$

¹⁰ The far SC sensor signals, s_{1r} , are used as the input signals for phase-locking the far SC's lasers such that the sensor signal is equal to the PLL's error signal, ϕ_{PLLr} , as shown in Figure 7-7 and Table. 6-1.

CHAPTER 7 TIME-DELAY INTERFEROMETRY SIMULATIONS

The following chapter present the details and results of the experiments described in chapter 6.3.2. In all of these measurements we will inject a 6.277 mHz GW binary with a strain amplitude of $4.35 \times 10^{-20} \text{ m/m}^1$ to simulate the RXJ0806.3+1527 binary described in the verification binary table (Table 2-1). Although this strain amplitude is a factor of 100 larger than what is expected in a actual LISA-like detection, it is used to prove the TDI combinations' ability to cancel the laser phase noise without canceling the modulated GW signals.

7.1 Transponder TDI Simulations

We first establish a baseline ranging and measurement precision with static arm-lengths ($\beta = 0$) and without noise being introduced by the 'far' SC. Referring to the experimental model shown in Figure 7-1, we take the $\text{Laser}_{\text{Ref}}/\text{Laser}_1$ beatnote and use it as the input for the TDI simulator. The PD beatnote is electronically mixed with a frequency modulation $f_{\text{Mod}}(t) = A \sin([\omega_o + 500 \sin(2 * \pi * t)]t)$ to apply the ranging tone² and to shift the laser beatnote to a PM measurable frequency, in this case, $\omega_{\text{PD}} - \omega_o = 7 \text{ MHz}$. This mixed output is electronically split, measured with a phasemeter, and processed by EPD units to simulate the 'out-going' inter-SC laser field transfer. Constant EPD delays of $\tau_2(0) \simeq \tau_{2'}(0) \simeq 16.75 \text{ s}$ and $\tau_3(0) \simeq \tau_{3'}(0) = 16.55 \text{ s}$ are programmed to the EPD units while Doppler shifts of $f_{\text{Dop}2} = +3 \text{ MHz}$ and $f_{\text{Dop}3} = -2 \text{ MHz}$ are applied to the frequency signals. The delayed 'out-going' signals are directly connected to another EPD unit to simulate the 'returning' inter-SC laser field transfer. This noise-less transfer between the EPD units, in a LISA model for example, will behave as though the laser

¹ $\nu(t) = 2 \sin(2\pi(6.227 \text{ mHz})t) \mu\text{Hz}$
 $\delta\phi_{\text{GW}}(t) \simeq 4\nu(t)/(2\pi(6.227 \text{ mHz})) = 204.4 \mu\text{cyc/Hz}$
 $h_{\text{GW}}(t) = \delta\phi_{\text{GW}}(t)\lambda/L = 4.3 \times 10^{-20} \text{ Hz}^{-1}$

² $f_{\text{mod}} = 1 \text{ Hz}$, $A_{\text{mod}} = 500 \text{ Hz}$

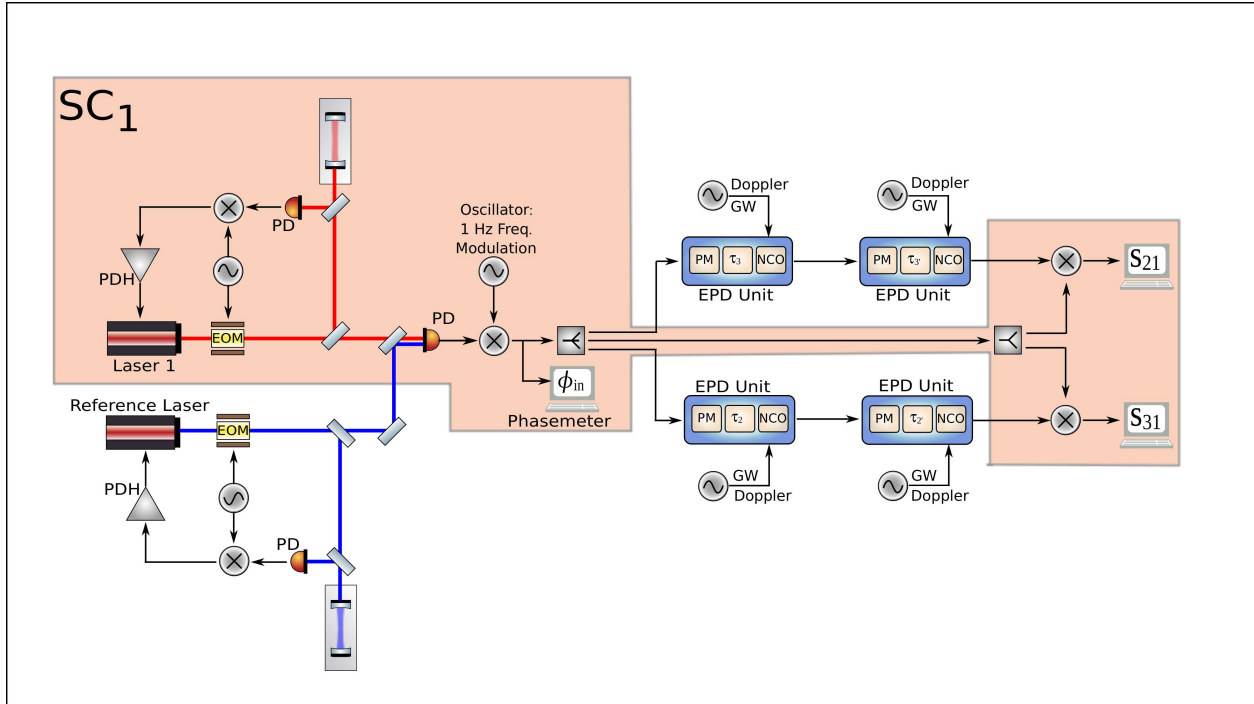


Figure 7-1. Model of the TDI-Transponder experimental benchtop: This TDI-Transponder model shows how the individual pre-stabilized laser fields are combined to form the input noise signal and how this signal is processed by the EPD units to replicate a LISA-like inter-SC laser link and produce the s_{sr} observables []. The input PD beatnote is demodulated to a PM-measurable frequency using an oscillator with a 1 Hz phase modulation. The PM-read-out signals are delayed by the $\tau_{2'}(t)$ and $\tau_{3'}(t)$ inter-SC light travel times, added with GW modulations, and regenerated with a Doppler offset. In these transponder measurements the delayed signals are immediately injected into the 'return' trip EPD units $\tau_2(t)$ and $\tau_3(t)$ as though the laser fields were reflected off mirrors at the far SC. GW modulations and Doppler offsets are added to the return-trip EPD units also. The round-trip delay signals are electronically mixed with the local $Laser_{Ref}/Laser_1$ beatnote to produce the s_{21} and s_{31} sensor signals.

fields were reflected off mirrors on the far SC such that the far sensor observables are signal-free, $s_{1r} = 0$, in the TDI combinations. Finally, the 'return' field EPD simulated output is heterodyned³ with the local laser phase, in this case the $Laser_{Ref}/Laser_1$

³ Electronically mixed

beatnote, to produce the local s_{21} , s_{31} PD observables. The PD signals are measured for 40000 s by phasemeters with the 60-bit precision at a 14.9 Hz data-rate.

We then introduce the time-changing arm-lengths defined in Table 6-1 such that the inter-SC time delays take the form defined in (4-39). Despite this definition, as we described in chapter 4.4, without any noise being introduced at the far SC we will only be able to constrain the round-trip delay times found in, (3-72) and (3-74) defined explicitly as:

$$\tau_{2'2}(t) = [(1 - \beta_2)((1 - \beta_{2'}) (t - \tau_{2'}(0)) - \tau_2(0))] \quad (7-1)$$

$$\tau_{33'}(t) = [(1 - \beta_{3'})((1 - \beta_3)(t - \tau_3(0)) - \tau_{2'}(0))]. \quad (7-2)$$

Fortunately, at the same time, this means we only have to scan over the 2-dimensional, $\tau_{2'2}$, $\tau_{33'}$, basis. We will also verify the TDI 1.0 limitations defined in chapter 4.3.3.2.

7.1.1 Static-Arm Transponder Simulation

Utilizing the PD measurements of s_{21} and s_{31} , the 40000 s data-set is broken into 40, 1000 s segments. The iterative formation of the TDI combination for each segment minimizes attempts to minimize the ranging tone and calculate the time-delay functions through linear regression as described in chapter 4.4.2.2 and shown in Figure 4-3. The first and only iteration produces a slope error (constraint on the arm-length velocities), of $|2\beta| < 50$ fs/s and a variance (round-trip ranging accuracy) of less than 0.6 ns (~ 0.18 m) as shown in Table 7-1⁴. In this experiment, we note that the TDI- X_1 combination's ranging-tone minimization produces the same estimation to within the measurement error of the round-trip light travel time as the TDI- X_2 combination. If $\beta \neq 0$, the different TDI combinations would produce different estimations since the ranging tone minimization using the TDI- X_1 combination would be limited by (4-32) and will

⁴ Refer to Figure 7-4 to see the results of the ranging-tone cancellation near the 1 Hz frequency bin.

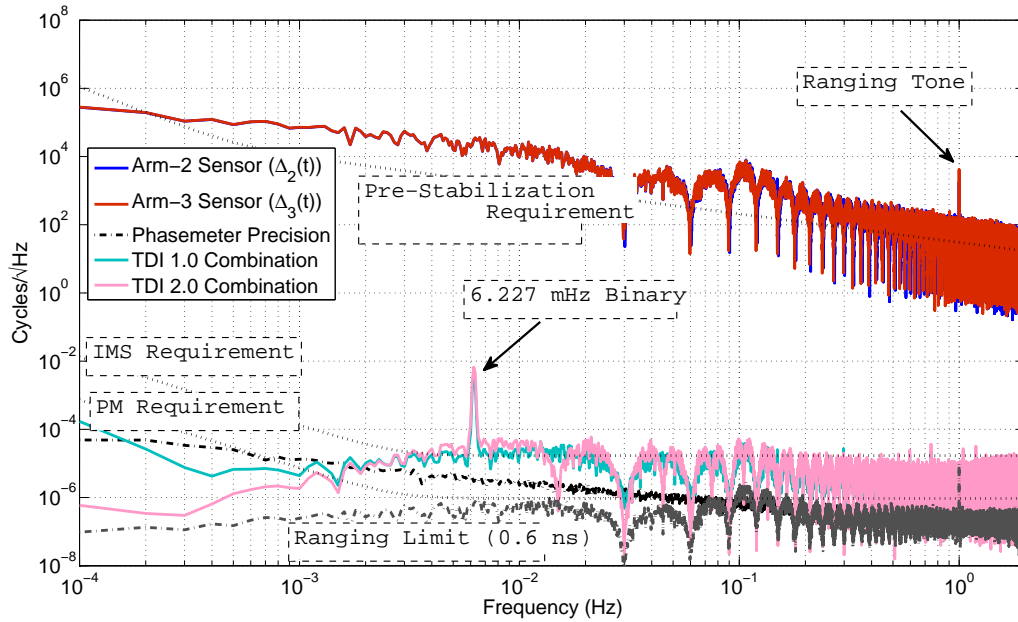


Figure 7-2. Raw static transponder experimental results: The sensor signals ($s_{21}(t) = \Delta_{21}(t)$, $s_{31}(t) = \Delta_{31}(t)$) are used with the ranging values found in Table 7-1 to generate the raw spectra of TDI- X_1 and TDI- X_2 combinations. The phasemeter measurement limitation for the 7 MHz input beatnote frequency is also plotted for comparison. The TDI-combinations drop below the measurement limitation due to the inherent TDI transfer functions but the GW signals are also suppressed by the TDI transfer function. The 6.227 mHz gravitational wave is only revealed once the laser noise has been removed. The expected ranging limitation is almost 2 orders of magnitude below the TDI combinations indicating that all the input laser noise has been suppressed beyond the measurement sensitivity.

estimate the light-travel time-delay as the mean delay for a particular data-segment. Thus, since each of these TDI-ranging methods produce the same result, even in the case where $\beta = 0$, we will use the TDI- $X_{2,0}$ combinations for all TDI-ranging estimations.

Using the ranging-calculated values (Table 7-1) we form the TDI- X_1 and TDI- X_2 combinations for the entire data-set. The linear spectral density of the TDI combinations, as plotted in Figure 7-2, show the laser noise cancellation and reveal the phase-modulated GW binary at 6.227 mHz. The expected ranging limitation based on the 0.6 ns variance calculated above and evaluated with (4-6) is well below the measurement sensitivity. We can also see the difference between the 8-pulse and 16-pulse response

transfer functions of the TDI- X_1 and TDI- X_2 combinations. Rescaling by the average inverse TDI response transfer functions given by:

$$T_{1.0}(s) = \frac{|1 - e^{-\text{stau}_{2'2}}| + |1 - e^{-\text{stau}_{33'}}|}{2} \quad (7-3)$$

$$T_{2.0}(s) = T_{1.0}(s) |1 - e^{-\text{stau}_{2'233'}}| \quad (7-4)$$

we see the TDI- X_1 and TDI- X_2 combinations result in identical effective sensitivities (Figure 7-3), as expected for a static interferometer. From this plot we can also see that both measurements are limited by the EPD unit's phase-transmission precision as was previously plotted in Figure 6-6. From this point forward we will interpret these static TDI- X_1 and TDI- X_2 combinations to represent the baseline precision of the UF-LISA-TDI simulator. We calculate the effective laser suppression magnitude by dividing the input spectrum by the input noise by the re-scaled TDI spectra; from Figure 7-6 we obtain greater than 10^{10} noise cancellation at 1 mHz.

7.1.2 Dynamic-Arm Transponder Simulation

Expanding the simulation characteristics, we include the time-dependent arm-lengths into the experiment with the β -values defined in Table 6-1 resulting in an expected TDI- X_1 limitation as defined by (4-32) with $|\Delta\beta| = 250 \text{ ns/s}$. Initially assuming $\beta = 0$, the 40000 s measurements of the s_{21} and s_{31} signals are broken into 40, 1000 s segments and processed using the methods described in chapter 4.4.2.2. These data segments are used to minimize the ranging tone and calculate the round-trip time-delay offsets, $\tau_{2'2}(0)$ and $\tau_{33'}(0)$, for each segment as shown in Figure 4-3. The linear regression of these time-delay offsets provides a first-order measure of the β to an accuracy of 100 ps/s as shown in Table 7-1. The process also calculates a first order measure of the round-trip time delay with a ranging precision of $< 7.5 \mu\text{s}$ ($\sim 1.7 \text{ km}$) but due to the incorrect $\beta = 0$ assumption, these values tend to equal the average delay for the data-segment. A second iteration improves the β accuracy to 80 fs/s and the ranging precision to $< 5.9 \text{ ns}$ ($\sim 1.8 \text{ m}$) providing a much more accurate measure of

Table 7-1. Transponder TDI-ranging estimation: The method outlined in Figure 4-3 and the experiments described in capters 7.1.1 and 7.1.2 are used to calculate estimates of the inter-SC delay functions, (4-37), and ranging errors. The estimates verify the TDI-ranging capabilities and are used to generate the TDI-combinations for Figures 7-3 and 7-5. The 'return' delay times tend to be longer than the 'outgoing' delay times by 250 ms as a result of internal delays within the DSP system's EPD units.

Iteration	β (Slope)	$\tau_{22'}(0), \tau_{33'}(0)$ (Offset)	$\delta\tau_{22'}, \delta\tau_{33'} (\sigma)$
TDI 1.0			
Transponder			
1 (TDI 1.0)	$2\beta_2 = -44.5 \text{ fs/s} \pm 20.9 \text{ fs/s}$	$\tau_{22'}(0) = 33.55204887148 \text{ s} \pm 0.23 \text{ ns}$	$\delta\tau_{22'} = 0.54 \text{ ns}$
	$2\beta_3 = -46.3 \text{ fs/s} \pm 12.5 \text{ fs/s}$	$\tau_{33'}(0) = 33.15222859583 \text{ s} \pm 0.14 \text{ ns}$	$\delta\tau_{33'} = 0.32 \text{ ns}$
1 (TDI 2.0)	$2\beta_2 = -41.0 \text{ fs/s} \pm 21.2 \text{ fs/s}$	$\tau_{22'}(0) = 33.55204887151 \text{ s} \pm 0.24 \text{ ns}$	$\delta\tau_{22'} = 0.55 \text{ ns}$
	$2\beta_3 = -46.3 \text{ fs/s} \pm 12.7 \text{ fs/s}$	$\tau_{33'}(0) = 33.15222859579 \text{ s} \pm 0.14 \text{ ns}$	$\delta\tau_{33'} = 0.33 \text{ ns}$
TDI 2.0			
Transponder			
1	$2\beta_2 = -200.247 \text{ ns/s} \pm 100 \text{ ps/s}$	$\tau_{22'}(0) = 33.5518847 \text{ s} \pm 2.3 \mu\text{s}$	$\delta\tau_{22'} = 7.5 \mu\text{s}$
	$2\beta_3 = +300.056 \text{ ns/s} \pm 95 \text{ ps/s}$	$\tau_{33'}(0) = 33.1525027 \text{ s} \pm 2.2 \mu\text{s}$	$\delta\tau_{33'} = 7.0 \mu\text{s}$
2	$2\beta_2 = -199.9998668 \text{ ns/s} \pm 80 \text{ fs/s}$	$\tau_{22'}(0) = 33.5519484187 \text{ s} \pm 1.8 \text{ ns}$	$\delta\tau_{22'} = 5.9 \text{ ns}$
	$2\beta_3 = +300.0001130 \text{ ns/s} \pm 23 \text{ fs/s}$	$\tau_{33'}(0) = 33.1523897572 \text{ s} \pm 0.51 \text{ ns}$	$\delta\tau_{33'} = 1.7 \text{ ns}$
3	$2\beta_2 = -200.0000058 \text{ ns/s} \pm 8.9 \text{ fs/s}$	$\tau_{22'}(0) = 33.55194832884 \text{ s} \pm 0.20 \text{ ns}$	$\delta\tau_{22'} = 0.65 \text{ ns}$
	$2\beta_3 = +300.0001361 \text{ ns/s} \pm 4.5 \text{ fs/s}$	$\tau_{33'}(0) = 33.15238977691 \text{ s} \pm 0.10 \text{ ns}$	$\delta\tau_{33'} = 0.33 \text{ ns}$

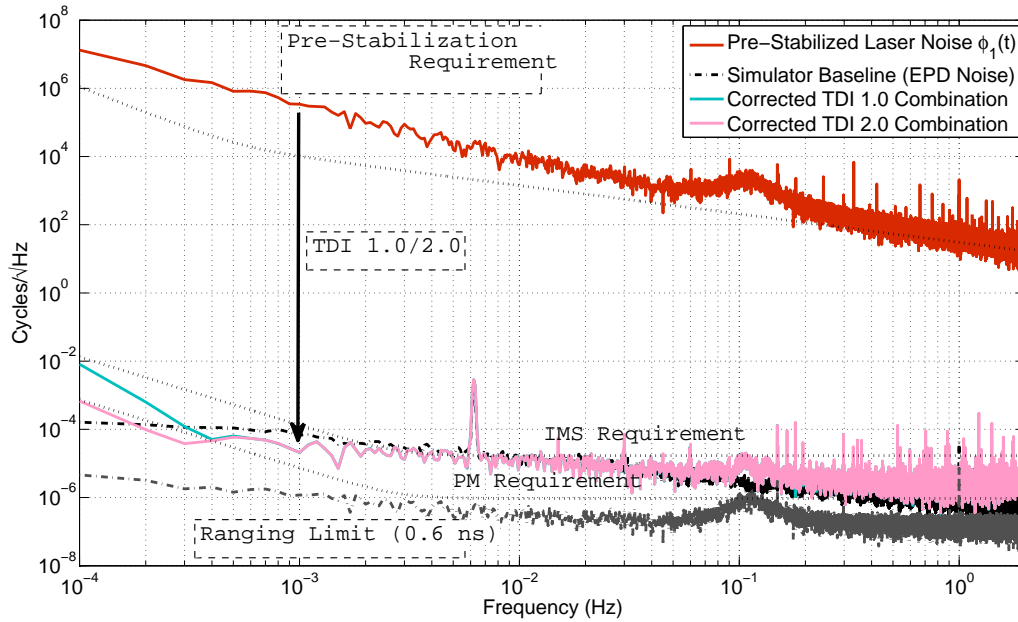


Figure 7-3. Corrected static transponder experimental results: The input signal, $\phi_1(t)$, is plotted along with the corrected TDI- X_1 and TDI- X_2 spectra which have been scaled by the inverse TDI transfer functions (7-3). Both TDI spectra match exactly once the inverse TDI-combination transfer function has been accounted for. The increased laser phase noise around 100 mHz is a result of an over-coupled temperature tracking in the PDH controller which may result in a ranging-limited sensitivity loss near 100 mHz. The EPD unit's phase transmission accuracy is plotted and is identified as the primary TDI simulation limiting noise source. This static TDI-transponder result will act as the simulator's 'baseline' performance for the rest of the chapter. The results meet the $18 \text{ pm}/\sqrt{\text{Hz}}$ IMS requirement (3-5).

the time-dependent arm-lengths, $\tau_{2'2}(t)$ and $\tau_{33'}(t)$. The final iteration optimizes the β precision to 8.9 fs/s and the ranging precision to less than 0.65 ns ($\sim 0.2 \text{ m}$). (Table 7-1)

Applying the calculated round-trip functional values from the third iteration of the ranging procedure, the entire data-set is used to produce the linear power spectral density for the TDI- X_1 and TDI- X_2 combinations as plotted in Figure 7-5. The TDI- X_1 combination is limited, as anticipated, by (4-32) with $\tau \simeq 16.6 \text{ s}$ and $|\Delta\beta| = 250 \text{ ns/s}$. The TDI- X_2 combination's correction terms account for this dynamic arm-length limitation and remove the velocity dependent laser phase noise resulting in a sensitivity equal to the experiment's baseline noise. This result meets the IMS requirement defined by the

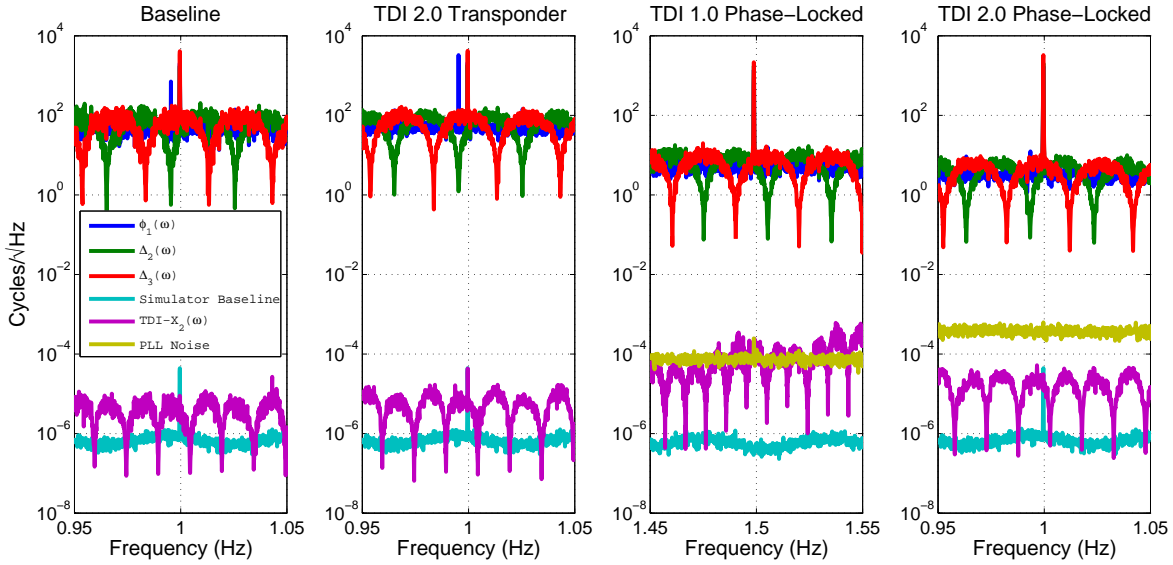


Figure 7-4. Ranging tone cancellation spectral results: The ranging tone modulated input are plotted along with the resulting TDI- X_2 combinations for the four primary experiments (Table 6-1). The decreased accuracy of the Δ_2 arm as compared to the Δ_3 arm in Table 7-1 is likely due to the proximity of the nearest arm zero. Note that the ranging tone for the TDI 1.0 with phase-locked lasers simulation is at 1.5 Hz instead of 1 Hz which results in a reduced one-way ranging accuracy (Table 7-2) from the reduced PLL noise.

LISA mission concept design. (Table 3-1) The 0.65 ns (~ 0.2 m) ranging precision, as calculated in Table 7-1 and plotted in Figure 7-5, is not expected to be a limiting noise source.

The TDI- X_1 's noise suppression (Figure 7-6) equals the theoretical inter-SC velocity dependent limit (4-32) while the TDI- X_2 's noise suppression equals that of the simulator's baseline suppression characteristics.

7.2 LISA-like (Master-Slave Phase Locked Laser) TDI Simulations

At this point, we include the phase-locking and transmission of the $L_{\text{Laser}_{2/3}}$ signals on the far spacecraft as shown in Figure 7-7. Thus, this experiment will generate and measure all four s_{SR} ⁵ beatnote observables as defined in (3-70). The two far sensor

⁵ Two local-SC measurements: s_{21}, s_{31} ; Two far-SC measurements: s_{12}, s_{13}

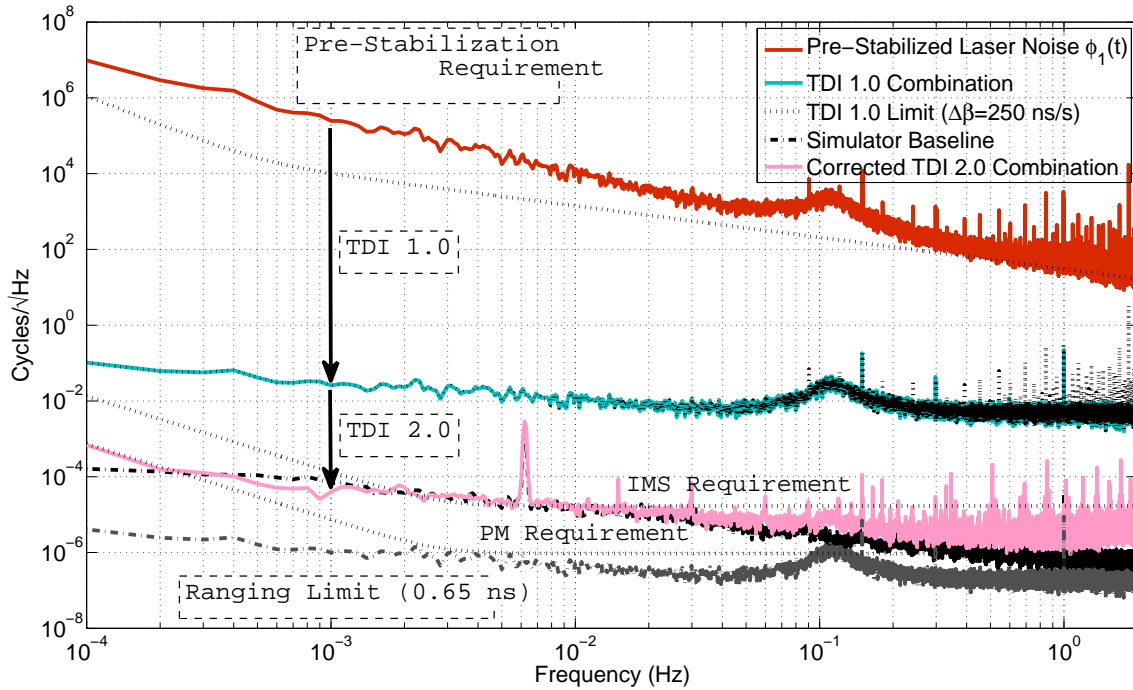


Figure 7-5. Dynamic transponder experimental results: The suppression of the TDI X_1 combination is limited by the arm-length time-dependence as defined by (4-32) with $\Delta\beta = 250 \text{ ns/s}$. The TDI X_2 combination removes the additional time-dependent-coupled laser noise and reveals the 6.277 mHz GW signal. As with the static case (Figure 7-3), the EPD unit's phase transmission accuracy is the primary limiting noise source in the TDI combinations although, some sensitivity loss may occur due to a limited ranging capability around 100 mHz (Figure 7-9).

signals, s_{12} , s_{13} , are used for, and are equal to, the phase noise of the PLL laser-locking error signal. Meanwhile, the heterodyned PD output represents the local laser phase and is used as the input for the 'return' field simulation of inter-SC light transmission. These signals are used to construct the TDI combinations and minimize the ranging tone using the iterative process described in chapter 4.4.2.2 and shown in Figure 4-3 through a 4-dimensional sweep of the individual light-travel times, $\tau_2(t)$, $\tau_{2'}(t)$, $\tau_3(t)$, $\tau_{3'}(t)$.

7.2.1 Static-Arm LISA-like Simulation

The reader should note that these measurements were taken earlier than both those presented in chapters 7.1.1, 7.1.2, and 7.2.2. As a result, the ranging tone was

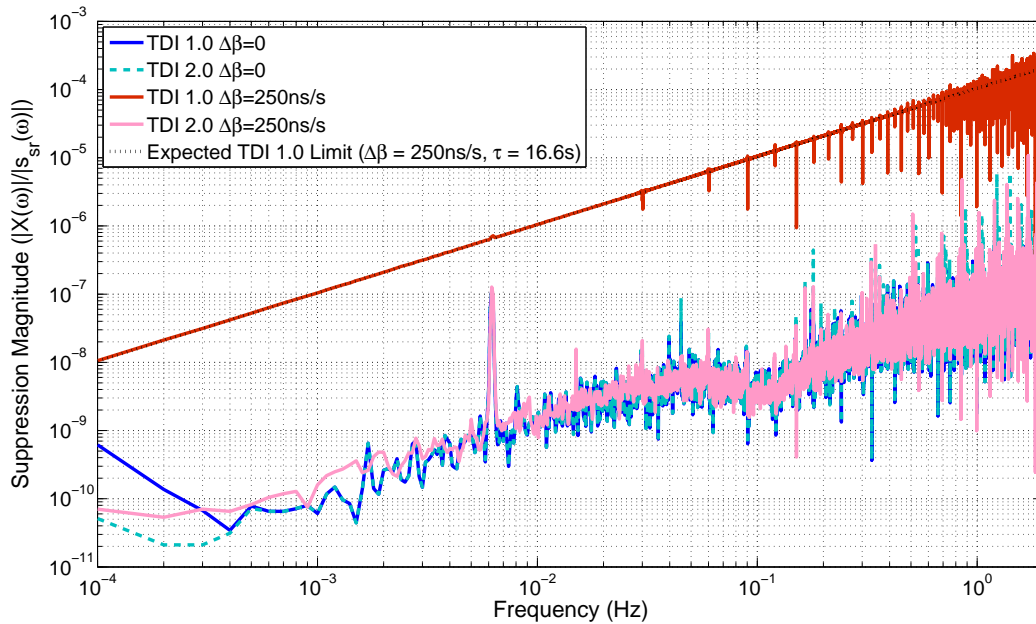


Figure 7-6. TDI laser phase noise suppression: The achieved laser noise suppression magnitudes for the transponder simulations of the static and dynamic TDI- X_1 and TDI- X_2 combinations are plotted. The TDI- X_1 combination's noise suppression equals the theorized limit (4–32) in the dynamic-arm simulation. The TDI- X_1 and TDI- X_2 result in the similar laser suppression characteristics in the static-arm simulation. The dynamic-arm TDI- X_2 combination's laser noise suppression equals that of the static case, verifying that the velocity coupled laser noise has been completely accounted for and removed.

placed at a different frequency (1.5 Hz) and the EPD data-rate was higher. Despite these changes, the effects are only noticeable through the reduced PLL ranging accuracy.

These same results have also been published in peer-reviewed literature [104].

The optimized outcome of the ranging process is found after a single iteration and results in a measure of 2β to an accuracy better than ~ 70 fs/s and a round-trip ranging precision of less than ~ 5.0 ns (~ 1.5 m) as shown in Table 7-2. Applying a linear regression to the calculated one-way delay times we find a one-way ranging error of ~ 100 μ s (~ 30 km). The outgoing and return delay times are un-equal by $\sim 250 \pm 0.1$ ms,

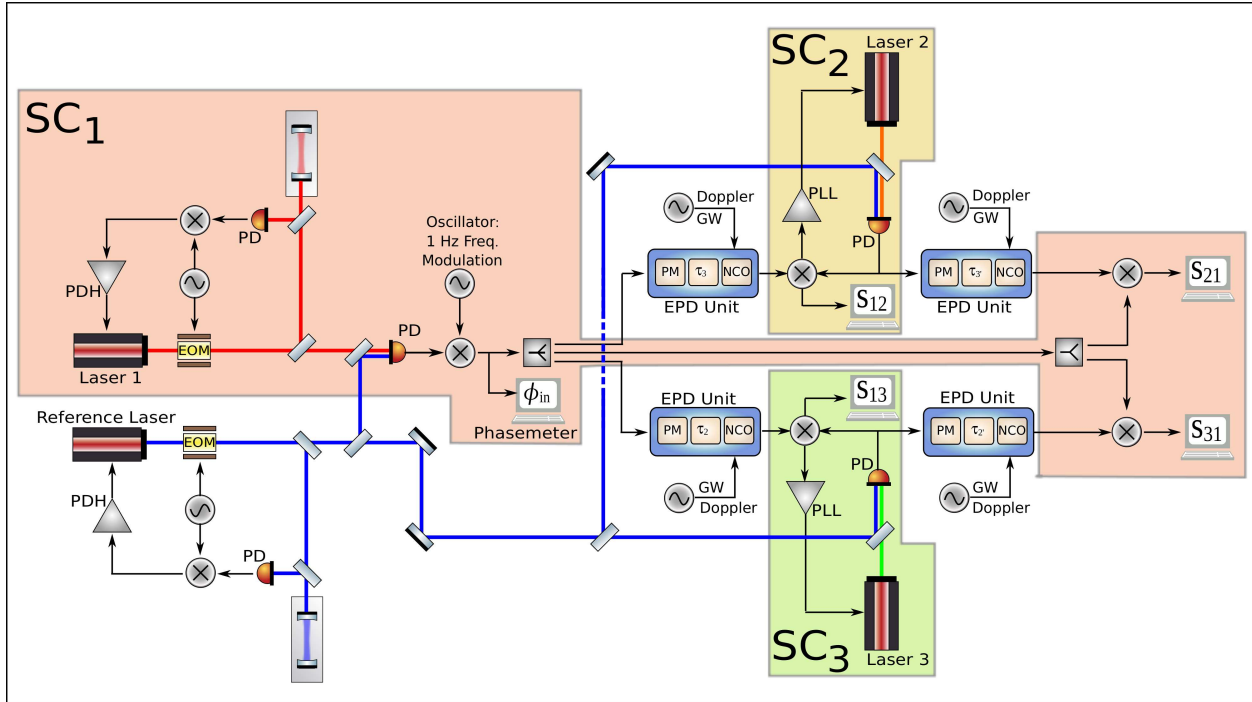


Figure 7-7. Model of the LISA-like TDI experimental benchtop: This TDI-PLL model shows how the individual pre-stabilized laser fields are combined to form the input noise signal and how this signal is processed by the EPD units and used to phase-lock the 'far' SC lasers, thus replicating all four LISA-like inter-SC laser link and produce all four s_{sr} observables. The setup is the same as is defined in Figure 7-1 expect that the 'transmitted' EPD outputs are used to phase-lock the far $Laser_2$ and $Laser_3$. The PLL error signals are exactly equal to the far SC sensor signals, s_{12} and s_{13} . The $Laser_{Ref}/Laser_{2/3}$ beatnotes are used as the input signals for the 'return' field light transmission simulation.

proving the TDI- $X_{1.5}$ combination's⁶ ability to extract individual phase errors despite un-equal delays along a single arm ($\tau_q(0) \neq \tau_{q'}(0)$).

Using the calculated one-way functional time-delays we form the TDI- $X_{1.0}$ and TDI- $X_{2.0}$ combinations; re-scaling the TDI spectral density by the inverse arm transfer functions in (7-3), we plot each TDI combinations' phase noise in Figure 7-8 resulting in the same measured sensitivity for both combinations. This noise level is likely due

⁶ Table 4-1

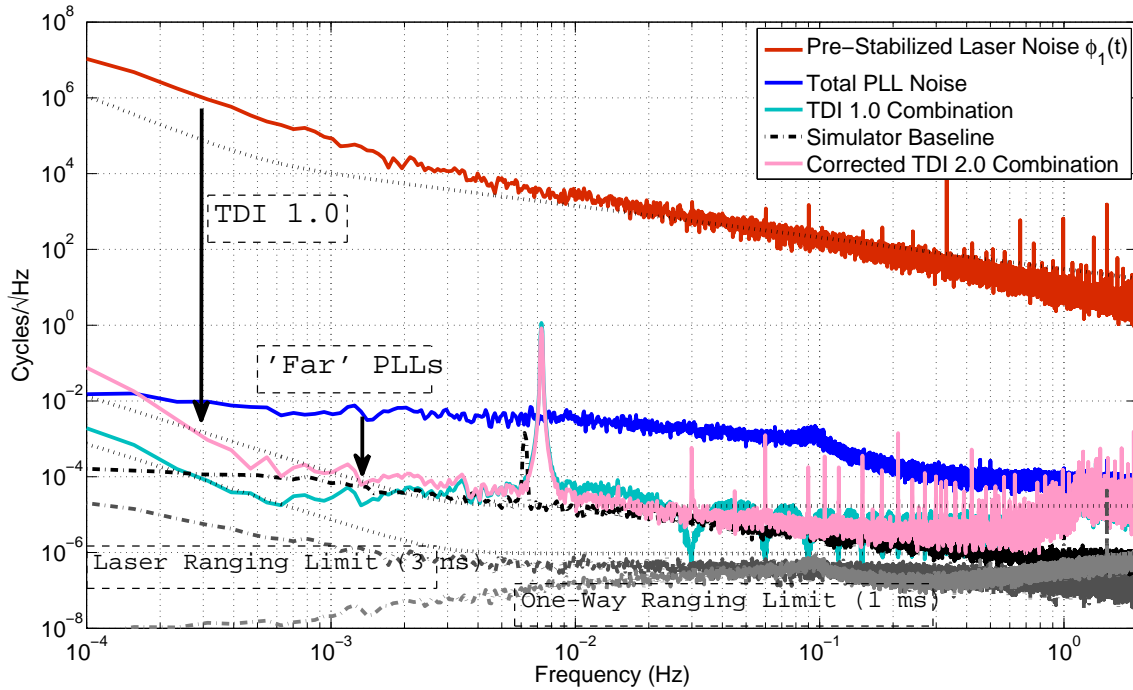


Figure 7-8. Static LISA-like laser experimental results: The TDI spectral results and comparisons with the input laser phase noise and PLL noise of the static-arm TDI simulation with phase-locked lasers is plotted. The corrected TDI-2.0 combination using the values from the TDI-ranging estimation (Table 7-2) matches with the baseline performance from Figure 7-3. The laser and PLL noise suppression as a result of the estimated ranging precision is not expected to be a limiting noise source which is verified by cross-correlating the TDI combination with the input signals as shown in Figure 7-9. If the PLL noise is not accounted for, the TDI combination is limited by these additional PLL noise sources (not pictured).

to the coupling of multiple un-correlated EPD clock noise sources, defined in (6-11), into the measurement. Based on the poor cross-correlations between the input noise and the the PLL noise sources with the resulting TDI combinations we conclude that the ranging precision is not a limiting noise source and that all the known sources have been removed from the final combination. We also note that the expected ranging precision using the round-trip and one-way variances along with (4-6) is well below the TDI combination as plotted in Figure 7-8.

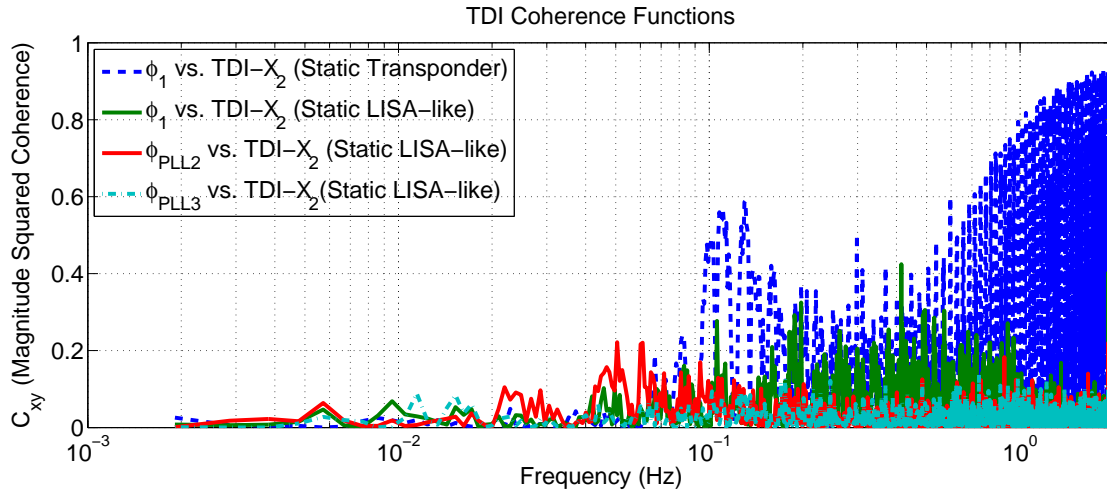


Figure 7-9. Cross-correlated TDI combinations - Static Transponder and LISA-like: The magnitude squared cross-correlation of the measured laser phase noise and PLL noise show a poor correlation with the TDI- X_2 combination for frequencies below for all frequencies in the static TDI-PLL simulation (4-way delay estimate: chapter 7.2.1). The laser noise correlates with the calculated TDI- X_2 combination for frequencies above 100 mHz in the static TDI-transponder measurement (2-way delay estimate: chapter 7.1.1). The poor correlation of the input noise sources with the TDI combinations verify that the input noises have been sufficiently removed using the TDI-ranging arm-length estimate.

7.2.2 Dynamic-Arm LISA-like Simulation

After three iterations of the ranging process, the optimized estimation of the inter-SC delay times results in a measure of 2β to an accuracy better than ~ 70 fs/s and a round-trip ranging precision of ~ 5.0 ns (~ 1.5 m) as shown in Table 7-2. The constraint's on the one-way delay times through the residual PLL noise removal can not be applied until the precision of the round-trip delay times are accurate enough to remove the input laser noise from the TDI combinations to reveal the residual PLL noises in the TDI combinations. Thus, it requires at least one iteration of the ranging process until the one-way delay times begin to be constrained. At the same time, the accuracy of the constrained one-way delay times will be significantly reduced in comparison to the constraints on the round-trip delay times resulting from the comparatively reduced noise suppression magnitude of the PLL noise (4–6). Applying

a linear regression to the calculated one-way delay times after the third iteration we find a one-way ranging error of about $\sim 100 \mu\text{s}$ ($\sim 30 \text{ km}$). Again, the outgoing and return delay times are un-equal by $\sim 250 \pm 0.1 \text{ ms}$, proving the capability to extract individual SC phase error with un-equal delays along each arm ($\tau_q(0) \neq \tau_{q'}(0)$).

Applying the optimized one-way functional values from the ranging procedure, outlined in Table 7-2, we generate the TDI- X_1 and TDI- X_2 combinations (Figure 7-10). Rescaling by the inverse arm response function, the TDI- X_1 combination meets the expected limitation (4-32). The TDI- X_2 combination meets the LISA IMS requirement to within a factor of 4 and is, again, limited by a combination of multiple EPD clock noise coupling sources resulting in a reduced sensitivity above the simulator's baseline performance. Again, the poor correlation of the input noise sources with the final combination, Figure 7-11, leads us to conclude that the ranging precisions are not a limiting noise source and that all known noise sources have been removed from the final combination. Further supporting this claim, the expected ranging precision using the round-trip and one-way variances along with (4-6) is well below the TDI combination as plotted in Figure 7-10.

Binary Confusion Noise Injection.

Finally, we introduce the low frequency simulated 'confusion noise' into the measurement to ensure that these low-frequency terms do not limit the ranging precision. The confusion noise background given by:

$$h_{\text{Background}}(\omega) \simeq \frac{.01}{\frac{s}{2\pi} + .001} \frac{\text{mHz}}{\sqrt{\text{Hz}}} \quad (7-5)$$

where 's' is the complex Laplace frequency, and 6.277 mHz mono-chromatic binary with a single-arm strain amplitude of 3.5×10^{-20} are simultaneously injected. The injected background noise level is set to match most estimations in the 0.1 mHz to 1.5 mHz but does not roll off as quickly at frequencies above 1.5 mHz as most confusion noise estimates do (Figure 8-1) [46, 103]. This is modified from the expected

Table 7-2. LISA-like TDI-ranging estimation: The method outlined in Figure 4-3 and the experiments described in chapters 7.2.1 and 7.2.2 are used to calculate estimates of the inter-SC delay functions, (4-37 and 4-39), and the associated ranging errors. The estimates verify the TDI-ranging capabilities and are used to generate the TDI-combinations for Figures 7-8 and 7-10.

Iteration	β (Slope)	$\tau_{22'}(0), \tau_{33'}(0)$ (Offset)	$\delta\tau_{22'}, \delta\tau_{33'} : \delta\tau_2, \delta\tau_{2'}, \delta\tau_3, \delta\tau_{3'} (\sigma)$
TDI 1.0 PLL			
1 (TDI 1.0) (Round-trip)	$2\beta_2 = -66.1 \text{ fs/s} \pm 45.4 \text{ fs/s}$	$\tau_{22'}(0) = 33.5508007898 \text{ s} \pm 1.01 \text{ ns}$	$\delta\tau_{22'} = 3.2 \text{ ns}$
	$2\beta_3 = 58.7 \text{ fs/s} \pm 37.4 \text{ fs/s}$	$\tau_{33'}(0) = 33.2152647154 \text{ s} \pm 0.83 \text{ ns}$	$\delta\tau_{33'} = 2.6 \text{ ns}$
1 (TDI 1.0) (One-Way)	$\beta_2 = -4.07 \text{ ns/s} \pm 13.6 \text{ ns/s}$	$\tau_2(0) = 16.694054656 \text{ s} \pm 301 \mu\text{s}$	$\delta\tau_{2'} = \delta\tau_2 = 1.12 \text{ ms}$
	$\beta_3 = 26.1 \text{ ns/s} \pm 15.9 \text{ ns/s}$	$\tau_{2'}^*(0) = 16.8567461 \text{ s} \pm 301 \mu\text{s}$	$\delta\tau_3 = \delta\tau_{3'} = 0.95 \text{ ms}$
		$\tau_3(0) = 16.51799231 \text{ s} \pm 352 \mu\text{s}$	
		$\tau_{3'}^*(0) = 16.6972724 \text{ s} \pm 352 \mu\text{s}$	
TDI 2.0 PLL			
1	$2\beta_2 = -199.984 \text{ ns/s} \pm 12 \text{ ps/s}$	$\tau_{22'}(0) = 33.59821021 \text{ s} \pm 0.28 \mu\text{s}$	$\delta\tau_{22'} = 0.895 \mu\text{s}$
	$2\beta_3 = +300.052 \text{ ns/s} \pm 7.8 \text{ ps/s}$	$\tau_{33'}(0) = 33.21476669 \text{ s} \pm 0.18 \mu\text{s}$	$\delta\tau_{33'} = 0.568 \mu\text{s}$
2	$2\beta_2 = -200.000015 \text{ ns/s} \pm 71 \text{ fs/s}$	$\tau_{22'}(0) = 33.5982645303 \text{ s} \pm 1.6 \text{ ns}$	$\delta\tau_{22'} = 5.2 \text{ ns}$
	$2\beta_3 = +300.000013 \text{ ns/s} \pm 26 \text{ fs/s}$	$\tau_{33'}(0) = 33.2146434958 \text{ s} \pm 0.58 \text{ ns}$	$\delta\tau_{33'} = 1.9 \text{ ns}$
3 (TDI-2.0) (Round-trip)	$2\beta_2 = -200.000028 \text{ ns/s} \pm 68 \text{ fs/s}$	$\tau_{22'}(0) = 33.5982645401 \text{ s} \pm 1.5 \text{ ns}$	$\delta\tau_{22'} = 5.0 \text{ ns}$
	$2\beta_3 = +300.000020 \text{ ns/s} \pm 25 \text{ fs/s}$	$\tau_{33'}(0) = 33.2146435166 \text{ s} \pm 0.58 \text{ ns}$	$\delta\tau_{33'} = 1.9 \text{ ns}$
3 (TDI-2.0) (One-Way)	$\beta_2 = -103.3 \text{ ns/s} \pm 1.4 \text{ ns/s}$	$\tau_2(0) = 16.68021 \text{ s} \pm 31 \mu\text{s}$	$\delta\tau_2 = \delta\tau_{2'} = 99 \mu\text{s}$
	$\beta_3 = +152.24 \text{ ns/s} \pm 1.4 \text{ ns/s}$	$\tau_{2'}^*(0) = 16.91805 \text{ s} \pm 31 \mu\text{s}$	$\delta\tau_3 = \delta\tau_{3'} = 105 \mu\text{s}$
		$\tau_3(0) = 16.48824 \text{ s} \pm 32 \mu\text{s}$	
		$\tau_{3'}^*(0) = 16.72640 \text{ s} \pm 32 \mu\text{s}$	
Confusion Noise TDI 2.0			
3 (Round-Trip)	$2\beta_2 = -199.999991 \text{ ns/s} \pm 50 \text{ fs/s}$	$\tau_{22'}(0) = 33.6012734891 \text{ s} \pm 1.1 \text{ ns}$	$\delta\tau_{22'} = 3.7 \text{ ns}$
	$2\beta_3 = +300.000137 \text{ ns/s} \pm 22 \text{ fs/s}$	$\tau_{33'}(0) = 33.2100302983 \text{ s} \pm 0.49 \text{ ns}$	$\delta\tau_{33'} = 1.6 \text{ ns}$
3 (One-Way)	$\beta_2 = -96.81 \text{ ns/s} \pm 2.3 \text{ ns/s}$	$\tau_2(0) = 16.73546 \text{ s} \pm 53 \mu\text{s}$	$\delta\tau_2 = \delta\tau_{2'} = 169 \mu\text{s}$
	$\beta_3 = +149.439 \text{ ns/s} \pm 1.4 \text{ ns/s}$	$\tau_{2'}^*(0) = 16.86582 \text{ s} \pm 53 \mu\text{s}$	$\delta\tau_3 = \delta\tau_{3'} = 102 \mu\text{s}$
		$\tau_3(0) = 16.53994 \text{ s} \pm 32 \mu\text{s}$	
		$\tau_{3'}^*(0) = 16.67009 \text{ s} \pm 32 \mu\text{s}$	

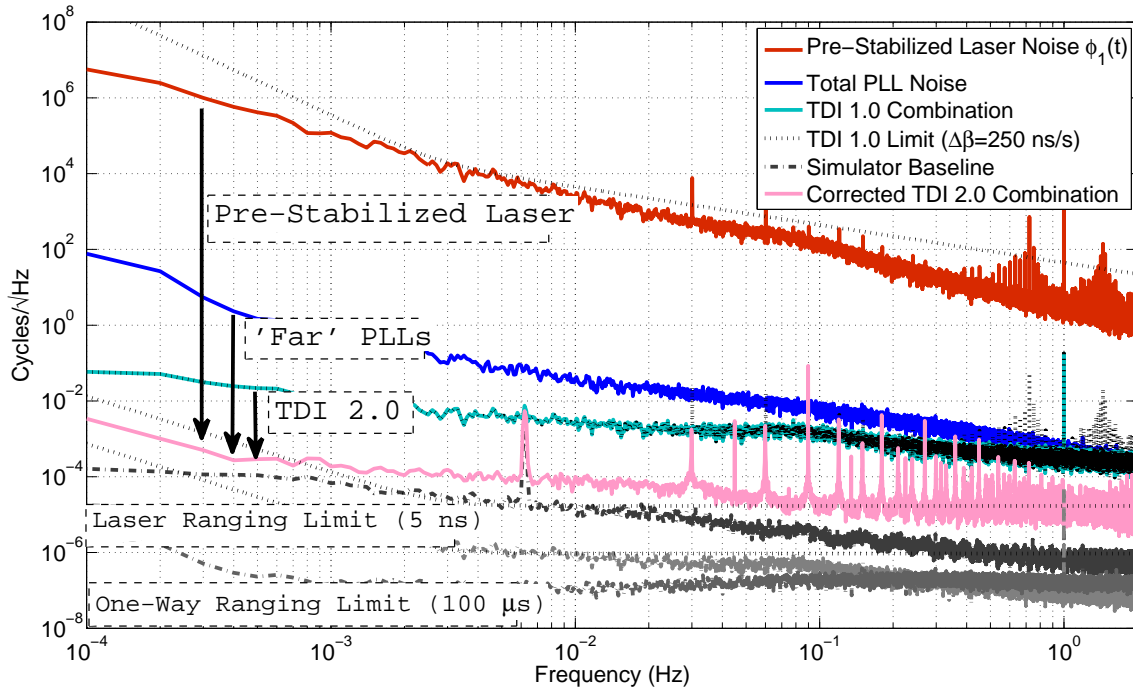


Figure 7-10. Dynamic LISA-like experimental results: The suppression of the TDI X_1 combination is limited by the expected arm-length time-dependence defined by (4-32) with $\Delta\beta = 250 \text{ ns/s}$. The TDI X_2 combination removes the input laser noise, the 'far' PLL residual phase noise, and the time-dependent coupled laser noise to reveal the 6.277 mHz GW signal. The sensitivity limitation comes, most likely, as a result of multiple unaccounted for EPD noise as a result of the time-changing delay. This is determined based on a comparatively improved performance using the static-PLL simulation and the fact that the time-changing delay is the major difference between these measurements.

situation to ensure that the addition low-frequency noise does not limit the ranging precision. The monochromatic GW phase modulation due to the RXJ0806.3+1527 binary is a factor of 100 smaller than the expected strain amplitude averaged over a 1 year measurement. That said, the GW phase modulation amplitude is simply programmed to be out-of-phase when injected into the individual arms simulator and with no consideration for the GW polarization or detector orientation over the course of the year.

Again, the optimized ranging estimation places bounds on the β accuracy better than $\sim 50 \text{ fs/s}$ and a round-trip ranging precision of $\sim 3.7 \text{ ns}$ ($\sim 1.1 \text{ m}$). Thus, this

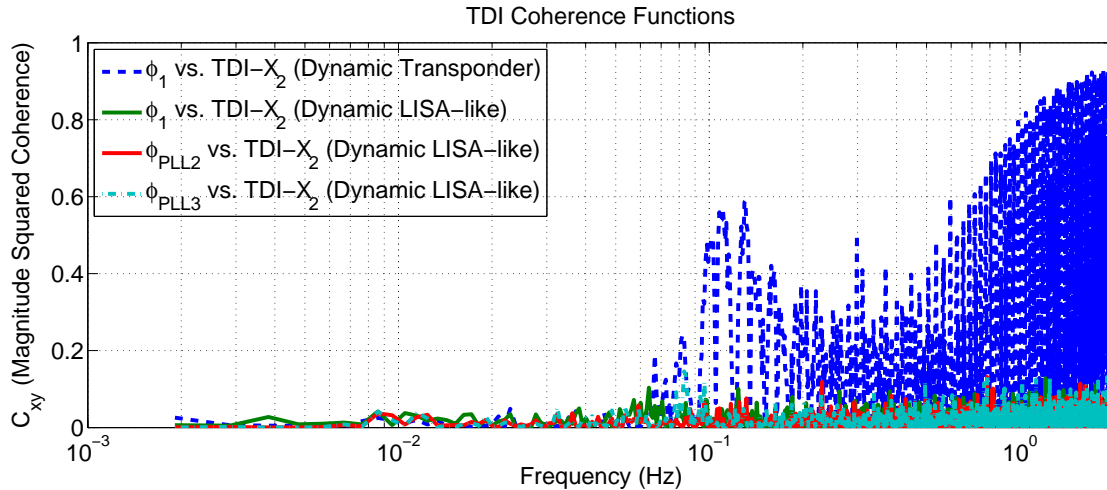


Figure 7-11. Cross-correlated TDI combinations - Dynamic Transponder and LISA-like: The magnitude squared cross-correlation of the measured laser phase noise and PLL noise show a poor correlation with the TDI- X_2 combination for frequencies below for all frequencies in the dynamic TDI-PLL simulation (4-way delay estimate: chapter 7.2.2). As with the static case (Figure 7-9), the laser noise correlates with the calculated TDI- X_2 combination for frequencies above 100 mHz in the dynamic TDI-transponder measurement (2-way delay estimate: chapter 7.1.2). The poor correlation of the input noise sources with the TDI combinations verify that the input noises have been sufficiently removed using the TDI-ranging arm-length estimate.

confusion noise result achieves a ranging precision on the same order as the simulator's phase-locked performance, proving that low-frequency noise has little to no effect on the ranging tone cancellation or the measured arm-lengths.

Finally, once the long-term residual quadratic phase drifts have been removed from the strain measurement, the time-domain comparisons between the TDI- X_2 outputs of the phase-locked and confusion noise experiments are plotted in Figure 7-12 to show the additional low-frequency noise. These TDI- X_2 noise spectra with and without the confusion noise are plotted, Figure 8-1, in particular, in terms of the actual LISA length strain in $\text{cycles}/\sqrt{\text{Hz}}$ along with the low-frequency acceleration noise, mid-frequency shot-noise, and scaled by the high-frequency sensitivity loss. We also plot the theoretical '1-year' averaged strain of a few actual gravitational wave sources and the expected GW confusion background [103] in comparison with the

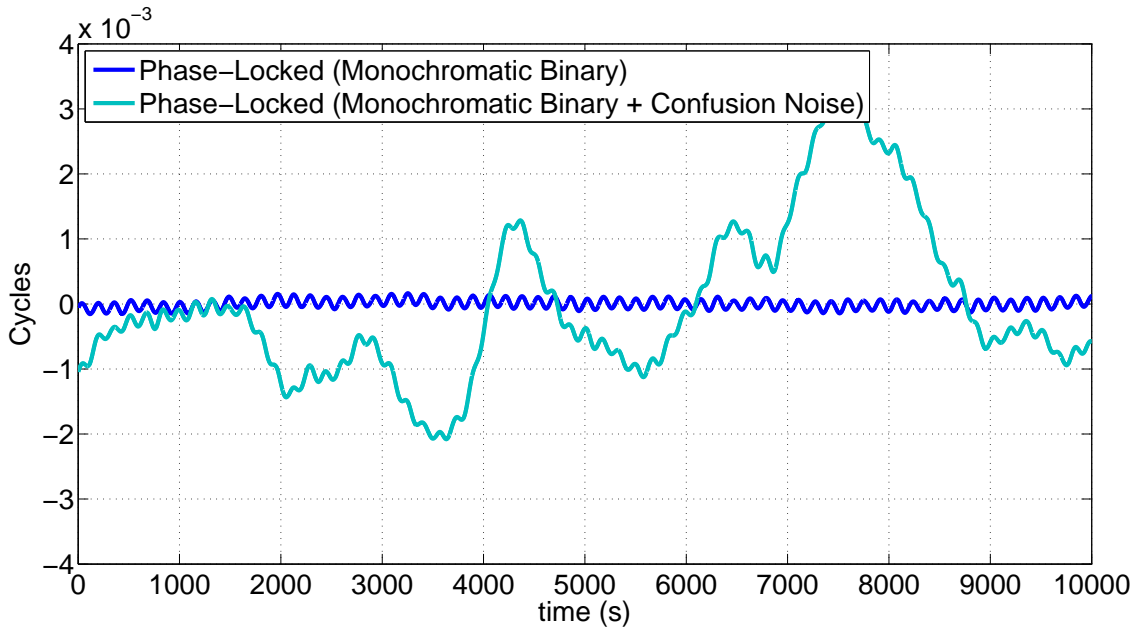


Figure 7-12. Confusion noise time-series comparison: The time series of the dynamic LISA-like simulations with and without a confusion noise background (chapters 7.2.2 and 7.2.2) are plotted explicitly after low-pass filtering the aliased noise near the sampling-frequency. The added low-frequency confusion noise is readily apparent when comparing the results of the measured 6.277 mHz binary with the binary plus confusion noise (7-5).

injected background (7-5) and GW signal. The deviation in the spectral amplitude ($\simeq 7 \text{ mCyc}/\sqrt{\text{Hz}}$) is caused by spreading of the GW into approximately 3 frequency bins⁷.

⁷ $204 \mu\text{cycles}/\text{Hz} \times \sqrt{10000 \text{ s}} = 20.4 \text{ mCyc}/\sqrt{\text{Hz}} \simeq 3 \times 7 \text{ mCyc}/\sqrt{\text{Hz}}$

CHAPTER 8 CONCLUSION

In this dissertation we have presented how LISA and other space-based interferometers will achieve the strain sensitivities required to measure astronomically interesting GW sources using advanced stabilization techniques such as cavity locking and arm locking as well as through the application of post-processing time-delay interferometry combinations. We have considered how the LISA-IMS science observables are formed and how the differential proof-mass length is constructed from these individual heterodyne PD observables. We have presented the design, phase precision, and likely low-frequency limiting noise sources of LISA-like phasemeters and how they are used in heterodyne interferometry. A method of using the phasemeters to electronically simulate the inter-SC laser field transmission characteristics including the time-changing delay, Doppler shift, and GW modulation was developed, tested, and used to perform some of the first hardware based arm-locking experiments.

Time-delay interferometry simulations using μcycle phasemeters, multi-second delay EPD units, and the UFLIS laser benchtop were developed and compared to the noise sources expected in LISA. The simulations tested the ability of time-delay interferometry combinations to cancel the laser phase noise and extract the GW information with, both, static (constant arm-length) and dynamic (time-changing arm-length) LISA-like characteristics. We have also presented a simple but powerful method of estimating the time-dependent arm-lengths using a TDI-ranging reference tone modulated onto the laser field at frequencies above the GW frequency measurement band. The post-processing formation of the TDI- X_2 combination which optimally cancels the ranging tone provides a functional constraint on the time-changing inter-SC delays to an accuracy better than that required to remove the laser phase noise from the TDI combinations.

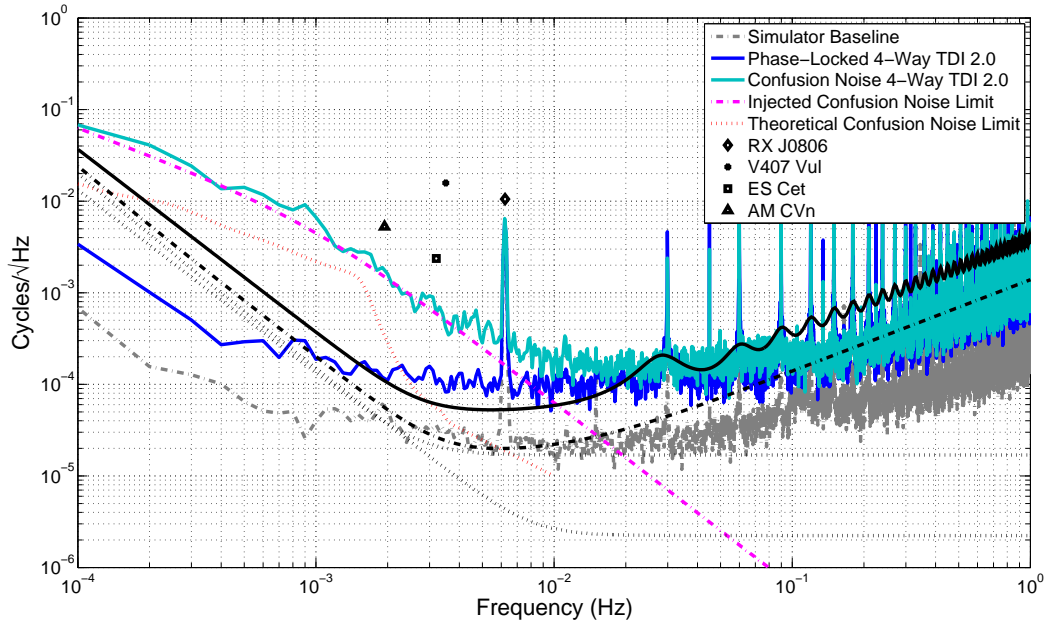


Figure 8-1. Compiled results and comparison with TDI for LISA: In this figure we have compiled all the results of the TDI simulations and attempt to make a direct comparison with the expected LISA strain sensitivity. The baseline spectral noise of the UFLIS simulator (grey-blue) from the TDI-Transponder (chapter.7.1.1) measurements is plotted. The velocity corrected TDI- $X_{2.0}$ spectrum of the dynamic arm TDI simulation with (cyan) and without (blue) the injected binary confusion noise (dotted-magenta) is plotted in comparison with the IMS sensitivity requirement. The three TDI simulations are scaled by the frequency factors of (3-2) to account for the high-frequency GW-sensitivity loss expected in LISA. The DRS and IMS requirement are root-square summed and scaled by (3-2) to produce the effective single-link LISA sensitivity with (black) and without (dotted-black) the $2\sqrt{5/3}$ sensitivity factor. An estimate of the confusion noise limit is plotted (dotted-red) along with the four brightest verification binaries rescaled from a 1-year averaged strain sensitivity to noise spectra in $\text{cycles}/\sqrt{\text{Hz}}$. The strain magnitude of the 1 year averaged RX-J0806 binary and the 10000 s EPD injected GW have amplitudes such that they result in similar LSD amplitudes in this figure. The results of these experiments verify the ability to account for a $\simeq 0.4$ s (0.1 Gm) un-equal arm-length mis-match and 75 m/s velocity coupled laser noise by TDI-ranging the inter-SC distance to an accuracy of 5 ns (1.5 m) and forming the TDI- X_2 combination to extract the GW information to within a factor of 5 of the single-link LISA sensitivity.

$\text{RX-J0806} \sim 4 \times 10^{-22}/\text{Hz}\sqrt{1\text{ year}} = 2.2 \times 10^{-18}/\sqrt{\text{Hz}} = 10.5 \text{ mCyc}/\sqrt{\text{Hz}}$
 $\text{EPD-GW} \sim 4.3 \times 10^{-20}/\text{Hz}\sqrt{10000\text{ s}} = 4.3 \times 10^{-18}/\sqrt{\text{Hz}} = 20.5 \text{ mCyc}/\sqrt{\text{Hz}}$

The experimental results show that more than 10 orders of magnitude of laser frequency noise can be canceled using appropriately time-shifted data streams with the TDI- X_2 data combination. We have also verified that the ability to cancel the laser frequency noise using a TDI- X_1 data combination is limited by the relative velocities between the spacecraft. Meanwhile, we have also demonstrated that the TDI- X_2 combination accounts for this inter-SC velocity limited TDI- X_1 combination. The simulations have also verified the removal of the residual phase lock loop noise added at the far spacecraft and have showed that the PLL noise extraction is possible with relaxed one-way ranging requirements due as compared to the round-trip requirements. The results of these TDI experiments demonstrated the ability to account for a $\simeq 0.4$ s (0.1 Gm) un-equal arm-length mis-match and 75 m/s velocity coupled laser noise by TDI-ranging the inter-SC distance to an accuracy of 5 ns (1.5 m) by forming the TDI- X_2 combination to extract the GW information to within a factor of 5 of the single-link LISA sensitivity.

In the process of developing the UFLIS-TDI simulator, we have developed and tested data analysis tools which use the raw phasemeter data streams to extract the light-travel time function and generate the TDI- X_2 data streams. We have also added a confusion noise GW-background to the TDI simulations and verified that this low-frequency background does not interfere with our ranging capabilities.

The combination of these experiments, validating the multi-second time-changing inter-SC characteristics, and the experiments performed in [105], verifying the optical noise couplings, represent the essential characteristics of a LISA-like interferometry measurement system and the post-processing cancellation of laser phase noise using the appropriate TDI combinations. Future UFLIS experiments should include real, LISA-like GW signals using data-sets generated with LISA-tools like Synthetic LISA [55]. The use of independent clock sources and the verification that clock noise sources can be accounted for in the TDI combinations would also be useful. Finally, simulations

with three independently stabilized lasers might also be valuable towards verifying the constraints on the one-way ranging capabilities.

APPENDIX A
TIME VARYING FRACTIONAL DELAY INTERPOLATION FUNCTION

```

function [xOut,tOut] = TVFDfilter(x,fs,beta,Tau,N)
% [xOut,tOut] = TVFDfilter(x,fs,beta,Tau,N)
%
% Computes a time-stretched/compressed and time-shifted data-set
% with an N-point Lagrange fraction delay filter as defined in
% "Post-processed time-delay interferometry for LISA" by Shaddock et. al.
%
% INPUTS:
% x = time series input [amplitude]
% fs = sampling frequency [Hz]
% beta = fractional shift rate (in s/s)
% Tau = absolute time-shifting value in seconds
% N = interpolation length (number of points to use in
%     Fractional Delay Filter)
%
% OUTPUTS:
% xOut = output amplitude vector
% tOut = output time vector
%
% Ira Thorpe, Shawn Mitryk
% Updated 2-18-12

L = length(x);
M = (N-1)/2;
k = (-(N-1)/2):1:((N-1)/2);
offset = floor(Tau*fs);
Dfrac = -(Tau-(offset/fs))*fs;
xOutShift(1:L-N+1) = 0;

    for i=1:L-N+1

        DTaufrac = beta*i;

        td = (N-1)/2+Dfrac-DTaufrac;
        b1 = gamma(td+1)/(gamma(N+1)*gamma(td-N+1));
        b2 = gamma(N)./(gamma(k+(N-1)/2+1).*gamma(N-k-(N-1)/2));
        w = ((pi*N)/(sin(pi*td)))*b1*b2;
        h = sinc(Dfrac-DTaufrac-k).*w;
        xOutShift(i) = sum(h.*(x(i:i+N-1)'));

    end

```

```
xOut = xOutShift(N+M+1:L-N+1)';  
tOut = (0:length(xOut)-1)'/fs;
```

An up-to-date version of these functions and their application in producing the results demonstrated in these experiments can be obtained from [\[106\]](#).

APPENDIX B TDI 2.0 COMBINATION FUNCTION

```

function [TDI2Out, TDI1Out] = TDIComb(fs, s21, s31, s12, s13, tau33,
                                     tau13, beta3o, tau22, tau12, beta2o)
% [TDI2Out, TDI1Out] = TDIComb(fs, s21, s31, s12, s13, tau33,
%                               tau13, beta3, tau22, tau12, beta2)
%
% Computes the TDI 1.0 and TDI 2.0 Combinations based on the 6-variable
% arm-length delays. Based on "Data combinations accounting for LISA
% spacecraft motion" by Shaddock et. al.
%
% INPUTS:
%   fs = Sample frequency
%
%   s21 = Sensor signal (sending: SC2 receiving: SC1)
%   s31 = Sensor signal (sending: SC3 receiving: SC1)
%   s12 = Sensor signal (sending: SC1 receiving: SC2)
%   s13 = Sensor signal (sending: SC1 receiving: SC3)
%
%   tau33 = Round-trip delay from SC1 through SC2 (Arm3)
%   tau13 = One-way delay time from SC1 to SC2 (Arm3)
%   beta3 = Arm3 time compression factor
%         beta = (velocity between SC1 & SC2/speed of light)
%   tau22 = Round-trip delay from SC1 through SC3 (Arm2)
%   tau12 = One-way delay time from SC1 to SC3 (Arm2)
%   beta2 = Arm2 time compression factor
%
% OUTPUTS:
%   TDI2Out = TDI2.0 Combination
%   TDI1Out = TDI1.0 Combination
%
% Shawn Mitryk
% Updated 2-18-12

L1 = length(s12);
N = 51;
M = (N-1)/2;

alpha2 = (1-2*beta2o);
alpha3 = (1-2*beta3o);

gamma2 = (1-beta2o);
gamma3 = (1-beta3o);

```

```

beta3 = 1-alpha3;
beta2 = 1-alpha2;

% TDI 2.0 shift values

Tau23 = (tau22)*alpha3+(tau33)
beta23 = 1-(alpha2*alpha3)

Tau32 = (tau33)*alpha2+(tau22)
beta32 = 1-(alpha3*alpha2)

Tau232 = alpha2^2*tau33 + alpha2*tau22 + tau22
beta232 = 1-(alpha2^2*alpha3)

Tau323 = alpha3^2*tau22 + alpha3*tau33 + tau33
beta323 = 1-(alpha3^2*alpha2)

% Calculate the sensor signals from the one-way signals

[chan12.data, chan12.t] = TVFDfilter(s12,fs,beta2o,tau12,N);
[chan13.data, chan13.t] = TVFDfilter(s13,fs,beta3o,tau13,N);

chan21.data = s21(2*N:L1-M);
chan31.data = s31(2*N:L1-M);

chan22.data = chan21.data + chan12.data;
chan33.data = chan31.data + chan13.data;

% Form the TDI Combinations based on the 6-variable delays

L2 = length(chan22.data);

[chan2_2s.data,chan2_2s.t]
    = TVFDfilter(chan22.data,fs,beta2,tau22,N);
[chan3_3s.data,chan3_3s.t]
    = TVFDfilter(chan33.data,fs,beta3,tau33,N);

[chan22_23s.data,chan2_23s.t]
    = TVFDfilter(chan22.data,fs,beta23,Tau23,N);
[chan33_32s.data,chan3_32s.t]
    = TVFDfilter(chan33.data,fs,beta32,Tau32,N);

[chan22_232s.data,chan2_232s.t]
    = TVFDfilter(chan22.data,fs,beta232,Tau232,N);

```

```

[chan33_323s.data,chan3_323s.t]
    = TVFDfilter(chan33.data,fs,beta323,Tau323,N);

chan22a.data = chan22.data(2*N:L2-M)';
chan33a.data = chan33.data(2*N:L2-M)';
chan22_2a.data = chan22_2s.data;
chan33_3a.data = chan33_3s.data;
chan22_23a.data = chan22_23s.data;
chan33_32a.data = chan33_32s.data;
chan22_232a.data = chan22_232s.data;
chan33_323a.data = chan33_323s.data;

tdi1a.data = chan22a.data + chan33a.data
            - chan22_2a.data - chan33_3a.data;
tdi1b.data = - chan22_23a.data - chan33_32a.data
            + chan22_232a.data + chan33_323a.data;

tdi2.data = tdi1a.data + tdi1b.data;

TDI10out = tdi1a.data;
TDI20out = tdi2.data;

```

An up-to-date version of these functions and their application in producing the results demonstrated in these experiments can be obtained from [\[106\]](#).

REFERENCES

- [1] I. S. Newton, *Philosophiae Naturalis Principia Mathematica*, S. Pepys, Reg. Soc. Praeses, London, 1687.
- [2] A. Einstein, "Relativitätsprinzip und die aus demselben gezogenen folgerungen," *Jahrbuch der Radioaktivität*, vol. 4, pp. 411–462, 1907.
- [3] A. Einstein, "Grundlage der allgemeinen relativitätstheorie," *Annalen der Physik*, vol. 4, no. 49, pp. 769–822, 1916.
- [4] D. Blokhintsev and F. Gal'perin, "Gipoteza neutrino i zakon sokhraneniya energii [neutrino hypothesis and conservation of energy]," *Pod Znamenem Marxisma* 6, vol. 67, pp. 147–157, 1934.
- [5] C. Cutler, W. A. Hiscock, and S. L. Larson, "Lisa, binary stars, and the mass of the graviton," *Phys. Rev. D*, vol. 67, pp. 024015, Jan 2003.
- [6] F. Zwicky, "On the masses of nebulae and of clusters of nebulae," *Astrophysical Journal*, vol. 86, pp. 217–+, Oct. 1937.
- [7] J. H. Oort, "Observational evidence confirming Lindblad's hypothesis of a rotation of the galactic system," *Bulletin Astronomical Institute of the Netherlands*, vol. 3, pp. 275, Apr. 1927.
- [8] "Nobel prize in physics 2011 - scientific background - the accelerating universe," 2012, http://www.nobelprize.org/nobel_prizes/physics/laureates/2011-/advanced.html.
- [9] F. W. Dyson, A. S. Eddington, and C. Davidson, "A determination of the deflection of light by the sun's gravitational field, from observations made at the total eclipse of may 29, 1919," *Philosophical Transactions of the Royal Society of London. Series A, Containing Papers of a Mathematical or Physical Character*, vol. 220, pp. pp. 291–333, 1920.
- [10] A. Einstein and N. Rosen, "On gravitational waves," *Journal of the Franklin Institute*, vol. 223, no. 1, pp. 43–54, 1937.
- [11] R. A. Hulse and J. H. Taylor, "Discovery of a pulsar in a binary system," *Astrophysical Journal*, vol. 195, pp. L51–L53, Jan. 1975.
- [12] J. Weber, "Detection and generation of gravitational waves," *Phys. Rev.*, vol. 117, pp. 306–313, Jan 1960.
- [13] B. P. Abbott, R. Abbott, et al., "Ligo: the laser interferometer gravitational-wave observatory," *Reports on Progress in Physics*, vol. 72, no. 7, pp. 076901, 2009.
- [14] A. Abramovici et al., "Ligo: The laser interferometer gravitational-wave observatory," *Science*, vol. 256, no. 5055, pp. 325–333, 1992.

- [15] C. L. Carilli and S. Rawlings, “Motivation, key science projects, standards and assumptions,” *New Astronomy Review*, vol. 48, pp. 979–984, Dec. 2004.
- [16] B. J. Burt, A. N. Lommen, and L. S. Finn, “Optimizing pulsar timing arrays to maximize gravitational wave single-source detection: A first cut,” *Astrophysical Journal*, vol. 730, no. 1, pp. 17, 2011.
- [17] E. Mauceli, Z. K. Geng, W. O. Hamilton, W. W. Johnson, S. Merkwitz, A. Morse, B. Price, and N. Solomonson, “The Allegro gravitational wave detector: Data acquisition and analysis,” *Phys. Rev. D*, vol. 54, pp. 1264–1275, July 1996.
- [18] C. Frajuca et al., “Searching for monochromatic signals in the allegro gravitational wave detector data,” *Journal of Physics: Conference Series*, vol. 228, no. 1, 2010.
- [19] L. Gottardi, A. de Waard, O. Usenko, G. Frossati, M. Podt, J. Flokstra, M. Bassan, V. Fafone, Y. Minenkov, and A. Rocchi, “Sensitivity of the spherical gravitational wave detector minigrail operating at 5 k,” *Phys. Rev. D*, vol. 76, pp. 102005, Nov 2007.
- [20] B. Abbott, R. Abbott, et al., “An upper limit on the stochastic gravitational-wave background of cosmological origin,” *Nature*, vol. 460, pp. 990–994, Aug 2009.
- [21] B. Abbott, R. Abbott, et al., “Setting upper limits on the strength of periodic gravitational waves from psr j1939+2134 using the first science data from the geo 600 and ligo detectors,” *Phys. Rev. D*, vol. 69, pp. 082004, Apr 2004.
- [22] B. Abbott, R. Abbott, et al., “Limits on gravitational-wave emission from selected pulsars using ligo data,” *Phys. Rev. Lett.*, vol. 94, pp. 181103, May 2005.
- [23] K. Glampedakis and S. Babak, “Mapping spacetimes with LISA: inspiral of a test body in a ‘quasi-Kerr’ field,” *Class. Quantum Grav.*, vol. 23, pp. 4167–4188, June 2006.
- [24] L. Barack and C. Cutler, “Using lisa extreme-mass-ratio inspiral sources to test off-kerr deviations in the geometry of massive black holes,” *Phys. Rev. D*, vol. 75, pp. 042003, Feb 2007.
- [25] C. L. MacLeod and C. J. Hogan, “Precision of hubble constant derived using black hole binary absolute distances and statistical redshift information,” *Phys. Rev. D*, vol. 77, pp. 043512, Feb 2008.
- [26] J. S. Bloom, D. E. Holz, et al., “Astro2010 Decadal Survey Whitepaper: Coordinated Science in the Gravitational and Electromagnetic Skies,” *ArXiv e-prints*, Feb. 2009.
- [27] T. Prince et al., “Lisa: Probing the universe with gravitational waves,” Tech. Rep., March 2009, http://list.caltech.edu/lib/exe/fetch.php?media=documents:science:-lisa_science_case_v1_2.pdf.

- [28] T. Prince et al., “Laser interferometer space antenna for the detection of gravitational waves, pre-phase a report,” Tech. Rep., Max-Planck-Institute for Quantum Optics, Garching, 1998.
- [29] “Lisa assessment study report (yellow book),” Tech. Rep., Feb. 2011, <http://sci.esa.int/science-e/www/object/index.cfm?fobjectid=48364#>.
- [30] O. Jennrich et al., “Ngo assessment study report (yellow book): Esa/sre(2011),” Tech. Rep., 2012, <http://sci.esa.int/science-e/www/object/index.cfm?fobjectid=49839#>.
- [31] S. Kawamura et al., “The japanese space gravitational wave antennadecigo,” *Class. Quantum Grav.*, vol. 23, no. 8, pp. S125, 2006.
- [32] “Lisa - laser interferometer space antenna - media gallery - lisa desktop backgrounds,” March 2012, reprinted with permission from ‘Using NASA Imagery and Linking to NASA Web Sites - http://www.nasa.gov/audience/formedia/features/MP_Photo_Guidelines.html’, <http://lisa.nasa.gov/gallery/index.html>.
- [33] K. Danzmann, T. Prince, et al., “Lisa science requirements document, v3.0,” Tech. Rep., 2005, http://list.caltech.edu/lib/exe/fetch.php?media=documents:-requirements:srd_v3_0_sb.pdf.
- [34] D. Shaddock and K. M. others, “Lisa frequency control white paper,” Tech. Rep., July 2009, unpublished.
- [35] G. Giampieri, R. W. Hellings, M. Tinto, and J. E. Faller, “Algorithms for unequal-arm michelson interferometers,” *Optics Communications*, vol. 123, no. 4–6, pp. 669–678, 1996.
- [36] “Request for information - concepts for the nasa gravitational-wave mission,” Sept 2011, <http://pcos.gsfc.nasa.gov/studies/gravwave/-gravitational-wave-mission-rfis.php>.
- [37] C. W. Misner, K. S. Thorne, and J. A. Wheeler, *Gravitation*, Twenty First Printing, 1 edition, 1998.
- [38] S. M. Carroll, *An Introduction to General Relativity: Spacetime and Geometry*, Addison Wesley, 1301 Sansome St., San Francisco, CA 94111, 1 edition, 2004.
- [39] J. D. Jackson, *Classical Electrodynamics, 3rd Ed*, Wiley, 2007.
- [40] C. W. F. Everitt, D. B. DeBra, et al., “Gravity probe b: Final results of a space experiment to test general relativity,” *Phys. Rev. Lett.*, vol. 106, pp. 221101, May 2011.

- [41] J. I. Thorpe, *Laboratory Studies of Arm-Locking Using Tthe Laser Interferometry Space Antenna Simulator at the University of Florida*, Ph.D. dissertation, University of Florida, 2006.
- [42] A. Stroeer and A. Vecchio, “The lisa verification binaries,” *Class. Quantum Grav.*, vol. 23, no. 19, pp. S809, 2006.
- [43] J. M. Weisberg and J. H. Taylor, “The Relativistic Binary Pulsar B1913+16: Thirty Years of Observations and Analysis,” in *Binary Radio Pulsars*, F. A. Rasio & I. H. Stairs, Ed., July 2005, vol. 328 of *Astronomical Society of the Pacific Conference Series*, p. 25.
- [44] D. R. Lorimer, “Binary and millisecond pulsars,” *Living Reviews in Relativity*, vol. 11, no. 8, 2008.
- [45] A. G. Lyne, M. Burgay, M. Kramer, A. Possenti, R. Manchester, F. Camilo, M. A. McLaughlin, D. R. Lorimer, N. D’Amico, B. C. Joshi, J. Reynolds, and P. C. C. Freire, “A double-pulsar system: A rare laboratory for relativistic gravity and plasma physics,” *Science*, vol. 303, no. 5661, pp. 1153–1157, 2004.
- [46] J. A. Edlund, M. Tinto, A. Królak, and G. Nelemans, “White-dwarf white-dwarf galactic background in the lisa data,” *Phys. Rev. D*, vol. 71, pp. 122003, Jun 2005.
- [47] G. Fabbiano, J. Wang, M. Elvis, and G. Risaliti, “A close nuclear black-hole pair in the spiral galaxy NGC3393,” *Nature*, vol. 477, pp. 431–434, Sept. 2011.
- [48] C. Hogan and P. Binetruy, “Gravitational Waves from New Physics,” in *astro2010: The Astronomy and Astrophysics Decadal Survey*, 2009, vol. 2010 of *ArXiv Astrophysics e-prints*, p. 129.
- [49] M. Armano, M. Benedetti, et al., “Lisa pathfinder: the experiment and the route to lisa,” *Classical and Quantum Gravity*, vol. 26, no. 9, pp. 094001, 2009.
- [50] R. W. P. Drever, J. L. Hall, F. V. Kowalski, J. Hough, G. M. Ford, A. J. Munley, and H. Ward, “Laser phase and frequency stabilization using an optical resonator,” *Applied Physics B: Lasers and Optics*, vol. 31, pp. 97–105, 1983, 10.1007/BF00702605.
- [51] E. D. Black, “An introduction to Pound-Drever-Hall laser frequency stabilization,” *American Journal of Physics*, vol. 69, pp. 79–87, Jan. 2001.
- [52] R. J. Cruz, *Development of the UF LISA Benchtop Simulator for Time Delay Interferometry*, Ph.D. dissertation, University of Florida, 2006.
- [53] B. S. Sheard, M. B. Gray, D. E. McClelland, and D. A. Shaddock, “Laser frequency stabilization by locking to a lisa arm,” *Physics Letters A*, vol. 320, no. 1, pp. 9–21, 2003.

- [54] Y. Yu, *Arm Locking for Laser Interferometer Space Antenna*, Ph.D. dissertation, University of Florida, 2011.
- [55] M. Vallisneri, "Synthetic lisa: Simulating time delay interferometry in a model lisa," *Phys. Rev. D*, vol. 71, pp. 022001, Jan 2005.
- [56] J. W. Conklin, S. Buchman, et al., "LAGRANGE: LAser GRavitational-wave ANtenna at GEO-lunar Lagrange points," *ArXiv e-prints*, Nov. 2011.
- [57] P. Amaro-Seoane, S. Aoudia, et al., "eLISA: Astrophysics and cosmology in the millihertz regime," *ArXiv e-prints*, Jan. 2012.
- [58] R. F. Voss and J. Clarke, "Flicker (1/f) noise: Equilibrium temperature and resistance fluctuations," *Phys. Rev B*, vol. 13, pp. 556–573, Jan. 1976.
- [59] M. Mansuripur, *The physical principles of magneto-optical recording*, Cambridge University Press, 1998.
- [60] J. Franz and V. Jain, *Optical communications components and systems: analysis, design, optimization, application*, CRC Press, 2000.
- [61] H. Nyquist, "Thermal agitation of electric charge in conductors," *Phys. Rev.*, vol. 32, pp. 110–113, Jul 1928.
- [62] L. G. Kazovsky and D. A. Atlas, "Miniature Nd:YAG lasers: noise and modulation characteristics," *Journal of Lightwave Technology*, vol. 8, pp. 294, 1990.
- [63] C. C. Harb, T. C. Ralph, E. H. Huntington, D. E. McClelland, H.-A. Bachor, and I. Freitag, "Intensity-noise dependence of nd:yag lasers on their diode-laser pump source," *J. Opt. Soc. Am. B*, vol. 14, no. 11, pp. 2936–2945, Nov 1997.
- [64] F. Isen, *DSP for MATLAB and LabVIEW: Fundamentals of discrete signal processing*, Synthesis lectures on signal processing. Morgan & Claypool Publishers, 2009.
- [65] I. Bilinskis, *Digital alias-free signal processing*, John Wiley, 2007.
- [66] R. Lyons, *Understanding Digital Signal Processing*, Prentice Hall, 2010.
- [67] D. Dallet and J. Silva, *Dynamic characterisation of analogue-to-digital converters*, Kluwer international series in engineering and computer science. Springer, 2005.
- [68] W. Klipstein, P. G. Halverson, R. Peters, R. Cruz, and D. Shaddock, "Clock noise removal in lisa," *AIP Conference Proceedings*, vol. 873, no. 1, pp. 312–318, 2006.
- [69] R. W. Hellings, "Elimination of clock jitter noise in spaceborne laser interferometers," *Phys. Rev. D*, vol. 64, pp. 022002, Jun 2001.
- [70] D. A. Shaddock, "Space-based gravitational wave detection with lisa," *Classical and Quantum Gravity*, vol. 25, no. 11, pp. 114012, 2008.

- [71] M. Tinto, D. A. Shaddock, J. Sylvestre, and J. W. Armstrong, "Implementation of time-delay interferometry for lisa," *Phys. Rev. D*, vol. 67, pp. 122003, Jun 2003.
- [72] T. Laakso, V. Valimaki, M. Karjalainen, and U. Laine, "Splitting the unit delay [fir/all pass filters design]," *Signal Processing Magazine, IEEE*, vol. 13, no. 1, pp. 30–60, jan 1996.
- [73] D. A. Shaddock, B. Ware, R. E. Spero, and M. Vallisneri, "Postprocessed time-delay interferometry for lisa," *Phys. Rev. D*, vol. 70, pp. 081101, Oct 2004.
- [74] S. Barke, M. Tröbs, B. Sheard, G. Heinzel, and K. Danzmann, "Eom sideband phase characteristics for the spaceborne gravitational wave detector lisa," *Applied Physics B: Lasers and Optics*, vol. 98, pp. 33–39, 2010, 10.1007/s00340-009-3682-x.
- [75] D. Sweeney, *Laser Communications for the LISA and the University of Florida LISA Laser Interferometry Simulator*, Ph.D. dissertation, University of Florida, 2012, unpublished.
- [76] W. Press, *Numerical recipes in FORTRAN: the art of scientific computing*, FORTRAN Numerical Recipes. Cambridge University Press, 1992.
- [77] J. Thorpe and G. Mueller, "Experimental verification of arm-locking for lisa using electronic phase delay," *Physics Letters A*, vol. 342, no. 3, pp. 199–204, 2005.
- [78] V. Wand, Y. Yu, S. Mitryk, D. Sweeney, A. Preston, D. Tanner, G. Mueller, J. I. Thorpe, and J. Livas, "Implementation of armlocking with a delay of 1 second in the presence of doppler shifts," *Journal of Physics: Conference Series*, vol. 154, no. 1, pp. 012024, 2009.
- [79] A. Sutton and D. A. Shaddock, "Laser frequency stabilization by dual arm locking for lisa," *Phys. Rev. D*, vol. 78, pp. 082001, Oct 2008.
- [80] K. McKenzie, R. E. Spero, and D. A. Shaddock, "Performance of arm locking in lisa," *Phys. Rev. D*, vol. 80, pp. 102003, Nov 2009.
- [81] Y. Yu, S. J. Mitryk, and G. Mueller, "Experimental validation of dual/modified dual arm locking for lisa," *Classical and Quantum Gravity*, vol. 28, no. 9, pp. 094009, 2011.
- [82] A. Preston, *Stability of Materials for Use in Space-based Interferometric Missions*, Ph.D. dissertation, University of Florida, 2010, unpublished.
- [83] J. C. Livas, J. I. Thorpe, K. Numata, S. Mitryk, G. Mueller, and V. Wand, "Frequency-tunable pre-stabilized lasers for lisa via sideband locking," *Classical and Quantum Gravity*, vol. 26, no. 9, pp. 094016, 2009.
- [84] Y. Yu, V. Wand, S. Mitryk, and G. Mueller, "Arm locking with doppler estimation errors," *Journal of Physics: Conference Series*, vol. 228, no. 1, pp. 012044, 2010.

- [85] M. Vallisneri, “Geometric time delay interferometry,” *Phys. Rev. D*, vol. 72, pp. 042003, Aug 2005.
- [86] M. Tinto, J. W. Armstrong, and F. B. Estabrook, “Discriminating a gravitational wave background from instrumental noise in the lisa detector,” *Phys. Rev. D*, vol. 63, pp. 021101, Dec 2000.
- [87] N. J. Cornish, “Detecting a stochastic gravitational wave background with the laser interferometer space antenna,” *Phys. Rev. D*, vol. 65, pp. 022004, Dec 2001.
- [88] D. A. Shaddock, “Operating lisa as a sagnac interferometer,” *Phys. Rev. D*, vol. 69, pp. 022001, Jan 2004.
- [89] J. W. Armstrong, F. B. Estabrook, and M. Tinto, “Time-delay interferometry for space-based gravitational wave searches,” *Astrophysical Journal*, vol. 527, no. 2, pp. 814, 1999.
- [90] N. J. Cornish and R. W. Hellings, “The effects of orbital motion on lisa time delay interferometry,” *Class. Quantum Grav.*, vol. 20, no. 22, pp. 4851–4860, 2003.
- [91] D. A. Shaddock, M. Tinto, F. B. Estabrook, and J. W. Armstrong, “Data combinations accounting for lisa spacecraft motion,” *Phys. Rev. D*, vol. 68, pp. 061303, Sep 2003.
- [92] D. A. Shaddock, “Space-based gravitational wave detection with LISA,” *Class. Quantum Grav.*, vol. 25, no. 11, pp. 114012, jun 2008.
- [93] J. J. Esteban, I. Bykov, A. F. G. Marín, G. Heinzel, and K. Danzmann, “Optical ranging and data transfer development for lisa,” *Journal of Physics: Conference Series*, vol. 154, no. 1, pp. 012025, 2009.
- [94] A. Sutton, K. McKenzie, B. Ware, and D. A. Shaddock, “Laser ranging and communications for lisa,” *Opt. Express*, vol. 18, no. 20, pp. 20759–20773, Sep 2010.
- [95] M. Tinto, M. Vallisneri, and J. W. Armstrong, “Time-delay interferometric ranging for space-borne gravitational-wave detectors,” *Phys. Rev. D*, vol. 71, pp. 041101, Feb 2005.
- [96] R. J. Coates, “Tracking and Data Acquisition for Space Exploration,” *Space Sci. Rev.*, vol. 9, pp. 361–418, May 1969.
- [97] S. E. Pollack and R. T. Stebbins, “A demonstration of lisa laser communication,” *Classical and Quantum Gravity*, vol. 23, no. 12, pp. 4201, 2006.
- [98] E. Hogenauer, “An economical class of digital filters for decimation and interpolation,” *IEEE Transactions on Acoustics Speech and Signal Processing*, vol. 29, no. 2, pp. 155–162, 1981.

- [99] A. Oppenheim, A. Willsky, and S. Nawab, *Signals and systems*, Prentice-Hall signal processing series. Prentice Hall, 1997.
- [100] Y. Levin, “Internal thermal noise in the ligo test masses: A direct approach,” *Phys. Rev. D*, vol. 57, pp. 659–663, Jan 1998.
- [101] “Rev. d m112648 adt4-5wt,” reprinted with permission from Samuel A. Baylis, <http://www.minicircuits.com/pdfs/ADT4-5WT.pdf>.
- [102] “Rev. c m112648 adt1-6t,” reprinted with permission from Samuel A. Baylis, <http://www.minicircuits.com/pdfs/ADT1-6T.pdf>.
- [103] P. L. Bender and D. Hils, “Confusion noise level due to galactic and extragalactic binaries,” *Classical and Quantum Gravity*, vol. 14, no. 6, pp. 1439, 1997.
- [104] S. J. Mitryk, V. Wand, and G. Mueller, “Verification of time-delay interferometry techniques using the University of Florida LISA interferometry simulator,” *Class. Quant. Grav.*, vol. 27, pp. 084012, 2010.
- [105] G. de Vine, B. Ware, K. McKenzie, R. E. Spero, W. M. Klipstein, and D. A. Shaddock, “Experimental demonstration of time-delay interferometry for the laser interferometer space antenna,” *Phys. Rev. Lett.*, vol. 104, pp. 211103, May 2010.
- [106] S. Mitryk, “Lisa-matlab data-analysis functions,” <http://www.phys.ufl.edu/research/lisa/DOCUMENTS/LISAFUNC/>.

BIOGRAPHICAL SKETCH

Shawn Mitryk was born in Willingboro, NJ in the summer of 1983. Growing up in close contact with a large family, Shawn was always surrounded by people who were more than happy to satisfy his curiosity. After moving to Florida, Shawn became interested in many aspects of both the arts and sciences, and eventually, found his niche in physics. After obtaining an engineering background education from the University of Florida in 2006, Shawn continued to obtain a PhD. in experimental physics with the Laser Interferometer Space Antenna Project in May of 2012.